Development of Novel Monocarboxylate Transporter Inhibitors as Potential Anticancer Agents

A THESIS

SUBMITTED TO THE FACULTY OF

UNIVERSITY OF MINNESOTA

BY

GRADY NELSON

IN PARTIAL FULFILLMENT OF THE REQUIREMENTS

FOR THE DEGREE OF

DOCTOR OF PHILOSOPHY

Venkatram R. Mereddy

APRIL 2019

ACKNOWLEDGEMENTS

I would like to express my appreciation and sincere gratitude to Dr. Venkatram R. Mereddy for his continued support and guidance in pursuing my PhD and professional career. Furthermore, I would like to express my deepest gratitude to my committee members Dr. Joseph Johnson for being there for me through my undergraduate and graduate programs. Dr. Teresa Rose-Hellekant for her invaluable help with *in vivo* studies and consultation in both my academics and career opportunities. Dr. Jon Holy for always being there to talk about everything from western blots to the future.

I would like to acknowledge Departments of Chemistry and Biochemistry, College of Pharmacy, Integrated Biosciences, DOD-BCRP, Whiteside Clinical Research Institute, University of Minnesota, Randy Shaver Cancer Research Community for the financial support during my Ph.D. studies.

I would like to thank Shirisha and Sravan Jonnalagadda, Lucas Solano, Conor Ronayne, Tanner Schumacher, Zachary Gardner and all the present and past members of our lab for their incessant support given to me for the past five years. I would also like to thank my family for being there with me ever step of the way and all their support throughout my career. Finally, I would like to thank Karen who supported me through the toughest times and longest hours as I finished the most important process of my PhD program and preparing for the next step of my life.

ABSTRACT

Grady Nelson, *Development of Novel Monocarboxylate Transporters For The Treatment of Cancer: In Vitro and In vivo Studies*, Doctor of Philosophy (Integrated Biosciences), University of Minnesota.

The metabolic phenotype of cancer cells is dependent on the differential oxygen and nutrient distribution in the tumor microenvironment. These diminishing resources coupled with increased energetic and biosynthetic demands of tumor cells further encourage the upregulation of glycolysis with overexpression of related enzymes and transporters. This shift towards a more glycolytic character results in a disruption of the intracellular pH as the cell rapidly becomes more acidic. The accumulation of acidic byproducts like lactic acid requires new strategies to maintain cellular homeostasis resulting in the overexpression of transporters. These extracellular acidic byproducts are taken up by neighboring cells and are utilized for oxidative phosphorylation (OxPhos). Cancer cells often switch between glycolysis and OxPhos to meet the energy demands, termed as metabolic plasticity, which is driven by a necessity to avoid conditions that would induce apoptosis. For this reason, cancer cells express proton coupled monocarboxylate transporters 1-4 (MCT1-4). Specifically, these transporters have been found to be expressed in the most aggressive tumors and ultimately been linked to poor patient outcome. Hence, this transporter can be targeted for therapeutic intervention to treat a wide variety of cancers.

One well known MCT1 inhibitor α-cyano-4-hydroxycinnamic acid (CHC) has been traditionally used to study the functions of these transporters and it has been found to

reduce tumor growth in mouse xenograft models. The therapeutic potential of CHC is hindered by its lack of efficacy at low concentrations and very high dose requirement for significant anticancer efficacy *in vivo*. In this regard, we have modified the CHC template with alkyl and aryl silyl substitutions and also introduced nitric oxide donors. These structural modifications have resulted novel candidate compounds which exhibit potent MCT1 and MCT4 inhibition and higher cell proliferation inhibition on several cancer cell lines. These drug candidates have also been evaluated for their effects on glycolytic and mitochondrial metabolic parameters. These studies have shown that all the lead derivatives have significant effects on both metabolic processes. Further *in vivo* preclinical evaluation of lead candidate compounds indicate that these compounds are generally well tolerated in healthy mice and exhibit growth inhibition in MCT1 and MCT4 expressing tumor models.

TABLE OF CONTENTS

LIST OF SCHEMES

LIST OF FIGURES

LIST OF TABLES

LIST OF ABBREVIATIONS

ATP	adenosine triphosphate
MCT	monocarboxylic acid transporter
SLC16	solute carrier 16
kDa	kilo Dalton
OxPhos	oxidative phoshprylation
ER	estrogen receptor
HER-2	human epidermal growth factor-2
TNBC	triple negative breast cancer
PR	progesterone receptor
Cav	caveolin
ROS	reactive oxygen species
RNS	reactive nitrogen species
HIF-1α	hypoxia inducing factor
NF-κB	nuclear factor kappa-light-chain-enhancer
DNA	deoxyribonucleic acid
GLS	glutaminase
GDH	glutamate dehydrogenase
αKG	α-ketoglutarate
CHC	α-Cyano-4-hydroxy cinnamic acid
µmol	micromoles
LLc	Lewis lung carcinoma

mM	millimolar
CAM	chicken chorioallantoic membrane
DIDS	disodium 4,4'-diisothiocyanatostilbene-2,2'-disulfonate
IC_{50}	inhibition of 50% of the activity or cell growth
K_i	inhibitor constant
VDAC	voltage-dependent anion channel
MPC	mitochondrial pyruvate carrier
FDA	food and drug administration
3-BPA	3-bromopyruvic acid
mg/Kg	dosage in milligram per kilogram of mouse
NSG	NOD/LtSz-scid IL-2Rγ null mice
RBE4	rat brain endothelial 4 cell line
F	fluoro
Br	bromo
CN	cyano functional group
NO_2	nitro functional group
CH_3CN	acetonitrile
NH_4Ac	ammonium acetate
dpm	disintegrations per minute
OH	hydroxy functional group
DMF	*N*,*N*-dimethylformamide
$POCl_3$	phosphorus (V) oxychloride

R-Br	alkyl/aryl bromide
H_2O	water
Bu_4NI	tetra-*n*-butyl ammonium iodide
$CNCH_2COOH$	cyanoacetic acid
HBr	hydrobromic acid
H_2SO_4	sulfuric acid
PBr_3	phosphorous tribromide
nM	nanomolar
SEM	standard error of the mean
SAR	structure-activity relationship
K_2CO_3	potassium carbonate
SRB	sulforhodamine-B
MTT	3-(4,5-dimethylthiazol-2-yl)-2,5-diphenyltetrazolium bromide
MEM	minimum essential medium
DMEM	Dulbecco's minimum essential medium
PI	propidium iodide
FCM	flow cytometry
acetyl CoA	acetyl coenzyme A
DMSO	dimethyl sulfoxide
ip	intraperitoneal
bid	twice a day
q.d	once a day

q.i.d	four times a day
CYP	cytochrome P450 enzyme
PBS	phosphate buffered saline
EtOH	ethanol
NaOH	sodium hydroxide
BBr_3	boron tribromide
HEPES	(4-(2-hydroxyethyl)-1-piperazineethanesulfonic acid)
GST	glycolysis stress test
MST	mitochondrial stress test
ECAR	extracellular acidification rate
OCR	oxygen consumption rate
mpH	milli pH
pmol	pico moles
AZD	AZD3965
FCCP	carbonyl cyanide-4-(trifluoromethoxy)phenylhydrazone
ETC	electron transport chain
Dox	doxorubicin
WT	wild type
KO	knock out
^{1}H NMR	Proton (^{1}H) nuclear magnetic resonance spectrum
^{13}C NMR	Carbon (^{13}C) nuclear magnetic resonance spectrum
HRMS	high resolution mass spectrometer

FBS	fetal bovine serum
ATCC	American type cell culture
TLC	thin layer chromatography
HCl	hydrochloric acid
Hz	Hertz
MHz	Mega Hertz
J	Coupling constant
$CDCl_3$	deuterated CDCl3
mA	milli amperes
PBST	phosphate buffered saline with Tween 20

CHAPTER 1: Introduction

CHAPTER 1: Introduction to Cancer Metabolism

1.1 Cancer Heterogeneity and Hallmarks

For the pursuit of effective therapeutics in the treatment of cancers, the emerging information and potential targets have exponentially expanded. A previously simplistic view of cancer progression being based on aberration and uncontrolled growth has compounded as the factors driving tumor promoting processes have been expanded upon. Now it is understood that tumor progression is a myriad of biochemical exchanges and recruitment of both cancerous and neighboring stromal fibroblast cells.[1–4] The development from aberrant cellular growth to an aggressive malignancy is driven through genetic instability, biochemical, and physical signaling and their resulting downstream mechanisms. These factors help in the development of the heterogeneity in the tumor environment required to persist and overcome many impasses that would prevent such aberrant growth of endogenous cells.[1,2] The various processes and tumor promoting environments have resulted in a need for categorizing and classifying these differences between the epithelial cancerous cells and stromal fibroblasts. The need for classification and defining these differences was satisfied through the landmark review *Hallmarks of Cancer*.[5,6] These hallmarks are important for they represent a classification system that can be used to drive therapeutic development. One of the important hallmarks in cellular signaling promote dysregulation of cellular energetics making it an attractive target for therapeutic intervention.[6–8] The deregulation of cellular energetics via glycolysis and other

factors are important for maintaining the bioenergetics and biosynthetic demands of rapid cellular proliferation.

1.2 Overcoming energetic impasse

Cancer progression favors cells that are capable of rapid proliferation, outcompeting the slow growing cells. This aberrant metabolic phenotype represents an impasse required for cellular progression as ATP production becomes a limiting factor. Normal cellular growth favors ATP production using oxidative phosphorylation (OxPhos). This is a more efficient process than glycolysis with the production of 32-36 moles of ATP for one mole of glucose.[9] While efficient, this process requires the usage of a complex electron transport system and the establishment of proton gradients which are all contained in the mitochondria. Another process that cancer cells extensively utilize for swift ATP production is glycolysis. Contrary to OxPhos, the method of ATP production via glycolysis is dependent on enzymatic activity and can easily be modified via overexpression of glycolytic proteins. The preference for glycolysis in ATP production, even in a well oxygenated environment, has led to the identification of a new characteristic of cancer cells which is called aerobic glycolysis. One of the main reasons behind the preference of a glycolytic phenotype within late stage cancer cells is due to the flexibility and relative ease of rapid ATP production via glycolysis when compared to OxPhos.[10–14] Previous studies have highlighted this preference, as cells were able to produce ATP quicker by overexpressing glycolytic proteins than cells that are dependent on ATP production via OxPhos.[15]

Preference for glycolysis also addresses another concern of rapidly proliferating cells, the development of hypoxic regions. Initial development of solid tumors occurs within oxygen and nutrient rich environments provided from the vasculature system. Rapid proliferation leads to cells outgrowing the existing blood vessels and the formation of hypoxic pockets. Glycolysis imparts a natural advantage for it does not require oxygen for ATP production like OxPhos. This advantage leads late stage cells to depend on glycolysis as a main ATP productions source.[11,16,17] The preference for glycolytic phenotype in cancer cells is a well observed phenomenon and has its own demerits that tumors must overcome in order to maintain and achieve a rapid proliferative advantage.

1.3 Warburg Effect and the tumor's dilemma

The extracellular acidification was first recorded by Otto Warburg who postulated that the reduction of the pH of the culture medium was due to a more glycolytic cell line. This insight is why the phenomenon has been termed the Warburg Effect (WE). The metabolic reprogramming that cancer cells undergo favors a dependency on glycolysis for most of the ATP production. One fundamental issue with glycolytic dependency is the need to maintain cellular homeostasis. The major byproduct of glycolysis is a surplus of lactic acid. Accumulation of lactic acid increases as a cell becomes more glycolytic resulting in apoptosis via cellular acidosis.[18–20] In order to maintain cellular homeostasis, cancer cells begin to upregulate glycolytic transport proteins. The proteins of our specific interest are proton coupled transporters that export the abundance of lactate to the extracellular environment. This flux of acidic byproducts results in a rapid acidification of the surrounding environment.

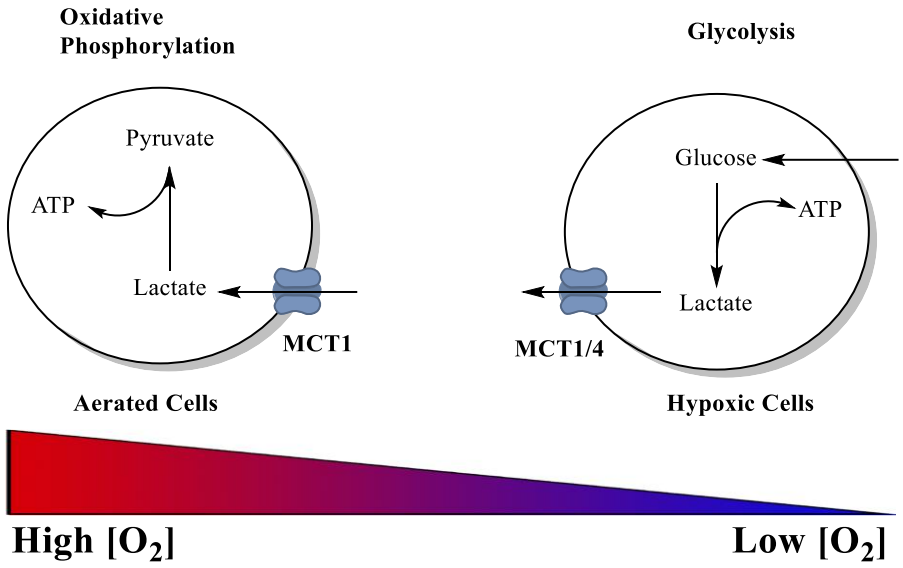

Figure 1a: The intratumoral symbiotic relationship based on lactate transport between aerobic OxPhos cells and glycolytic hypoxic cells.

Aerobic glycolytic phenotype is an initial response to the ATP deficiency because of rapid cellular proliferation and further glycolytic dependency is stimulated by the formation of hypoxic regions as the tumor growth outpaces angiogenesis.[12,13,21] The next problem as a result of increased acidic byproducts which is a rapid decrease in the extracellular pH. This represents another impasse as the rapid lowering of pH can result in the cellular death. To maintain the tumor microenvironment, aerobic cells import the excess lactate converting it into pyruvate and utilize it as an energy source for OxPhos. This metabolic symbiosis between hypoxic and aerobic cancer cells results in the optimal usage of glucose and maintenance of an acidic microenvironment (**Figure 1a**). The slight acidity of the tumor microenvironment is well documented and has been linked to pro-oncogenic events like stimulation of angiogenic factors, invasion, metastasis, and reduction of immune responses.[22–24] The transporters directly involved in the shuttling of lactate into

and out of the cell have been extensively studied and their over expression has been linked to treatment failure, relapse, and patient mortality.[25] Their role in the maintenance of cellular energetics and tumor homeostasis makes them an excellent target for therapeutic intervention.

1.4 Monocarboxylic acid transporters (MCTs)

The MCTs belong to a family of the *SLC16* gene that codes for a wide variety of different transporters. All the transporters of this family are proton-linked in the plasma membrane. Their role is to shuttle small monocarboxylic acids such as lactate, pyruvate and other ketone bodies across the cellular membrane.[26,27] Within the *SLC16* gene family, there are 14 known isoforms of MCT and it is known that MCT1 and MCT4 are critically involved in the symbiotic relationship of lactate transport between aerobic and hypoxic cells within the tumor.[28] The MCT1 is a 40 kDa protein that spans 12 transmembrane domains with hydrophobic α-helical segments.[29] The transmembrane nature of the protein makes it difficult to discern the crystal structure but there have been some good homology models created for the design of therapeutic derivatives.[30,31] Differences in these transporters results in MCT1 favoring the export of lactate and MCT4 favoring the import. For this system, glucose is actively being taken up by the hypoxic cells for glycolysis and the aerobic cells become dependent on the extracellular lactate for most of their energy production. The role that MCT1 and MCT4 play in the maintenance of cellular homeostasis makes them attractive target for cancer treatment. MCTs are overexpressed in cancer cells due to their glycolytic switch, and only minimally expressed in normal tissues.[32–34] Previous studies have revealed that successful inhibition of MCT1 and/or MCT4 has led to

rapid decrease of intracellular and extracellular pH resulting in cellular acidosis and the development of intratumoral necrosis.[35–38].

1.5 Previously reported MCT1 and MCT4 inhibitors

The α-cyano-4-hydroxy cinnamic acid (CHC) is a well-known inhibitor of MCT1 for more than four decades (**Figure 1b**). Classically, its function has been reserved to plant growth regulation but has been gaining some attention due to its significant *in vivo* anticancer efficacy in various tumor models.[12,35,39]

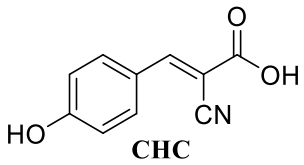

CHC

Figure 1b: Chemical structure of MCT1 inhibitor CHC.

Anticancer efficacy studies using CHC were conducted by Sonveaux et al. CHC was used in the treatment of SiHa, a human cervix squamous cell carcinoma, and WiDr, a human colorectal adenocarcinoma. It was found that the treatment with MCT1 inhibitor *in vitro* results in the reprogramming of the cells' metabolic phenotype and cause cell death.[39] Furthermore, intraperitoneal administration *in vivo* at a concentration of 25 μM showed significant reduction in Lewis Lung carcinoma and WiDr xenograft models. A non-MCT1 expressing cell line hepatocarcinoma TLT conducted in a syngenic Rj:NMRI mice did not exhibit any significant anti-cancer efficacy. This study supports the significance of MCT1 inhibition for therapeutic effect in cancer treatment. The results presented in this study warranted further research and development of the potent CHC analogs and MCT inhibition as a viable therapeutic target.

Our lab synthesized a large library of CHC derivatives and evaluated for their *in vitro* MCT1 inhibitory potential and *in vivo* efficacy. The simplicity and tolerance of the Knoevenagel condensation with cyanoacetic acid allowed for rapid synthesis of novel CHC analogs based on a wide variety of benzaldehydes (**Scheme 1a**).

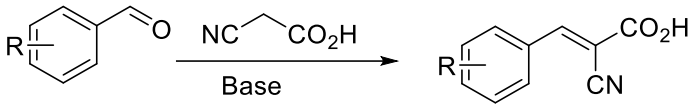

IC50: 1-50 μM

R= OMe, OEth, Br, Cl, F, NO_2, CN, Me, Et, iPr, tButyl, etc.
NR'_2
Where R'=Me, Eth, Propyl, Butyl, Pentyl,
phenyl, benzyl, pyrrolidinyl, piperidinyl, etc...

Scheme 1a: Knoevenagel condensation of substituted benzaldehydes with cyanoacetic acid to form CHC based derivatives.

A myriad of benzaldehydes was condensed with the cyanoacetic acid and the resulting products were evaluated for their MCT1 inhibition properties. Initial studies indicated that substitution of the *p*-hydroxyl group in CHC with electron withdrawing groups such as halides, CN, and NO_2 and electron donating groups such as methoxy, 3,4-methylenedioxy, alkyl, and *N,N*-dialkyl improved MCT1 inhibition compared to parent CHC. These results from MCT1 inhibition assay highlighted the importance of lipophilic alkyl/aryl substitution on the *para* position of the phenyl ring of CHC. Especially, the MCT1 inhibition activity was enhanced when simple *N,N*-dialkyl groups such as methyl, ethyl, propyl, and butyl groups were introduced. Extending the lipophilicity to more than four carbons resulted in reduction of activity. The MCT1 inhibition properties were also enhanced when diphenyl and benzyl groups were incorporated to the amino CHC template.

Our further SAR studies indicated that introduction of a methoxy group at the *ortho* position to the cyano acrylic acid group further enhanced the efficacy of *N,N*-dialkyl CHC template (**Scheme 1b**). The results of this SAR along with other *in vitro* assays identified compound **1.6** for further preclinical development (**Figure 1c**).

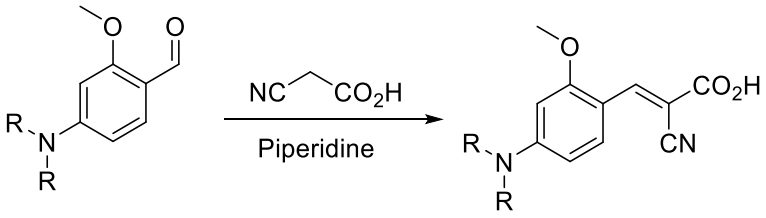

Scheme 1b: A representative scheme for the synthesis of the library of *N,N*-dialkyl amino CHC derivatives.

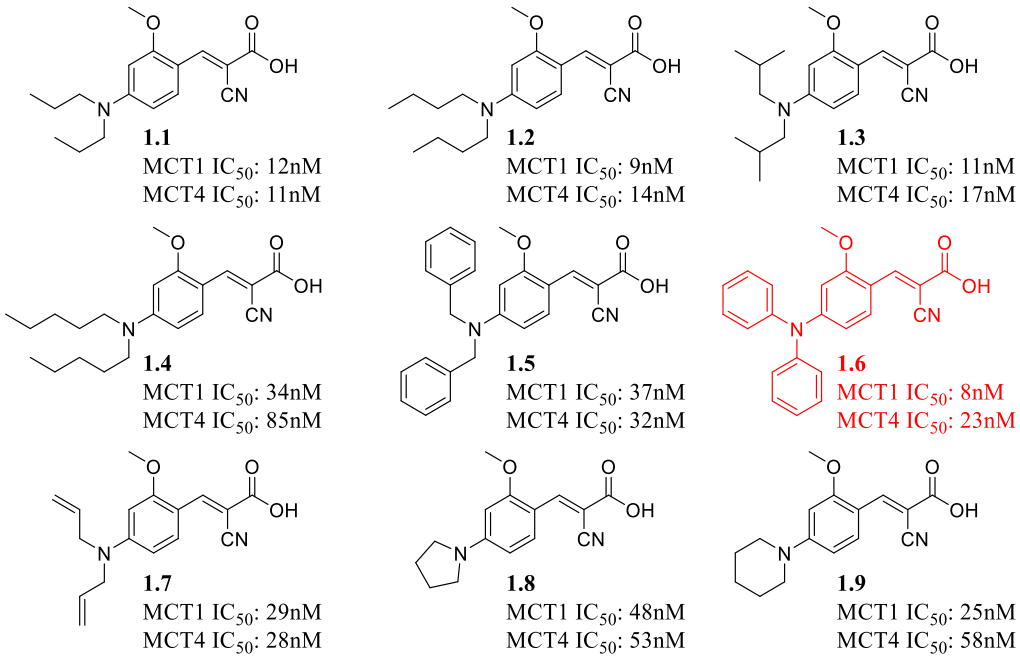

Figure 1c: The SAR study of the *N,N*-dialkyl/diaryl substituted CHC derivatives

Studies into various modifications of the cyano (-CN), carboxylic acid (-CO_2H) resulted in the lowered activity towards MCT1. Reduction of the double bond also lead to a complete loss of activity. As previously described, MCT4 plays a vital role in the metabolic symbiosis of intratumoral region (**Figure 1a**). Since the CHC based derivatives exhibited significant MCT1 inhibition activity, we envisioned the cyanoacrylic acid unit may also play a significant role in the inhibition of similar transporters such as MCT4. In this regard the most efficacious derivatives, *o*-methoxy *N,N*-dialkyl CHCs described in **Figure 1c**, were evaluated for their inhibition of MCT4. All the tested derivatives showed MCT4 inhibition activity similar to that of MCT1.[30]

The *N,N*-diphenyl CHC (**1.16**) with a methoxy *ortho* substitution (**Figure 1c**) and the *N,N*-dibenzyl coumarin carboxylic acid were identified as a lead candidate compounds based on their selective inhibitory capacity towards MCT1 and/or MCT4. These derivatives have been identified as lead candidate compounds and selected for further preclinical development *in vivo*.

Another structural analog that was found to have strong MCT1 inhibition was coumarin carboxylic acid. Owing to the importance of coumarin in providing pharmacological and pharmaceutical properties, our group also explored structurally similar but bicyclic aminocarboxy coumarin derivatives as potential MCT inhibitors. Modification of this structure started with various dialkyl substitutions to the amino group on the amino salicylaldehyde. Condensation of dialkylated salicylaldehydes with diethyl malonate followed by base hydrolysis and subsequent acidic workup provided dialkyl aminocarboxy coumarins (**Scheme 1c**). Similar to CHC derivatives, the synthesized *N,N*-

dialkyl aminocarboxy coumarins had increased specificity to MCT1 inhibition albeit lower than the CHC derivatives (**Figure 1d**). Interestingly, none of the coumarin derivatives have any significant MCT4 activity up to 1µM concentration except the lead dibenzyl derivative which has an IC_{50} of ~200nM.[38,40]

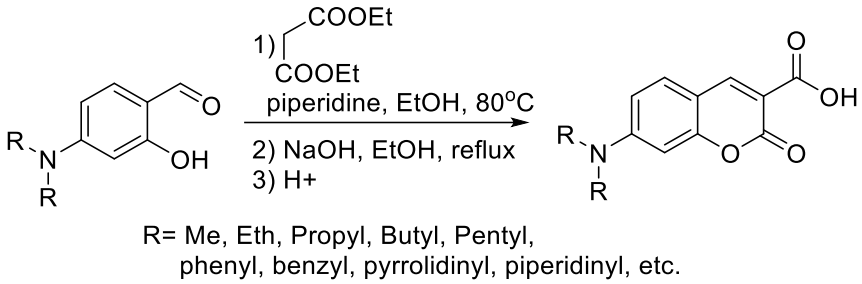

Scheme 1c: A representative scheme for the synthesis of the library of *N*,*N*-dialkyl aminocoumarin derivatives.

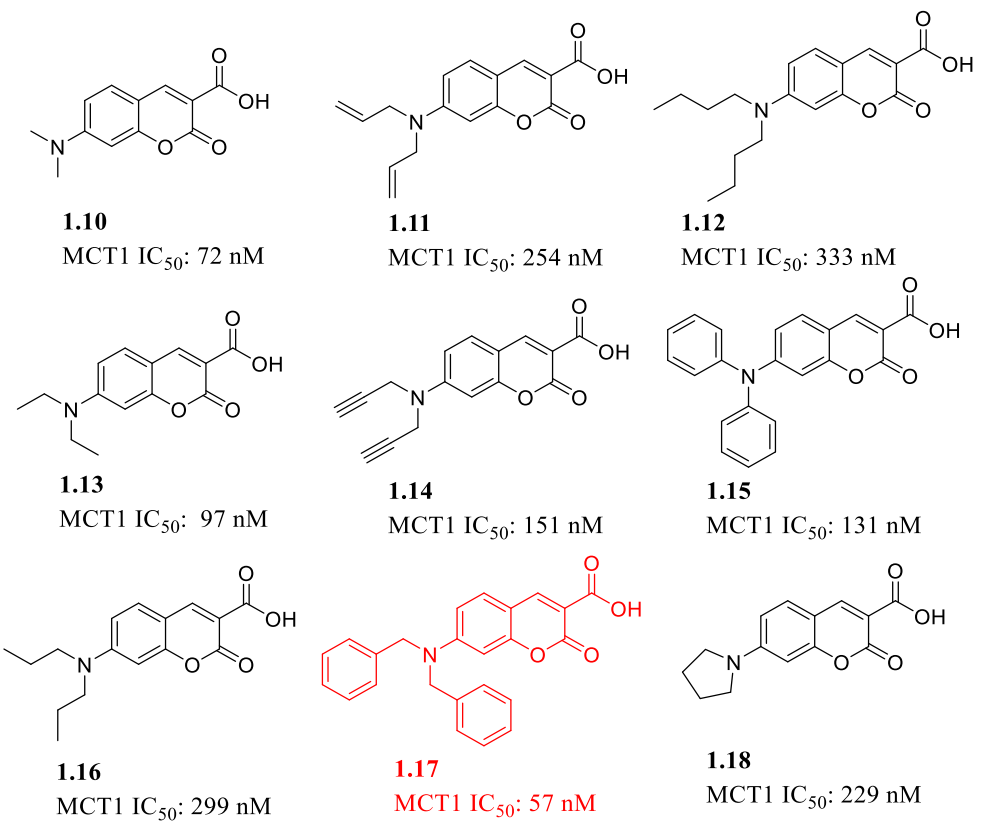

Figure 1d: List of the *N,N*-dialkyl aminocoumarin derivatives and their corresponding MCT1 inhibition activity.

The candidate coumarin derivative **1.17** was evaluated *in vivo* in MCT1 expressing glioma cell line GL261-luc2 in C57BL/J6 mice and this compound exhibited significant tumor growth inhibition of 77% and was comparable to clinically used temozolomide. [40]

A

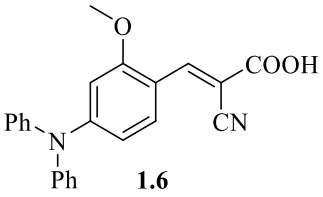

1.6

In vitro IC_{50} values
MCT1 IC_{50} = 8nM
MCT4 IC_{50} = 23nM
MDA-MB-231 EC_{50} = 80µM
4T1 EC_{50} = 50µM

In vivo tumor growth inhibition
TNBC MDA-MB-231: ~60%
Colorectal WiDr: ~50%

B

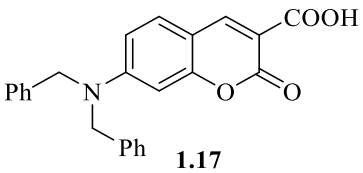

1.17

In vitro IC_{50} values
MCT1 IC_{50} = 48nM
MCT4 IC_{50} = 200nM
MDA-MB-231 EC_{50} = 242µM
4T1 EC_{50} = 109µM

In vivo tumor growth inhibition
Glioma GL261-luc2: ~80%

Figure 1e: The *in vitro* and *in vivo* activity of the candidate compounds designed in the CHC and the coumarin based project.

Based on the excellent *in vitro* MCT1 inhibition results from the dialkyl aminocarboxy coumarins, Draoui et al. conducted further preclinical development on these compounds. Initial evaluation using MCT1 uptake assays identified the most potent MCT1 inhibitors **1.18** and **1.19** (**Figure 1f**). Further preclinical development of these derivatives via several anticancer efficacy studies on MCT1 expressing tumor models were carried out with excellent results.

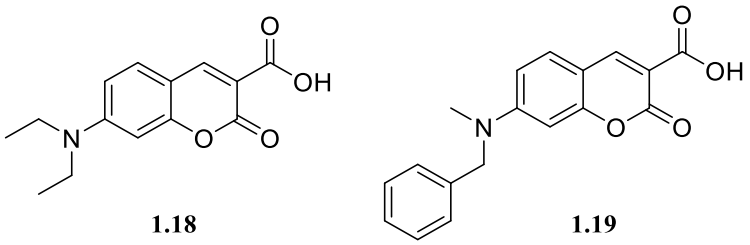

Figure 1f: Structures of the lead coumarin based MCT1 inhibitors **1.18** and **1.19**

Candidate compounds **1.18** and **1.19** were tested against SiHa based cervical tumor model and the HCT-116 colorectal model. Administration of **1.18** and **1.19** was at a dosage of 3 mg/Kg. Even at a low dosage, the candidate compounds exhibited significant anticancer efficacy against MCT1 expressing SiHa and HCT-116. As a negative control, candidate compounds **1.18** and **1.19** were tested against low MCT1 expressing UM-UC-3 bladder cancer tumor model. The UM-UC-3 xenograft study did not have any significant reduction in the tumor burden highlighting the importance of MCT1 expression as a target for chemotherapy.[38]

1.6 Competing MCT1 inhibitors for therapeutic applications

Utilizing MCT1 as a potential target for therapeutic intervention is actively being investigated by other labs for the development of chemotherapeutics. The pharmaceutical company AstraZeneca has developed a series of MCT1 inhibitors. SAR study on thienopyrimidones had identified candidate compounds AZD3965 and ARC155858 (**Figure 1g**). Both these inhibitors are selective towards MCT1 inhibition only and do not exhibit any MCT4 inhibition properties.[41] The MCT1 efficacy was evaluated using L-lactate transport study on rat erythrocytes and xenopus oocytes.

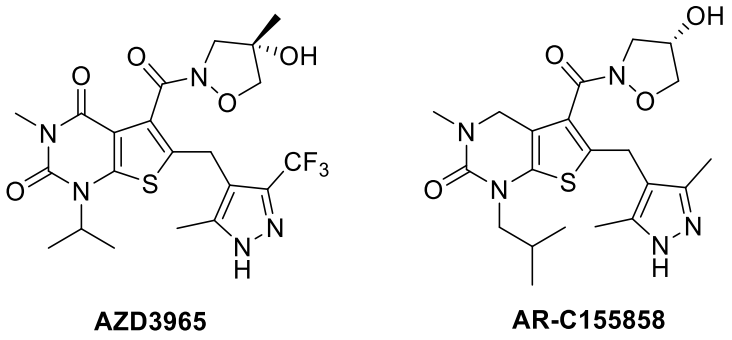

Figure 1g: Structures of AZD3965 and ARC158858

The ARC155858 exhibited significant efficacy towards the transporter in rat erythrocytes and xenopus oocytes with K_i values of 2.3nm and 100nM, respectively. To evaluate the therapeutic potential of this enhanced efficacy for the transporter, ARC155858 was screened against 64 different cancer cell lines from NCI. These derivatives were especially active against MCT1 expressing cell lines DLBCL, Burkitt's lymphoma, and other haemotological cell lines that predominantly express MCT1. [42]

By carrying out further studies, the derivative AZD3965 was identified as the lead candidate compound. Anticancer efficacy studies were conducted with this compound in nonobese diabetic scid-γ mice xenografted with COR-L103 which was isolated from human lung small cell carcinoma. AZD3965 was administered at a dosage of 100mg/kg and the candidate compound exhibited ~60% tumor growth inhibition.[43] Furthermore, immunohistochemistry studies on whole tumor after treatment found that AZD3965 caused increased intracellular lactate accumulation in the COR-L103 cells.

Another preclinical evaluation of AZD3965 for its potential therapeutic benefits against a metastatic model was also carried out using luciferase-expressing CA46 Burkitt lymphoma cell line in NOD/LtSc-scid IL-2Rγ null (NSG) mice. Candidate compound

AZD3965 was administered at 100mg/kg with significant reduction in tumor burden and metastatic sites.[44] These studies were enough to elevate the lead candidate compound to be filed as an investigative new drug. It is now currently in phase-I clinical trials for diffuse large B-cell lymphoma, Burkitt lymphoma, and other solid tumors.

Investigation of substituted pteridine diones and triones

Another SAR study in the pursuit of a more efficacious and selective MCT1 inhibitor was conducted by Wang et al. In this SAR study, various substitutions on the pteridine diones and triones were employed and their effect on MCT1 activity was evaluated. MCT1 evaluation was conducted in MCF7 cell line that have been transfected to overexpress the MCT1 transporter. The synthesis of the inhibitors focused the importance of hydrophobic side groups to enhance the lipophilic characteristics of the derivatives. Furthermore, introduction of strategically placed hydroxyl groups into the template were found to have enhanced activity towards MCT1.

Evaluation of the MCT1 inhibitory activity indicated that trione substitutions (MCT1 IC_{50}: 548 nM) resulted in less activity when compared to the dione derivatives (MCT1 IC_{50}: 116-192 nM). This was largely attributed to the placement of the hydroxyl tether placement on the C5 or C6 carbon (**Figure 1h**).

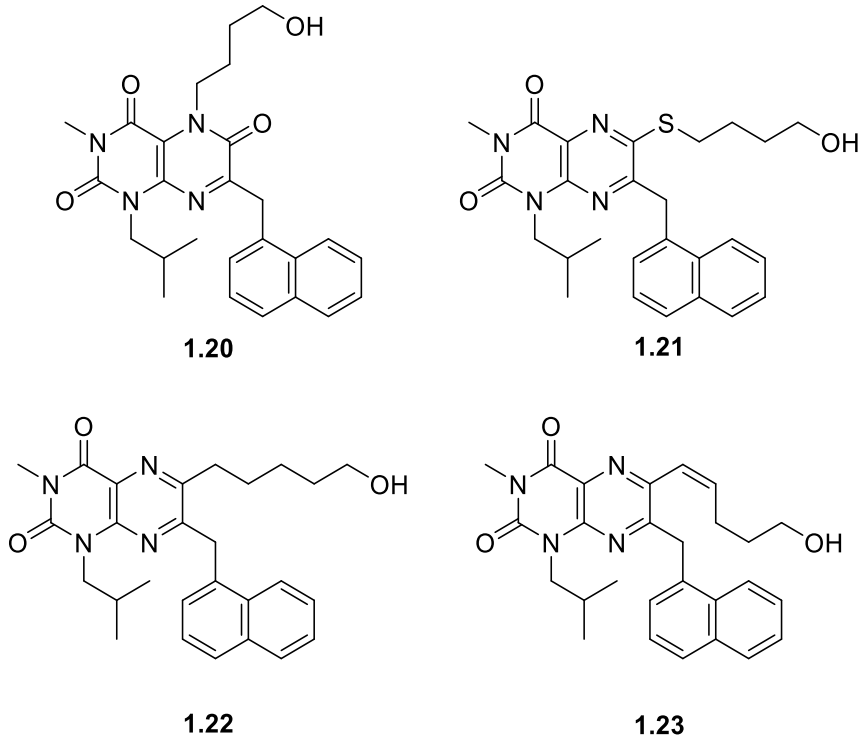

Figure 1h: Structures of pteridine trione and diones.

As seen with derivative **1.20**, the hydroxyl tether is directed to the C5 nitrogen group. This significantly reduced the MCT1 selectivity and a higher IC_{50} value. When placed on the C6 carbon in the dione derivatives **1.21-1.23**, there is a significant increase in the activity of the derivatives. This degree of selectivity is important for driving a more efficacious inhibitor for MCT1 activity.

The enhanced potency of the inhibitors also correlated with improved antiproliferative activity. These derivatives were tested against an MCT1 expressing cell line Raji lymphoma. The MTT assay supported the direct connection between MCT1 inhibition and antiproliferative activity. The most potent MCT1 inhibitors had major antiproliferation with nanomolar activity towards this cell line. This work helped to identify

candidate compounds and a scaffold for further SAR study for the preclinical development of a new therapeutics that could take advantage of the MCT1 transporter inhibition.[45]

Pyrazole methylpropanoic acid derivatives as MCT4 inhibitors

As further studies identify the therapeutic importance of MCT1 inhibitors, researchers have begun to conduct SAR studies to identify therapeutics that are selective to MCT4 transporter as well. In developing a more efficacy inhibitor for MCT4, a library of 2-((1-(2-chlorobenzyl)-5-(3-substituted phenyl)-1H-pyrazol-3-yl)methoxy)-2-methylpropanoic acids were reported (**Figure 1i**). These derivatives exhibited excellent specificity towards the MCT4 activity.

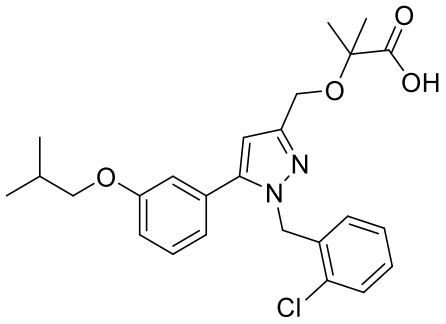

isobutyl substituted pyrazole methyl propanoic acid

Figure 1i: Lead MCT4 inhibitor 2-((1-(2-chlorobenzyl)-5-(3-substituted phenyl)-1H-pyrazol-3-yl)methoxy)-2-methylpropanoic acid

A library of derivatives was evaluated for their MCT4 inhibition activity against the MCT4 expressing cell line MDA-MB-231. The pyrazole derivatives exhibited potent MCT4 inhibition in nM range. The pyrazole methylpropanoic acid (**Figure 1i**) was very effective at inhibition of lactate transport exhibiting an IC_{50} for MCT4 at 1nM. This

derivative has excellent specificity as the IC_{50} for MCT1 was 5600 nM and was evaluated in the for MCT1 expressing BT20 cell line.

1.7 Further development and improvements

While the CHC derivatives exhibited a significant reduction in tumor burden *in vivo* there is room for improvement in the PK/PD parameters of the drug. Furthermore, there is significant room for increasing the antiproliferative nature of these derivatives. One potential route is combining two anti-metabolic derivatives into one molecular aggregate. In previous research had hinted at the therapeutic advantage of an MCT inhibitor with another derivative causing mitochondrial disfunction. The proposed idea was to take a known MCT1 and MCT4 inhibitor syrosingopine and metformin which is a known derivative with selective inhibition of mitochondrial activity (**Figure 1j**). Metformin disrupts mitochondrial activity by targeting complex I in the electron transport chain. The result of this is a significant reduction in mitochondrial activity.

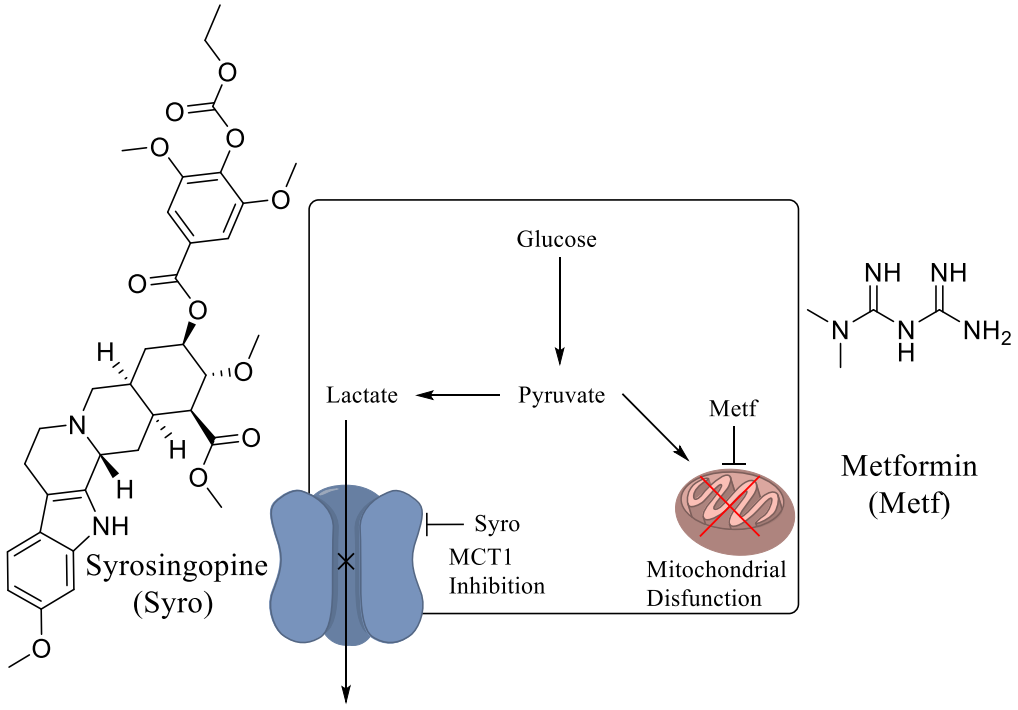

Figure 1j: Proposed duel mechanism of action for inducing apoptosis in cells.

The result of the study showed that MCT1 and/or MCT4 inhibition using syrosingopine resulted in significant increase in lactate accumulation. This led to inhibition of lactate dehydrogenase activity leading to a significant reduction in NAD+ regeneration. The inhibition activity of metformin on complex I resulted in a significant reduction in NAD+ regeneration via mitochondrial activity. The cumulative decrease in NAD+/NADH ratio severely hinders any ATP production within the cell and ultimately leads to cell death.[46] This study supports the merits of utilizing a dual mechanistic approach in order to enhance the therapeutic potential of the MCT inhibitors. The incorporation of a mitochondrial disrupting functional group could potentially enhance the activity and selectivity of the derivatives towards cancerous cells.

Using MCT1 and MCT4 as potential targets for therapeutic intervention has been supported by successful development of therapeutics for cancer treatment. There are some areas for improvement on these inhibitors. The first of which is the pharmacokinetic properties of the derivatives. In most cases the inhibitors are found to be 99% protein bound and have a relatively quick clearance from the system.[40] Furthermore, the derivatives were effective at reducing the tumor growth but do not exhibit any tumor elimination. The impact of the following projects is the improvement on the well-established MCT1 and MCT4 inhibitors by combing various chemical and biological approaches. These strategies aim to exploit the tumor microenvironment and over expression of various proteins for selective targeting of MCT1 and MCT4 inhibitors and the cytotoxic components coupled to them. The hypothesis is to develop derivatives with enhanced pharmacokinetic properties that could lead to not only tumor reduction but elimination as well.

CHAPTER 2: Literature survey on the importance of silyl groups in improving the pharmacological and pharmaceutical properties of drug candidates

2.1 Silicon as an emerging chemical entity for therapeutics development

Most of the therapeutics created for the treatment of wide variety of diseases contain elements such as hydrogen, carbon, nitrogen, oxygen, sulfur etc. Recent therapeutic development has focused on expanding upon the classically used elements and incorporating other hetero atoms. Silicon is the 14th element and is located under carbon in the periodic table. The proximity to each other help to highlight the chemical similarities between the two elements. Both elements have a valency of four and readily form tetrahedral compounds (**Figure 2a**).

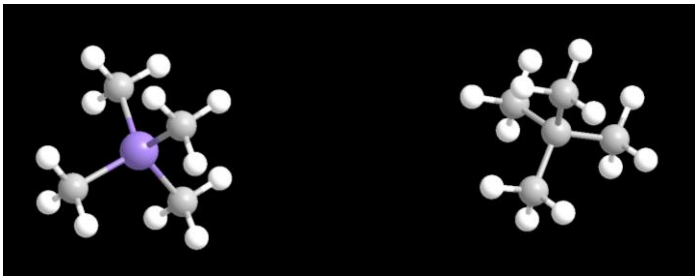

Figure 2a: Comparison of the four valance of silicon (purple) and carbon (gray) with simple methyl groups attached to the center atom.

Where the two elements diverge is their ability to form π bonds. Carbon has a unique self-linking property called catenation, that allows it to form double and triple bounds. Furthermore, C-C bonds are very stable entities while Si-Si bonds are generally unstable. The Si-O bond is very stable when compared to the C-O bond and explains why silicon is naturally found as silicates instead of Si-Si complexes.[47] These differences in bond properties are a consequence resulting from the differences in the electronegativity

of the two atoms. While carbon has an electronegativity of 2.55, the electronegativity of the silicon atom is 1.99. This difference results in a larger sharing of electrons between the silicon atom and those it binds to when compared to the carbon atom.

Even with some major differences in the electronegativity and radii between the two elements, silicon has gained some attention as a bioisosteric replacement of carbon. Bioisosteres are elements or groups that exhibit similar physicochemical properties and are commonly used to improve pharmacological and pharmaceutical properties of a drug entity without changing the mechanism of action.[48,49] The replacement of carbon with silicon is known as the "silicon switch" and this replacement could provide some therapeutic advantages.[50]

The most prevalent advantage of the "silicon switch" is a change in the pharmacokinetic properties of the drug. Normal enzymatic reactions convert therapeutics into more polar metabolites that are water soluble and easily excreted. Enzymatic reactions require very specific chemical configurations of the ligands where substrates for metabolic clearance commonly involve carbon-oxygen, carbon-nitrogen, carbon-sulfur, nitrogen-oxygen, and oxygen-hydrogen bonds. In contrast, silicon represents a foreign element that does not fit the normal configuration. The silicon atom has a different electronegativity resulting in a very different bond polarity because the silicon atom has a larger radius and the silicon bond length is almost 20% longer when compared to carbon.[47] This change from carbon to silicon has been used to create new molecular entities with desired therapeutic benefit but lack toxic side effects from secondary metabolites.

One example is haloperidol which is commonly used as an antipsychotic drug but is metabolized readily into a pyridinium derivative that is a quaternary amine. This pyridinium metabolite has been found to cause neurotoxic side effects as it is a structural analog of the known neurotoxin 1-methyl-4-phenylpyridinium (MMP^+).[51] The bioisoteric replacement with the silicon atom in silahaloperidol results in a different metabolic pathway and metabolites (**Figure 2b**). The resulting metabolites do not include the pyridinium structure and therefore no neurotoxic effects are observed.

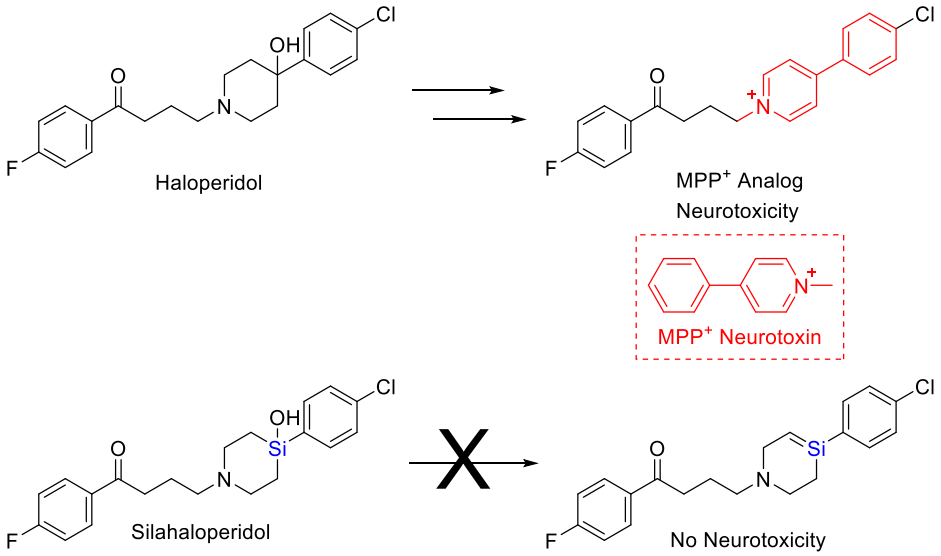

Figure 2b: The antipsychotic drug haloperidol and its downstream neurotoxic metabolite.

The silicon analog silahaloperidol has an alternative metabolic process that lacks the neurotoxic pyridinium structure. Another example of the improved therapeutic potential by a "silicon switch" is with loperamide. This therapeutic is an antidiarrheal drug with three major metabolites that are stable under physiological conditions and the N-desmethyl loperamide has been linked to increased cardiomyopathy and QTc prolongation.[52] The incorporation of the silicon atom within this compound resulted in a

change in the metabolism of the drug resulting in three new metabolites. One of the metabolites is highly water soluble and easily excreted (**Figure 2c**).[51,53,54] The result of this high clearance metabolite is an overall reduction of the metabolite burden and potential reduction of cardiomyopathy and QTc elongation.

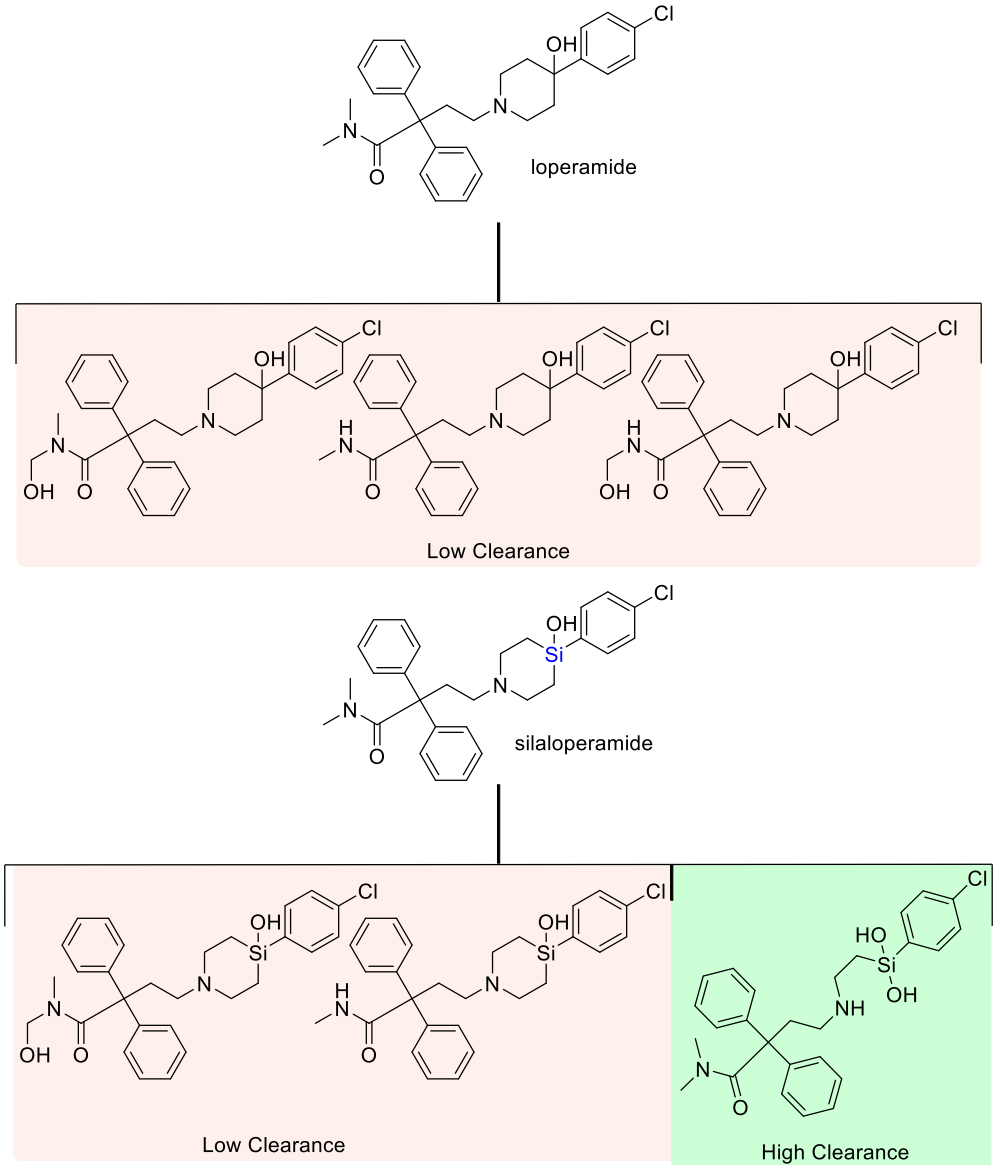

Figure 2c: The two drugs loperamide and its silicon analog silaloperamide along with the observed metabolites and clearance.

The introduction of a silicon atom has another added benefit with an increase in the lipophilicity of the derivative. The silicon atom is more lipophilic when compared to carbon.[55] This substitution has been linked to improved cell penetration and a better therapeutic potential.[56] Furthermore, the blood-brain barrier represents a very difficult impasse for majority of anticancer agents. The diffusion of small molecules across this barrier is correlated to the lipophilicity of the drug. The replacement with a more lipophilic element has been connected to increased permeability of that drug across the blood-brain barrier. [57] This strategy was employed to enhance the transport of oxazolidinone antibiotics by incorporating the silicon atom (**Figure 2d**).

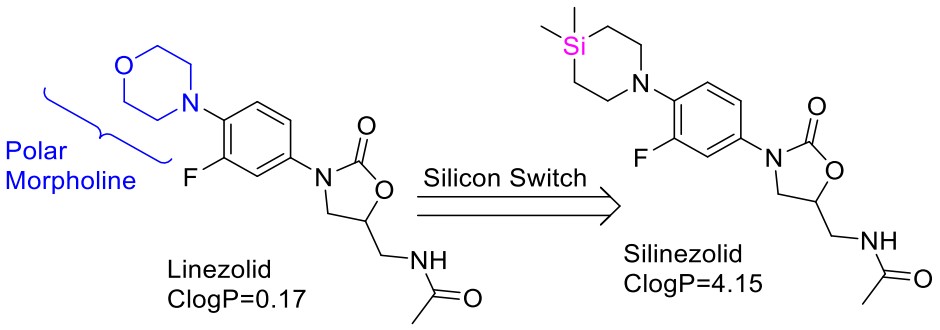

Figure 2d: Substitution of the oxygen in linezolid to form the silinezolid.

One study looked to improve the therapeutic potential of the antibiotic drug linezolid by replacing the carbon with silicon atom.[58] It was found that replacement of the oxygen in the morpholine ring with silicon significantly increased the distribution of the compound in the brain when compared to the plasma. This increase in blood-brain barrier permeability has been attributed to the increased lipophilicity of the compound.[58]

Lipophilicity also enhances the partitioning of drugs *in vivo*. The anticancer drug camptothecin is commonly bound to albumin where the lactone is easily hydrolyzed.

Incorporation of silicon entity increased the lipophilic nature of camptothecin resulting in increased partitioning into the red blood cells (**Figure 2e**). This increase partitioning in the red blood cells resulted in better distribution and a longer half-life of the silyl Camptothecin derivatives.

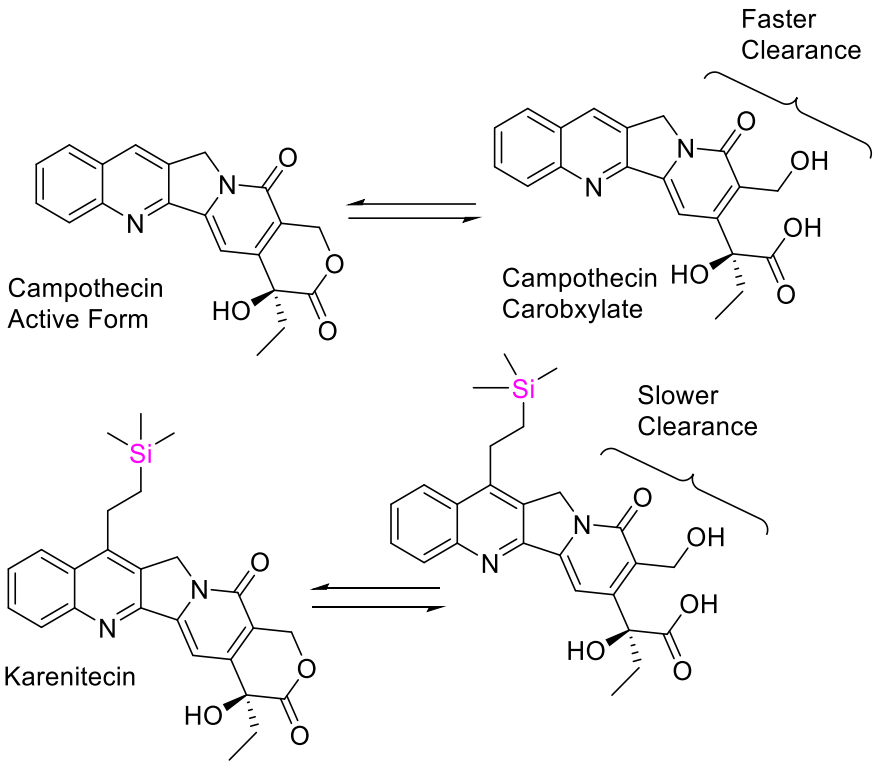

Figure 2e: The difference between the Camptothecin and its more hydrophilic silicon analog Karenitecin.

Furthermore, these derivatives were able to pass the blood-brain barrier more efficiently when compared to the unsilylated derivative.[59,60]

2.2 Silyl ethers-more than just a protecting group

One of the more interesting properties of silylated derivatives is their usage as a prodrug. Silyl ethers can easily be cleaved yielding a hydroxyl group. Silyl ethers represent a class of protecting groups commonly used in organic chemistry. These protecting groups are used to prevent the undesired reaction of hydroxyl groups. There are many different variations of silyl ethers with varying degrees of stability. The general trend in stability is tightly correlated with the bulkiness of the functional groups and aromaticity (**Figure 2f**).[61]

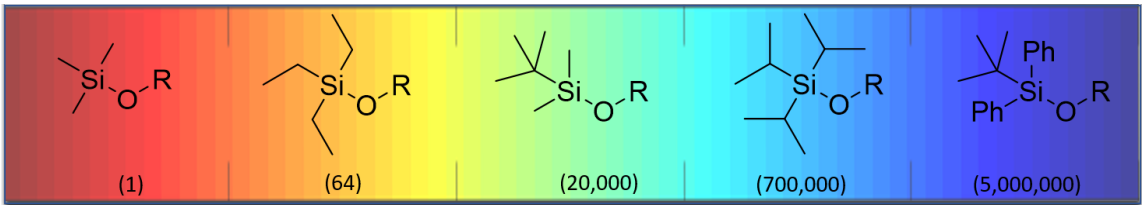

Figure 2f: Various silyl protecting groups and their relative stabilities under acidic conditions (1% HCl in MeOH) when compared to trimethyl silyl ether.

The ease of reactivity of these derivatives combined with the variety of different hydrophobic derivatives have made them an attractive molecular entity to modulate the efficacy of chemotherapeutics. The usage of these derivatives led to an increase in the metabolic parameters such as stability and lipophilicity.[55] Literature reviews indicate that silyl ethers incorporated into therapeutic agents such as testosterone and ephedrines which were evaluated for their drug latency properties. Drug latency is the selective and timely release of the drugs and is known to promote slow release so that the action is apparent over a longer period. This native latency was then compared to the latency of their silyl ether analogs. In all cases, a strong correlation was observed between the silyl protecting group and the increase in the drug latency. In the case of the steroid testosterone, the

testosteroxytrimethylsilane analog extended the drug latency and maximal androgenic activity from 10 days to 30 days when administered in mice.[62] These results support the importance of the silyl ether in enhancing the metabolic stability of a therapeutic (**Figure 2g**).

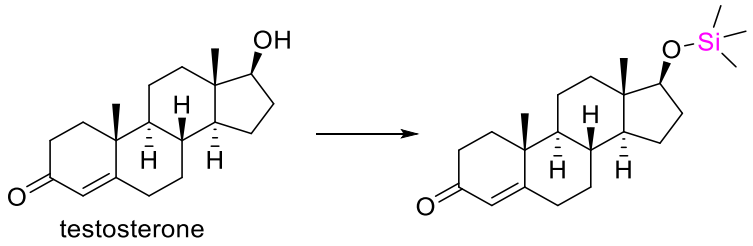

Figure 2g: Incorporation of the silyl ether for enhanced drug latency

Another study investigated the silyl protection of methylephedrine, ephedrine, and norephedrine. Extensive studies were carried out on these silylated derivatives on the stability in phosphate-citrate buffers and partition coefficients. These results indicate that the selective release and hydrophobicity could be modified by changing the substituents on the silicon atom.[63]

More recent studies into the practical therapeutic application using a pro-drug approach observed the enhancement of the antiproliferative activity of ureidoadenosine derivatives (**Figure 2h**). It is well documented that the hydroxyl ureidoadenosine is a potent inhibitor of the kinase BMPR1b but lacks any cytotoxicity *in vitro*. This study indicated that protection of the hydroxyl groups of the ribose with silyl ethers resulted in enhanced antiproliferative effects. This improved activity was attributed to better lipophilic character after silyl ether incorporation. This silyl ether derivative also resulted in an enhanced cell permeability. The incorporation of the silyl ethers as a lipophilic entity has

also enhanced selectivity towards cancerous cells which highlights the potential therapeutic application of this group.

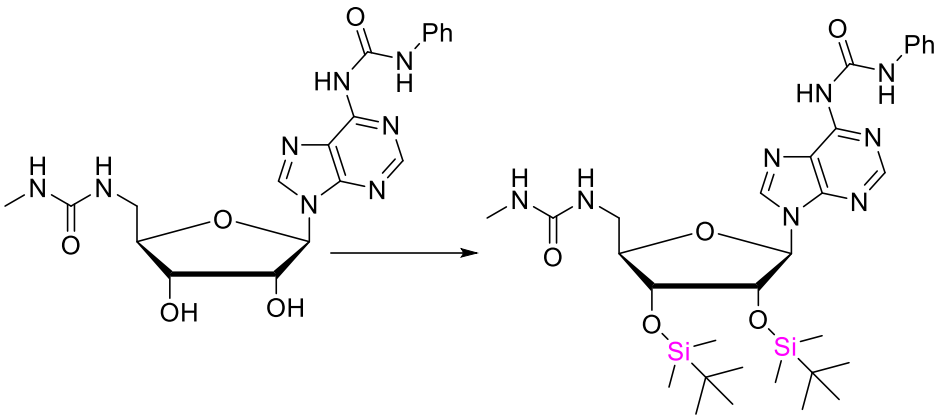

Figure 2h: The prodrug silyl ether of ureidoadenosine

The silyl ether facilitates the membrane penetration of the ureidoadenosine resulting in more accumulation of the drug within the cancer cells. Once in the cytoplasm, the silyl ether is cleaved yielding the potent hydroxyl ureidoadenosine which inhibits the BMPR1b signaling cascade.[64]

2.3 Silyl Ethers as a targeted therapy:

Literature reports show that the acidic microenvironment has been exploited for the selective delivery of chemotherapeutics. For example, acid liable functional groups such as trityls have been previously used in the selective delivery of a chemotherapeutic LY207702 which has acute cardiotoxicity.[65] The theory behind the usage of trityls was that the linked trityl functional group would allow for the selective release of LY207702. The carrier was COL1 which is a murine IgG_{2a} mAb that binds to CEA which is overexpressed in late stage tumors (**Figure 2i**).

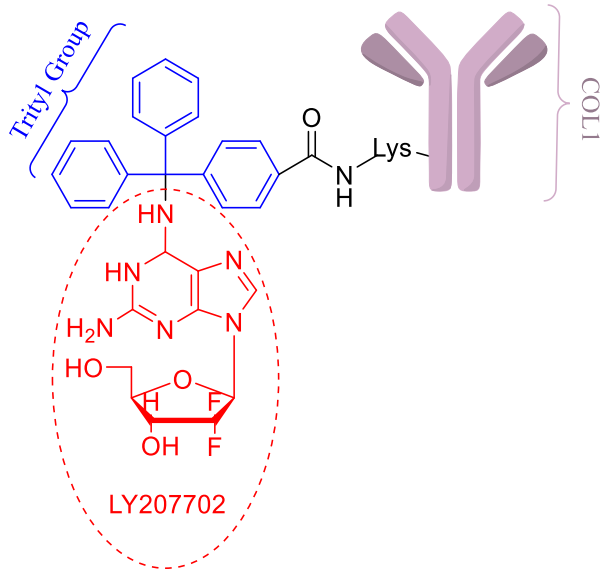

Figure 2i: The structure of the chemotherapeutic LY207702 using an acid liable linker to COL1 for selective delivery to mitigate the cardiotoxicity.

The trityl linked chemotherapeutic had selective release within acidic conditions of 6.4-5.4 while relatively stable under physiological conditions with long $t_{1/2}$ ranging from 146 hours to 33 days. This derivative maintained its anti-proliferative character *in vitro* and exhibited similar antitumor effects against HCT1 based human colon carcinoma in mice. The novelty of this conjugation increased selectivity resulting in a reduction of the cardiotoxicity of LY207702. *In vivo* cardiotoxicity study also showed that the acid labile conjugate did not exhibit any cardiotoxicity in mice while the non-conjugated derivative exhibited some cardiotoxicity. The issue with this approach is that it is synthetically difficult and requires harsh conditions. Furthermore, the release window is longer requiring three hours for a significant release with any therapeutic benefit.

Another example of using acid labile function groups for therapeutic intervention is vinyl ethers.[66] The primary benefit of vinyl ethers was the liposomal delivery of

therapeutics into cancer cells. It was found that the proposed liposomes exhibited excellent stability under physiological conditions, but the resulting PEG vinyl ether was easily cleaved under acidic conditions. This acid labile property was integrated into their liposome carrier by incorporating it into diplasmalogen (DPPlsC). The new entity would result in a liposome of acid-sensitive DPPlsC encapsulating the vinyl ether with the target chemotherapeutic (**Figure 2j**).

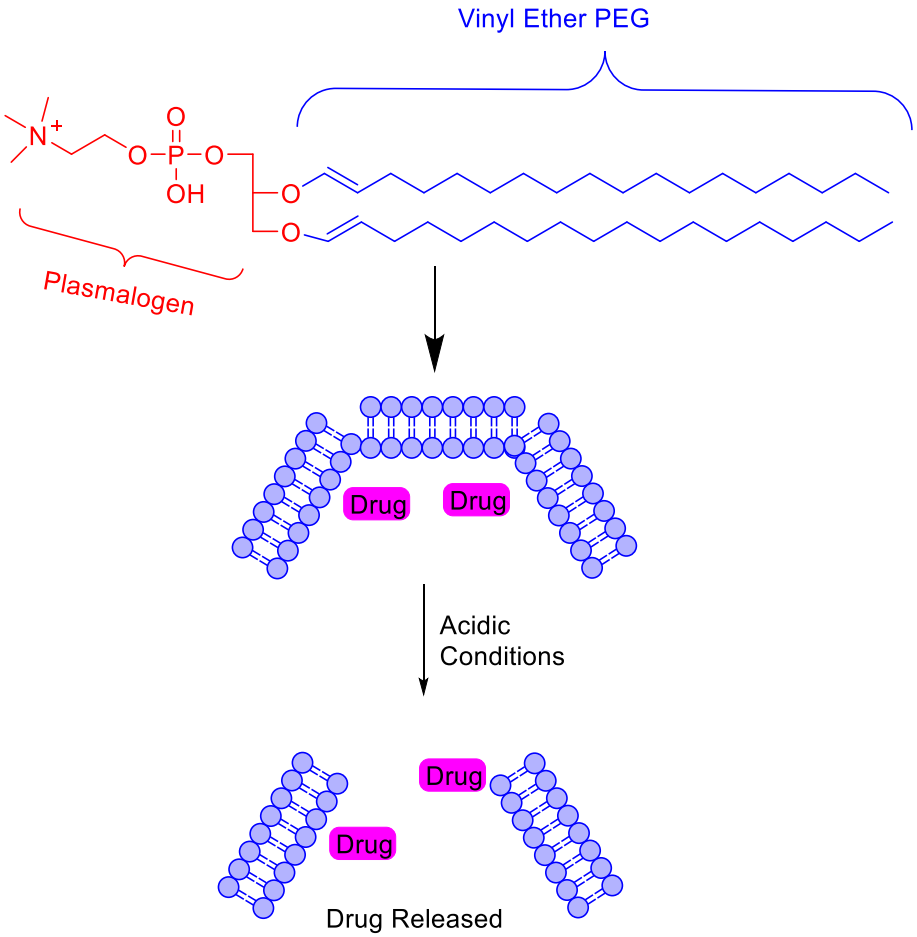

Figure 2j: selective release of the drug payload from the liposome under acidic conditions.

The hypothesis behind this modification was that the liposome carrier would transport the drug safely under physiological conditions. Upon exposure to the acidic microenvironment the drug would be released. The synthesized vinyl ether PEG derivatives exhibited selective release under acidic conditions resulting in increased therapeutic uptake within the cancer cells. The resulting cleavage of the pegylated plasmalogen led to a lamellar-to-micellular phase transition ($L\alpha$-H_I). The issue here is the difficulty of the chemistry required to form the acid liable lipids. Furthermore, there is a lack of flexibility due to limited PEG vinyl ethers[67].

Another approach for selective delivery of chemotherapeutic via acid liable function groups was conducted on an anticancer agent doxorubicin. Previous studies have resulted in the synthesis of a doxorubicin pro-drug with an acid labile hydrazine.

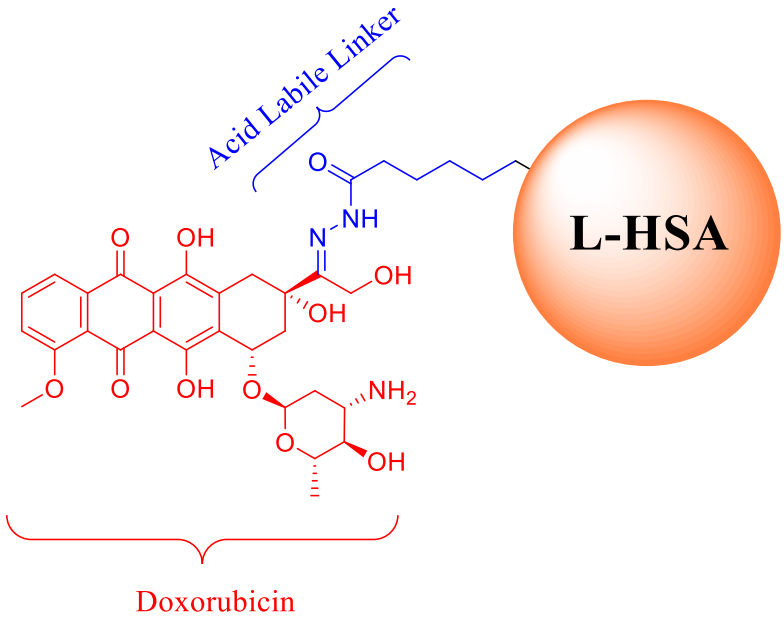

Figure 2k: The combination of doxorubicin with the protein L-HSA and the acid liable linker allowing for the selective release under acidic conditions.

The doxorubicin derivative was linked to lactosaminated human albumin (L-HAS). The selectivity of L-HAS was attributed to the over expression of asialoglycoprotein receptors in the human hepatocellular carcinomas (HCCs). The result of this study was a selective pro-drug of doxorubicin that exhibited very little systemic toxicity when evaluated in mice. Furthermore, this study showed that there was selective accumulation of the drug in the liver at the site of the carcinoma. These results support the effectiveness of acid liable pro-drugs, especially when linked to a targeted carrier such as L-HSA (**Figure 2k**).[68]

Using a similar approach, the silylated protecting groups can be employed as acid labile groups. There are several advantages of this strategy compared to other acid labile groups. First advantage is the ability to "tune" the stability of the protecting group. As stated previously, the substituents on the silyl atom have a strong effect on the stability of the derivative prodrug under acidic conditions. If a quicker release is required, a prodrug that utilizes the TBS group could be used. If a longer and more stable derivative is required, the DPS protection group can be attached instead. Another advantage is the release of non-toxic byproducts. Upon cleavage of the silyl protection group, the resulting silyl oxide by itself is not known to be toxic. Finally, the procedures and conditions required for the synthesis of the product are simple, mild and amenable to large scale synthesis.

Previous research studied the incorporation of acid labile silicate groups to scaffolds that selectively target the tumor. In all cases, this was accomplished via a bifunctional silyl bridge (**Figure 2l**). Initial synthesis resulted in the coupling of a toxic chemotherapeutic such as camptothecin or gemcitabine to a polymerizable monomer like acrylate. The resulting coupling of the two entities resulted in reactive acrylate group which

could couple the chemotherapeutic to a delivery particle of choice. This selective delivery of the chemotherapeutic was dependent on the linker. Various acid liable substitutions were incorporated into the linker region with varying results.[69,70]

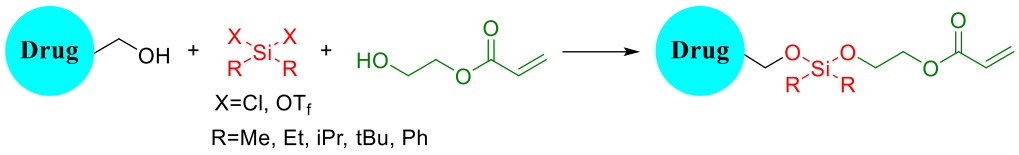

Figure 2l: Silyl ether a prodrug approach for selective delivery of toxic therapeutic agents to the tumor site for payload delivery of cancer chemotherapeutics.

This selective releasing mechanism was also tested using mesoporous silica nanoparticles. Various silylated linking groups were used to tailor the release of the active drug camptothecin under weakly acidic conditions (pH 6.8), while no release was detected at a physiological pH of 7.4.[69] In both studies, it was found that there was a significant increase in drug retention with the increase in bulkiness on the silyl group. The change in the R group from simple ethyl group to ^{t}Butyl (**Figure 2l**) resulted in the difference in $t_{1/2}$ from 1.36 hours to 6995 hours.[70]

2.4 Mitochondrial dysfunction via biomineralization of accumulated silyl ether

A recent report on the therapeutic potential of simple silyl ether supported an interesting claim of the silyl ether template. In this study, silyl ether was coupled via a simple carbon chain to a quaternary triphenyl phosphonium salt. The triphenyl phosphonium salt is well known to act as a selective carrier to the mitochondria within cancer cells (**Figure 2m**).

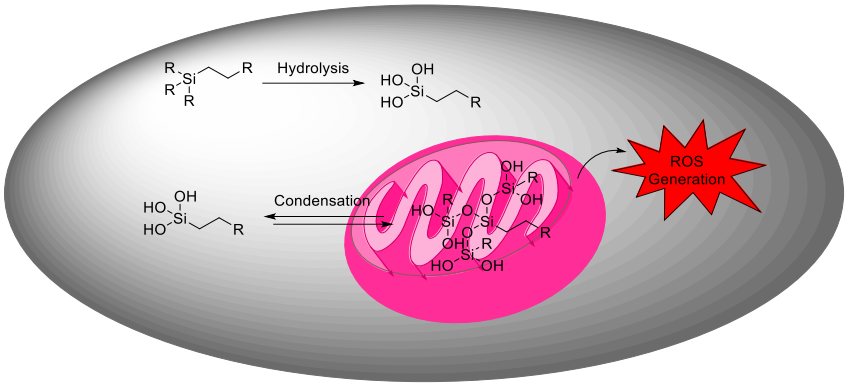

Figure 2m: The synthesized triphenylphosphine silicate was transported into the cell and the silicate was hydrolyzed followed by biomineralization within the mitochondria leading to ROS release.

Selective accumulation of silicate followed by hydrolysis were shown to result in condensation or biomineralization forming aggregates of the hydroxy silyl within the mitochondrial matrix. This biomineralization was supported using time dependent light scattering and *in vitro* TEM imaging techniques. Mitochondrial destabilization was also supported by mitotracker red imaging which showed fragmentation and membrane depolarization of mitochondria after exposure with the silylated derivatives. Translation of the study into SCC7 xenograft model yielded excellent therapeutic benefit with a significant reduction in the tumor over a 15-day study.[71]

CHAPTER 3 Synthesis and Evaluation of Novel Silylated CHC Derivatives as MCT1 Inhibitors

3.1 Rationale for proposed synthesis of silyl CHC derivatives

Our previous SAR studies highlighted the importance of lipophilic functional groups in the para position of the CHC template in improving MCT inhibition properties. Although our previously reported *N*,*N*-dialkyl CHC derivatives exhibited potent and dual MCT1 and MCT4 inhibition properties,[30,40,72–74] but they suffered from few drawbacks such as lack of potent cell proliferation inhibition, metabolic stability and lack of anticancer efficacy at low concentrations in highly aggressive tumor models. As reported in the literature, introduction of silyl groups has significantly improved pharmaceutical and pharmacological properties of several drug candidates. We envisioned that the "silicon switch" can enhance the lipophilicity of the inhibitors as the silicon atom is more lipophilic when compared to nitrogen of the dialkylamino CHC template. In this regard, we proposed to introduce alkyl and aryl silyl groups in place of *N*,*N*-dialkyl groups on CHC template with the goals to improve the lipophilicity, cytotoxicity, and if possible, selectivity towards cancer cells (**Figure 3a**).

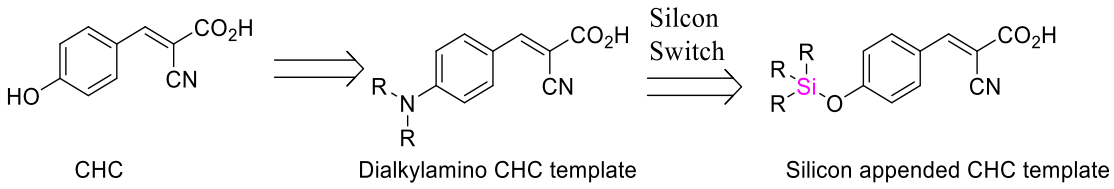

Figure 3a: The proposed silicon switch in place of *N*,*N*-dialkyl/aryl groups on CHC template.

Within the CHC molecule, there is a phenol group at the para position which renders it labile for metabolic sulfonation and glucuronidation resulting in quick clearance from the system. The introduction of the silyl ether group could provide silyl CHC derivatives higher stability and improved pharmacokinetic properties. The proposed template represents a small SAR study to evaluate the effects of incorporating silyl groups into the para position of CHC and their relation to the MCT inhibition properties.

Tumor progression and proliferation are highly dependent on metabolic plasticity between glycolysis and mitochondrial OxPhos. This ability to reprogram metabolic parameters to meet energy demands under unfavorable conditions is vital to survive in a dynamic tumor microenvironment. [75] This metabolic switch to a very flexible source of ATP production ultimately results in a dependency for cells found in hypoxic regions within the tumor. This upregulation of glycolytic enzymes and processes leads to an increased rate of lactic acid production. Rapid export of lactate is facilitated by MCT1 and MCT4 to maintain metabolic symbiosis (**Figure 3b**).

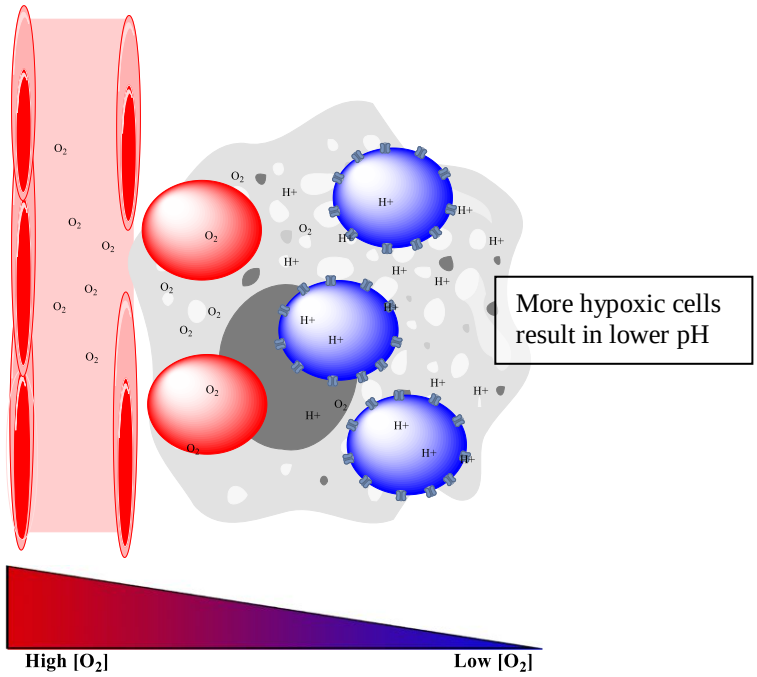

Figure 3b: Graphical representation of distribution of oxygen in the tumor mass. The larger the tumor gets, the more hypoxic (blue cells) it becomes. This results in a buildup of the acidic by product lactic acid (H+) and a lower pH.

We hypothesize that our proposed silyl derivatives would potently inhibit MCT function, enter cytoplasm efficiently, disrupt mitochondrial properties, and affect the metabolic plasticity that exists in many solid tumors. This in turn should effectively limit the options for ATP production stalling cell growth and inducing apoptosis in tumors.

Synthesis of the silylated CHC (**Scheme 3a**) was performed by taking commercially available α-cyano-4-hydroxy cinnamic acid and protecting it using TBSCl and TBDPSCl in the presence of Hunig's base. The silyl protected CHC derivatives **3.1a-b** were readily purified via ethyl acetate extraction followed by silica gel column chromatography. Attempts to attach the isopropyl protecting group TIPS were

unsuccessful due to the low yield of formation and lack of the stability on the silica gel-based column. The TBDPS **3.1a** and TBS **3.1b** protected derivatives were stable at room temperature and were purified using a base quenched silica gel column chromatography.

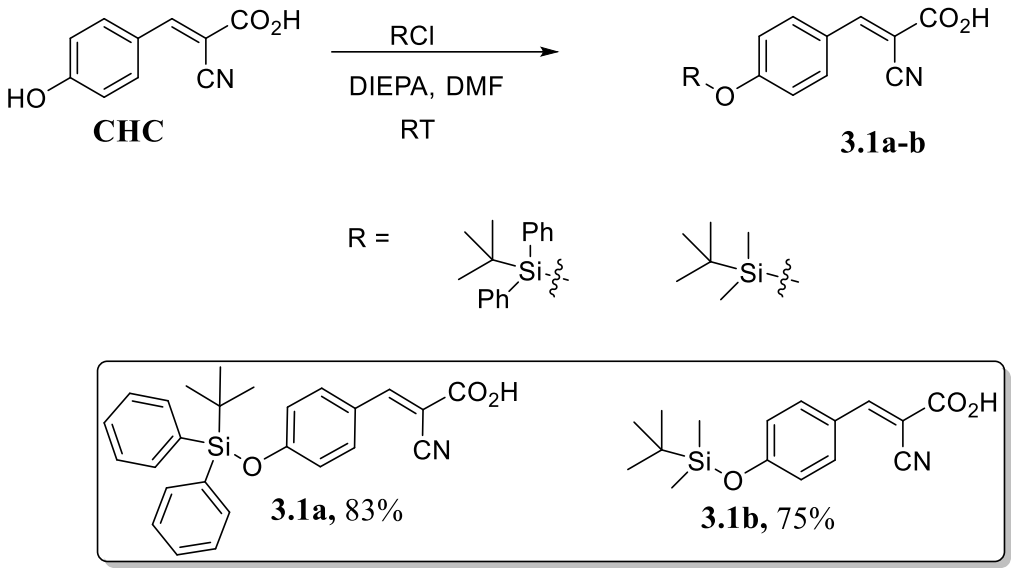

Scheme 3 a: The synthesis of the directly attached silylated CHC derivative **3.1a-b**

Next, we sought to investigate the effect of increased carbon content and lipophilicity on the activity of the silyl protected CHC derivatives. In this regard, we introduced a carbon linker chain which would increase the carbon content and potentially the lipophilicity. Furthermore, this substitution would also change the electron donating property in the *para* position and illustrate the electronic effects on MCT1 inhibition. There is a significant change in the electronegative properties associated with the bond of the *p*-phenolic oxygen-silyl in compounds **3.1a** and **3.1b** when compared to *p*-phenolic oxygen-carbon bond in compounds **3.5a-c** (**Scheme 3.1b**).

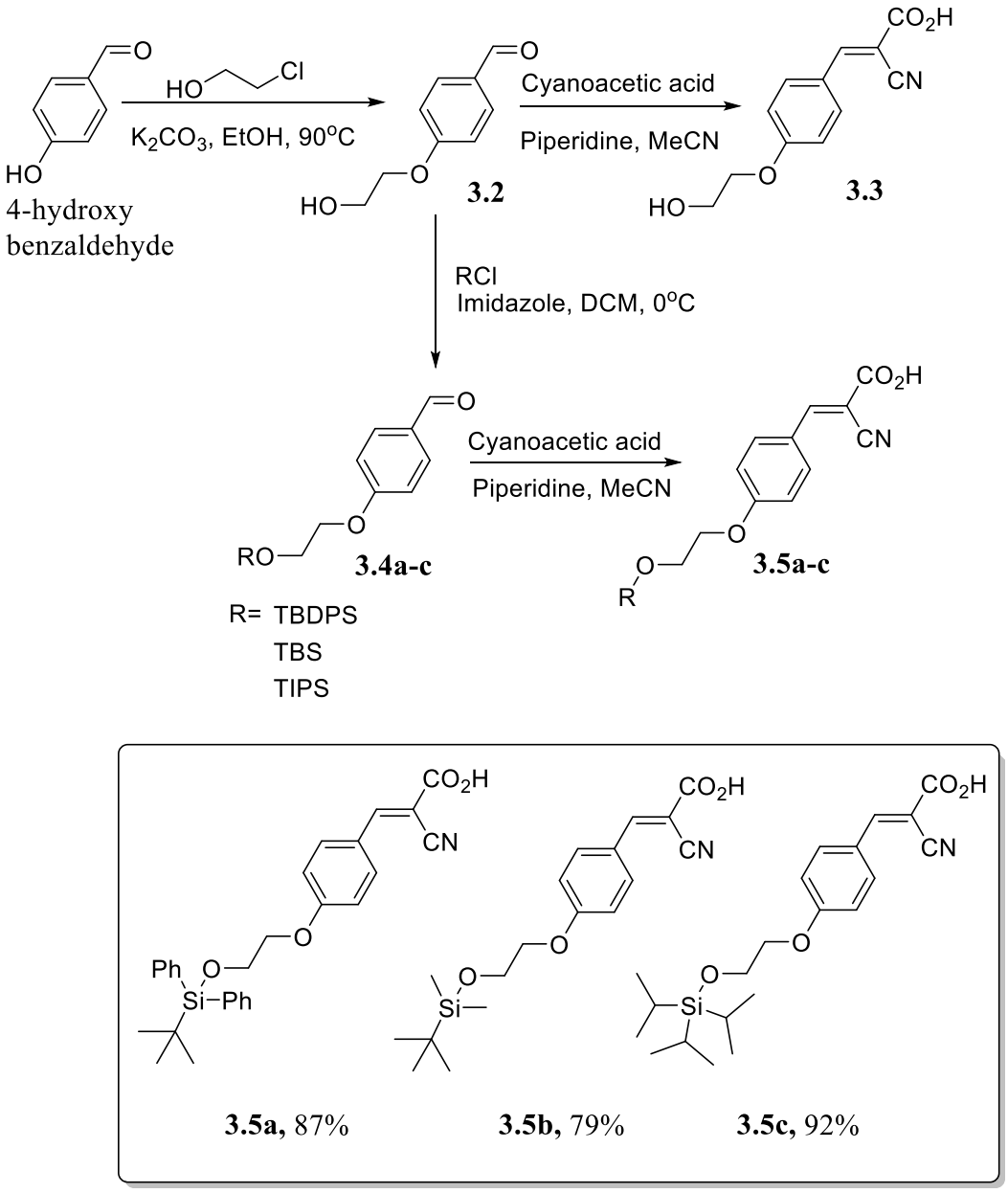

Scheme 3b: The synthesis of the extended ethyl linked silylated CHC derivatives **3.5a-c** and **3.3**

Synthesis of the silylated extended CHC derivatives started with 4-hydroxybenzaldehyde in excess of chloroethanol (4 equivalent) in the presence of potassium carbonate in an S_N2 fashion giving the corresponding ethanolic phenyl ether **11**.

This derivative was then protected with TBS, TIPS, and TBDPS chlorides in the presence of imidazole yielding various silylated benzaldehydes **3.4a-c**, respectively. Knoevenagel condensation with the benzaldehydes **2.4a-c** in the presence of cyanoacetic acid yielded the desired silyl linked CHC derivatives **3.5a-c**. The non-silylated CHC derivative **2.3** was synthesized by treatment of **11** with cyanoacetic acid under Knoevenagel condensation conditions**.**

3.2 Evaluation of compounds 3.1a-b, 3.5 a-c, and 3.3 for in vitro antiproliferation activity:

Synthesized CHC derivatives **3.1a-b, 3.5a-c,** and **3.3** were evaluated for their antiproliferation properties against a MCT4 expressing triple negative breast cancer cell line MDA-MB-231. These derivatives were also tested against two MCT1 expressing cell lines; murine metastatic breast cancer cell line 4T1 and human colorectal cancer cell line WiDr. Furthermore, these five derivatives were tested against a non-cancerous human mammary epithelial cell line MCF10A. Cell proliferation was measured using 3-(4,5-dimethylthiazol-2-yl)-2,5-diphenyl tetrazolium bromide (MTT). The amount of MTT converted to formazan is an indication of cell viability which is measured at 570 nm wavelength.[76] All these test compounds were diluted to a concentration of 500 µM except CHC. The lipophilicity of the silyl ether derived cyanocinnamates limits the solubility beyond this concentration. The difference in lipophilicity is essential for enhanced inhibition activity towards cell proliferation. Due to its polar phenolic hydroxy with cinnamic acid, the parent CHC was soluble even at 100 mM concentration.

Table 3a. Cell proliferation inhibition IC_{50}*(μM) properties of compounds **3.1a-b**, **3.5a-c**, and **3.3**.

	MDA-MB-231	**4T1**	**WiDr**	**MCF10A**
3.1a	93±0	56±1	41±2	44±2
3.1b	>500	>500	>500	>500
3.5a	71±1	22±1	6 ± 1	139 ± 7
3.5b	>500	82 ± 1	123±4	>500
3.5c	134±5	41 ± 6	5 ± 1	75 ± 5
3.3	>500	>500	>500	>500
CHC	5300±130	3600±300	1100±96	>10000

***** Values represent the average IC_{50} ± SEM (μM) of at least three independent experiments.

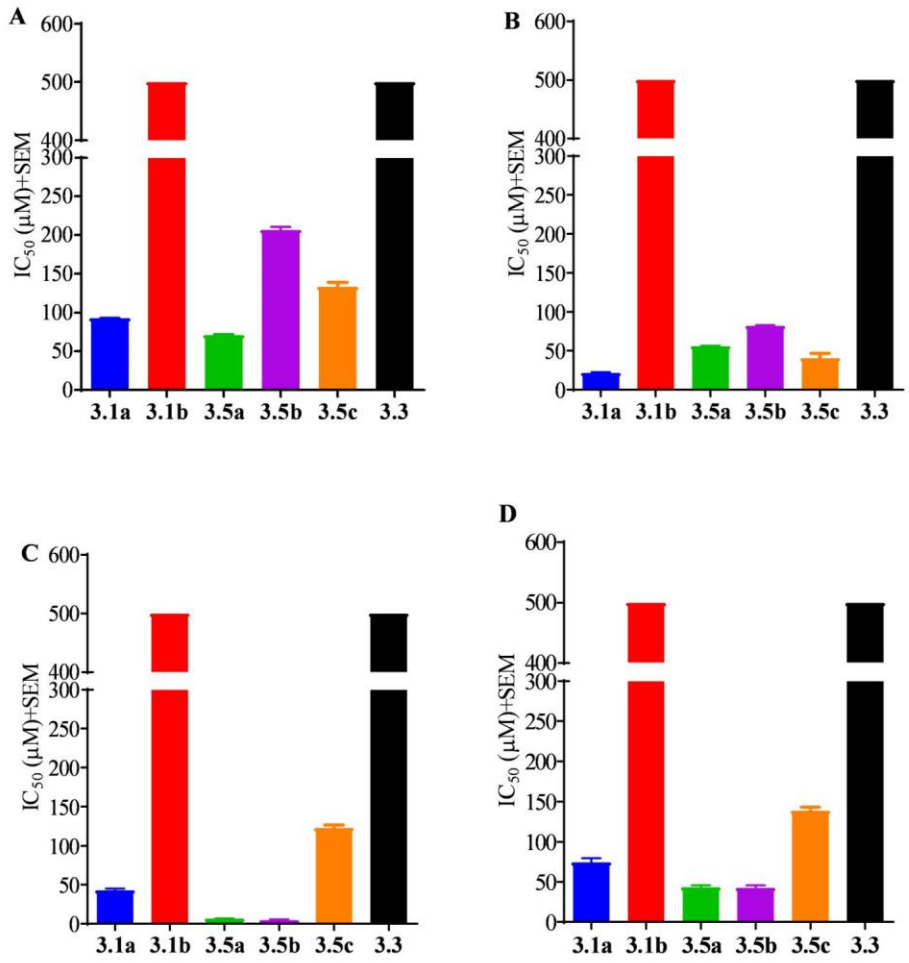

Figure 3c. Cell proliferation inhibition properties of compounds **3.1a-b, 3.5a-c** and the non-silylaetd derivative **3.3**. Values represent the average IC_{50} ± SEM (µM) of at least three independent experiments in (**A**) MDA-MB-231, (**B**) 4T1, (**C**) WiDr, and (**D**) MCF10A cell lines

Compound **3.1a** exhibited enhanced cell proliferation inibition properties with IC_{50} values in the range of 44-93 µM, which is a 100-fold increase in activity when compared to the parent molecule CHC (**Table 3a, Figure 3c**). The IC_{50} of DPS derivative **3.1a**

seemed to be more effective against the MCT1 expressing cell lines WiDr (41 µM) and 4T1 (56 µM) when compared to the MCT4 expressing cell line MDA-MB-231 (93 µM). The extended derivative **3.5a** did provide some enhanced activity lowering the IC_{50} to 6-71 µM. These derivatives also have higher potency towards MCT1 expressing cell lines. Interestingly, the extended derivative **3.5a** exhibited selectivity towards the cancerous cell lines as the activity was greatly reduced in non-cancerous MCF10A cell line (139 µM). The TBS derivative **3.1b** did not exhibit any cell proliferation inhibition even up to its maximum concentration of 500 µM. This trend was also seen in its extended derivative **3.5b** which had some enhanced activity against 4T1 (82 µM) and WiDr (123 µM), but was comparatively inferior compared to the other silylated CHC derivatives. The extended derivatives **3.5a** and **3.5c** are similarly active against the MCT1 expressing cell lines 4T1 and WiDr. Interestingly, there was a marked reduction in the cell proliferation inhibition of extended TIPS **3.5c** when compared to WiDr (5 µM) to MDA-MB-231 (134 µM). The similarties between **3.5a** and **3.5c** can be extended to the selectivity in antiproliferative activity. Similarly, these two derivatives were not as effective against MCF10A cell line. Next, these derivatives were evaluated for their MCT1 inhibition activity.

3.3 Evaluation of 3.1a-b and 3.5a-b for MCT1 inhibition using ^{14}C-lactate uptake assay:

The incorporation of the silyl group in the *para* position seemed to greatly enhance the antiproliferation activity of the derivatives. We then evaluated these derivatives for their MCT1 inhibition properties using ^{14}C-lactate uptake assay. The radiometric assay uses ^{14}C-lactate and for the evaluation of MCT1 inhibition activity, an MCT1 expressing cell line rat brain endothelial 4 (RBE4) was chosen as previously reported.

Table 3b. MCT1 IC_{50} values of compounds **3.1a-b** and **3.5a-b**.

Compound	MCT1 IC_{50} (μM)
3.1a	0.408±0.005
3.1b	0.095±0.007
3.5a	0.097±0.007
3.5b	0.010±0.0003

*Values represent the average IC_{50} ± SEM (**μM**) of at least three independent experiments.

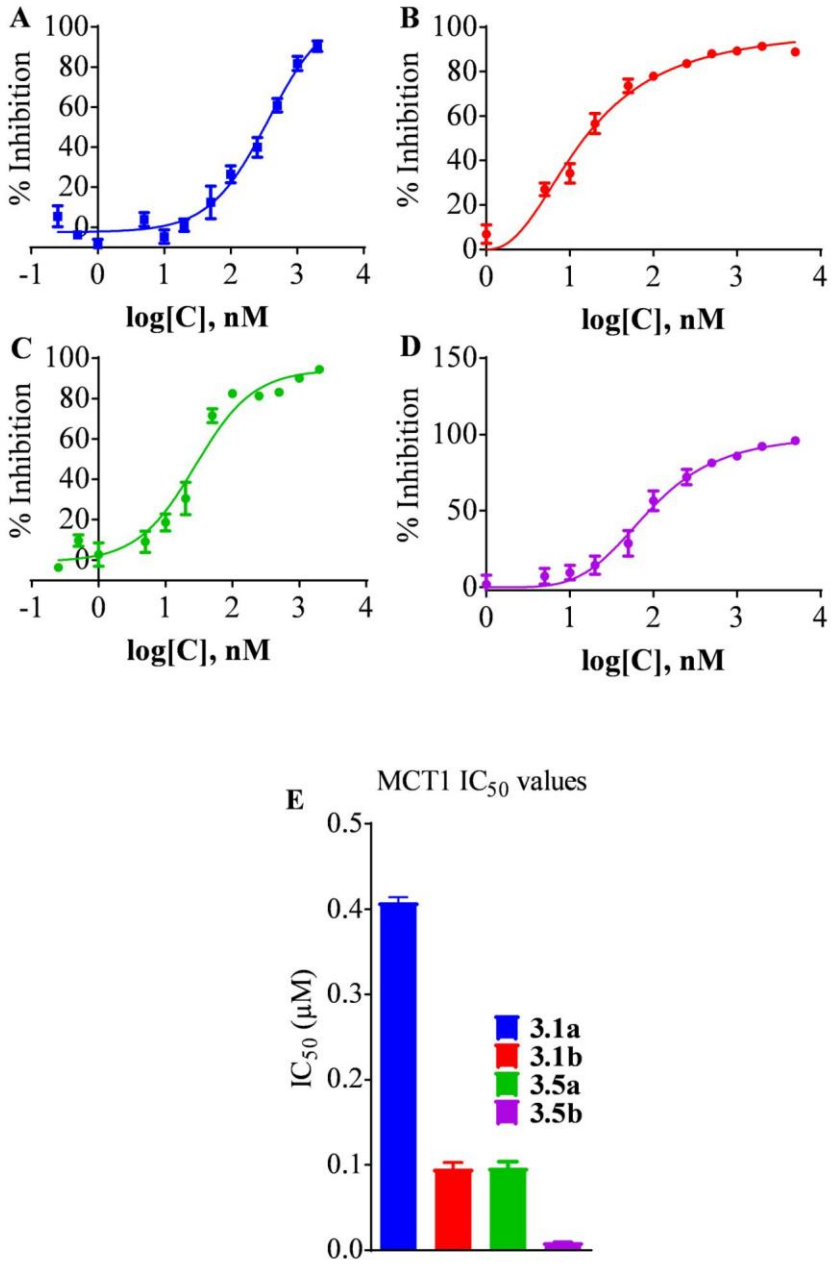

Figure 3d. MCT1 inhibition properties of compounds (**A**) **3.1a**, (**B**) **3.1b**, (**C**) **3.5a**, and (**D**) **3.5b**. Graphs represent the average IC_{50} ± SEM (µM) of at least three independent experiments (representative figures). (**E**) Bar graph of the IC_{50} values of compounds.

The results of the uptake assay highlight the importance of the hydrophobic region in the *para* position as there was a significant improvement on the MCT1 inhibitory properties of these derivatives when compared to the native CHC derivative (**Table 3b, Figure 3c**). The extended TBS derivative **3.5b** exhibited the highest potency towards MCT1 inhibition with an IC_{50} of 0.01 µM. The more effective antiproliferative agent **3.1a** expressed the lowest IC_{50} with 40-times reduction in activity (0.4 µM). In fact, the derivative with the lowest antiproliferatie activity, **3.1b** (~0.1 µM) had enhanced MCT1 inhibition properties when compared to **3.1a**. The TBDPS linker derivative **3.5a** also exhibited improved MCT1 inhibition properties compared to parent CHC with an IC_{50} value of ~0.1 µM, comparable to **3.1b**.

3.4 Evaluation of the effect on the metabolic profile of WiDr and MDA-MB-231 cell lines when exposed to candidate compounds

As discussed previously, metabolic plasticity is tightly controlled by the expression and activity of MCT1. The critical role that MCT1 plays in both glycolytic and mitochondrial activity can be understood by using the XFe Seahorse-based flux assays. We sought to evaluate cellular effects of compound treatment on these two energy pathways. In this regard, we evaluated the ability of compounds **3.1a-b**, **3.5a-c**, and **3.3** at disrupting both glycolysis and mitochondrial respiration. Various metabolic parameters can be modeled using the widely employed Seahorse extracellular flux assays. Specifically, due to the potential downstream effects of MCT1 inhibition, glycolysis and mitochondrial stress tests were performed.

The assay was conducted by seeding MDA-MB-231 or WiDr cells into 96 well plates and incubating 16-24 hours before the experiment. Cells are washed with assay medium three times before the experiment. Assay medium consists of a base DMEM supplemented with L-glutamine and pyruvate. Before the experiments, the cells were acclimatized to the glucose free media for 20 minutes in the incubator. Initially the basal proton flux effects were recorded in glucose free conditions (**Figure 3e**).

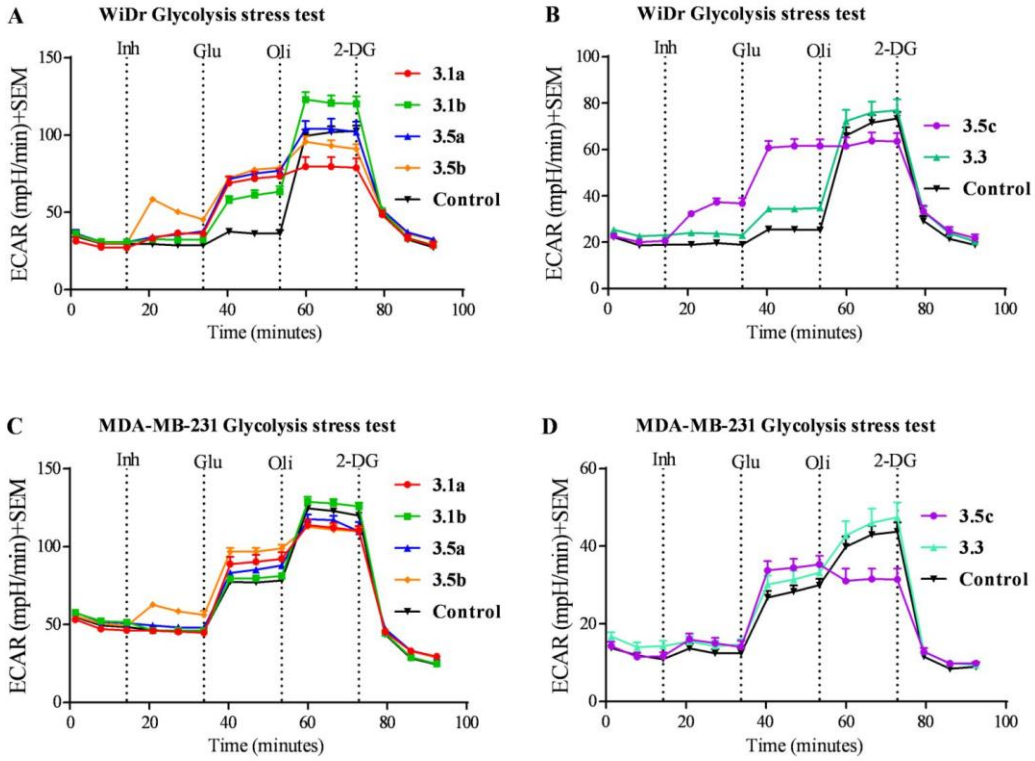

Figure 3e: Glycolytic profile of MCT1 expressing WiDr cell line with (**A**) **3.1a-b**, **3.5a-b** (**B**) **3.5c** and **3.3**. Against the MCT4 expressing cell line MDA-MB-231 with (**C**) **3.1a-b, 3.5a-b** (**D**) **3.5c** and **3.3**.

Following initial reads, the cells were exposed to the test compounds setting a control read before induction of glycolysis. Next, glucose was added to the cells at a concentration of 10 mM. The introduction of glucose stimulates glycolysis within the cells resulting in a spike in the ECAR values. This increase in ECAR is used in the determination of the glycolysis parameters (**Figure 3e**).

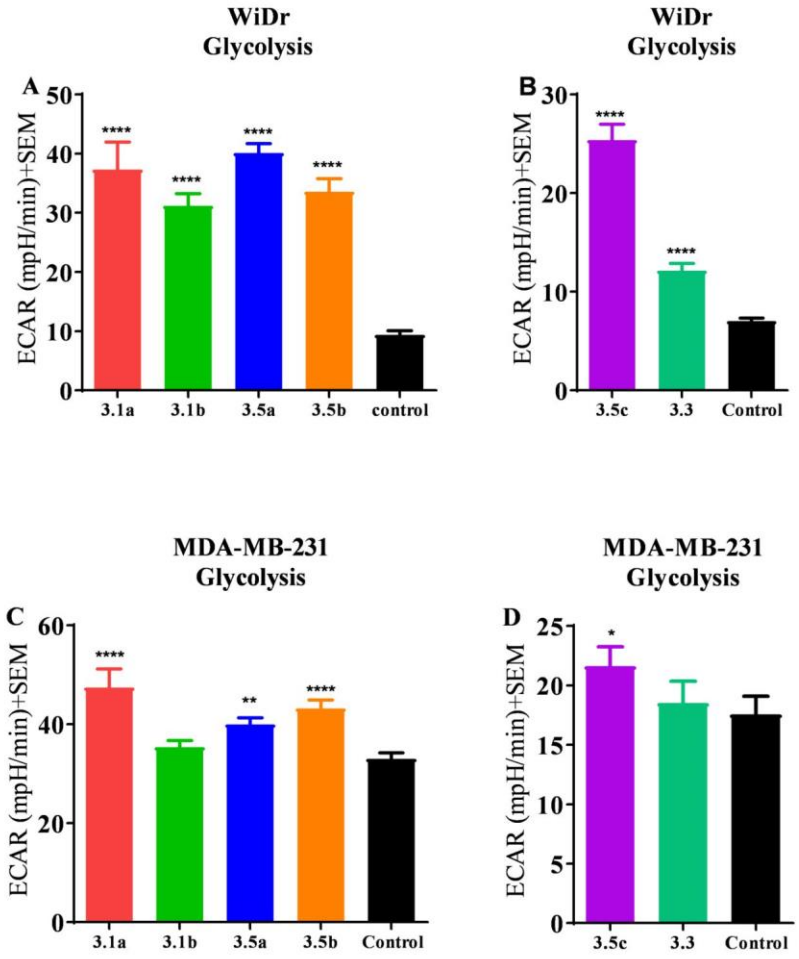

Figure 3f: Comparison of the glycolysis parameters calculated from glycolysis stress test assay in (**A**) MCT1 expressing WiDr cell line for compounds **3.1a-b**, **3.5a-b** and (**B**) **3.5c** and **3.3**. (**C**) MCT4 expressing cell line MDA-MB-231 for compounds **3.1a-b, 3.5a-b** and (**D**) **3.5c** and **3.3**. Bar graphs represent the average ± SEM of at least three independent experiments. Statistical significance was calculated using repeated measures one-way ANOVA (****$p<0.0001$).

Interestingly, all silylated derivatives (**3.1a-b** and **3.5a-c**) increased glycolysis significantly in WiDr cell line. In MDA-MB-231 cell line, this spike was not as significant compared to the control, but there was some significant effect after exposure to **3.1a** and **3.5a-c**. Interestingly, the TBS silylated CHC derivative **3.1b** did not exhibit any change in glycolysis and with the TIPS derivative **3.5c**, change was significantly lower when compared to the other silylated CHC derivatives. This increase in glycolysis signifies a metabolic reprogramming of the cells due to **3.1a** and **3.5a-c**. This new observed glycolytic phenotype could signify mitochondrial dysfunction when treated with test compounds as the cells are more dependent on glycolysis after introduction of the compounds to the assay media. This could explain why the effect was significant in the WiDr cell line which depends more on OxPhos for ATP production when compared to the more glycolytic MDA-MB-231 cell line.

The next drug introduced is the ATP synthase inhibitor oligomycin. This drug shuts down the main route of proton flow across the mitochondrial intramembrane space resulting in an increase in the proton gradient and subsequent stalling of the electron transport chain.

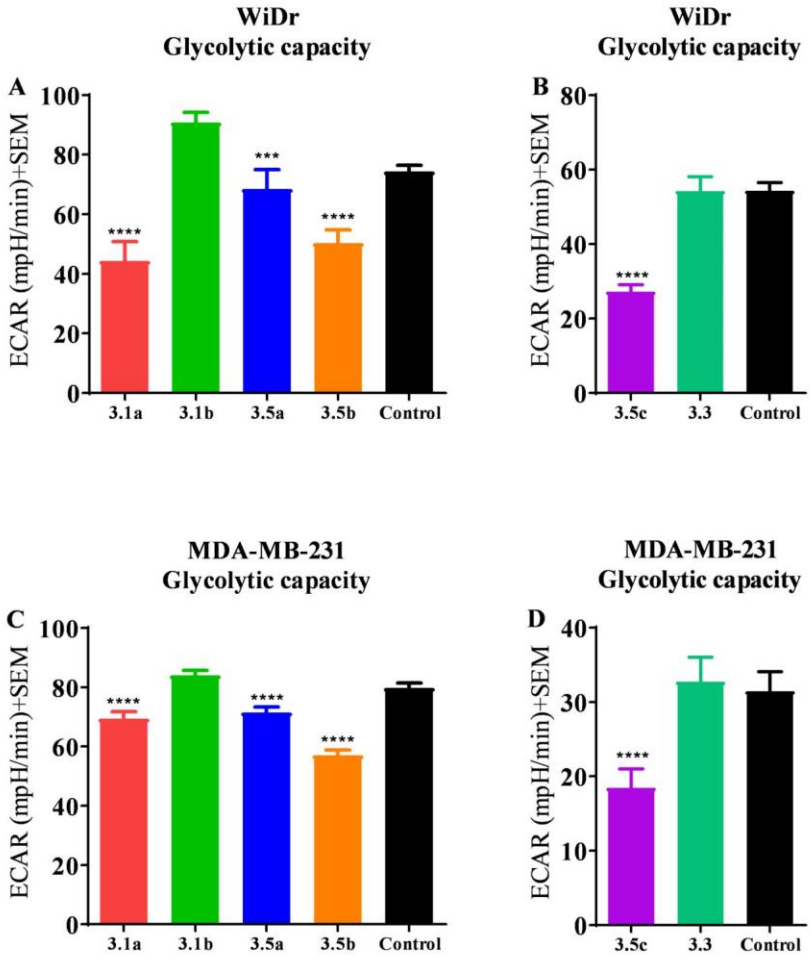

Figure 3g: Comparison of the glycolytic capacity parameters calculated from glycolysis stress test assay in (**A**) MCT1 expressing WiDr cell line for compounds **3.1a-b**, **3.5a-b** and (**B**) **3.5c** and **3.3**. (**C**) MCT4 expressing cell line MDA-MB-231 for compounds **3.1a-b, 3.5a-b** and (**D**) **3.5c** and **3.3**. Bar graphs represent the average ± SEM of at least three independent experiments. Statistical significance was calculated using repeated measures one-way ANOVA (****$p<0.0001$).

The resulting increase in ECAR is due to the shift away from ATP production through mitochondrial respiration. The cell now becomes dependent on glycolysis for most of its energy production and reaches its maximum glycolytic activity or the glycolytic capacity. A reduction in the glycolytic capacity could be attributed to the MCT inhibition property of these derivatives. Effective inhibition of the efflux of lactate would limit the maximum rate of glycolysis as MCT1 is critical for maintenance of cellular homeostasis (**Figure 1a**).

The apparent reduction in glycolytic capacity was seen in both WiDr and MDA-MB-231 cell lines with all silylated CHC derivatives except with the TBS derivative **3.1b**. The extended derivatives TBS (**3.5b**) and TIPS (**3.5c**) showed significant inhibition activity in both WiDr and MDA-MB-231. Interestingly, the derivative **3.1a** had a significant reduction in its activity against the MDA-MB-231 cell line. Furthermore, its extended derivative **3.5a** did exhibit reduction in the glycolytic capacity parameter. This could support the lack of MCT1 activity and the reduction in specific to bulkier DPS when compared to TBS and TIPS (**Figure 2.1h**).

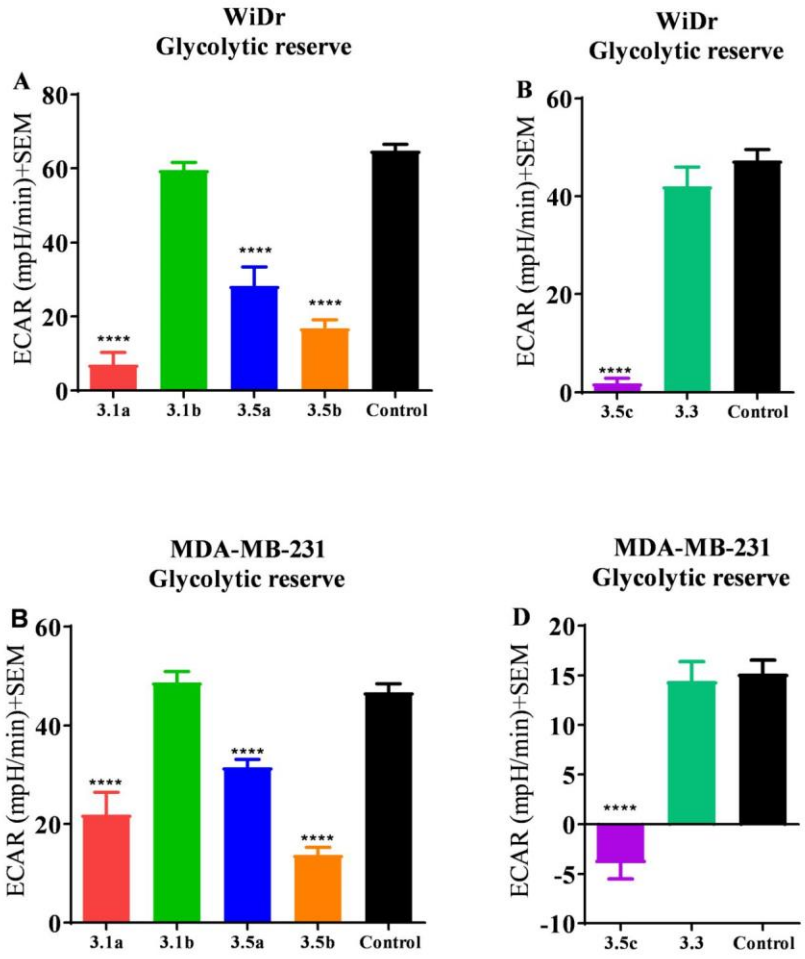

Figure 3h: Comparison of the glycolytic reserve parameters calculated from glycolysis stress test assay in (**A**) MCT1 expressing WiDr cell line for compounds **3.1a-b**, **3.5a-b** and (**B**) **3.5c** and **3.3**. (**C**) MCT4 expressing cell line MDA-MB-231 for compounds **3.1a-b, 3.5a-b** and (**D**) **3.5c** and **3.3**. Bar graphs represent the average ± SEM of at least three independent experiments. Statistical significance was calculated using repeated measures one-way ANOVA (****$p<0.0001$).

The final parameter, glycolytic reserve, is the difference between basal glycolysis and the glycolytic capacity. It represents a cell's ability to switch from its dependence on ATP production from OxPhos to complete dependence on glycolysis. In both cell lines WiDr and MDA-MB-231, there was significant reduction in the glycolytic reserve after exposure to **3.1a** and **3.5b-c.** In the case of **3.5c** there was almost a complete elimination of the glycolytic reserve in both WiDr and MDA-MB-231 cell lines (**Figure 2.1h**).

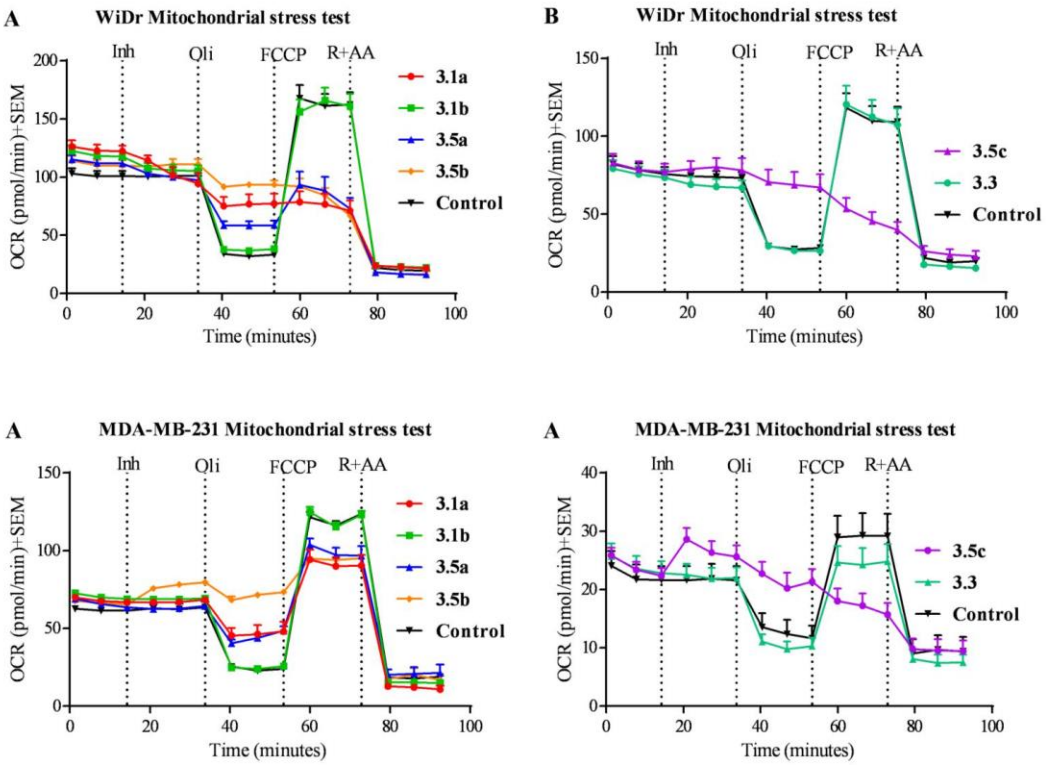

Figure 3i: Glycolytic profile of MCT1 expressing WiDr cell line with (**A**) **3.1a-b**, **3.5a-b** (**B**) **3.5c** and **3.3**. Against the MCT4 expressing cell line MDA-MB-231 with (**C**) **3.1a-b, 3.5a-b** (**D**) **3.5c** and **3.3**.

Based on these results, we next evaluated the state of mitochondrial respiration via the mitochondrial stress test. The mitochondrial stress test is conducted in glucose-rich media. After initial exposure to the compound, the ATP synthase inhibitor oligomycin is added. This inhibition results in the mitochondrial respiration stalling as the main driving force of proton movement is ATP synthase. Without the ATP synthase, the electron transport chain stalls as the oxidative driving force of the electron transport chain is not enough to pump more protons against the steep gradient. This reduction in OCR gives an idea of how much ATP is produced via mitochondrial respiration (**Figure 3j**).

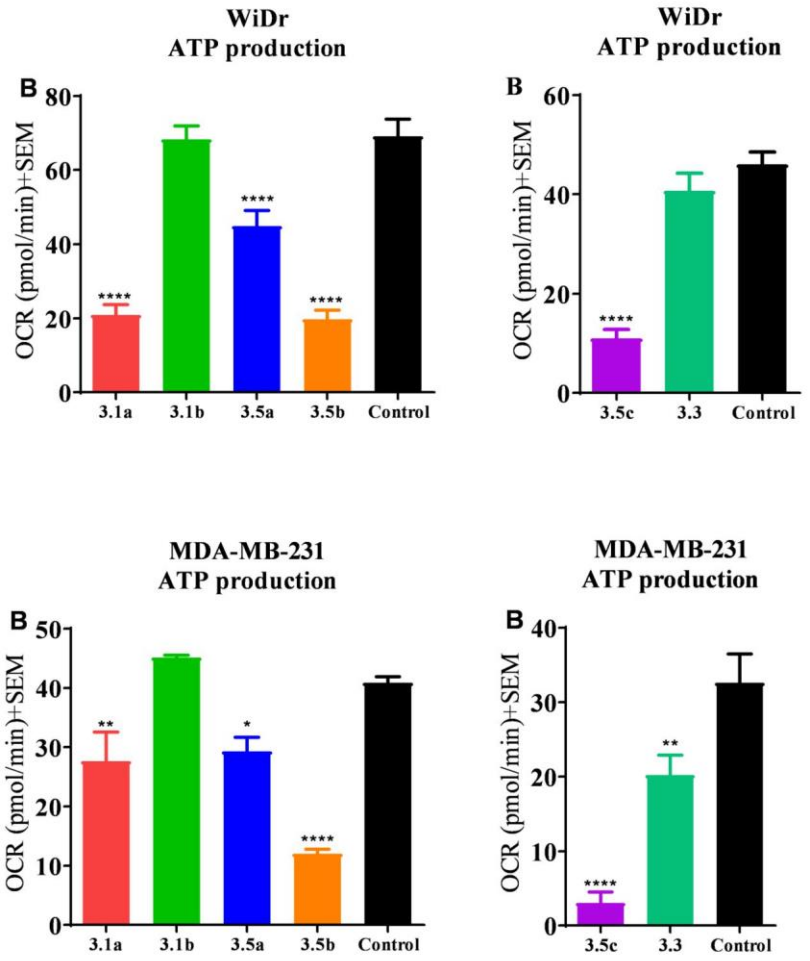

Figure 3j: Comparison of the ATP production parameters calculated from mitochondrial stress test assay in (**A**) MCT1 expressing WiDr cell line for compounds **3.1a-b**, **3.5a-b** and (**B**) **3.5c** and **3.3**. (**C**) MCT4 expressing cell line MDA-MB-231 for compounds **3.1a-b, 3.5a-b** and (**D**) **3.5c** and **3.3**. Bar graphs represent the average ± SEM of at least three independent experiments. Statistical significance was calculated using repeated measures one-way ANOVA (****$p<0.0001$).

In most of the silylated derivatives, there was a significant reduction in the ATP production via mitochondrial respiration in both WiDr and MDA-MB-231 cell lines. The DPS CHC derivative **3.1a** exhibited significant reduction in ATP production in WiDr cell line but had slightly reduced activity in the MDA-MB-231 cell line. Interestingly, the extended DPS derivative **3.5a** exhibited significant reduction in this parameter only in WiDr cell line whereas its activity in MDA-MB-231 was comparably less significant. The extended derivatives **3.5b** and **3.5c** had similar activity in WiDr and MDA-MB-231 cell lines. Interestingly, the directly attached TBS derivative **3.1b** did not seem to affect the ATP production via mitochondrial respiration in either cell line.

The study of TIPS substituted CHC derivative **3.5c** against the unsilylated CHC derivative **3.3** clearly indicates that the presence of the lipophilic silylated group as opposed to the polar hydroxy group had higher impact on the ATP production. These results were true in both the WiDr and MDA-MB-231. TIPS derivative **3.5c** had a significant reduction in the ATP production while the derivative **3.3** did not exhibit significant reduction in WiDr and only minor reduction in the MDA-MB-231 cell line.

The next activity evaluated was the maximal respiration which can be calculated following addition of FCCP. The ionophore FCCP disrupts the intramembrane of the mitochondria resulting in the rapid efflux of protons down the gradient. The electron transport chain has a spike in activity as it tries to reestablish the proton gradient. The spike in OCR is known as the maximal respiration activity (**Figure 3k**).

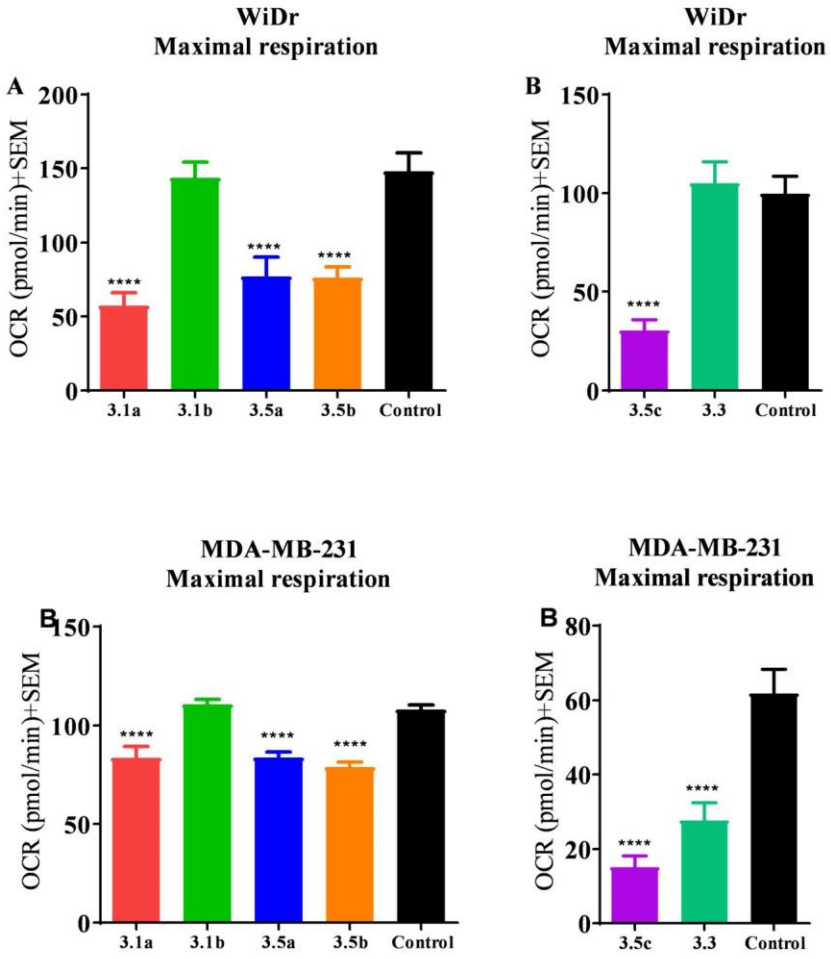

Figure 3k Comparison of the maximal respiration parameters calculated from mitochondrial stress test assay in (**A**) MCT1 expressing WiDr cell line for compounds **3.1a-b**, **3.5a-b** and (**B**) **3.5c** and **3.3**. (**C**) MCT4 expressing cell line MDA-MB-231 for compounds **3.1a-b, 3.5a-b** and (**D**) **3.5c** and **3.3**. Bar graphs represent the average ± SEM of at least three independent experiments. Statistical significance was calculated using repeated measures one-way ANOVA (****$p<0.0001$).

The maximal respiration of both WiDr and MDA-MB-231 cell lines was significantly reduced after exposure to all derivatives except the TBS derivative **3.1b.** When compared to the control, derivatives **3.1a** and **3.5a-b** where significantly more effective in the WiDr cell line when compared to the MDA-MB-231 cell line. There was little difference between the reduction in maximal respiration between **3.1a** and **3.5a-b** in both cell lines.

In the study comparing the TIPS derivative **3.5c** and the unsilylated derivative **3.3**, it is apparent that the activity is enhanced by the presence of the silyl ether group. Interestingly, the unsilylated derivative **3.3** exhibited significant reduction in the maximal respiratory activity in MDA-MB-231 cell line. In WiDr cell line, there was no observed activity after exposure to **3.3**.

The next parameter spare respiratory capacity can be evaluated form the difference in maximal respiration and the respiration attributed to ATP production. The spare respiratory capacity is used to determine the plasticity of the cell via mitochondrial respiration (**Figure 3j**).

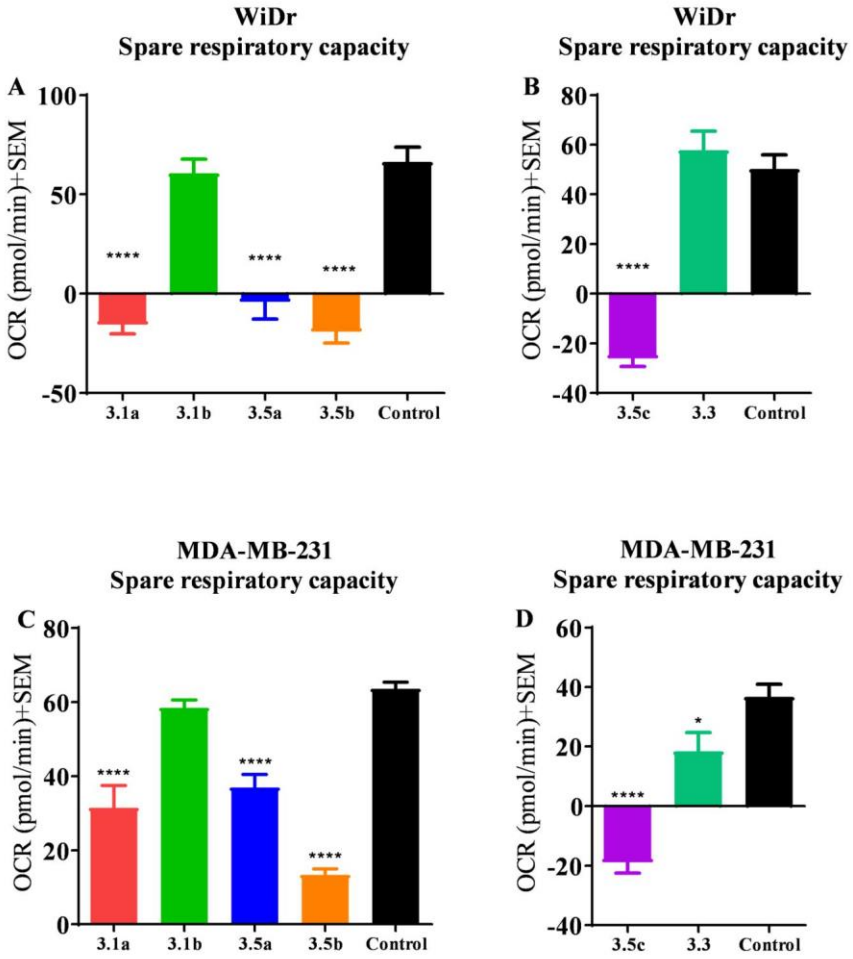

Figure 3l. Comparison of the spare respiratory capacity parameters calculated from mitochondrial stress test assay in (**A**) MCT1 expressing WiDr cell line for compounds **3.1a-b**, **3.5a-b** and (**B**) **3.5c** and **3.3**. (**C**) MCT4 expressing cell line MDA-MB-231 for compounds **3.1a-b, 3.5a-b** and (**D**) **3.5c** and **3.3**. Bar graphs represent the average ± SEM of at least three independent experiments. Statistical significance was calculated using repeated measures one-way ANOVA (****$p<0.0001$).

As expected, derivatives that exhibited significant reduction in the maximum level of respiration also had a significant effect on the spare respiratory capacity. **3.5c** completely eliminated the cells' spare respiratory capacity. This means that the cancer cells had reached the maximum level OCR for ATP production. Interestingly, there was a significant reduction in the spare respiratory capacity with the unsilylated derivative **3.3** in the MDA-MB-231 cell line. Outside of this result, there seems to be a strong indication of mitochondrial dysfunction within WiDr and MDA-MB-231 cells after exposure to the silylated derivatives (**Figure 3m**).

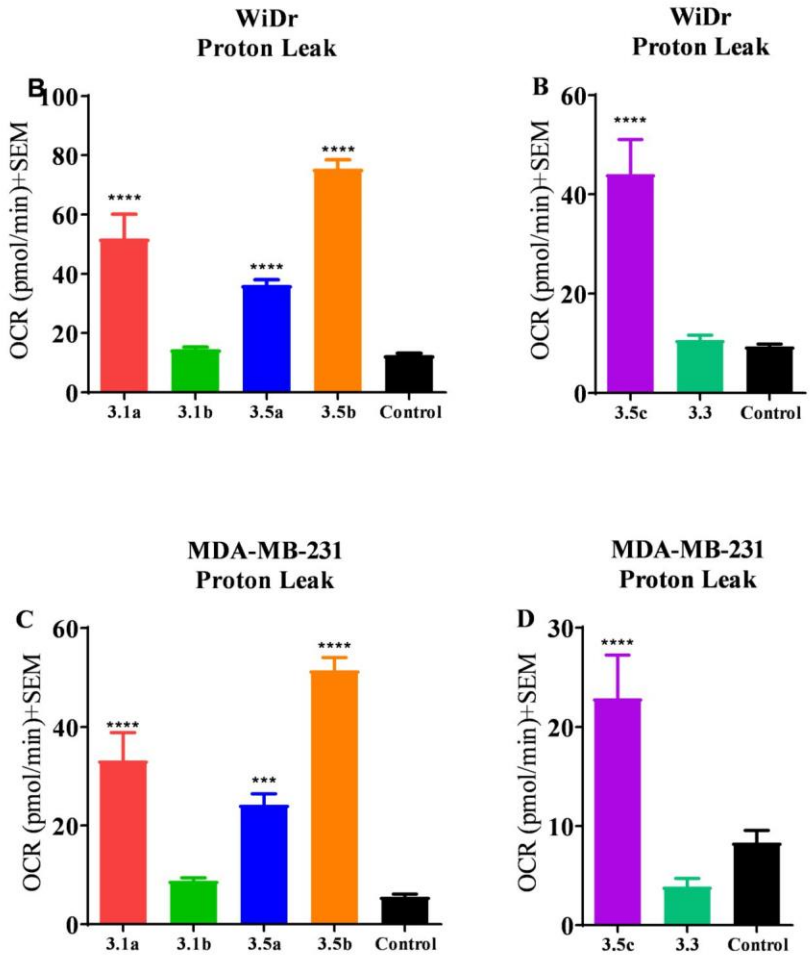

Figure 3m: Comparison of the spare respiratory capacity parameters calculated from mitochondrial stress test assay in (**A**) MCT1 expressing WiDr cell line for compounds **3.1a-b**, **3.5a-b** and (**B**) **3.5c** and **3.3**. (**C**) MCT4 expressing cell line MDA-MB-231 for compounds **3.1a-b, 3.5a-b** and (**D**) **3.5c** and **3.3**. Bar graphs represent the average ± SEM of at least three independent experiments. Statistical significance was calculated using repeated measures one-way ANOVA (****$p<0.0001$).

The next parameter measured was the proton leak. This is a measure of the mitochondrial membrane structural integrity. The membrane is responsible for the establishment of a proton gradient to drive the ATP production via the ATP synthase complex. Structural damage to these membranes can result in proton leak. Therefore, this parameter might support drug induced mitochondrial dysfunction. There was a substantial increase in proton leak with all derivatives in both WiDr and MDA-MB-231 cell lines except for the directly attached TBS derivative **3.1b.** Interestingly, the derivative **3.1a** seemed to exhibit a greater degree of proton leak when compared to its extended derivatives but was very closely tied for second with the extended TBS derivative **3.5b**. This enhanced proton leak could support silyl ethers' improved lipophilicity resulting in greater membrane permeability and subsequent targeting of the mitochondria. To understand the effect of these derivatives, the derivative **3.1a** was chosen for it exhibited one of the greatest levels of proton leak and subsequent increase in glycolytic dependence.

3.5 Assessment of mitochondrial damage using epifluorescence microscopy

The extracelluar flux assay via Seahourse XFe analyzer supports the hypothesis that these derivatives have the potential to damage the mitochondria resulting in proton leak. Mitotracker Red CMXROS is a fluorescent small molecule that binds and accumulates in the mitochondria as a function of mitochondrial membrane potential. This fluorophore is widely utilized to study the location, morphology, and vitality of the mitochondria. We utilized epifluorescent microscopy technique to investigate the effect of compound treatment on the mitochondria. Derivative **3.1a** and its corresponding extended dervative **3.5a** were chosen for their excellent metabolic profiles and as a comparitive study

to understand the importance of a spacer group in the silylated CHC derivatives (**Figure 3o**).

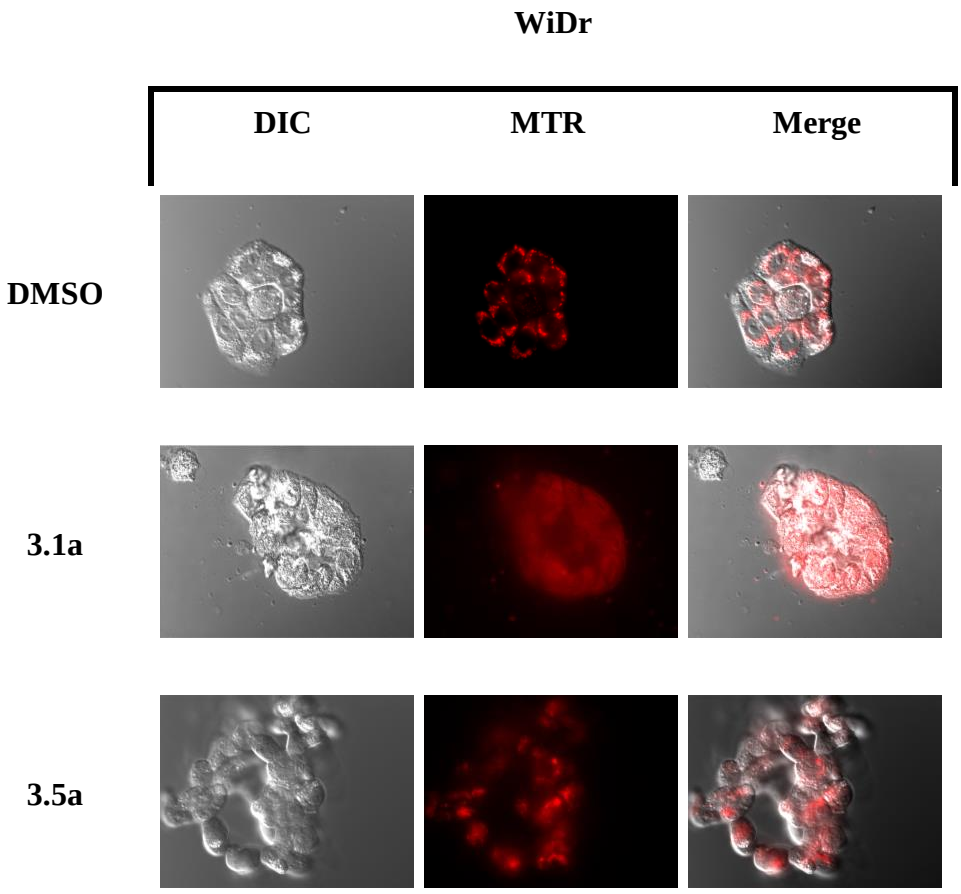

Figure 3o: Results after 24 hours of exposure to test compounds. The bright field image of WiDr after exposure to test compounds **3.1a** and **3.5a** or the vehicle DMSO.

The fluorescence of the MTR dye following exposure along with the overlay between the brightfield image and the MTR dye. The fluorescence and DIC images were recorded with similar exposure times and neutral density filters. These epifloruescent images were taken after a 24 hours of exposure with **3.1a** and **3.5a.** The morphological

changes due to the exposure to the compound on the mitochondria can be observed using mitotracker red and the cells morphology using DIC was also imaged. In the control images, the WiDr cell line has tightly packed mitochondria with very distinct groups within each cell. Furthermore, cells are tightly packed together rather then being spread out. The exposure to the DPS derivative **3.1a** resulted in observable cell stress like blebbing and in some cases significant lysing events. Interstingly, with exposure to the extended DPS derivative **3.5a** the cells are no longer able to keep their tightly packed formation anymore and can be seen floating. After exposure to both derivatives, it is apparent that the mitochondria is significantly stressed. The mitochondria is much more diffused throughout the cell which is indicative of signifcant loss of function in the mitochondria.

The next cell line evaluated was the more glycolytic MDA-MB-231 which is also known to predominantly express the MCT4 protein. Similar to the WiDr study, the cells are exposed to the compounds over a 24 hour period of time. Following exposure, the cells were washed and DIC along with epifluorescence was recorded (**Figure 3p**).

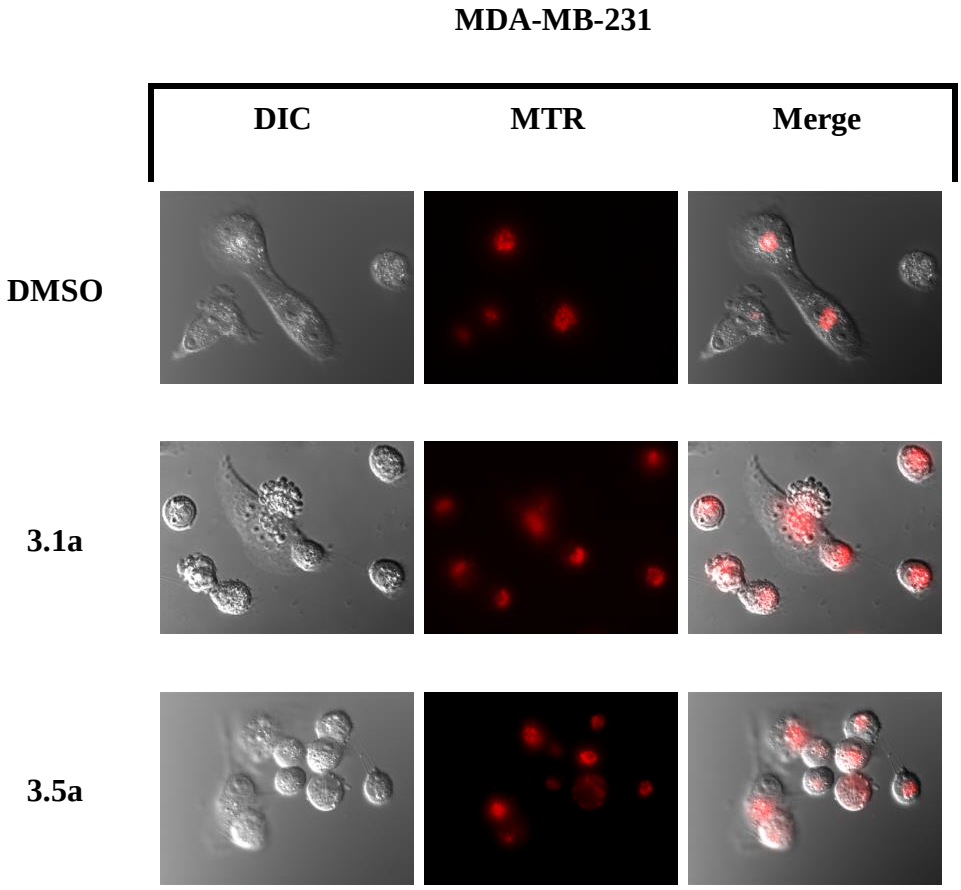

Figure 3p: Results after 24 hours of exposure to test compounds. The bright field image of MDA-MB-231 after exposure to test compounds **3.1a** and **3.5a** or the vehicle DMSO.

The fluorescence of the MTR dye following exposure to **3.1a** and **3.5a** along with the overlay between the brightfield image and the MTR dye. The fluorescence and DIC images were recorded with similar exposure times and neutral density filters. After 24 hours of exposure to the compounds, the MDA-MB-231 cells DIC and epifluorescent images were recorded. In the DMSO control images, the cells are flattened out with well

defined shapes and no indication of much blebbing. The epfluorescence shows healthy mitochondria forming tightly packed structures centered within the cell. When compared to the DMSO treated cells, it was apparent that cells were extremely stressed with balling up and in some cases lysing. The linked derivative **3.5a** seemed to have a significant impact on the viability of the MDA-MB-231 cells as most of the cells had allready balled up and were becoming detached from the dish. Similarly, exposure to **3.1a** had signifcant rounding up of the cells and also many lysing events were observed in the attached cells. The epifluorcence further supported this conclusion as the mitochondria was now spread out with no discernable clusters. All of the above-mentioned results are indications of significant dysfunction in the mitochondria after exposure to our compounds.

3.6 Evaluation of DNA damage and apoptosis with 3.1a

Mitochondrial damage, glycolytic deregulation, and inhibition of metabolite shuttling with the synthesized compounds may cause cancer cells to trigger programmed cell death pathways. Hence, we investigated the ability of the test compounds to turn on apoptotic pathways via common molecular proteins involved in this pathway including PARP-1, p53 and γ-H2AX. The protein PARP1 and specifically, its cleaved product Cl. PARP1 are strong indicators of early apoptotic events being triggered within the cell. The other protein γ-H2AX is an indication of double stranded breaks and DNA damage. DNA damage is also a strong indicator of apoptosis being pursued in the cells after exposure. The wild type p53 (wt-p53) is a transcription factor that binds to specific sequences in the DNA activating the transcription of the gene. In cancer cells mutant type p53 (mut-p53) is well documented to enhance the survivability of the tumor. The mut-p53 codes for a

deffective transcription regulator that has a loss of normal activity. In fact there is strong support that the mut-p53 activates pro-oncogenic proteins resulting in unregulated growth and lack of tumor suppressing activity.[77,78] There is potential for activation of wt-p53 via γ-H2AX especially in the presence of ROS induced DNA damage. This regain of p53 expression could result in downfield apoptotic effects like increased caspase expression and induce apoptosis in cancer cells. In evaluating the potential events that could be happening intracellularly and whether the derivatives are inducing apoptosis, **3.1a** was chosen for it had consistently exhibited significant antiproliferation charactersitics against all the cell lines tested. Furthermore, this compound showed significant effect in metabolic phenotype in the Seahorse Flux Assay. A concentration study was conducted to evaluate the lowest concentraiton that could exhibit the activation of these markers. Compounds were compared to the parent derivative CHC which has similar inhibitory property but lacks the antiproliferative character when compared to the silylated CHC derivatives, and therefore should have a similar level of expression of the target proteins (**Figure 3q**).

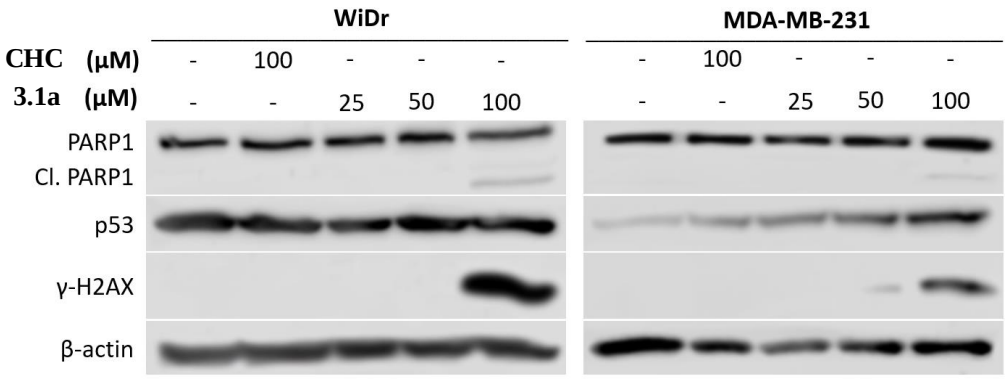

Figure 3q: The western blot analysis after exposure to **3.1a** in WiDr and MDA-MB-231 cell lines at three different concentrations. The proteins probed for were p53, γ-H2AX, and PARP1.

The silylated CHC derivative resulted in an increase in the expression of PARP cleaved product. This result indicated that these derivatives were causing apoptosis in the cells. Interestingly there is also expression of γ-H2AX after exposure to **3.1a** at 100 μM. These results showed that DNA damage was observed at this concentration. Both MDA-MB-231 and WiDr cell lines express an oncogeneic mutant form of p53, [77,79] and expression levels may vary depeding on the degree that each cell line depends on p53 for prolifereation. In MDA-MB-231 cells, there was a substantial concentration dependent increase in mut-p53 expression. This could indicate that the γ-H2AX expression is a downstream effect of the increase in mut-p53 expression as a result of reactive oxygen species (ROS) from mitochondrial damage. Interestingly, in WiDr cells which also express mut-p53, an increase in p53 expression was not observed. This cell line did exhibit a similar trend in Cl. PARP1 and γ-H2AX when compared to MDA-MB-231 cell line, indicating

that apoptosis is being induced following exposure to our compounds. Interested by the western blots results, the potential mechanism for DNA damage was investigated. [71]

3.7 Assessment of potential ROS induced DNA damage through mitochondrial dysfunction with 3.1a

Previous literature reports indicate that accumulation of deprotected silyl derivatives induced mitochondrial damage and increased ROS that may result in heightened levels of DNA damage.[4] Phosphorylation of histone H2AX is the result of DNA damage which can be caused by many kinds of cellular stress. One potential cause of cellular stress is ROS release from damage mitochondria. The ROS can freely diffuse into the nucleus causing DNA damage resulting in the increase in γ-H2AX expression. Bioaccumulation of silicon atoms could stimulate ROS via mitochondrial damage resutling in the DNA damge and subsequent γ-H2AX expression. To test this theory, WiDr cell line was treated with the test compound in the presence of a known antioxidant and ROS scavenging agent N-actyl cystine (NAC) which will quench free radicals reducing any potential DNA damge they might cause. If ROS is the main source of DNA damage and subsequently γ-H2AX expression, then NAC treatment should reverse the expression of γ-H2AX in the western blot (**Figure 3r**).

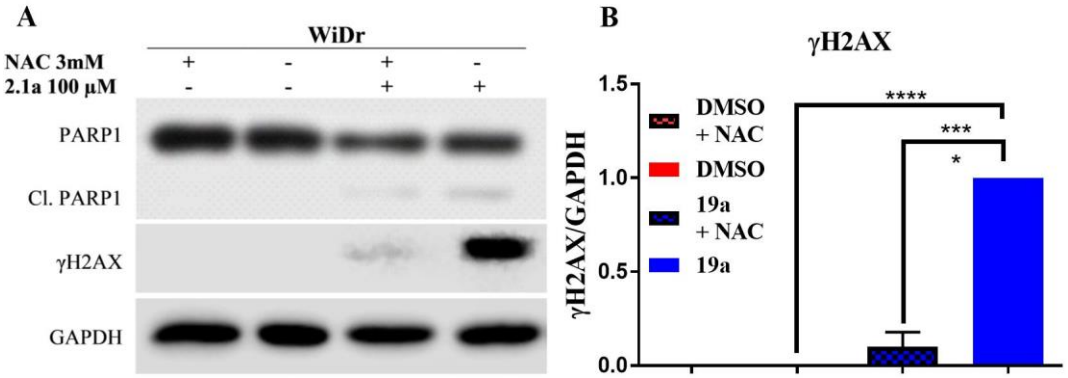

Figure 3r: NAC reverses **3.1a** induced H2AX phosphorylation (**A**) western blot analysis of WiDr after exposure to NAC with or without **3.1a** and (**B**) analysis of protein expression when compared to GAPDH.

NAC by itself did not seem to affect the expression of the various apoptotic proteins sampled in the western blot. Furthermore, we observed that exposure to just the compound **3.1a** at 100 µM resulted in a similar set of expression as seen in the previous western blot analysis. Interestingly, in the combined exposure of NAC with **3.1a**, there was a significant decrease in γ-H2AX. Densitometric analysis with GAPDH as a control showed a 10 fold decrease in γ-H2AX. Remarkably, this reduction in expression did not seem to effect the Cl. PARP1 expression indicating that while ROS seems to be present and causing DNA damage, it is not the reason for induced apoptosis within the cell. This result supports the theory that there is a dual mode of action within our silylated CHC derivative where both mitochondrial dysfunction and MCT1 inhibition are taking place.

3.8 Systemic toxicity evaluation of candidate compounds 10a-c in CD1 mice

Considering the excellent antiproliferation activities, MCT1 inhibition activity, and disruption of both glycolysis and OxPhos, compound **3.1a** and its sister two carbon spaced derivative **3.5a** were elevated to candidate compounds to be translated to *in vivo* systems. Before translation to a xenograft model, initial toxicity studies were conducted in healthy CD1 mice to evaluate the maximum tolerated dose (**Figure 3p**).

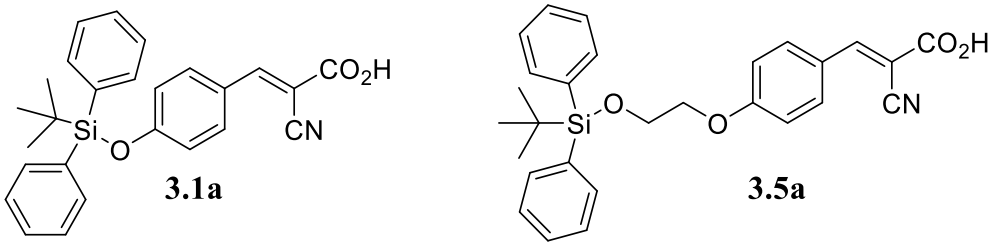

Figure 3s: Candidate compounds used for translation into *in vivo* models for evaluation of chemotherapeutic potential.

For solubility purposes, the silylated derivatives were converted into their corresponding sodium salts using sodium bicarbonate. The derivatives **3.1a** and **3.5c** had some trouble with solubility at high concentrations in just 10% DMSO in saline, so a formulation was used. The commonly used formulation was as follows: 10% DMSO, 10% PEG-400, 7.5% HS-15, and 72.5% water to guarantee full solubility when the compound is injected into the mice. The healthy CD-1 mice were purchased from Charles River and allowed to acclimatize for one week before administration of candidate compounds. The mice were assigned into groups (n=6 mice). Selection was based on the average weight of the group and mice were selected to ensure the average was consistent amongst all treatment groups. Toxicity evaluation was conducted over a period of 16 days. Compounds

3.1a and **3.5c** were administered daily at a dosage of 20mg/kg and the body weights of the mice were monitored to ensure the dosage was not causing any significant stress on the mice. The control group was given vehicle (10% DMSO, 10% PEG-400, 7.5% HS-15, and 72.5% water) daily along with the administration of derivatives **3.1a** and **3.5c**.

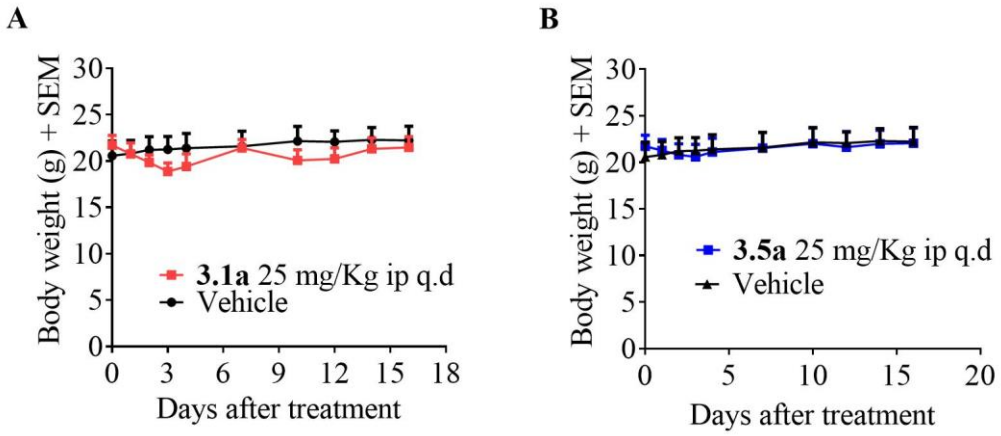

Figure 3t: Systemic toxicity of (**A**) **3.1a** and (**B**) **3.5a** in CD-1 mice at a concentration of 25 mg/kg given i.p daily indicate normal body weight gains in treated mice when compared to the vehicle control.

The derivatives **3.1a** and **3.5c** did not exhibit any significant reduction in body weights or visibly toxic side effects at the end of the study (**Figure 3t**). Encouraged by these results, the next step was to evaluate the efficacy of these candidate compounds in *in vivo* tumor xenograft studies.

3.9 Tumor growth inhibition study of 3.1a and 3.5a in WiDr xenograft

Selection of candidate compound **3.1a** and **3.5a** for further translation was based on its excellent selectivity towards cancerous cell lines and its potent metabolic inhibitory profile. Furthermore, the "silicon switch" of the atom should reduce their susceptibility to CYP450 oxidation and elimination allowing the metabolic inhibitors to persist longer within the system.

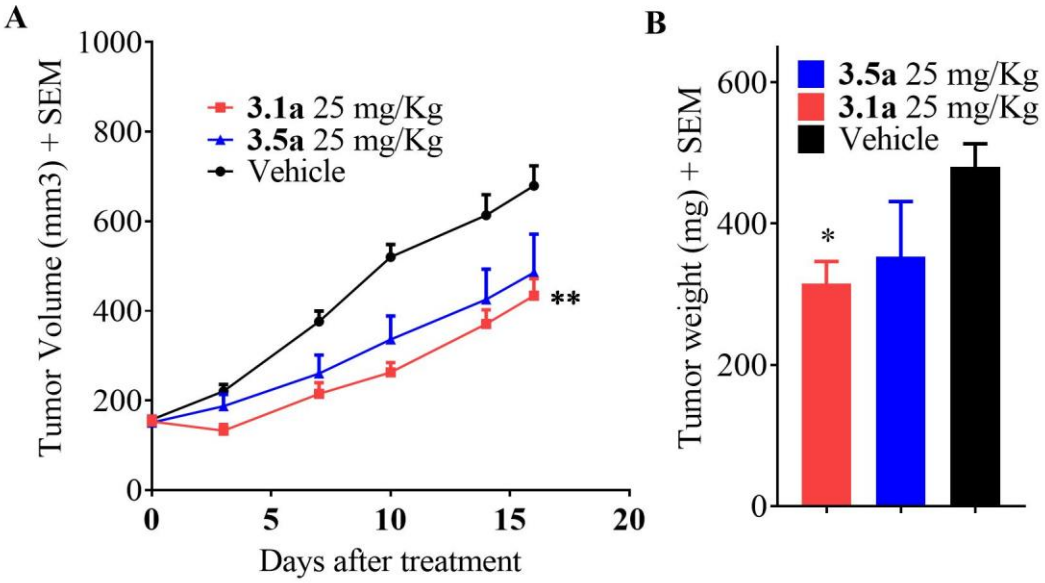

Figure 3u. *In vivo* WiDr xenograft model indicated significant reduction in (**A**) tumor volume when compared to vehicle treated mice. At the end of the study, tumors were resected and (**B**) weighed. Statistical significance of tumor growth inhibition was calculated using the Mann-Whitney test (*** P <0.001).

The WiDr xenograft model was chosen for it is an MCT1 expressing cell line and was previously evaluated against the lead candidate compound for transport inhibition, cell proliferation, and metabolic disruption capabilities. Mice were inoculated with WiDr cells.

The tumor growth was monitored every 2-3 days and after the tumor had reached 100 mm^3 the compound was administered. The mice were treated with **3.1a** and **3.5a** at a dosage of 25 mg/Kg, intraperitoneally (i.p), once daily and treatment was continued for 14 days. Each day before injection, the body weights of the mice were monitored to ensure that the mice were not being negatively impacted by the treatment. The tumor volume was measured every three days to evaluate tumor reduction via candidate compounds. After 14 days, the mice were euthanized, and tumor masses were isolated and weighed. **3.1a** exhibited a significant tumor growth inhibition, 36% by volume (**Figure 3r**) and ~30% by tumor mass (**Figure 3r**), when compared to the control group.

3.10 Discussion

Previously synthesized *N*,N-dialkyl/aryl CHC based MCT1 and MCT4 inhibitors showed significant anticancer effects *in* vivo at high concentrations (50 mg/kg or higher) due to lower biological half-life and lack of potent cell proliferation inhibition properties.[40,74] To improve the therapeutic potential of these MCT inhibitors, the integration of alkyl and aryl silyl groups into the *para* position of the aromatic ring of CHC was pursued. This substitution greatly improved cell proliferation inhibition properties with IC_{50} values in low µM concentration against numerous tumorigenic cell lines. Furthermore, all the synthesized derivatives **3.1a-b** and **3.5a-b** maintained their potent MCT1 inhibition similar to *N,N*-dialkyl/ aryl CHC derivatives. Interestingly, there was not a direct correlation between MCT1 inhibition activity and an increased antiproliferative activity presumably due to pleotropic mechanistic properties of these derivatives.

To evaluate the mechanism of action, the XFe Seahorse flux instrument was used to study the glycolytic and mitochondrial stress parameters after exposure to the compounds. The MCT1 expressing WiDr cell line and MCT4 expressing cell line MDA-MB-231 were utilized for these studies. In WiDr cell line, there is a significant increase in glycolysis when exposed to silylated CHC derivatives **3.1a** (**Figure 3c**). Our studies indicated that WiDr cell line is more OxPhos for ATP generation as opposed to MDA-MB-231 cell line which has more glycolytic phenotype. The changes in glycolysis of the MDA-MB-231 cell line was not apparent after the addition test compounds. The glycolytic capacity was significantly reduced in WiDr cell line when exposed to the silylated derivatives but not as effective in MDA-MB-231 cells. This could be attributed to the potent MCT1 inhibition property of the derivatives. The inhibition of the transporter would ultimately influence the cells' ability to pursue glycolysis as a source of ATP production. Without the ability to maintain cellular homeostasis, the rapid increase in glycolysis is no longer a viable option for ATP production. This would effectively reduce the glycolytic capacity and the glycolytic reserve of the cancer cells.

In the mitochondrial stress test, most of the parameters were significantly affected by the silylated CHC derivatives **3.1a** and **3.5a-c**. These results indicated that the derivatives caused significant stress on the mitochondria resulting in reduction of ATP production from its respiratory capacity. Furthermore, there was a significant spike in proton leak in both WiDr and MDA-MB-231 cell lines, which indicated significant mitochondrial dysfunction upon treatment with candidate compounds. This could also explain the sudden increase in the pursuit of glycolysis in WiDr cell line. WiDr is

dependent on both glycolysis and mitochondrial activity for ATP production and as mitochondrial activity is reduced, the cell line pursued more glycolysis to meet the deficit in ATP production. In MDA-MB-231 cell line, glycolysis was already being pursued for a majority of its ATP production. This more glycolytic phenotype could mean that the cell is not going to experience a major glycolytic shift should the mitochondrial ATP production be significantly reduced.

To further evaluate whether these derivatives were causing mitochondria dysfunction, the florescence microscopy studies were carried out. The studies using MTR dye supported the hypothesis that these derivatives were in fact causing mitochondrial dysfunction (**Figure 3m**). Furthermore, this assay indicated that there was significant cellular stress and apoptotic events being triggered after exposure to the compounds. This was later confirmed using western blot analysis as PARP1 cleavage was being observed after exposure to the candidate compounds. One theory was the apoptotic events were triggered via ROS signaling from the silicon induced mitochondrial dysfunction which could also explain the increase in γ-H2AX expression and DNA damage.[71] The introduction of ROS signaling from the mitochondria was not the primary trigger of apoptotic events. It was found after exposure to the ROS quencher NAC, there were no observed changes in PARP1 cleavage indicating that apoptosis was being induced through other means. Although, NAC did cause a significant reduction in γ-H2AX expression supporting the theory that ROS was being induced and causing DNA damage in the cells. All the mechanism studies indicate that the candidate compounds effectively arrest the metabolic plasticity between glycolysis and the mitochondrial OxPhos.

We then conducted *in vivo* systemic toxicity studies in CD-1 mice with candidate compound **3.1a** and **3.5a**. Initial toxicity study indicated that the derivatives could be administered at 20 mg/kg I.P daily for 14 days with no apparent stress on the mice. The treatment with candidate compound in a WiDr xenograft model in mice exhibited significant tumor reduction, both in volume and weight of the tumor. This result supports the potential therapeutic applications of silylated CHC derivatives for the treatment of cancer.

CHAPTER 4: Synthesis and evaluation of *o*-silylated *p*-amino CHC derivatives as MCT inhibitors

4.1 Introduction

Previous SAR studies reported by us indicated that there was a strong correlation between lipophilic functional groups in the *para* position and increase in the MCT1 inhibition activity. Furthermore, these SAR studies also highlighted the importance of the *para* N, N-dialkylamino substitution along with the placement of an *ortho* ether group for further enhancement of MCT1 inhibition to low nM potency. As discussed in the previous chapter 3, the "silicon switch" presented a way to enhance the lipophilic character of the synthesized silylated CHC derivatives with improved cell proliferation inhibition properties.

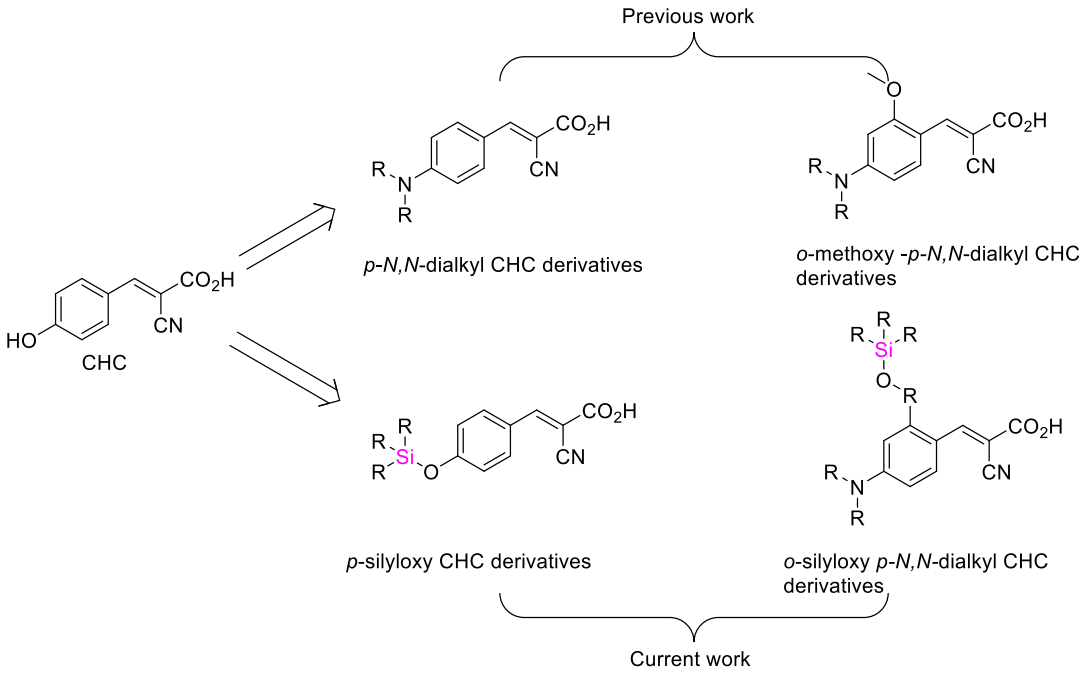

Figure 4a: Proposed *o*-silyloxy-*p*-*N*,*N*-dialkyl CHC derivatives

Furthermore, these derivatives significantly inhibited glycolytic and mitochondrial parameters and induced apoptosis. In this regard, we combined *p-N,N*-dialkyl/aryl CHC derivatives with *o*-silyl substitution as a way to further improve MCT inhibition, mitochondrial disruption properties along with increased cell proliferation inhibition (**Figure 4a)**.

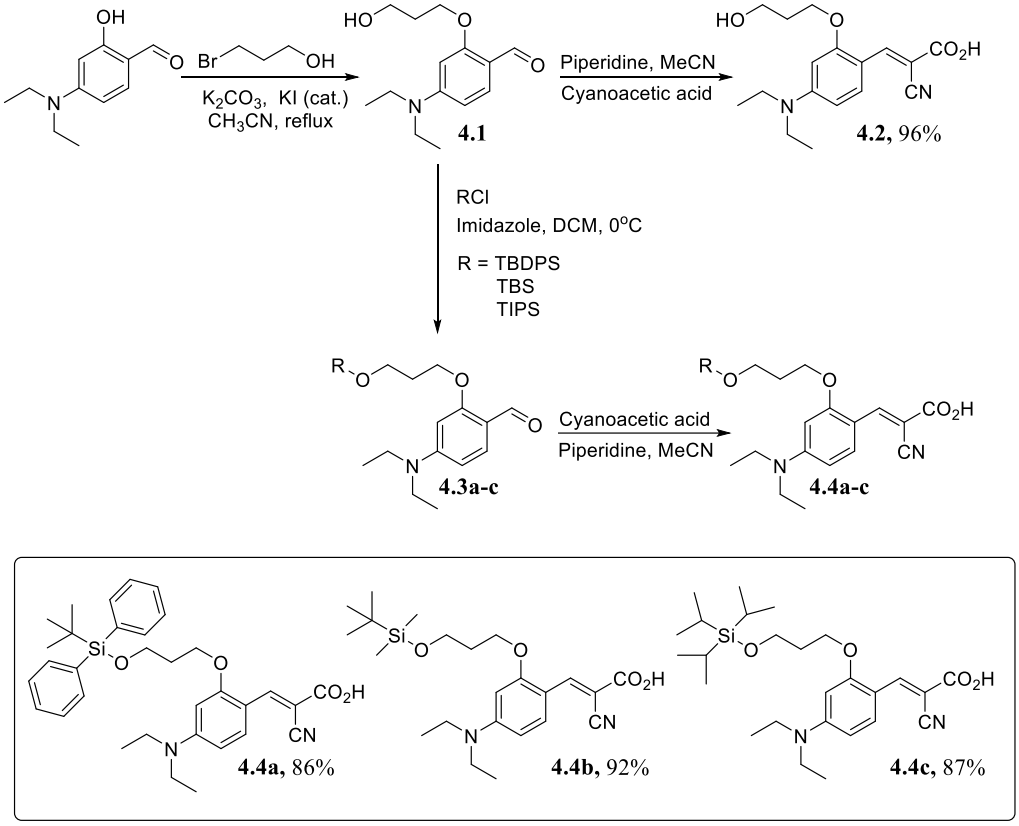

Scheme 4a: The synthetic route for the formation of the *p-N,N*-diethylamino CHC derivatives **4.4a-c** with *o*-silylether substitution.

4.2 Synthesis of silylated amino CHC derivatives

Synthesis of the proposed new *p*-*N*,*N*-diethylamino *o*-silylated CHC derivatives began by starting with commercially available 4-(diethylamino)salicylaldehyde and alkylating it with 1-bromopropanol in the presence of potassium carbonate and catalytic amount of potassium iodide to obtain the corresponding benzaldehyde **4.1**. A negative control to evaluate the therapeutic benefit of silylated amino CHC derivative was synthesized by Knoevenagel condensation of aldehyde **4.1** with cyanoacetic acid in the presence of piperidine to provide non-silylated amino CHC derivative **4.2**. To form the *o*-silylated amino CHC derivatives, the benzaldehyde **4.1** was protected with various silyl chlorides in the presence of imidazole yielding the corresponding silylated benzaldehydes **4.3a-c**. These aldehydes were subjected to Knoevenagel condensation providing the desired *o*-silylated *p*-*N*,*N*-diethyl CHC derivatives **4.4a-c**.

4.3 Evaluation of compounds 4.2 and 4.4a-c for antiproliferation activity in cancer cells

The synthesized silylated amino CHC derivatives **4.4a-c** and their un-silylated amino CHC derivative **4.2** were evaluated for their antiproliferation ability against MCT4 expressing triple negative breast cancer cell line MDA-MB-231. Furthermore, these derivatives were evaluated for their antiproliferation activity against two MCT1 expressing metastatic murine cell line 4T1 and human colorectal adenocarcinoma WiDr cell line. Finally, candidate compounds were also tested against a non-cancerous epithelial cell line MCF10A to evaluate the selective antiproliferative character (**Table 4a**). The MTT assay can be used to evaluated cell density and activity. The dye is reduced by cellular

mitochondrial reductase to the corresponding formazan dye which can be measured at 570 nm wavelength.[76] The lipophilicity of the synthesized derivatives made it difficult to test past 1000 µM. Hence any derivative that did not exhibit any significant IC_{50} at that concentration was designated as >1000 µM.

Table 4a Cell proliferation inhibition (IC_{50})* properties of compounds **4.2** and **4.4a-c** against MDA-MB-231, 4T1, WiDr, and MCF10A.

	MDA-MB-231	**4T1**	**WiDr**	**MCF10A**
4.4a	26 ± 6.1	13 ± 0.75	21 ± 1.7	38±5
4.4b	128 ± 10	16 ± 1.4	15 ± 0.69	67±9
4.4c	15 ± 0.02	5.7 ± 0.83	13 ± 0.59	24 ± 2
4.2	>1000	>1000	>1000	>1000

***** Values represent the average IC_{50} ± SEM (µM) of at least three independent experiments.

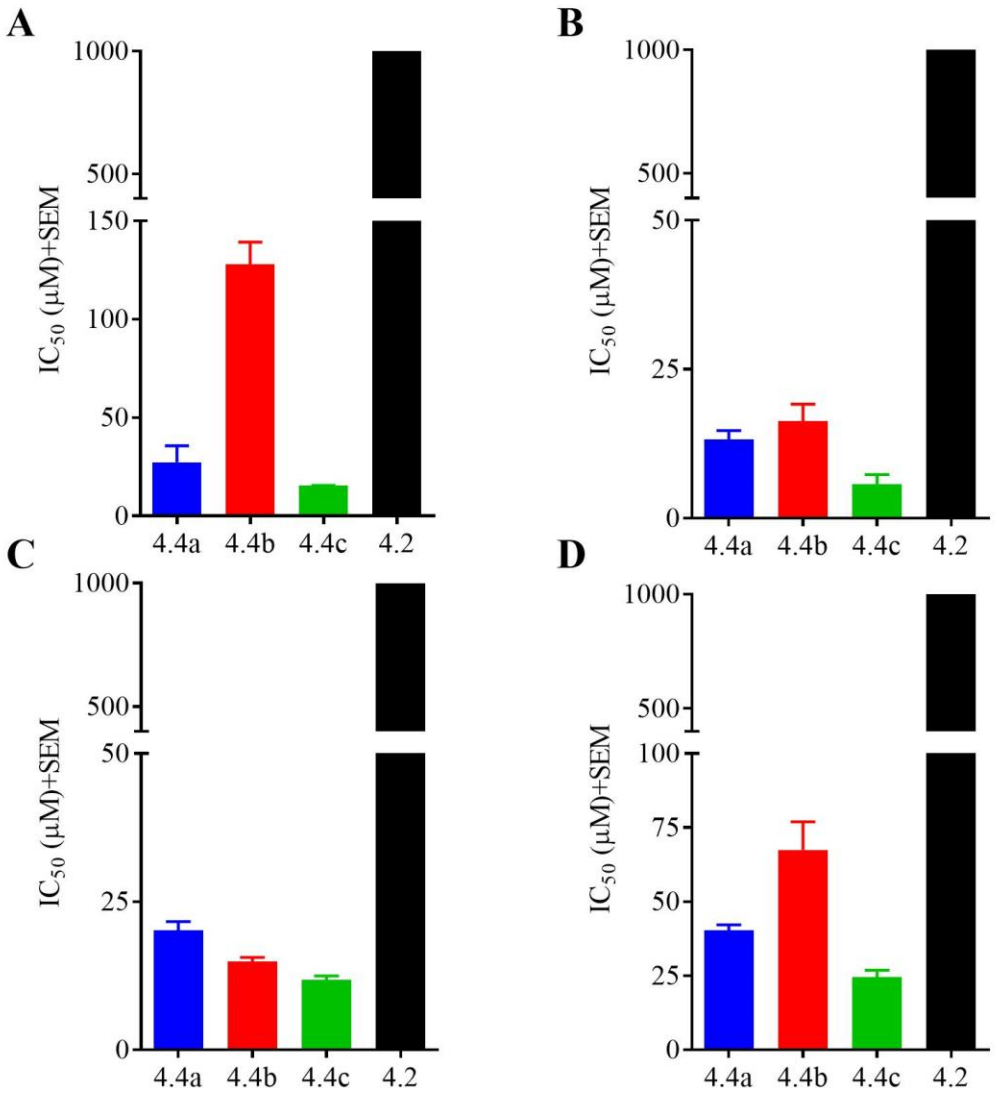

Figure 4b. Cell proliferation inhibition properties of compounds **4.2** and **4.4a-c**. Values represent the average IC_{50} ± SEM (µM) of at least three independent experiments in (**A**) MDA-MB-231, (**B**) 4T1, (**C**) WiDr, and (**D**) MCF10A cell lines.

The antiproliferation study showed the significance of the silylated group. The unsilylated amino CHC **4.2** did not exhibit any cell proliferation inhibition even at 1000 µM but the silylated amino CHC derivatives **4.2** exhibited excellent activity with a significant increase in potency ranging from 5 to 128 µM concentration. Similar to the previous chapter 3, these derivatives showed significant activity against MCT1 expressing cell lines 4T1 and WiDr when compared to MCT4 expressing cell line MDA-MB-231 (**Figure 4a**). Interestingly in WiDr cell line, the DPS derivative **4.4a** showed activity with an IC_{50} of ~21 µM which was lower when compared to the TBS and TIPS derivatives **4.4b-c** with IC_{50} values of ~15 and 13 µM, respectively. The TIPS silylated amino CHC **4.4c** exhibited the best activity against all three cell lines and was especially effective in the 4T1 cell line with the IC_{50} value of ~6 µM. This derivative also exhibited reduced antiproliferative activity against the non-cancerous MCF10A cell line with an IC_{50} at ~140 µM concentration. Compared to the other silylated amino CHC derivatives **4.1a-b** and **4.4a-c** (MCF10A IC_{50}: 44-41 µM) the TIPS derivative **4.4c** was observed to have ~28-fold reduction in activity.

These derivatives were further evaluated for their broad-spectrum cell proliferation inhibition against three additional cell lines. The first cell line 67NR was isolated from the same malignance as 4T1 but lacks the aggressive metastatic character. The MCF-7 cell line is an estrogen receptor positive breast cancer cell line and MIAPaCa-2 is a pancreatic cancer cell line.

Table 4b. Cell proliferation inhibition (IC_{50})* properties of compounds **4.2** and **4.4a-c** against 67NR, MCF7, and MIAPaCa-2.

	67NR	MCC-MCF-7	MiaPaCa
4.4a	18 ± 2	6.2 ± 0.63	38±3
4.4b	41 ± 1	34 ± 5.5	82±7
4.4c	10 ± 1	4.2 ± 0.47	28 ± 2
4.2	>1000	>1000	>1000

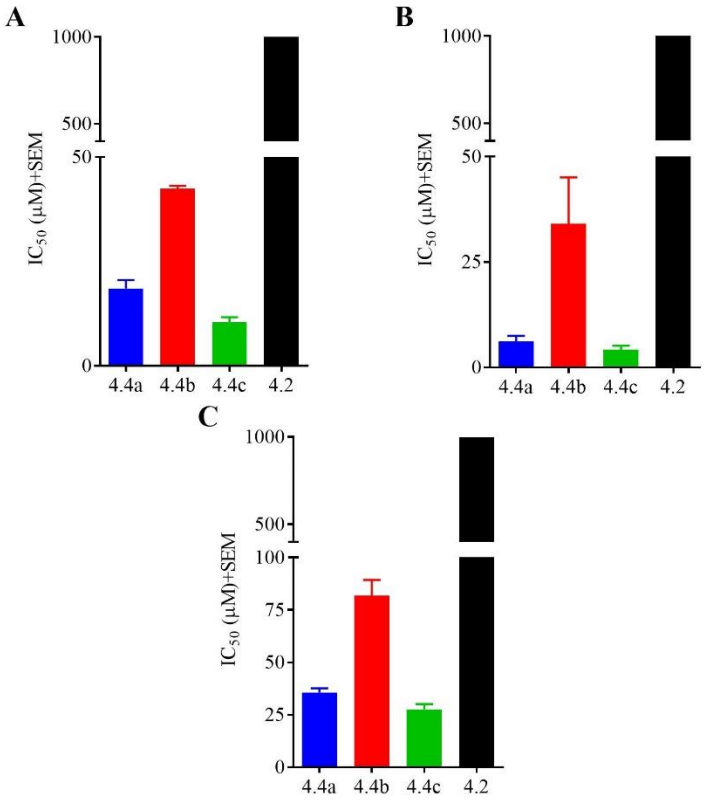

Figure 4c. Cell proliferation inhibition properties of compounds **4.2** and **4.4a-c**. Values represent the average IC_{50} ± SEM (μM) of at least three independent experiments in (**A**) 67NR, (**B**) MCC-MCF7, and (**C**) MiaPaCa cell lines.

The silylated amino CHC derivatives **4.4a-c** exhibited excellent antiproliferation and enhanced activity when compared to the unsilylated amino CHC derivative **4.2**. These derivatives exhibited a broad spectrum of activity especially against 67NR and MCF7. Interestingly, these derivatives were not as effective against MIAPaCa-2 cell line. This reduction in activity in all silylated amino CHC derivatives supports the cooperative effect of MCT1 inhibition and the mitochondrial disrupting silyl functional group.

4.4 Evaluation of metabolic profile in WiDr and MDA-MB-231

Silylated derivatives exhibited excellent antiproliferation ability against a broad spectrum of tumorigenic cell lines. Previously, silylated CHC derivatives **3.1a-b** and **3.5a-c** exhibited excellent metabolic disruption within the cancer cells WiDr and MDA-MB-231. To understand whether these properties are enhanced with the silylated amino CHC derivatives **4.4a-c**, the glycolysis and mitochondrial stress tests were conducted in WiDr and MDA-MB-231 cell lines. In this regard, we evaluated the ability of compounds **4.2** and **4.4a-c** at disrupting both glycolysis ATP production and mitochondrial respiration. Utilizing the two stress assays, we evaluated the various metabolic parameters and compared their differences with control cells (**Figure 4c**). The differences in the parameters can help understand the effects on the cells after exposure to our compounds.

Introduction of glucose into the media results in a spike in ECAR which is attributed to the cells glycolytic activity. The change in ECAR can be compared to the control group in order to understand how the test compounds are influencing glycolysis in the cell.

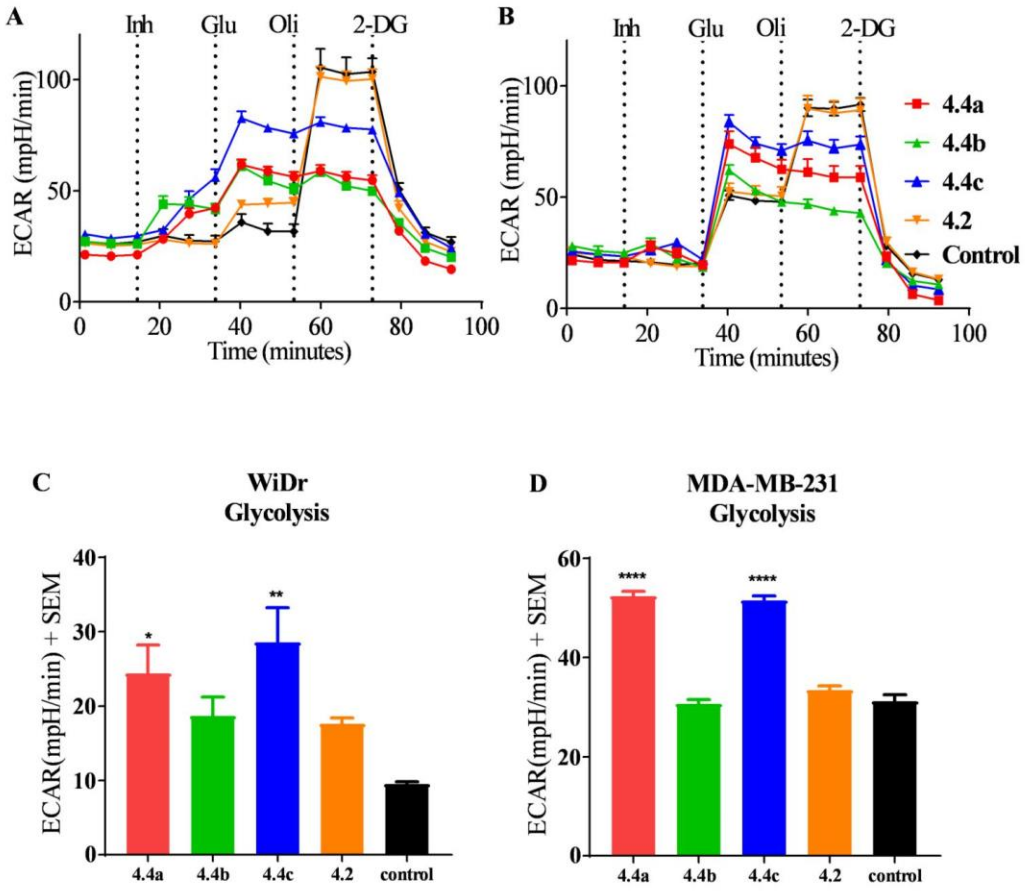

Figure 4d Comparison of the glycolytic parameters calculated from seahorse assay against (**A**) WiDr and (**B**) MDA-MB-231 cell lines. Comparison of the glycolysis parameters in (**C**) WiDr and (**D**) MDA-MB-231. Bar graphs represent the average ± SEM of at least three independent experiments. Statistical significance was calculated using one-way anova (****$p<0.0001$).

The resulting area allows for the quantification of ATP production from glycolysis. Similar to the silylated CHC derivatives **3.1a-b** and **3.5a-c** from the chapter 2.1, WiDr

exhibited apparent spikes in glycolysis after exposure to test compounds. Specifically, the **4.4a** and **4.4c** derivatives had significant effect on the glycolysis parameter in WiDr cell line. Interestingly, these derivatives had a greater impact on the MDA-MB-231 cell line with spikes in ECAR reaching ~50 mpH/min. This increase in MDA-MB-231 glycolysis was exclusive to derivatives **4.4a** and **4.4c**.

The next parameter evaluated was the glycolytic capacity. Determination of this parameter follows addition of oligomycin. The result is a sharp increase in ECAR. The maximum of this response is the glycolytic capacity and represents the maximum rate of glycolysis the cell can achieve after exposure to test compounds (**Figure 4e**).

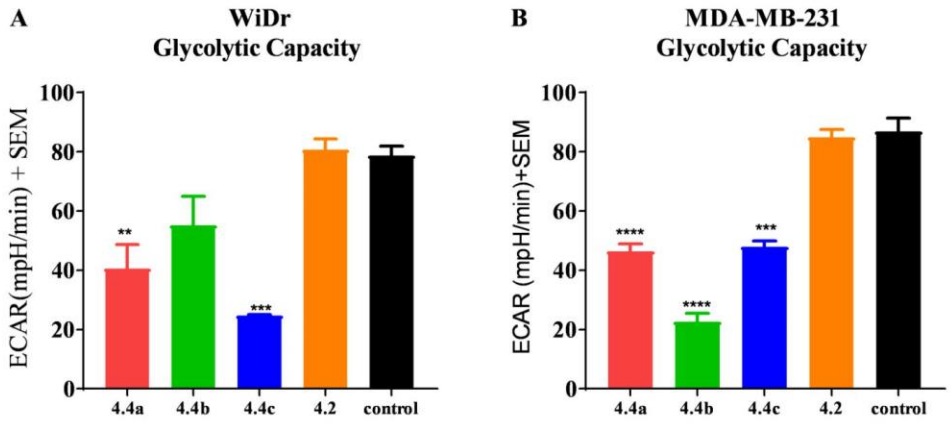

Figure 4e: Comparison of the glycolytic capacity calculated from seahorse assay against (**A**) WiDr and (**B**) MDA-MB-231 cell lines. Bar graphs represent the average ± SEM of at least three independent experiments. Statistical significance was calculated using one-way anova (****$p<0.0001$).

The glycolytic capacity was reduced significantly in the presence of test compounds **4.4a** and **4.4c** in the WiDr cell line. There was an observable difference in the TBS

derivative **4.4b** but it was not statistically significant. Conversely, **4.4b** exhibited a greater reduction in the glycolytic capacity when compared to the other silylated derivatives **4.4a** and **4.4b**. Interestingly, the MDA-MB-231 cell line seems to have greater susceptibility towards the silylated amino CHC derivatives **4.4a-c**.

The final parameter that was calculated is the glycolytic reserve. The glycolytic reserve is the difference between basal glycolysis and the glycolytic capacity. This parameter represents cells' metabolic plasticity and ability to switch ATP production from mitochondrial respiration to glycolysis. Inhibition of this parameter is indicative of a cell line that is more sensitive to metabolic disruption as response via glycolysis will be severely truncated.

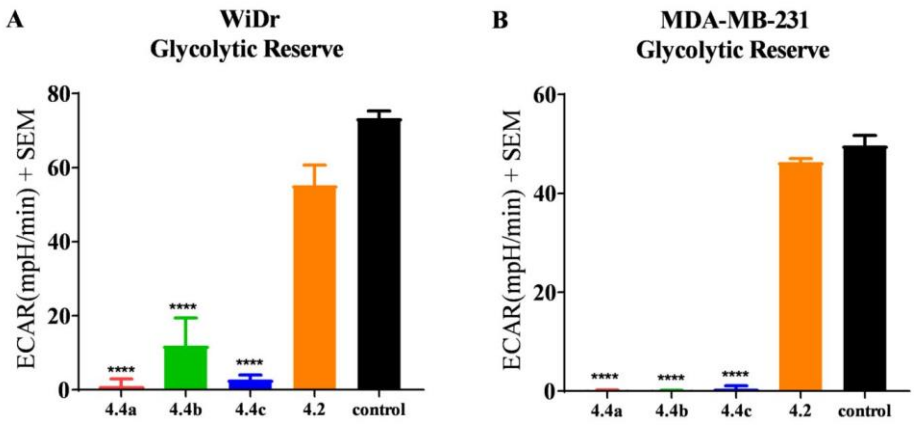

Figure 4f: Comparison of the glycolytic reserve calculated from Seahorse assay against (**A**) WiDr and (**B**) MDA-MB-231 cell lines. Bar graphs represent the average ± SEM of at least three independent experiments. Statistical significance was calculated using one-way anova (****$p<0.0001$).

In both cell lines WiDr and MDA-MB-231, there is significant reduction in the glycolytic reserve after exposure to the silylated amino CHC derivatives. The reduction and in some cases complete elimination of this property is closely related to the glycolytic capacity of the cell after exposure to the compounds. The parallels between these two properties highlight major glycolysis inhibitory effects of candidate inhibitors. The cells could no longer achieve their maximum glycolytic capacity. Furthermore, the glycolytic reserve property supports the theory that the cells are also pursuing most of their ATP production via glycolysis after exposure to the test compound. This dependency on glycolysis could be a result of mitochondrial dysfunction which can be examined using the mitochondrial stress test.

We then conducted the mitochondrial stress test which evaluates the state of mitochondrial respiration after exposure to the test compounds. The mitochondrial stress test is conducted in glucose rich media. After initial exposure to the compound, the ATP synthase inhibitor oligomycin was added. The resulting inhibition causes a rapid build-up of protons in the intramembrane region of the mitochondria. The resulting gradient stalls the electron transport chain as the energetic requirements to shuttle protons against this gradient is no longer energetically favorable. The stalling of the electron transport chain results in a significant reduction in oxygen use and subsequently a reduction in the OCR. This reduction in OCR is used to evaluate how much ATP is produced via mitochondrial respiration and furthermore can be used to evaluate the proton leak.

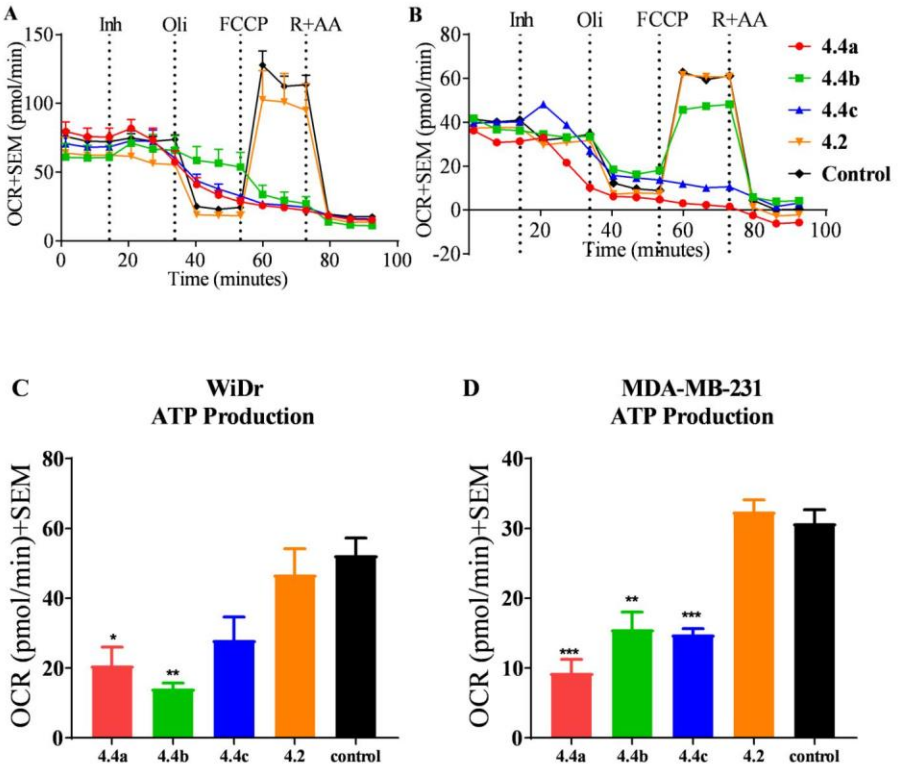

Figure 4g: Comparison of the ATP production parameter for (**A**) WiDr and (**B**) MDA-MB-231 cell lines. Comparison of the ATP production in (**C**) WiDr and (**D**) MDA-MB-231. Bar graphs represent the average ± SEM of at least three independent experiments. Statistical significance was calculated using one-way anova (****$p<0.0001$).

In most of the silylated derivatives, there was a significant reduction in the ATP production via mitochondrial respiration in both WiDr and MDA-MB-231 cell lines. The derivatives **4.4a** and **4.4b** exhibited significant reduction in ATP production in WiDr cell line. Conversely, the TIPS derivatives **4.4c** did not exhibit any effect on ATP production in this

cell line. In MDA-MB-231 cell line, there was a significant reduction in the OCR after exposure to all silylated derivatives **4.4a-c**. This result further supports the selectivity of these derivatives towards the MDA-MB-231 cell line.

The next step is the addition of FCCP. This derivative is an uncoupler effectively eliminating the proton gradient. This rapid reduction in the intramembrane potential results in increased electron transport chain activity. This activity subsequently increases the amount of oxygen the cell is using and causes a large spike in the OCR. This spike in OCR represent the maximum achievable mitochondrial respiration that the cell can pursue following exposure to the test compounds and is used to evaluate the relative efficiency of the mitochondria.

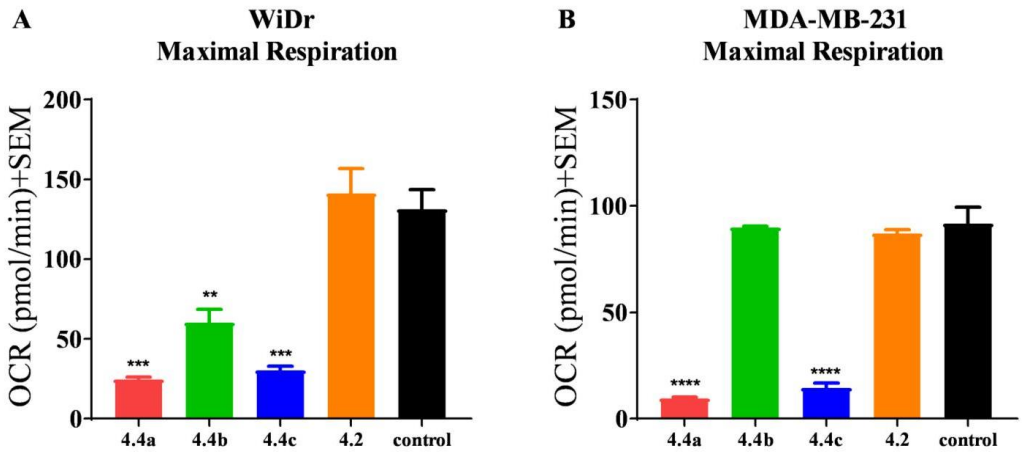

Figure 4h: Comparison of the maximal respiration parameter for (**A**) WiDr and (**B**) MDA-MB-231 cell lines. Bar graphs represent the average ± SEM of at least three independent experiments. Statistical significance was calculated using one-way anova (****$p<0.0001$).

The maximal respiration parameter supports effective disruption within the WiDr cell line after exposure to the candidate compounds. There is significant reduction in all silylated amino CHC derivatives **4.4a-c**. Conversely, in the MDA-MB-231 cell line, the **4.4b** derivative had no apparent effects on the maximal respiration parameter. The TBDPS **4.4a** and TIPS **4.4c** silylated amino CHC derivatives did exhibit significant reduction in the maximal respiration of MDA-MB-231. In fact, there was a 2-fold increase in efficacy of these two derivatives towards MDA-MB-231 cell line, again supporting the significance in selectivity towards this cell line when compared to WiDr.

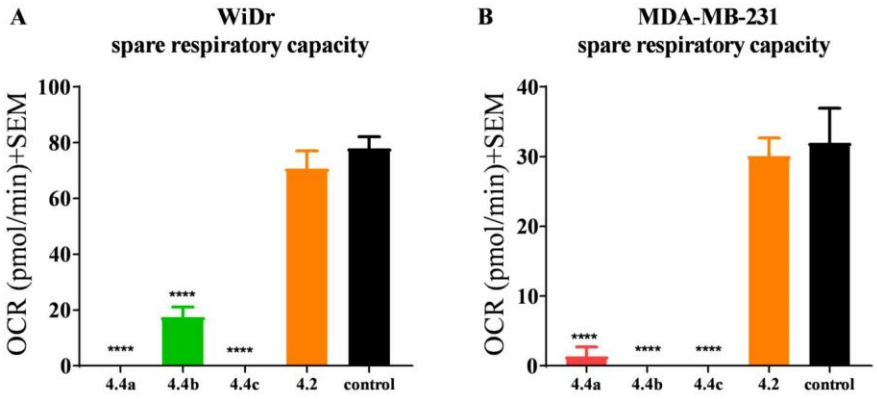

Figure 4i: Comparison of the spare respiratory capacity parameter for (**A**) WiDr and (**B**) MDA-MB-231 cell lines. Bar graphs represent the average ± SEM of at least three independent experiments. Statistical significance was calculated using one-way anova (****$p<0.0001$).

The next parameter evaluated is the spare respiratory capacity which is similar to glycolytic reserve in that it represents the difference in ATP production via ATP synthase

and the theoretical maximum respiration that the cells can pursue. As expected, derivatives that exhibited significant reduction in the maximum level of respiration and had a significant effect on the spare respiratory capacity. Some derivatives like **23c** completely eliminated the cells' spare respiratory capacity. These results indicated that the cancer cells had reached the maximum level OCR for ATP production.

The final step in the mitochondrial stress test is the addition of rotenone and antimycin A. The combination of these two derivatives effectively shuts down any OCR related to the electron transport chain and mitochondrial respiration. Any remaining OCR is non-respiratory associated OCR. The difference between this and OCR following oligomycin addition allows for the determination of proton leak.

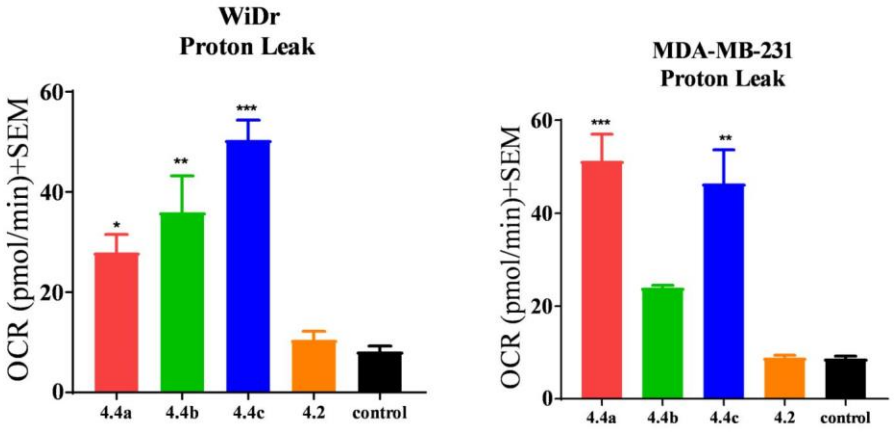

Figure 4j: Comparison of the ATP production parameter for (**A**) WiDr and (**B**) MDA-MB-231 cell lines. Bar graphs represent the average ± SEM of at least three independent experiments. Statistical significance was calculated using one-way anova (****$p<0.0001$).

Proton leak would be the main source of any OCR activity as electron transport activity would actively work to maintain the proton gradient resulting from the leaking protons. This parameter is directly associated with mitochondrial damage and effects the efficient production of ATP through mitochondrial respiration.

There was a major increase in proton leak with all derivatives in WiDr cell line. The TIPS derivative **4.4c** exhibited the greatest activity followed by TBS **4.4b** and TBDPS **4.4a**. Contrary to WiDr cell line, only the TBDPS **4.4a** and TIPS **4.4c** exhibited significant proton leak in MDA-MB-231 cell line. Interestingly, the TBS derivative did not exhibit any significant or apparent activity in this cell line. Furthermore, these results support the antiproliferation results observed in the MTT assay of these derivatives. The TBS derivative **4.4b** was the only derivative that had a significant reduction in activity towards the MDA-MB-231 cell line. Both these results support the selectivity of **4.4b** towards cell lines that are still dependent on cellular respiration for a significant portion of ATP production.

These studies also show how the silyl substitution could enhance the anti-cancer activity of these derivatives. In most of the parameters, the unsilylated amino CHC derivative **4.2** did not exhibit any enhanced activity towards both WiDr and MDA-MB-231. This emphasizes the importance of incorporating the silyl derivative and supports the hypothesis that silyl ethers could enhance mitochondrial stress.

4.5 Assessment of mitochondrial damage using epifluorescence microscopy

The Seahorse flux assay supports the theory that there exists mitochondrial damage. There was a significant increase in the proton leak of the cell's mitochondria. To understand the effects on the cells after exposure to test compounds MTR dye was used. MTR is used to monitor the mitochondria intracellularly. It not only identifies the location of the mitochondria but can also help identify the relative health of the mitochondria. The intensity of the dye is associated to the relative health of the membrane polarization and is a strong indicator of health of mitochondria as well. Furthermore, the study helps to identify the morphological changes that the cell is undergoing. These morpholigical changes can be used to identify the relative health of the cell and whether the cell is undergoing apoptosis. All the candidate compounds **4.4a-c** and **4.2** were imaged using this method. The concentration of 30 µM was chosen since this concentration was used for the Seahorse flux assays. This concentration is important for it allows for direct comparison of the metabolic parameters and the distribution and realative health of the mitochondria and cells. The silylated amino CHC derivatives **4.4a-b** and the unsilyated derivative **4.2** were evaluated. The unsilylated derivative will provide a good comparison to see what type of therapeutic advantage the silylatation of the amino CHC derivatives introduces.

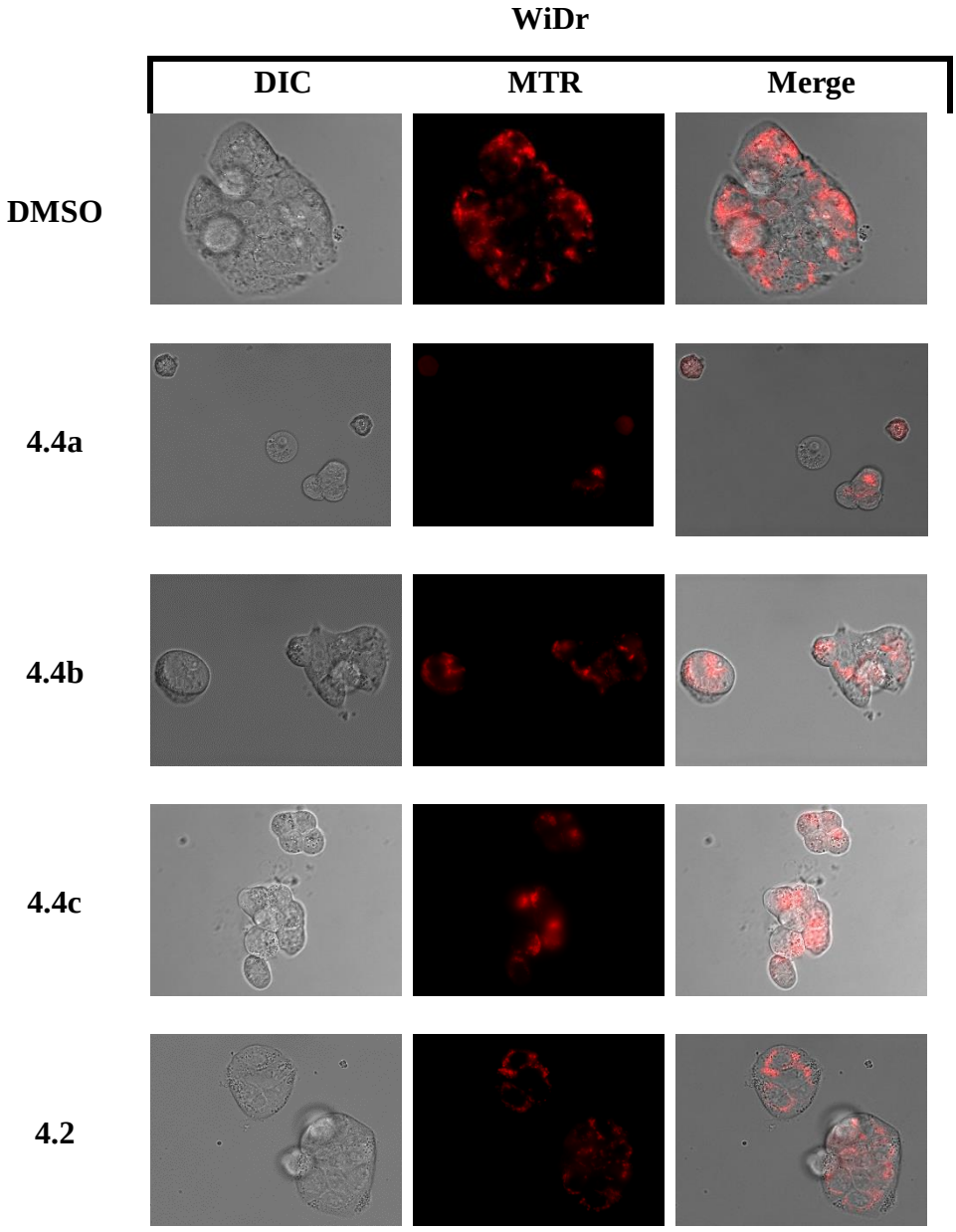

Figure 4k: Results after 24 hours of exposure to test compounds. The bright field image of WiDr after exposure to test compounds **4.4a-c** and **4.2** or the vehicle DMSO. The fluorescence of the MTR dye following exposure along with the overlay between the brightfield image and the MTR dye. The fluorescence and DIC images were recorded with similar exposure times and neutral density filters.

Following exposure to the compounds, the cells were imaged using DIC and fluorescence (**Figure 4k**). From these images, we can clearly observe that the mitotracker red for the DMSO control exhibits tight packing of the mitochondria. This is indicative of a healthy distribution of functional mitochondria within the cell. Following treatment with the silylated amino CHC derivatives **4.4a-c,** the DIC images show much lower number of cells congregating together. Additionally, many of the cells were observed to lose their adherence and balling up. These are all classic signs of a cell that is significantly stressed and undergoing apoptosis. MTR fluorescence, images from **Figure 4k** indicated that tightly packed pockets of mitochondria were absent. The dye was much more diffused and diminished in intensity. All these observations support the hypothesis that the silylated amino CHC derivatives **4.4a-c** induce significant mitochondria damage. When compared to the unsilylated derivative **4.2,** the importance of the silyl group for mitochondrial disfunction activity is apparent. Interestingly, the cell morphology was visibly changed as the cells congregation was in lower numbers when compared to the control DMSO treatment. This might indicate the importance of the transport inhibition property as the cells could not maintain cellular homeostasis of the surrounding microenvironment preventing large congregations of cellular mass.

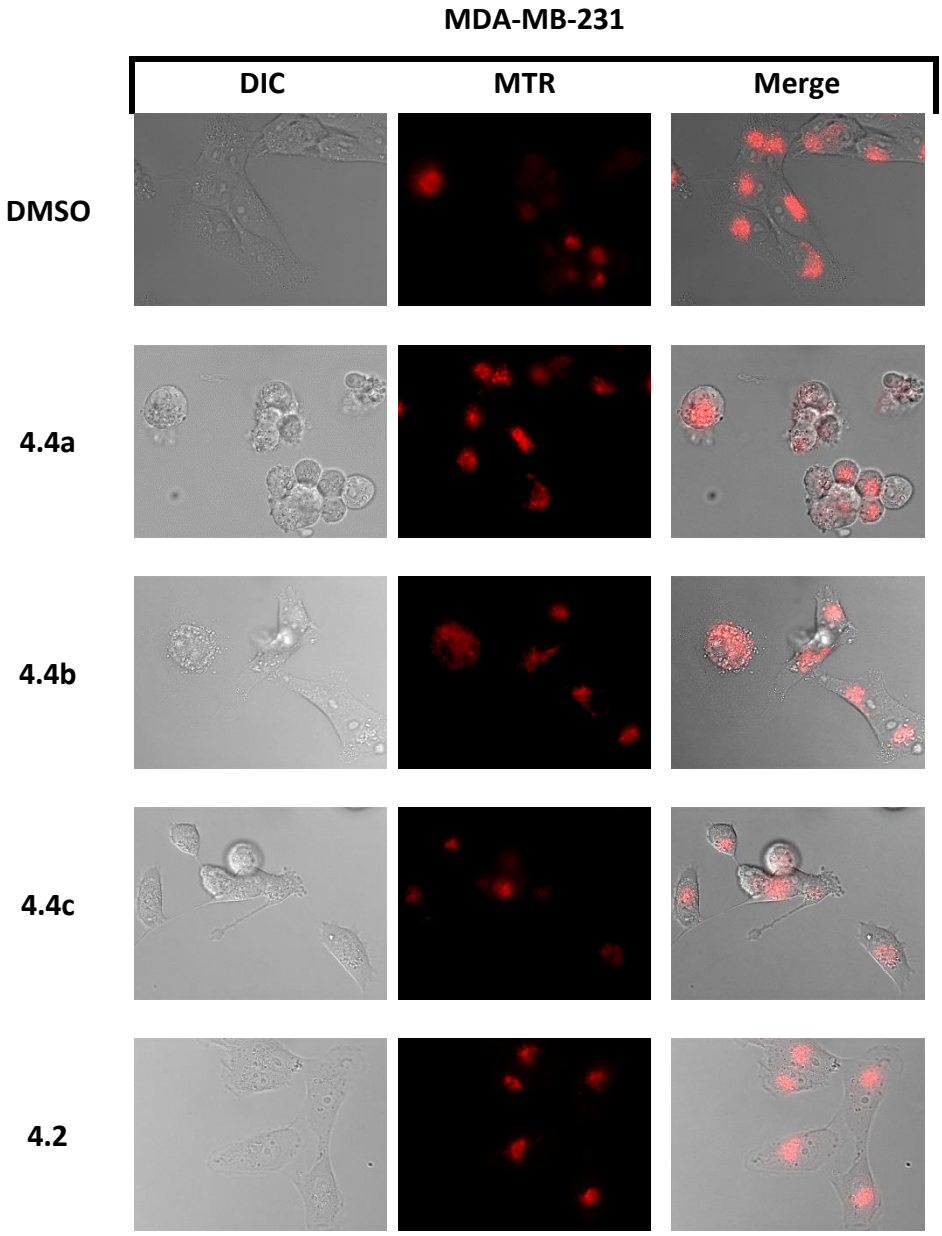

Figure 4l: Results after 24 hours of exposure to test compounds. The bright field image of MDA-MB-231 after exposure to test compounds **4.4a-c** and **4.2** or the vehicle DMSO. The fluorescence of the MTR dye following exposure along with the overlay between the brightfield image and the MTR dye. The fluorescence and DIC images were recorded with similar exposure times and neutral density filters.

The images in **Figure 4l** are after MDA-MB-231 cell were exposed for 24 hours to silylated amino CHC derivatives **4.4a-b** and the unsilylated amino CHC derivative **4.2**. The DIC images of the MDA-MB-231 gave an indication of the overall health of the cells and any changes in cellular morphology. When compared to the DMSO images, it was apparent that cells were extremely stressed, and was a strong evidence of the cells undergoing apoptosis. The cells began to ball up and there was signficant blebbing events visible after exposure to the silylated derivatives **4.4a-c**. Interestingly, the cells that were exposed to the unsilyalted derivative **4.2** had similar mophological properties to the control samples. These results support the importance of the silyl functional group in triggering apoptotic events within the tumorigenic cell lines as the cells started to ball up and in some cases, were being lyzed. The DPS **23a** seems to also have a significant impact on the congregation of WiDr cells, completely eliminating the tightly packed structure seen in the control DIC images. The fluorescent images highlight the stressed state of the cells. When compared to the DMSO control group, the neatly packed mitochondrial structures were observed to be more diffused throughout the cells. Furthermore, the intensity of the mitotracker seemed to be reduced. All these results were indications of significant dysfunction in the mitochondria after exposure to our compounds.

4.6 Discussion

Improvement on the *p*-silylated CHC template resulted in the integration of the *p*-*N*,*N*-dialkyl/aryl CHC derivative with *o*-silylation. The silyl ether was integrated into the ortho position using an aklyl spacer which conserved the *N*,*N*-dialkyl substitution required for potent MCT inhibiton. Intial evaluation of the cytotoxic elements supported the increased efficacy of these derivatives as broad spectrum chemotherapeutics. The derivatives exhibited excellent proliferation inhibition activity towards most of the cancerous cell lines. The metabolic parameters evaluated using the seahorse extracellular flux assays highlight the effectiveness of reducing glycolytic activity as well as mitochondrial activity. The derivatives **4.4a** and **4.4c** seem to exhibit the greatest activity with the derivative **4.4c** being slightly more effective. Future studies will involve systemic toxicity, *in vivo* pharmacokinetic and anticancer efficacy studies with the lead candidate compound.

CHAPTER 5: Introduction to introduction to NOS and its potential therapeutic application

5.1 Nitric Oxide Species (NOS) and Cancer Progression

Nitric oxide (NO) exhibits numerous physiological roles in cancer biology and tumor progression. Specifically, it has been known that an increase in elevated NO signaling is linked to have anti apoptotic effects and promotes angiogenesis. Enhanced NO release is achieved by the over expression of the three isoforms of nitric acid synthase which have been linked to chemo resistance and poor clinical outcome leading to the theory that increased NO release is important for tumor progression.[80–82] Thus NO release has to be carefully calibrated and controlled as NOS release is a double edged sword (**Figure 6a**).

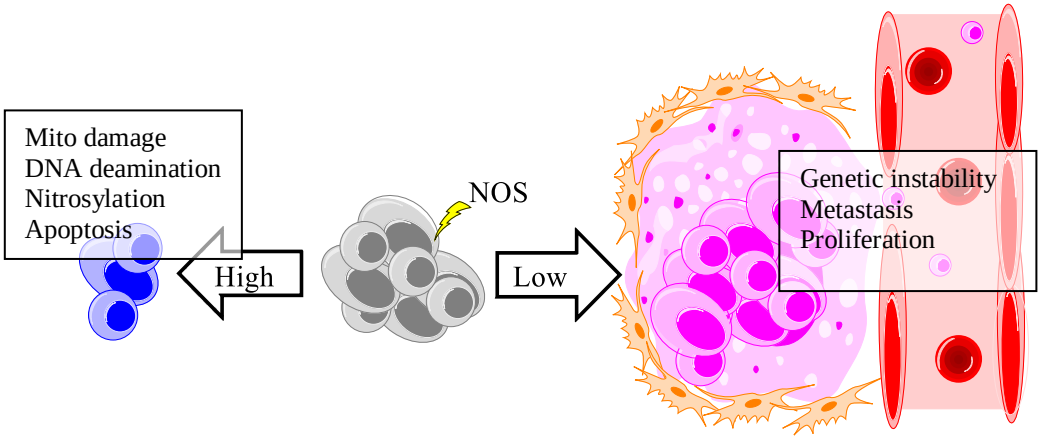

Figure 5a: The effects of NOS on the progression of tumors in patients. Low levels have been linked to tumor promoting events while high levels of induced NOS can lead to apoptosis.

Conversely, increased levels of intracellular NOS via xenobiotics has a similar effect to other reactive oxygen species (ROS). Ultimately, micromolar concentrations of NOS results in DNA deamination, nitrosylation of enzymes, mitochondrial dysfunction,

and cellular apoptosis.[83] There have been numerous strategies employed to shift the balance of NO within the tumor cells between anti-NO and pro-NO effects for therapeutic intervention in cancer. The purpose of anti-NO strategy is to decrease the release of NO by inhibiting nitric oxide synthase. This method of therapeutic intervention requires chronic administration of the drug and can lead to serious side effects like hypertension.[84] Pro-NO strategies pursue the selective induction of NO species within the tumor via NO-donors. This method is ideal as it does not require chronic systemic administration and can be tailored for selective induction of NO release. Selective delivery of NONOates have been classically studied as a model pro-NO strategy with excellent anti-proliferative effects.[85] Further expansion of the NONOates resulted in the development of NO donors that were physiologically stable until activated by enzymatic activity like nucleophilic aromatic substitution by glutathione S-transferase or an external trigger like photo-labile NO releasing elements.[86–90]

5.2 Literature known NO donors

Development of more effective pro-NO structures have led to metabolically stable entities that require a trigger for the release of the reactive NOS. In most of the cases, these triggers are enzymes that are specifically overexpressed in late stage cancers.[91–93]

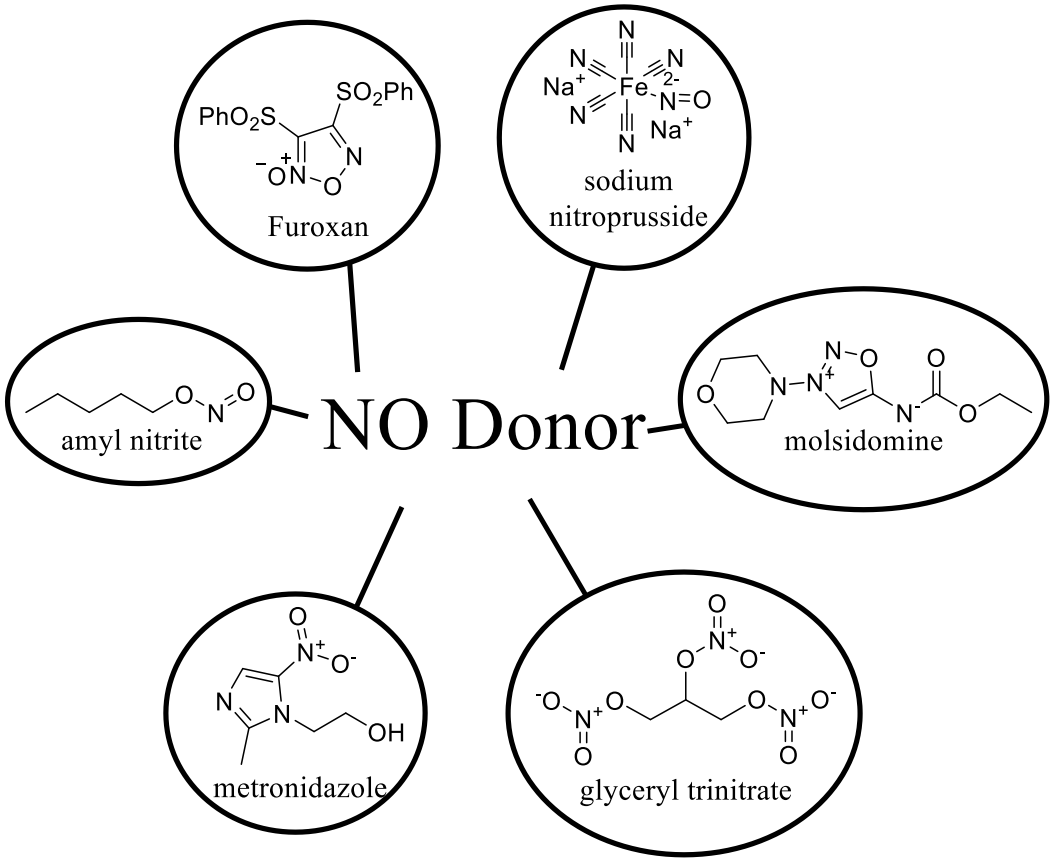

Figure 5b: Modern NO donors that have been used for selective release of NO.

The development of heterocyclic pro-NO structures yielded a more stable molecular entity with increased biological half-life. The initial work was aimed at developing a pro-NO entity with enhanced pharmacological properties than nitroglycerine. Amyl nitrite is a clinically used antihypertensive medicine with well characterized NO donating properties but has little selectivity. The result of administration was a systemic effect leading to elevated blood flow and a decrease in vascular resistance.[94] Melsidomine is a class of sydnonimines which are prodrug entities that are activated upon hydrolysis by the enzymes in the liver to yield the active 3-morpholinosydnonimine (SIN-1) (**Figure 5b**). Under alkaline conditions, the SIN-1 complex releases NO.[92] The active metabolite has a

very short biological half-life of only two hours and has been linked to peroxynitrite toxicity limiting the therapeutic potential of this molecular entity.[95] Glycerol trinitrate (GTN) is an organic nitrite prodrug requiring denitration for activation of the pro-NO molecular entity. The denitration is facilitated by sulfhydryl groups, enzymes like glutathione S-transferase, and mitochondrial aldehyde dehydrogenase. The therapeutic potential of this derivative has been evaluated for its anti-cancer properties and it has been found to translate well into xenograft and murine models resulting in the reduction of metastatic events, increasing chemo-sensitization, and tumor reduction.[96,97] Sodium nitroprusside (SNP) represents a special class of pro-NO based on metal-NO complexes **(Figure 5b**). NO has a high affinity to iron metals and this complex releases in a 1:1 ratio of SNP to NO. The mechanism of NO release is mediated via thiol reduction or with irradiation.[92] Studies with this pro-NO metal complex have shown promise in its anticancer efficacy but suffers from toxic side effects including the formation of cyanide, peroxinitrite, and hydrogen peroxide.[98]

Metronidazole represents a heterocyclic NO-donor and is commonly used for its antimicrobial properties via selective NO release (**Figure 5b**). Metronidazole has been the optimal drug for its selective targeting of anaerobic or microaerophilic microbes which incorporate the metronidazole molecular entity into its electron transport chain forming NO.[99] Most recently, it has been incorporated into molecular entities for selective delivery of therapeutically important anti-cancer derivatives.[100,101]

Phenylsulfonylfuroxan is another NO-donor heterocycle that has gained a lot of interest for its pro-NO donor abilities (**Figure 5b**). The structure has been favored for its

stability under physiological conditions and does not cause nitrate tolerance over chronic exposure *in vivo*. Two well-known furoxan derivatives CAS1609 and CHF2363 have been extensively evaluated for their cardiovascular properties (**Figure 5c**). Both the derivatives have been very attractive therapeutics due to their long term potency, oral bioavailability, and lack of tolerance development. [102,103]

CAS 1609 CHF 2363

Figure 5c: Commonly used furoxan derivatives for their treatment of various cardiovascular disease via vasodilatory effects.

Evaluation of both compounds for their cytotoxic properties as potential anticancer treatment have shown that CHF 2363 is more effective at much lower concentrations when compared to CAS 1609. The specificity of CHF 2363 is largely attributed to the electronegative properties of the heterocyclic ring.[104] This increased efficacy of CHF 2363 has driven further development of the phenylsulfonylfuroxan group. The diphenylsulfonylfuroxan heterocyclic ring comprises of strong electron-withdrawing nature resulting in an activated electrophilic carbon atom. The widely accepted mechanism of NO release of substituted phenylsulfonylfuroxan begins with a nucleophilic attack on the electrophilic carbon C3 or C4 via thiols in glutathione S-transferase followed by intramolecular reaction resulting in a cleavage of the N-O bond. The resulting unstable anion decomposes to form isomeric nitrosoethylenes followed by release of the nitroxyl anion (**Figure 5d**).[91]

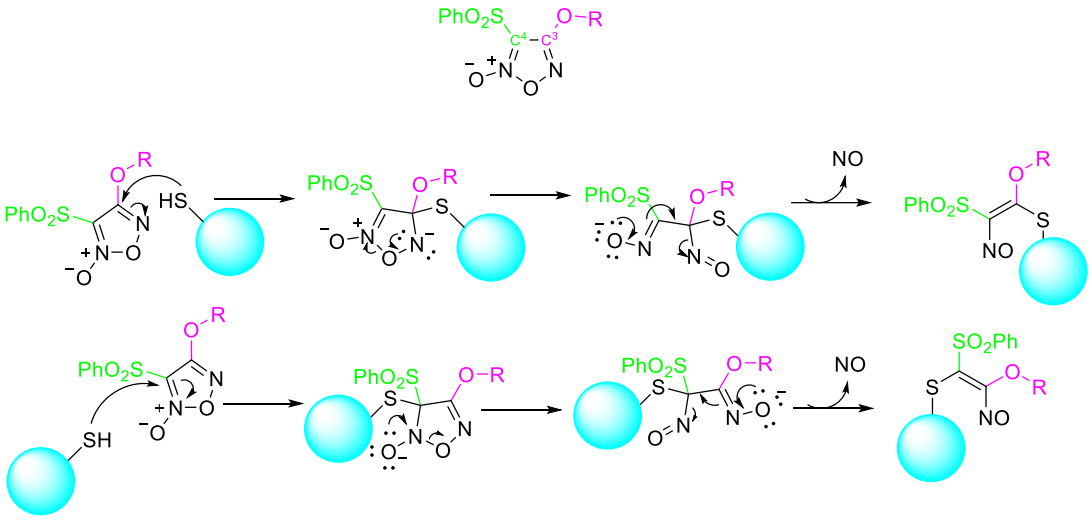

Figure 5d: The two glutathione S-transferase mediated release mechanisms of the phenylsulfonylfuroxan group leading to intracellular release of NO.

The above mechanism makes use of the active site of glutathione S-transferase which has been found to selectively target the furoxan derivatives to cancer cells resulting in the release of NO intracellularly.[105] The targeted release of NO via glutathione S-transferase has been widely supported by other researchers as the main mechanism and have highlighted the therapeutic relevance of selectively exploiting them in the development of furoxan based chemotherapeutics.[81,106,107]

5.3 Glutathione S-Transferase (GST)

Cancer progression is marked by adoption of strategies to promote drug resistance. One approach that cancers commonly adopt is the overexpression of various enzymatic entities like GST. The GST family is a select group categorized as phase II detoxification enzymes. Normally, these enzymes maintain benign cells through protection of cellular

macromolecules. This is achieved by conjugating the macromolecules with glutathione (GSH). Conjugation of GSH protects the macromolecules from intra/extracellular electrophilic compounds and oxidative stress. [108,109]

This protection properties of the GSH and GSTs have been exploited by cancer cells imparting resistance to therapeutic agents. The result of this overexpression is an ever-decreasing benefit from chemotherapeutics. Recently, the overexpression of GST within late stage tumors represent a potential opportunity for selective therapeutic intervention. This over expression can be exploited by the pro-NO donor furoxan which is activated when it comes in contact with GST active site.

CHAPTER 6 Synthesis and Evaluation of NO Donor CHC Hybrid Derivatives as Anti-Cancer Agents

6.1 MCT 1 and 4 inhibitor-NO donor conjugates

The electrophilic carbons are liable to nucleophilic attacks allowing for easy substitutions and incorporation into novel molecular hybrids for various therapeutic effects.[91] Recently, the molecular conjugation of novel phenylsulfonylfuroxans have produced interesting chemotherapeutics that were able to induce necrosis *in vivo* at a dose that exhibited no negative side effects in mice.[110] This multifaceted design of coupling two pharmacologically privileged structures has led to many phenylsulphaforoxan derivatives with excellent chemotherapeutic potential demonstrated *in vivo* xenograft models.[86,110–118] In this regard, we envisioned to combine toxicity enhancing furoxan based NO donor with our previously studied MCT1 and 4 inhibitors to evaluate their efficacy as anticancer agents (**Figure 6a**).

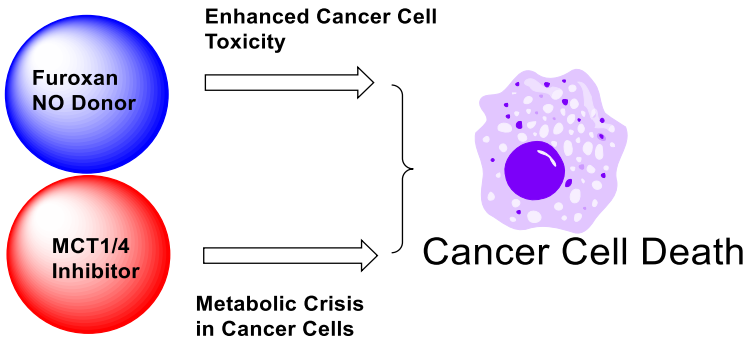

Figure 6a: Hypothesis and rationale of MCT1/4 NO donor hybrids as anticancer agents.

The *p*-*N*,*N*-dialkylamino CHC inhibitors reported by us exhibited excellent MCT1 and MCT4 inhibition and reduced growth in various tumor models. However due to the lack of cytotoxicity of these MCT inhibitors, these compounds had to be given at higher

concentration (~50mg/kg or higher) to observe significant tumor growth inhibition. In this regard, we envisioned that conjugating metabolically stable NO donor phenylsulfonylfuroxan to *p-N,N*-dialkylamino CHC template would provide novel candidate compounds with potent MCT inhibition and higher cytotoxicity. We hypothesized that this molecular hybridization would produce novel candidate compounds with a higher therapeutic potential for cancer treatment.

6.2 Synthesis of hybrid NO Donor N,N-dialkyl CHC Derivatives

The NO Donor diphenylsulphafuroxan (**Scheme 6a**) was synthesized via literature known procedures by starting with thiophenol and reacting it with bromoacetic acid in the presence of potassium hydroxide as a base to yield **6.1**. The desired product was formed by initial oxidation with hydrogen peroxide followed by nitration, dimerization, and cyclization using fuming nitric acid. The reaction mixture was then cooled, and the product was crystallized from the mixture at -20°C to yield a white to off white solid **62**.

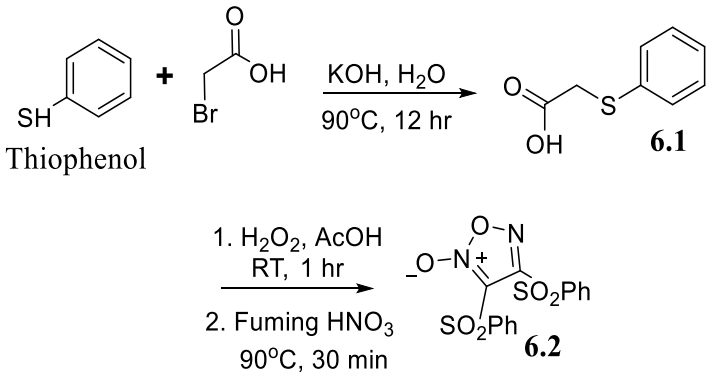

Scheme 6a: The synthesis of the NO donor diphenylsulphafuroxan starting with thiophenol **6.2**.

Next, the *N,N*-dialkyl CHC-NO donor conjugates **40a** and **b** were synthesized by starting from commercially available N-ethyl/benzyl anilines. Reaction of these amines with methyl acrylate in the presence of sodium bromide under acidic conditions resulted in Michael addition products **6.3a** and **b**. The esters **6.3a** and **b** were reduced to corresponding alcohols **6.4a** and **b** with lithium aluminum hydride by refluxing in THF for two hours. The hydroxy group in hydroxydialkyl aniline **6.4a** and **b** was protected with acetyl chloride to yield the corresponding acetate **6.5a** and **b**. Next Vilsmeier-Haack formylation reaction was performed using $POCl_3$ in DMF to obtain the corresponding aldehydes **6.6a** and **b**. The acetate group in aldehydes **6.6a** and **b** were deprotected with potassium carbonate to yield the monohydroxydialkyl benzaldehydes **6.7a** and **b**. Knoevenagel condensation of the benzaldehyde **6.7a** with cyanoacetic acid resulted in the hydroxycyanocinnamic acid **6.8**. The aldehydes **6.7 a** and **b** were coupled to diphenylsulphafuroxan **6.2** to in the presence of DBU to provide the furoxan aldehydes **6.9a** and **b**. Knoevenagel condensation of **6.9a** and **b** with cyanoacetic acid gave the desired NO donor furoxan- *N,N*-dialkyl CHC derivatives **6.10a** and **b** (**Scheme 6b**).

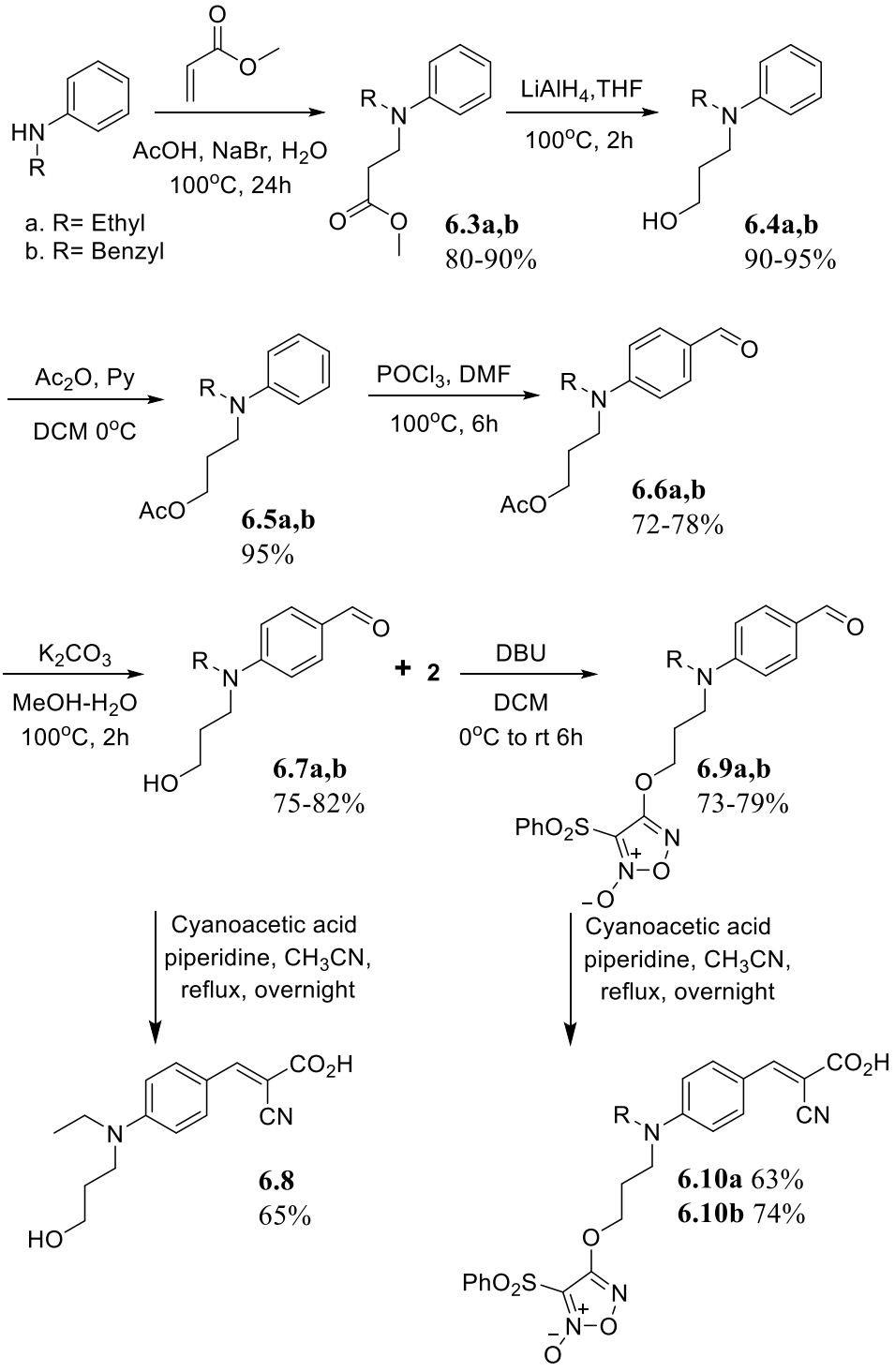

Scheme 6b: Synthetic procedure for the preparation of the *N,N*-dialkyl amino CHC **6.8** and furoxan *N,N*-dialkyl amino CHC's **6.10a,b**

To test the effects of the size of the spacer between the furoxan and the CHC, we incorporated the butanol side chain to ethyl aniline (**Scheme 6c**). To synthesize this derivative **6.10c,** N-ethylaniline was reacted with succinic anhydride yielding the amido acid **3c**. Complete reduction of amido and carboxylic acid groups in **6.3c** to amino alcohol with $LiAlH_4$ lead to poor yields Hence, to improve the yield of this reaction, the acid group in **6.3c** was esterified by treatment with thionyl chloride in methanol to yield the corresponding amido methyl ester **6.11**. Complete reduction of amide and ester to the corresponding amino alcohol **6.4c** was accomplished in good yields upon treatment with $LiAlH_4$ in refluxing THF. The alcohol in **6.4c** was then protected with acetyl chloride yielding the corresponding acetate **6.5c** followed by Vilsmeier-Haack formylation with $POCl_3$ in DMF to yield the aldehyde **6.6c**. Deprotection of the acetate group in **6.6c** was performed in the presence of potassium carbonate to yield the corresponding amino butanol aldehyde **6.7c**. The alcohol group in **6.7c** was coupled to diphenylsulphafuroxan **6.2** in the presence of DBU to get the NO donor conjugated product **6.9c**. The aldehyde in **6.9c** was subjected to Knoevenagel condensation with cyanoacetic acid to yield the desired furoxan CHC hybrid **6.10c** (**Scheme 6c**).

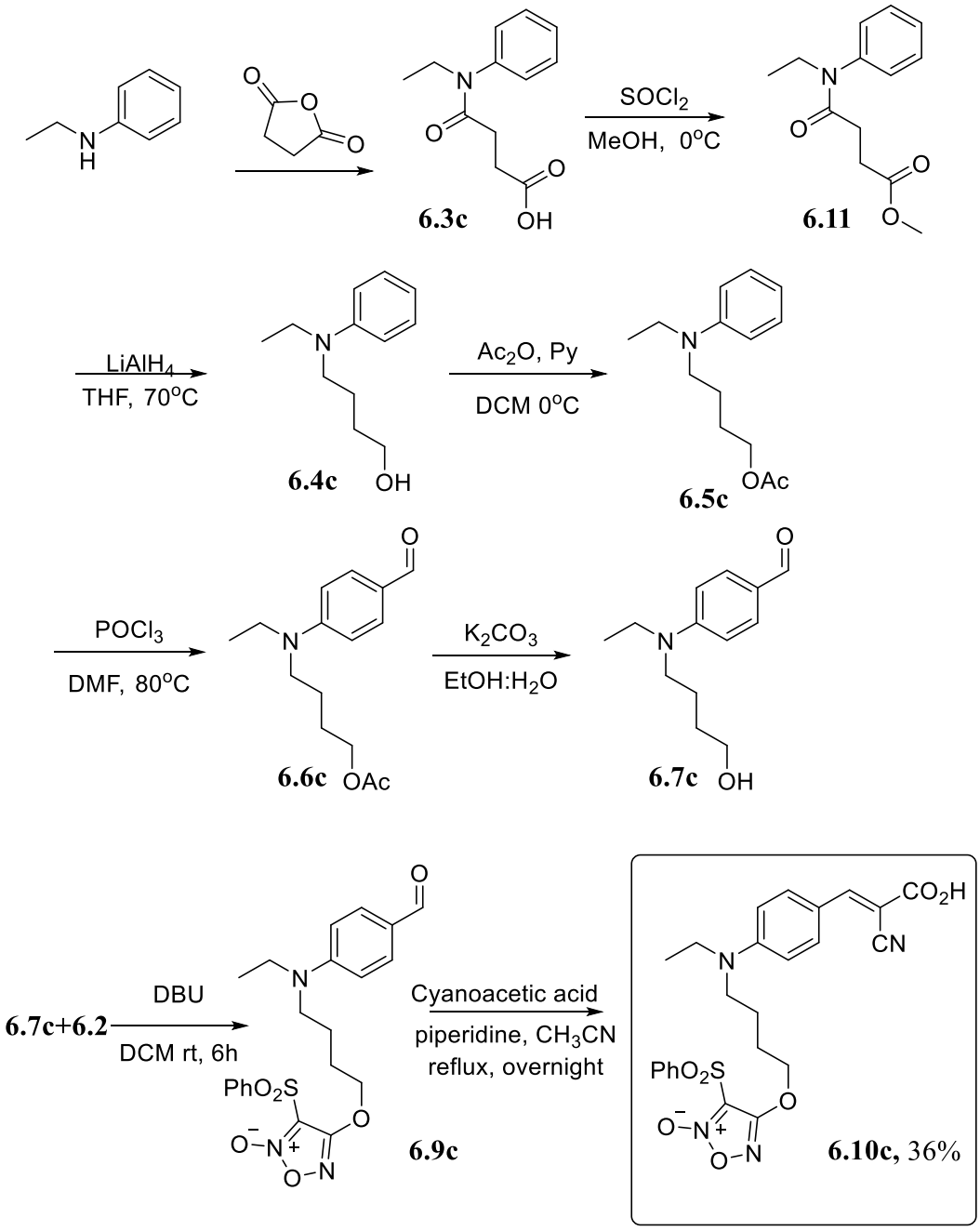

Scheme 6c: The synthesis of the furoxan *N*,*N*-dialkylamino CHC with a butyl linker **6.10c** with the corresponding yields as % next to the identifying number.

To help evaluate the importance of *N*,*N*-dialkyl groups in the CHC derivative, a novel furoxan ether CHC derivative **6.13** without *N*-alkyl groups was synthesized. In this case, the *N*,*N*-dialkyl subunit was replaced with hydroxyethoxy group of the furoxan to synthesize the hybrid derivative **6.13**.

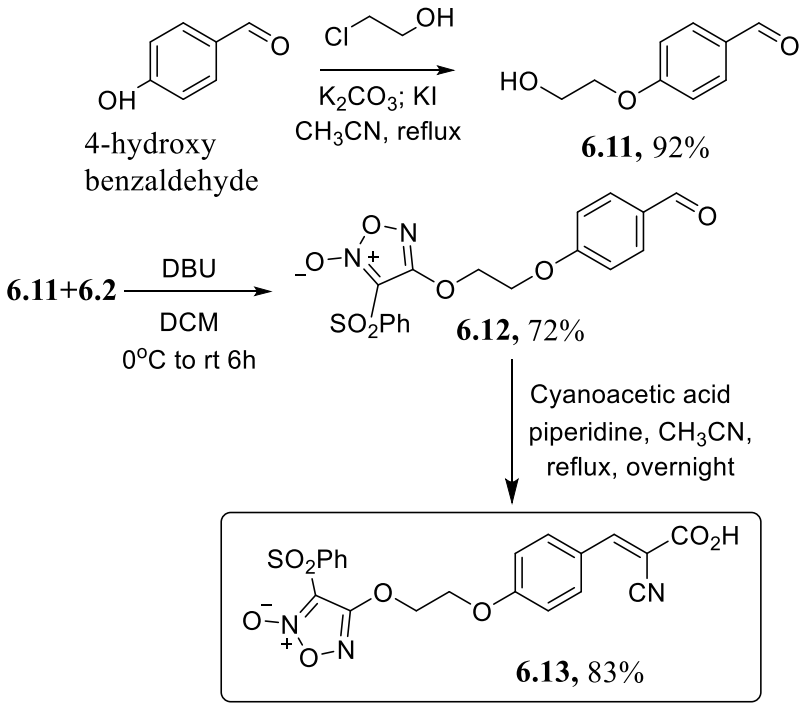

Scheme 6d: The synthesis of furoxan ether CHC **6.13** derivative starting from commercial grade 4-hydroxybenzaldehyde.

The synthesis of this derivative started with alkylation of commercially available 4-hydroxybenzaldehyde with chloroethanol in the presence of potassium carbonate. This reaction is followed by coupling 4- hydroxyethoxy benzaldehyde **6.11** to furoxan **6.2** in the presence of DBU followed by Knoevenagel condensation to yield the desired furoxan ethoxy CHC hybrid **6.13** (**Scheme 6d**).

6.3 Evaluation of compounds 6.10a-c, 6.13, and 6.8 for antiproliferation activity

The synthesized NO donor-CHC derivatives **6.8, 6.10a-c,** and **6.13** were evaluated for their antiproliferation ability against MDA-MB-231, which is an MCT4 expressing triple negative breast cancer cell line. These derivatives were also tested against 4T1, a metastatic murine model breast cancer cell line and WiDr, a human colorectal cancer cell line. Both 4T1 and WiDr predominantly express MCT1.[40,74] The immortalized Non-cancerous mammary epithelial cell line MCF10A was used to evluate the effectiveness of the compounds on a non-cancerous cell line. Cell proliferation inhibition was measured using 3-(4,5-dimethylthiazol-2-yl)-2,5-diphenyl tetrazolium bromide (MTT) colorimetric assay. The MTT is reduced by cellular mitochondrial reductase to the corresponding formazan dye which can be measured at 526 nm. The amount of MTT converted to formazan is an indication of the density and activity of the cells.[76]

Table 6a: Cell proliferation inhibition (IC_{50}) properties of compounds **6.10a-c**, **6.13**, and **6.8**.

	MDA-MB-231	**4T1**	**WiDr**	**MCF10A**
6.10a	3.2±0.58	8.3±0.7	5.16±1.71	36.0±7.5
6.10b	2.9±0.63	6.1±1.5	31.1±3.6	1.7±0.16
6.10c	2.0±0.63	8.2± 0.4	9.3± 2.0	21.8±3.3
6.13	168.0±7.2	131.2±13.2	8.3±0.7	15.1±0.7
6.8	>250	>250	>250	>250

***** Values represent the average IC_{50} ± SEM (μM) of at least three independent experiments.

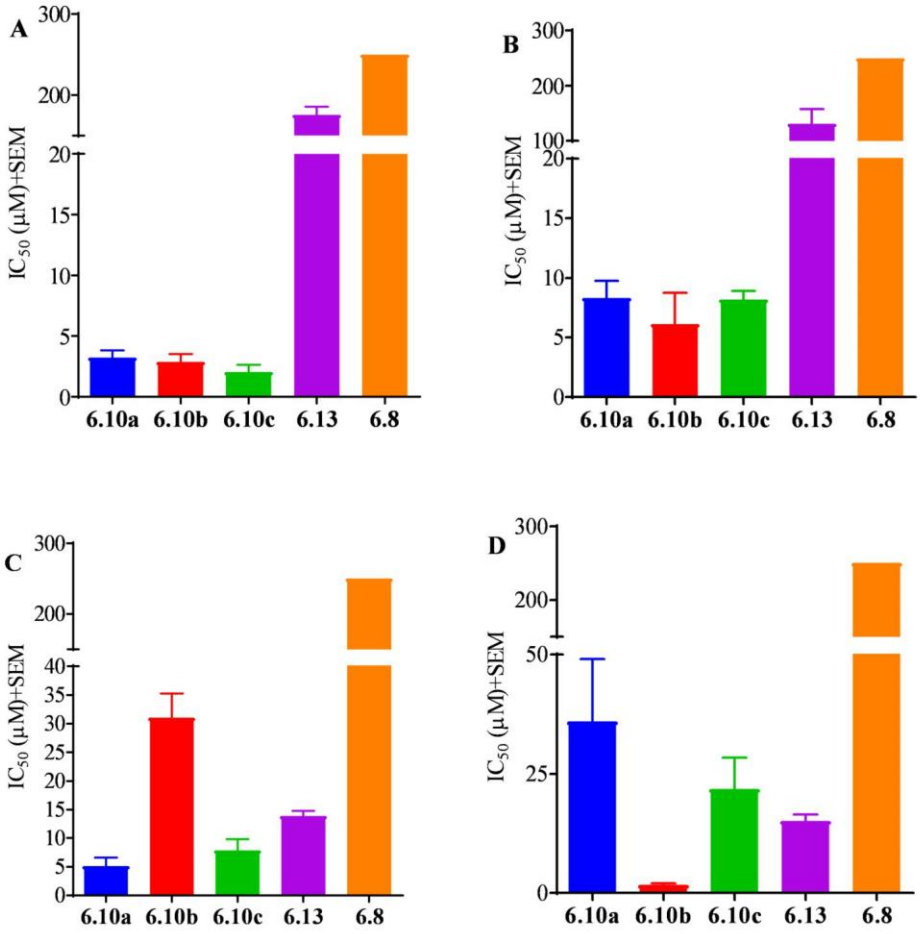

Figure 6b: Cell proliferation inhibition properties of compounds **6.10a-c**, **6.13**, and **6.8**. Values represent the average IC_{50} + SEM (µM) of at least three independent experiments in (**A**) MDA-MB-231, (**B**) 4T1, (**C**) WiDr, and (**D**) MCF10A cell lines.

Compounds **6.10a-c** exhibited cell proliferation inibition properties with IC_{50} values in the range of 2-36 µM against the cell lines tested (**Table 6a**). The derivatives **6.10a-c** were consistantly more effective against the cell line MDA-MB-231 (IC_{50} 2 to 3 µM). As expected, the replacement of the *N*,*N*-diamino group with the ethoxy in **6.13** had

a reduced activity against all of the cell lines except WiDr (IC_{50} ~8 μM). Interestingly, derivatives **6.10a** and **6.10c** were more effective on the cancerous cell lines (IC_{50} ~2 to 9 μM) but had diminished cell proliferation inhibition activity against MCF10A (IC_{50} ~20-30 μM) (**Table 6a, Figure 6b**).

Incorporation of the cell proliferation inhibition enhancing furoxan derivatives **6.10a-c** based on the pro-NO release were in general more cytotoxic. This was supported by the lack of any observed cell proliferation inhibition in non furoxan CHC derivative **6.8**. When No donors were conjugated with the MCT1 and MCT4 inhibitors, there was an enhanced antiproliferative activity with compounds **6.10a** and **6.10c** in cancerous cell lines with apparently lower antiproliferative activity towards the MCF10A cell line. With these encouraging cell proliferation inhibition results, we then proceeded to evaluate these derivatives for MCT inhibition to see if they retain their MCT inhibition activities.

6.4 Evaluation of test compounds for MCT inhibition using ^{14}C-lactate uptake assay

Incorporation of the furoxan subunit in **6.10a-c, 6.13** and **6.8** in place of the free alcohol **2.8** greatly enhanced the antiproliferation activity of these derivatives. Derivatives **6.10a-c, 6.13** and **6.8** were evaluated for MCT1 and MCT4 inhibition using ^{14}C-lactate uptake assay to determine whether there was a loss of inhibition activity due to the furoxan unit. The uptake assay is a radiometric assay that uses ^{14}C-lactate. Plated cells were exposed to ^{14}C-lactate in the presence of the test compounds. After lysing the cells, the β-radiations from the ^{14}C-lactate that were internalized in the cell were measured using a scintillation counter. The change in lactate uptake with varied concentrations of inhibitor allowed for the determination of the IC_{50} value. The two cell lines that have been used for

the assay are the MCT1 expressing RBE4 for MCT1 inhibition and the MCT4 expressing MDA-MB-231 for MCT4 inhibition.[30]

Table 6b: MCT1 and MCT4 IC_{50} values of compounds **6.10a-c**, **6.13,** and **6.8**.

Compound	**MCT1 IC_{50} (µM)**	**MCT4 IC_{50} (µM)**
6.10a	0.057±0.016	0.116±0.002
6.10b	0.114±0.014	0.161±0.019
6.10c	0.229	0.106±0.005
6.13	0.099±0.004	TBD
6.8	>10	>10

*Values represent the average IC_{50} ± SEM (µM) of at least three independent experiments.

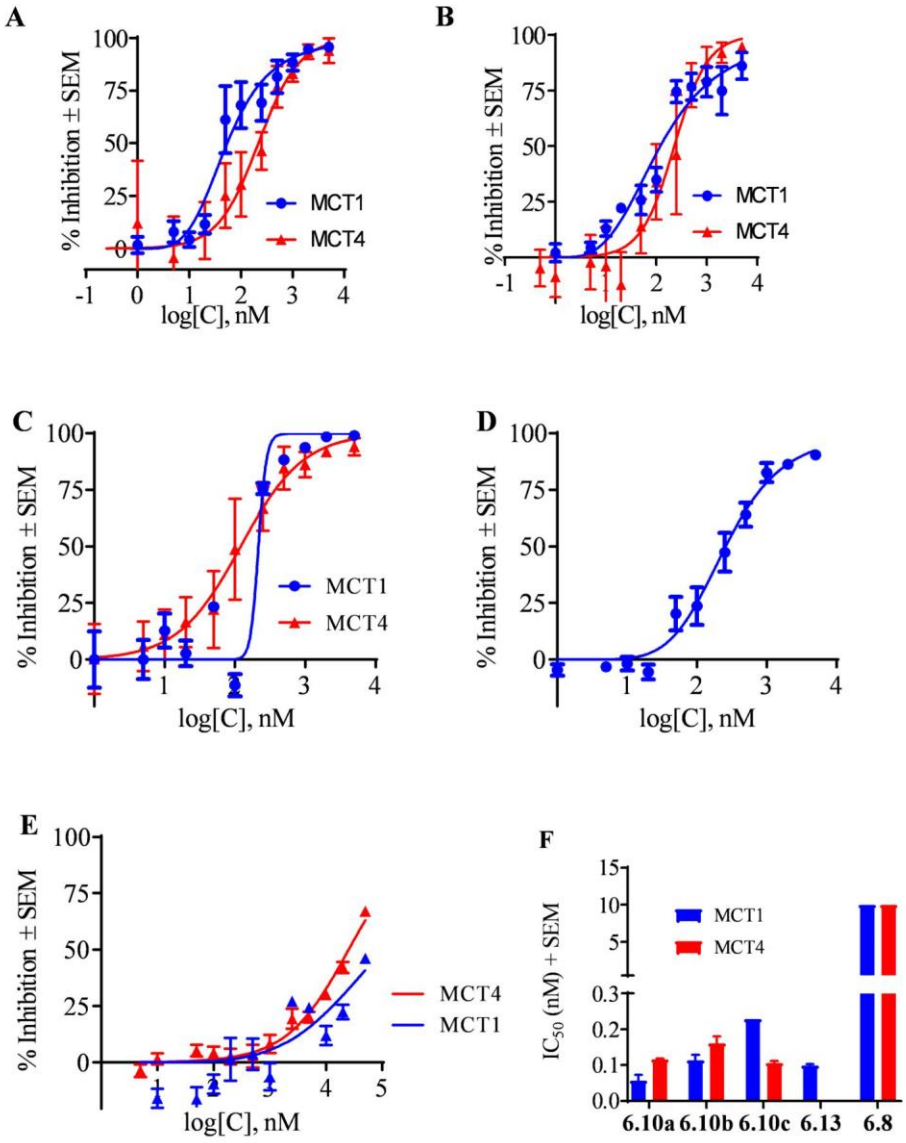

Figure 6c: MCT1 and MCT4 inhibition properties of compounds (**A**) **6.10a**, (**B**) **6.10b**, (**C**) **6.10c**, (**D**) **6.13**, (**E**) **6.8**. Bar graphs represent the average IC_{50} ± SEM (µM) of at least three independent experiments. (**E**) Bar graph of the IC_{50} values of compounds.

The results of the lactate uptake assay highlighted the importance of the lipophilic alkyl chain in the para position. All the four derivatives in conjugation with furoxan CHC

hybrids exhibited low nanomolar inhibitor activity against MCT1 and MCT4. Incorporation of the polar hydroxyl group on the side chain in **6.8** resulted in a loss of inhibition of MCT1 or MCT4 even up to 10 µM concentration. The derivative **6.10a** exhibited the highest activity against MCT1 with an IC50 of ~0.065 µM. The same compound **6.10a** had lower selectivity to MCT4 of ~0.11 µM. A similar trend in activity was seen for **6.10b** derivative as well. Compound **6.10c** was interesting as it showed great selectivity towards MCT4 (IC_{50} 0.11 µM) but slightly lesser towards MCT1 (IC_{50} ~0.23 µM). This could be explained by a potential threshold on the chain length and an impact on lipophilicty towards MCT1 or MCT4. Higher lipophilic molecules such as **6.10c** had a slightly higher selectivity towards MCT4 activity and **6.10a** with slightly lower lipophilicity was more selective towards MCT1 **(Table 6b, Figure 6b**).

6.5 Evaluation of the glucose stress test of test compounds

MCTs play a vital role in the cellular transport of glycolytic metabolites including lactate and pyruvate which are shuttled into the mitochondria for use in the TCA cycle for OxPhos. Hence, inhibition of this transport may result in perturbation of the processes involved in efficient glycolysis and/or OxPhos. In this regard, we evaluated the ability of compounds **6.10a-c, 6.13** and **6.8** at disrupting various metabolic parameters. These discrepancies in the metabolic parameters were evaluated using established glycolysis stress test and mitochondrial stress test.

Prior to running the assay, cells were washed twice with glucose free assay media. This allows for the measurement of non-glycolytic ECAR followed by addition of the test compounds. Next, glucose was added stimulating glycolysis within the cell. The spike in

ECAR can be used to determine the rate of glycolysis within the cells. The induction of the ATP synthase inhibitor oligomycin results in another spike in ECAR. This represents the cells' maximum obtainable rate of glycolysis as most ATP production will be produced through glycolysis. Finally, 2-deoxyglucose was added to completely shut down the process of glycolysis which is required to interpret the glycolytic capacity. The glycolytic reserve is the difference between the glycolytic capacity and glycolysis.

Previously our lab utilized MCT1 expressing WiDr and MCT4 expressing MDA-MB-231 cell lines to study the glycolytic parameters. Metabolic profile of these two cell lines are markedly different since, WiDr uses greater amounts of OxPhos and MDA-MB-231 uses more glycolysis as their energy source.[30]

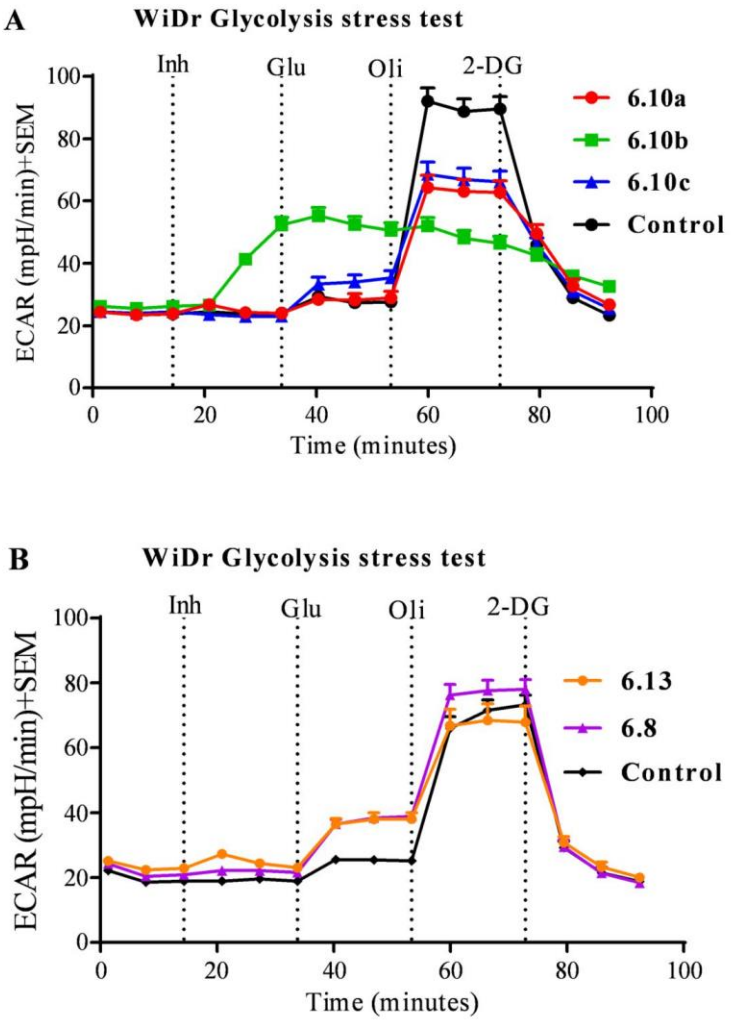

Figure 6d: GST profile in WiDr cell line for compounds (**A**) **6.10a-c** and (**B**) **6.13** and **6.8**.

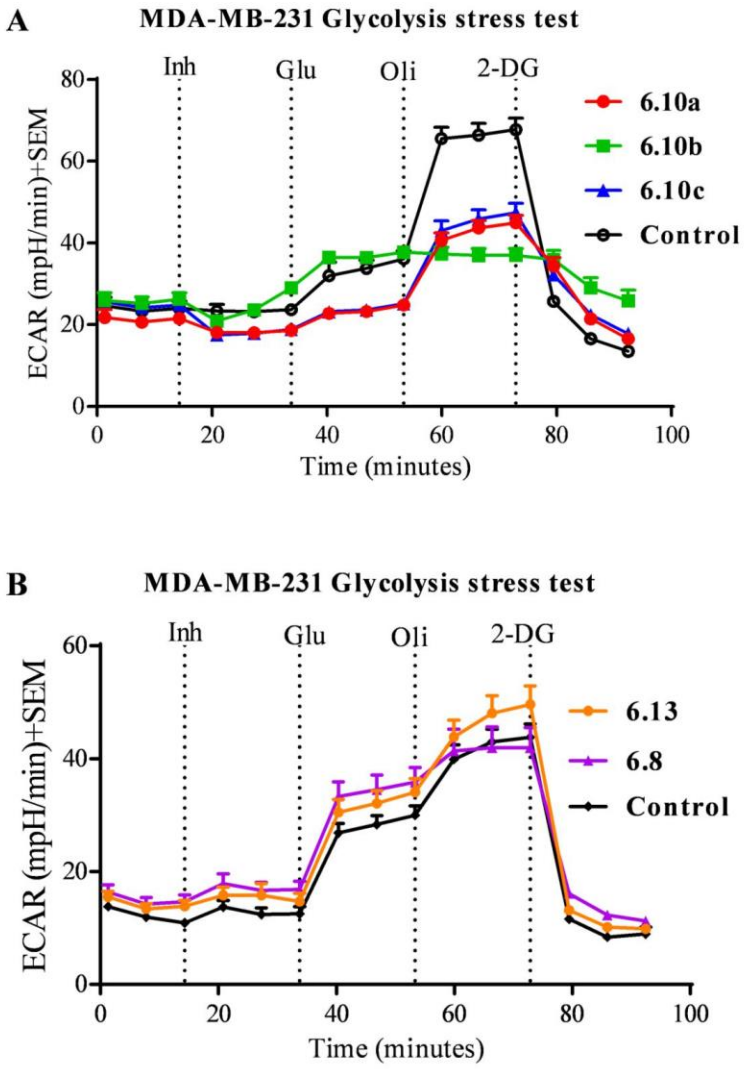

Figure 6e: GST profile in MDA-MB-231 cell line for compounds (**A**) **6.10a-c** and (**B**) **6.13** and **6.8**.

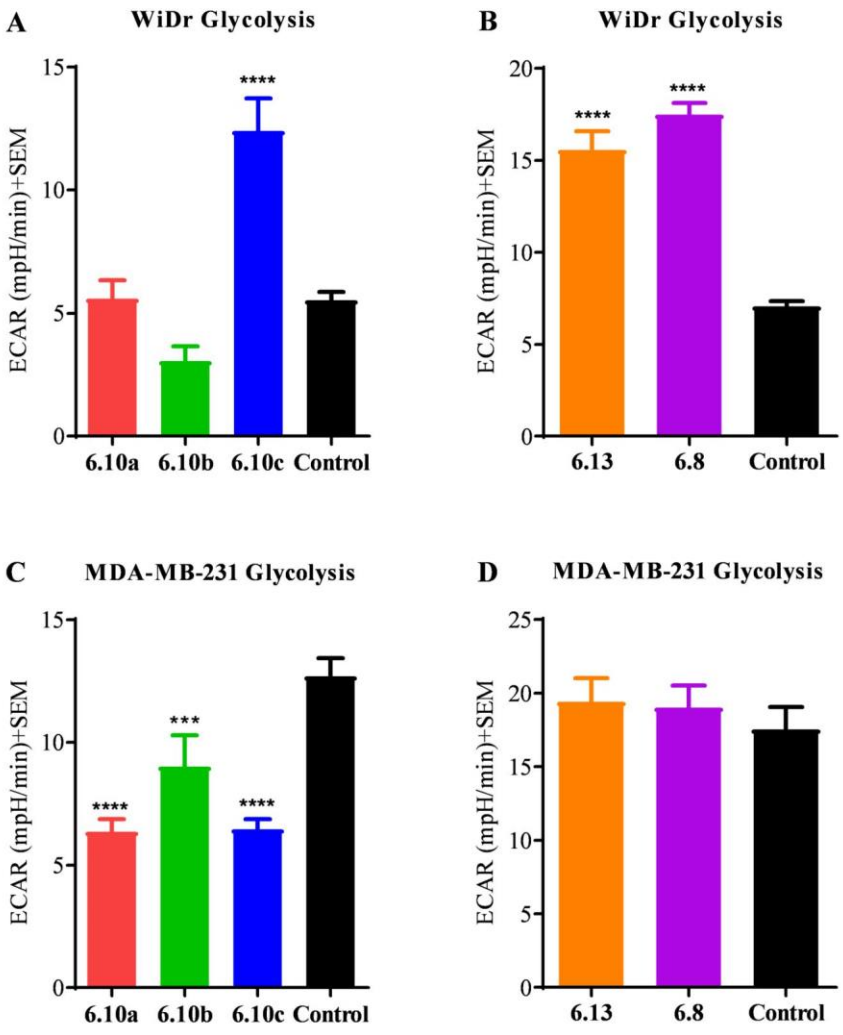

Figure 6f: Comparison of the glycolytic parameters calculated from glycolytic stress test in (**A**) WiDr cell line for compounds **6.10a-c** and (**B**) **6.13** and **6.8**; (**C**) MDA-MB-231 cell line for compounds **6.10a-c** and (**D**) **6.13** and **6.8**. Bar graphs represent the average + SEM of at least three agreeing independent experiments. Statistical significance was calculated using repeated measures one-way ANOVA (****$p<0.0001$).

In the presence of the test compounds, there was a significant increase in glycolysis in WiDr cell line (**Figure 6c**). The derivatives **6.10a** and **6.10b** did not affect glycolysis. The ethyl derivative **6.10c** with a butyl spacer exhibited a significant increase in the glycolysis in WiDr cells. In MDA-MB-231 cell line, there was a significant reduction in glycolysis following exposure to compounds **6.10a-c**. Both the ethyl derivatives **6.10a** and **6.10c** had similar reduction in the glycolysis of MDA-MB-231. This supports that the length of the linker group by one carbon had little effect in changing the activity of the amino CHC derivatives. The disparity in activity between WiDr and MDA-MB-231 cell lines could be attributed to secondary effect of the furoxan amino CHC derivative resulting in a reduction of cellular glycolysis in MDA-MB-231 cell line. Furthermore, the ether linked furoxan CHC derivative **6.13** seemed to enhance glycolysis in WiDr cell line along with the non-furoxan derivative **6.8** when compared to the control. This could indicate a fundamental shift in the metabolic phenotype of the cells to a more glycolytic nature. These two derivatives did not have any effect on MDA-MB-231 cell line which had been shown to be more glycolytic in nature **(Figure 6f A-D)**.

The next parameter evaluated is after the addition of the ATP synthase inhibitor oligomycin. Inhibiting the source of ATP production from mitochondrial respiration results in a significant increase in ECAR as the cell approaches its maximum glycolytic activity or glycolytic capacity.

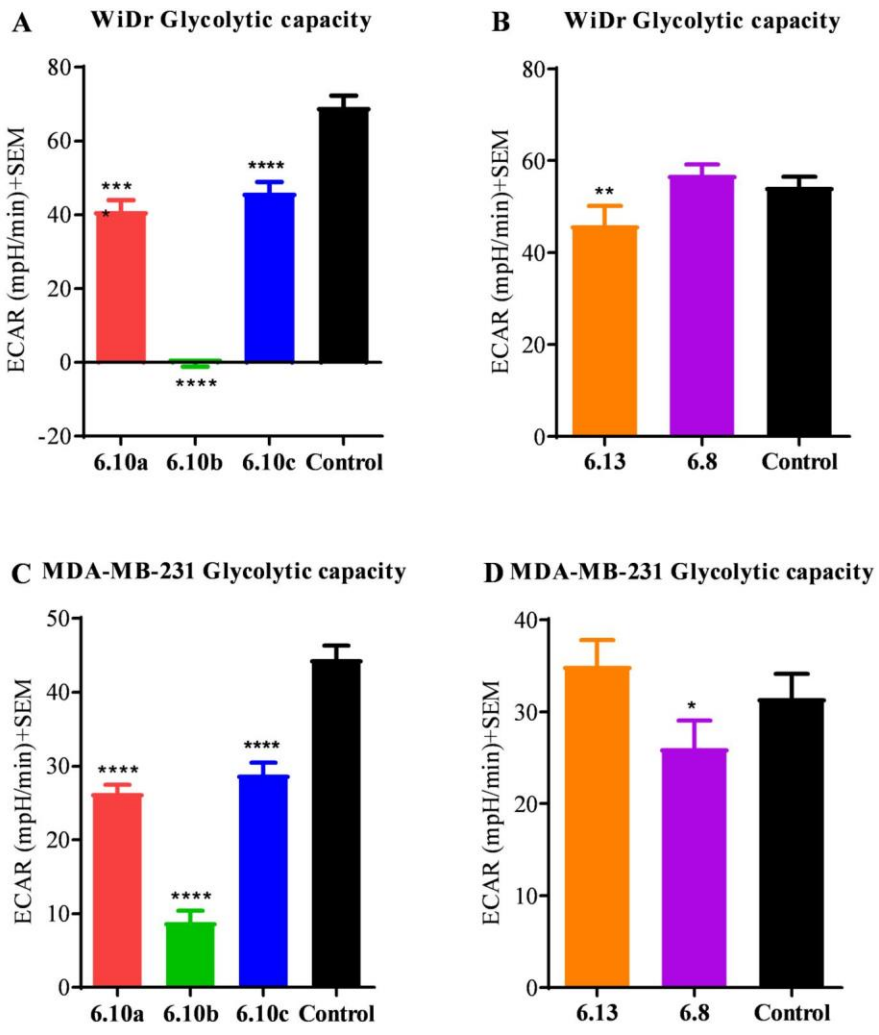

Figure 6g: Comparison of the glycolytic capacity calculated from glycolytic stress test in (**A**) WiDr cell line for compounds **6.10a-c** and (**B**) **6.13** and **6.8**; (**C**) MDA-MB-231 cell line for compounds **6.10a-c** and (**D**) **6.13** and **6.8**. Bar graphs represent the average + SEM of at least three independent experiments. Statistical significance was calculated using repeated measures one-way ANOVA (****$p<0.0001$).

The glycolytic capacity was significantly affected following exposure to the compounds. The importance of the amino CHC structure in reduction of the glycolytic capacity through MCT1 inhibition had already been discussed previously.[30,73] This reduction in the glycolytic capacity could be attributed to the significant MCT1 inhibition activity of **6.10a-c**. The greatest activity was exhibited by the benzyl amino CHC derivative **6.10b** which almost eliminated the glycolytic capacity in WiDr cell line and had a significantly greater reductive activity in MDA-MB-231 when compared to the other derivatives. Both the ethyl derivatives **6.10a** and **6.10c** had similar activity again showing that linker length of the furoxan group does not significantly impact the activity of these derivatives. Furthermore, the derivatives **6.10a** and **6.10c** did not differ much in their activity between WiDr and MDA-MB-231 cell lines either. In the study of the furoxan ethoxy linker derivative **6.13,** the activity was largely reduced in WiDr when compared to the amino furoxan CHC derivatives and no activity was found in the MDA-MB-231 cell line. Contrarily, the hydroxyl amino CHC derivative **6.8** was not effective in MDA-MB-231 but exhibited some significant reduction in the glycolytic capacity in WiDr. These two studies highlight the importance of the furoxan amino CHC derivative at enhancing the activity towards both WiDr and MDA-MB-231 cell lines (**Figure 6g A-D)**.

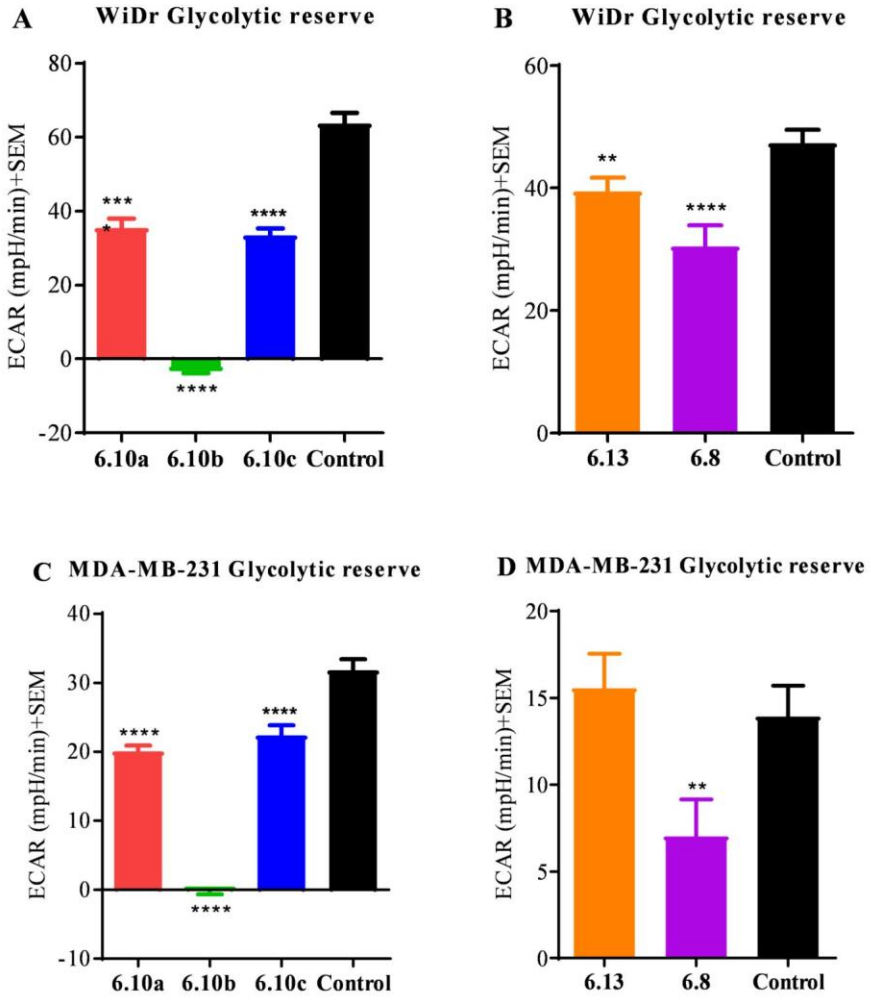

Figure 6h: Comparison of the glycolytic reserve calculated from glycolytic stress test in (**A**) WiDr cell line for compounds **6.10a-c** and (**B**) **13** and **6.8**; (**C**) MDA-MB-231 cell line for compounds **6.10a-c** and (**D**) **6.13** and **6.8**. Bar graphs represent the average + SEM of at least three independent experiments. Statistical significance was calculated using repeated measures one-way ANOVA (****$p<0.0001$).

The next parameter that we calculated was the glycolytic reserve. This is simply the difference between the rate of glycolysis and the glycolytic capacity. This parameter is closely tied to the metabolic plasticity of the cell and its response to ATP deficiency using glycolysis. A reduction in this parameter means the cell is no longer able to respond as efficiently to microenvironmental metabolic changes, which could be due to inhibitory effects caused by exposure to the test derivatives (**Figure 6h A-D**).

There was a direct correlation between the reduction in the glycolytic parameters and the glycolytic reserve with derivatives **10a-c**. The derivatives that exhibited the highest reduction in the glycolytic capacity also had similar activity in the glycolytic reserve. Interestingly, in the second study, both derivatives **6.13** and **6.8** had a significant reduction in the glycolytic reserve of both cell lines. If glycolytic reserve was reduced significantly, the cell could no longer reach the maximal glycolysis that it could previously, and as a result the cells' metabolic plasticity was reduced. With significant reduction in the glycolytic parameters supported by the glycolysis stress test, we planned to evaluate whether there was any significant mitochondrial stress after exposure to the compounds (**Figure 6i A-B** and **Figure6j A-B**)

As previously discussed, the MCT inhibition activity could have a significant effect on reducing the glycolytic parameters of the cells. This inhibitory activity would eliminate a primary way to maintain cellular homeostasis which would reduce the cells' ability to pursue glycolysis.

6.6 Evaluation of the mitochondrial stress test of 6.10a-c, 6.13, and 6.8

Mitochondrial stress test measures the oxygen consumption rate (OCR) of the cell. The respiratory parameters were calculated using the changes in the OCR. This assay differs from the glycolysis stress test for the cells are washed with glucose enriched media so that normal metabolism is maintained at basal levels (**Figure 6h** and **Figure 6i**).

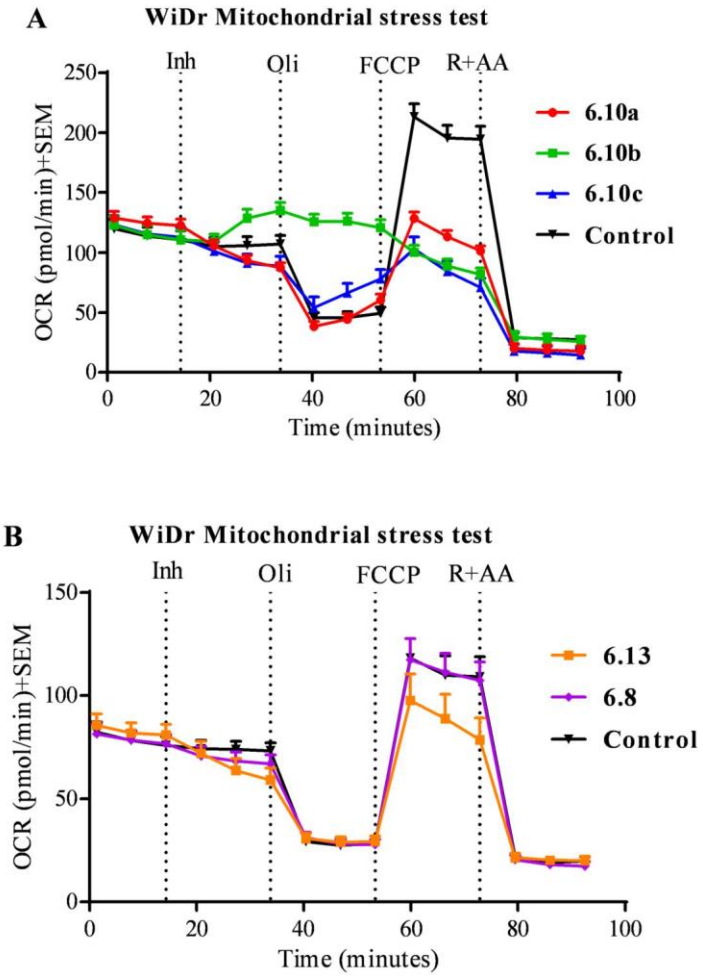

Figure 6i: Mitochondrial stress test profile in WiDr cell line for compounds (**A**) **6.10a-c** and (**B**) **6.13** and **6.8**.

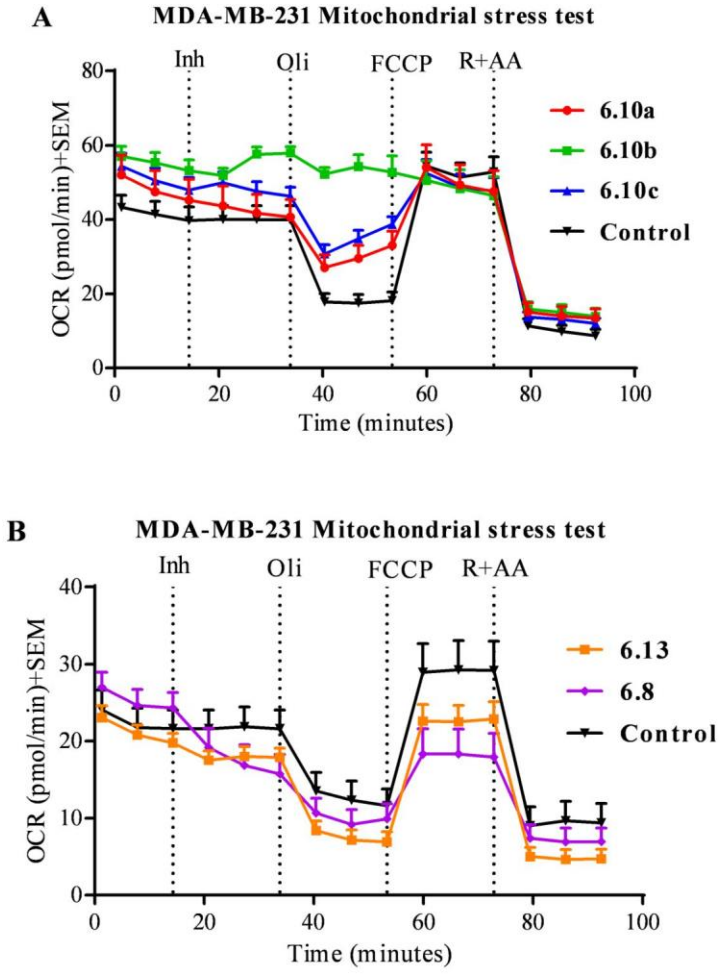

Figure 6j: Mitochondrial stress test profile in MDA-MB-231 cell line for compounds (**A**) **6.10a-c** and (**B**) **6.13** and **6.8**.

The first addition for the stress test is oligomycin, an ATP synthase inhibitor. The initial result of ATP synthase inhibition is a subsequent reduction in the cells oxygen consumption rate. This is due to stalling of the mitochondrial transport chain as the oxidative potential is no longer greater than the steep energetic requirements to pump protons against the gradient. As a result, this reduction in oxygen consumption allows for the determination of the ATP produced from mitochondrial respiration (**Figure 6k**).

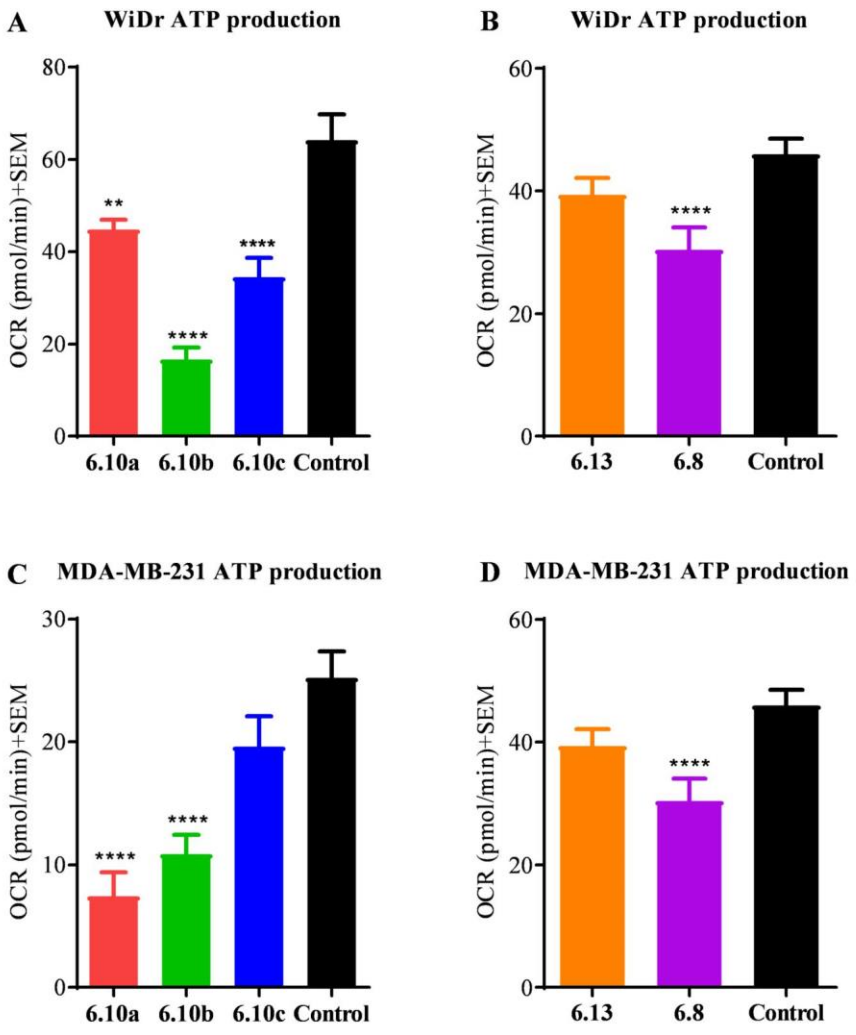

Figure 6k: Comparison of the ATP production calculated from mitochondrial stress test in (**A**) WiDr cell line for compounds **6.10a-c** and (**B**) **6.13** and **6.8**; (**C**) MDA-MB-231 cell line for compounds **6.10a-c** and (**D**) **6.13** and **6.8**. Bar graphs represent the average + SEM of at least three independent experiments. Statistical significance was calculated using repeated measures one-way ANOVA (****$p<0.0001$).

The ATP production was reduced in WiDr cell line after exposure to the derivatives **6.10a-c**. In this cell line, the benzyl derivative **10b** exhibited the greatest activity, whereas the activity of **6.10a** and **6.10c** were similar in WiDr cell line. In MDA-MB-231 cell line, the ethyl derivative **10a** exhibited the greatest activity. Interestingly, the other ethyl derivative **10c** did not exhibit any activity in this cell line (**Figure 6h A-D)**

In the second study, there was no significant reduction in ATP production in either WiDr or MDA-MB-231 cell lines following exposure to the furoxan ethoxy CHC derivative **6.16.** Interestingly, the derivative that did not contain the furoxan functional group **6.8** had significant reduction in ATP production from cellular respiration. This result combined with the previous study indicated that the inhibition of ATP production was largely dependent on the amino CHC template rather than the NO donor functional group. Furthermore, the benzyl derivative **10b** was found to be very selective towards WiDr cell line in its ATP reducing activity (**Figure 6h A-D)**

The next compound added is FCCP, a proton uncoupler. The mechanism of action is equivalent to perforating the mitochondrial membrane leading to an efflux of protons out of the transmembrane region down the gradient. The result of rapid efflux of protons drives the electron transport chain into overdrive as it tries to reestablish this gradient. This activity causes an artificial spike in oxygen consumption as the cell achieves the theoretical maximum mitochondrial respiration rate (**Figure 6l**).

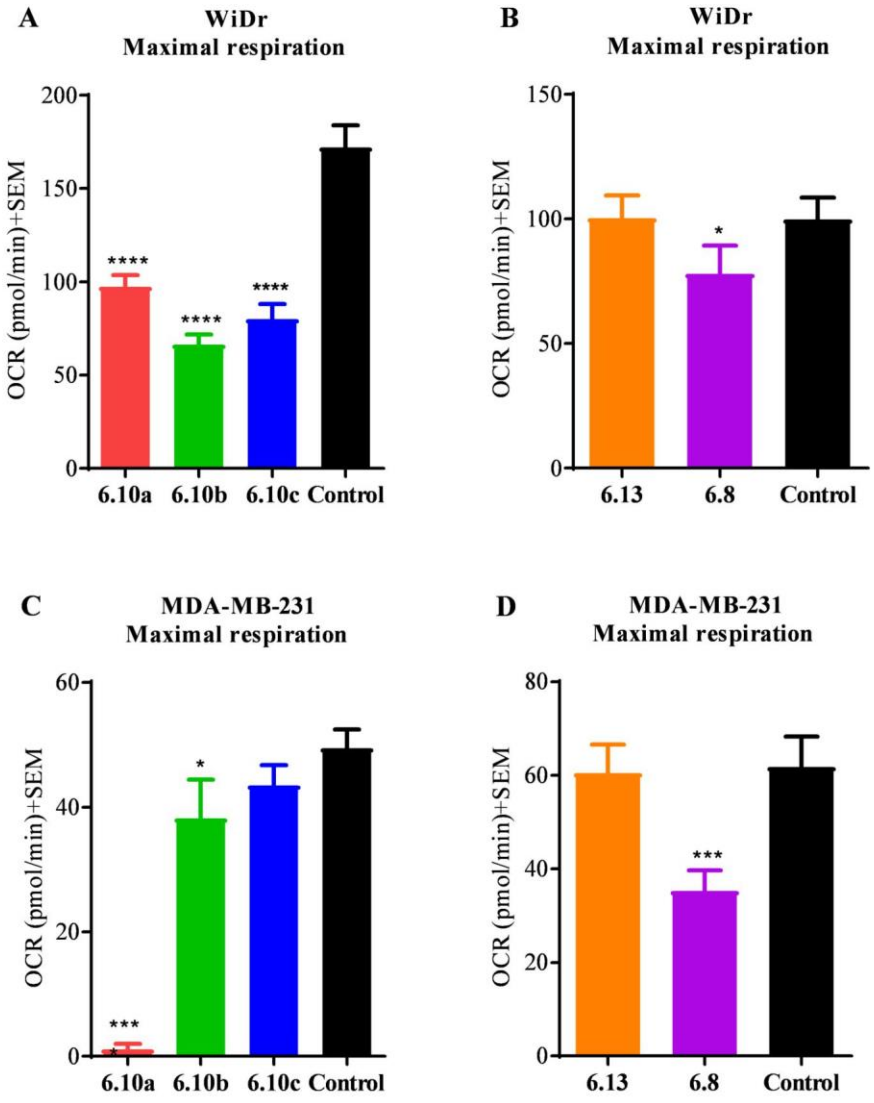

Figure 6l: Comparison of the maximal respiration calculated from mitochondrial stress test in (**A**) WiDr cell line for compounds **6.10a-c** and (**B**) **6.13** and **6.8**; (**C**) MDA-MB-231 cell line for compounds **6.10a-c** and (**D**) **6.13** and **6.8**. Bar graphs represent the average + SEM of at least three independent experiments. Statistical significance was calculated using repeated measures one-way ANOVA (****p<0.0001).

After exposure to the compounds, there was a significant reduction of the maximal respiration in WiDr cell line with **6.10a-c** and the activities were comparably similar between the three derivatives. Contrarily, this activity was significantly reduced except with the derivative **6.10a,** which had a complete reduction in the maximal respiration. The derivative **6.10b** exhibited significant activity in MDA-MB-231 cell line, but the derivative **6.10c** had no activity. In the second study, the furoxan ethoxy CHC d6jrivative **6.13** did not show any affect in either WiDr or MDA-MB-231 cell line. Again, the hydroxy amino CHC derivative **6.8** significantly reduced maximal respiration in both WiDr and MDA-MB-231 cell lines (**Figure 6l A-D)**.

These results indicated that the derivatives lacking a lipophilic character was more effective in disrupting mitochondrial activity in WiDr cell line. The mitochondrial parameters in MDA-MB-231 cell line were found to be significantly inhibited by exposure to the more polar derivative **6.8.** As for the furoxan derivative, it did not significantly modify the activity of the amino CHC template.

The next parameter that can be evaluated is the spare respiratory capacity. This is simply the ability of the cell to respond to stress that would result in increased ATP production from mitochondrial respiration. This parameter is obtained by the difference between basal level respiration and the maximal respiration parameter(**Figure 6m**).

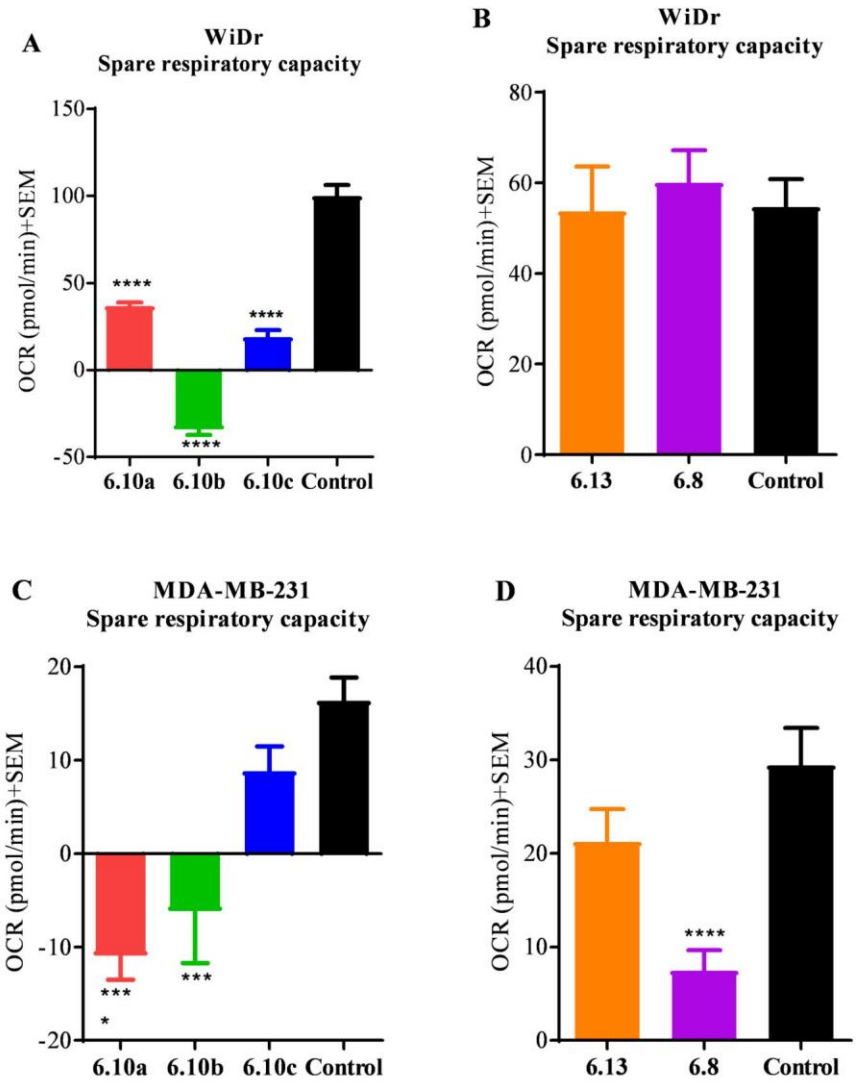

Figure 6m: Comparison of the spare respiratory capacity calculated from mitochondrial stress test in (**A**) WiDr cell line for compounds **6.10a-c** and (**B**) **6.13** and **6.8**; (**C**) MDA-MB-231 cell line for compounds **6.10a-c** and (**D**) **6.13** and **6.8**. Bar graphs represent the average + SEM of at least three independent experiments. Statistical significance was calculated using repeated measures one-way ANOVA (****$p<0.0001$).

The spare respiratory capacity is usually correlated with the maximal respiration. Any significant reduction in the maximal respiration parameter usually results in a significant reduction in the spare respiratory capacity. This could be seen in WiDr cell line where the most effective derivatives **6.10b** exhibited a complete elimination and further reduction of the spare respiratory capacity. Furthermore, both the ethyl amino CHC derivatives **6.10a** and **6.10c** had comparable reduction in the spare respiratory capacity. Interestingly, in MDA-MB-231 cell line, the spare respiratory capacity was significantly reduced with derivative **6.10b**. In the second study, **6.13** and **6.8** had no reduction in the spare respiratory capacity. In the derivative **6.8** there was a significant reduction in the spare respiratory capacity while the derivative **6.13** had no apparent activity in MDA-MB-231 cell line (**Figure 6k A-D)**.

The final metabolic inhibitors that we added were rotenone and antimycin A. Rotenone is an isoflavone that disrupts complex I in the electron transport chain. The metabolic inhibitor antimycin A effectively inhibits complex III. The result of these two derivatives is the complete shutdown of oxygen consumption via the electron transport chain and subsequently any mitochondrial respiration. This final step is important for it allows for the determination of the proton leak parameter. In short, proton leak is indicative to any destabilization in the mitochondrial membrane integrity. The result is small levels OCR from the activity of electron transport chain even after ATP synthase inhibition. This proton leak is a strong indicator of significant compound induced mitochondrial dysfunction(**Figure 6m**).

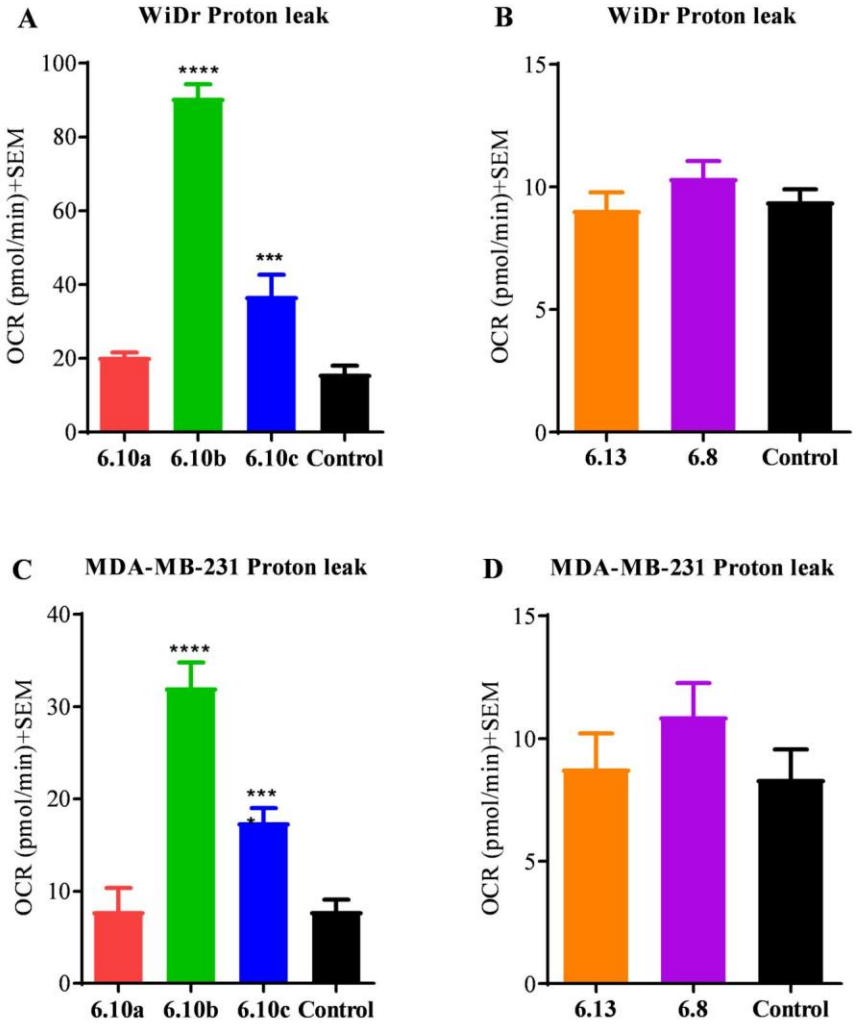

Figure 6n: Comparison of proton leak calculated from mitochondrial stress test in (**A**) WiDr cell line for compounds **6.10a-c** and (**B**) **6.13** and **6.8**; (**C**) MDA-MB-231 cell line for compounds **6.10a-c** and (**D**) **6.13** and **6.8**. Bar graphs represent the average + SEM of at least three independent experiments. Statistical significance was calculated using repeated measures one-way ANOVA (****$p<0.0001$).

There was a significant increase in the proton leak after exposure to the derivatives **6.10b** and **6.10c** in both WiDr and MDA-MB-231 cell lines. Specifically, the benzyl derivative was the only compound with the greatest spike in proton leak. Interestingly, the ethyl derivative **10a** did not exhibit any increase in proton leak in either WiDr or MDA-MB-231 cell lines. Mostly, the effect on the mitochondrial respiratory activity was likely a combination of different effects that could potentially include the mitochondrial dysfunction activity of NO release intracellularly. In the second study, the furoxan ethoxy CHC derivative **6.13** did not exhibit any increase in the proton leak in both WiDr and MDA-MB-231 cell lines. Furthermore, the hydroxy ethyl CHC derivative **6.8** did not have any effect on the proton leak as well (**Figure 6l A-D**).

6.7 Systemic toxicity evaluation of candidate compounds 6.10a-c in CD1 mice

Considering the excellent activities of derivatives **6.10a-c** at disrupting cellular energetic production via glycolysis and mitochondrial respiration, we decided to elevate them as candidate compounds for *in vivo* evaluation (**Figure 6o**). Initial systemic toxicity studies were conducted in healthy CD1 mice.

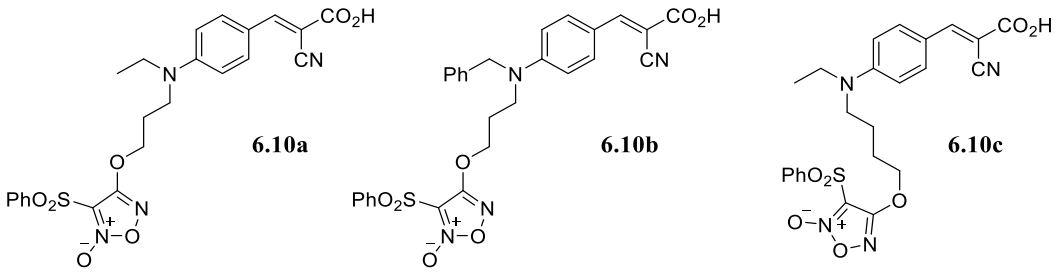

Figure 6o: Candidate compounds used for translation into *in vivo* models for evaluation of chemotherapeutic potential.

For solubility purpose, derivatives **6.10a-c** were converted into their corresponding sodium salts using sodium bicarbonate. The derivatives **6.10b** and **6.10c** even as sodium salts had some trouble with solubility at 1mg/ml in 10% DMSO in water. All the derivatives were soluble in the formulation consisting of 10% DMSO, 10% PEG-400, 7.5% HS-15, and 72.5% water. CD-1 mice were purchased from Charles River and allowed to acclimatize for one week before administration of candidate compounds. The mice were assigned into groups (n=6 mice). Selection was based on the average weight of the group and mice were selected to ensure the average was consistent amongst all test groups. Toxicity evaluation was conducted over a period of 14 days. Dosage of **6.10a-c** was administered at 20mg/kg daily intraperitoneally. This dosage was chosen based on the relative maximum solubility at room temperature. The body weights of the mice along with behavior were monitored to ensure the dosage was not causing any significant stress on the mice. The control group was given vehicle (10% DMSO, 10% PEG-400, 7.5% HS-15, and 72.5% water) daily along with the administration of derivatives **6.10a-c** (**Figure 6p**).

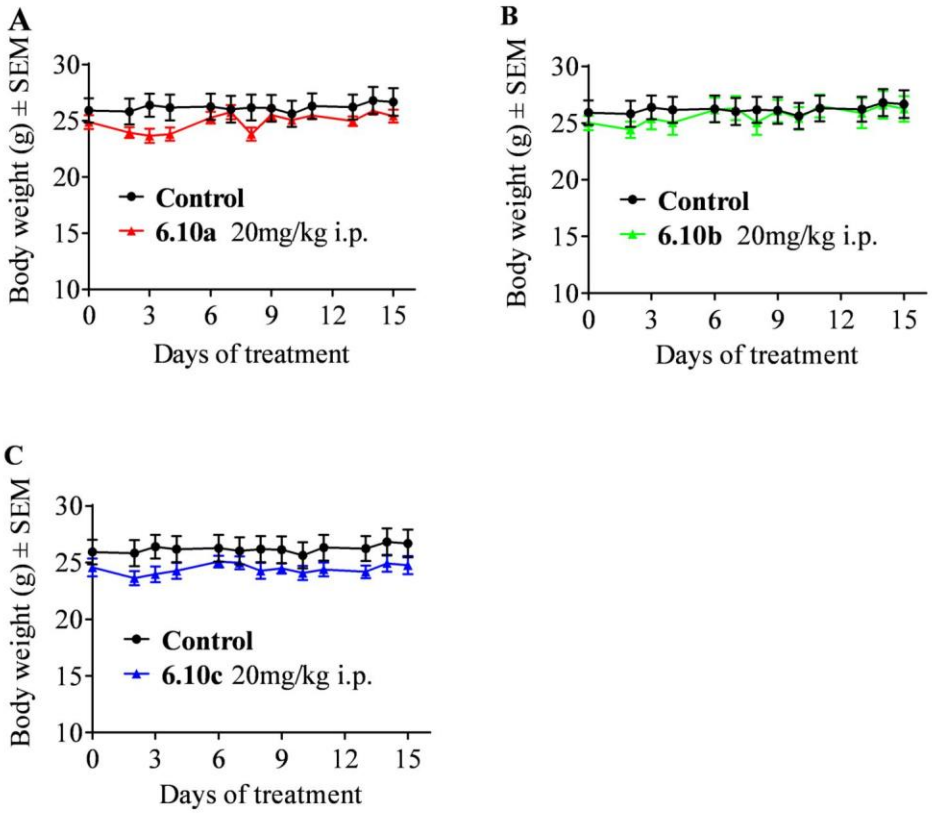

Figure 6p: Systemic toxicity of (**A**) **6.10a**, (**B**) **6.10b**, and (**C**) **6.10c** in CD-1 mice at a concentration of 20mg/kg i.p indicate normal body weight gains in treated mice when compared to controls.

Mice treated with the derivatives **6.10a-c** did not exhibit reduction in body weights and did not show any noticeable side effects at the end of the study (**Figure 6n**). Encouraged by these results, we then evaluated the efficacy of one of one lead derivative **6.10a** in an *in vivo* tumor xenograft study with MDA-MB-231 tumor model.

6.8 *In vivo* tumor growth inhibition study in MDA-MB-231 xenograft model

Selection of the lead candidate compound **6.10a** for further preclinical development was based on its high cell proliferation inhibition and MCT1/4 inhibition activity. Furthermore, derivative **6.10a** has less vulnerable phenyl groups when compared to **6.10b** that could be susceptible to CYP450 oxidation and elimination resulting in a decrease in therapeutic exposure. Additionally, the solubility of **6.10a** was greater than that of **6.10b-c** making it a better candidate compound for further anticancer efficacy evaluation.

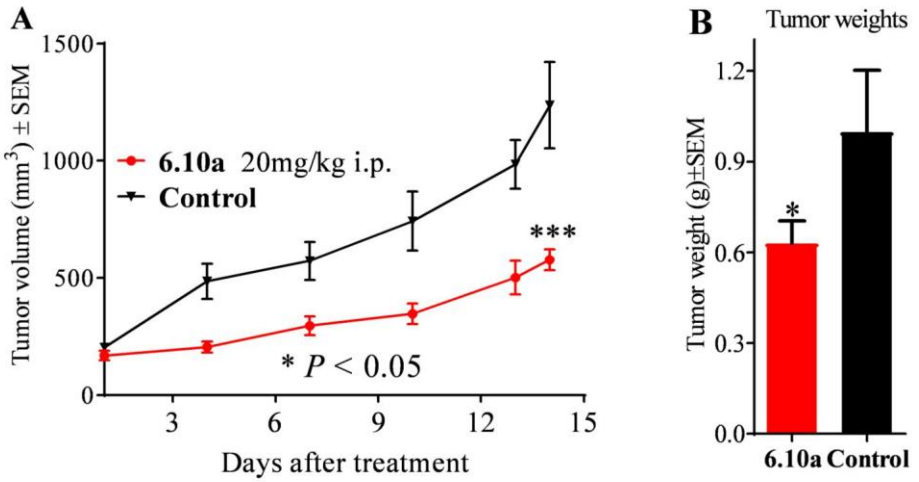

Figure 6q. (**A**) *In vivo* MDA-MB-231 xenograft model indicated significant reduction in tumor volume when compared to vehicle treated mice. (**B**) At the end of the study, tumors were resected and weighed. Statistical significance of tumor growth inhibition was calculated using the Mann-Whitney test (*** P <0.001).

The MDA-MB-231 xenograft model was chosen as it is an MCT4 expressing cell line and was previously evaluated against the lead candidate compound for transport inhibition, cell proliferation, and metabolic disruption capabilities. Mice were inoculated with MDA-MB-231 cells in a 1:1 mixture with Matrigel and PBS. Treatment was started after the tumors reached an average volume of 100 mm^3. Group 1 mice were treated with **6.10a** at a dosage of 20 mg/Kg, intraperitoneally, once daily and group 2 mice were given vehicle (10% DMSO, 10% PEG-400, 7.5% HS-15, and 72.5% water). The weights of the mice were monitored daily and tumor volume was measured every three days with calipers (**Figure 6q**). After 14 days of treatment, mice were euthanized, and tumor masses were isolated and weighed. Compound **6.10a** exhibited a significant tumor growth inhibition, ~50% by volume (**Figure 2q, A**) and ~30% by tumor mass (**Figure 6q, B**) when compared to the control group.

6.9 Discussion

The integration of the NO donor furoxan into the *p*-*N*,*N*-dialkylamino CHC template resulted in a significant increase in the antiproliferative nature of the compounds. These results support the effectiveness of the pro-NO strategy as a potential therapeutic. There was some degree of selectivity between the cell lines with higher activity against the tumorigenic cell lines MDA-MB-231, 4T1, and WiDr. The degree of activity was lower against the immortalized epithelial cell line MCF10A. The candidate compounds exhibited potent MCT1 and MCT4 inhibition properties. These results were expected as the

derivatives are structurally similar to our previously reported *p-N,N*-dialkylamino CHC based dual MCT1and MCT4 inhibitors.[119]

To evaluate the effects on the metabolic profile, two cells lines were used. The first was an MCT1 expressing cell line WiDr and the second was an MCT4 expressing cell line MDA-MB-231. Evaluation of glycolytic parameters revealed that the NO donor CHC hybrids were more effective in the MCT1 expressing WiDr cell line when compared to the MDA-MB-231 cell line. Interestingly, the derivative that lacked the NO donor showed similar reduction in the glycolytic properties. These results support the hypothesis that the changes in the glycolytic parameters could be attributed largely to the amino CHC template rather than the NO donor activity.

The mitochondrial stress test parameters were more effective in the WiDr cell line that is more dependent on mitochondrial respiration for ATP production. The largely glycolytic dependent MDA-MB-231 cell line showed some indication of mitochondrial stress but was largely unaffected when compared to WiDr. Mitochondrial parameters such as maximal respiration and ATP production were also significantly reduced in the presence of candidate compounds. The amino CHC derivatives **6.10a-c** specifically had the greatest effect on these parameters when compared to the furoxan ethoxy derivative **6.13**. Furthermore, based on the increase in proton leak, the *N,N*-dialkylamino group and pro-NO release strategy in the CHC derivative could influence mitochondrial dysfunction.

Excited by these studies the three NO donor amino CHC hybrids were selected as candidate compounds for further development. The systemic toxicity was conducted in CD-1 mice with little to no weight loss. Ultimately, the **6.10a** derivative was chosen for

xenograft model based on its *in vitro* activity and selectivity towards tumorigenic cell lines. This derivative translated well into the MDA-MB-231 xenograft model with significant reduction in the volume and tumor weight. The result of the study was a successful development of a small library of NO donor amino CHC hybrids with significant *in vitro* and *in vivo* anti-cancer activity.

CHAPTER 7 Synthesis and Evaluation of NO Donor Aminocarboxy Coumarin Conjugates as Anticancer Agents

7.1 Introduction

Previous SAR study reported in chapter 1 highlighted the importance of the conjugation of two molecular entities *N*,*N*-dialkylamino CHC and the NO donor furoxan. The current chapter focuses on the hybridization of the potent dibenzylcoumarin derivative **1.16** with NO donor furoxan. Here we employed a pro-drug strategy where a bicyclic system of coumarincarboxylic acid which is a cyclic ester (a class of 6 membered lactone) was linked to furoxan unit. For this purpose, we employed two different linker groups to combine the coumarincarboxylic acid and furoxan derivatives. The linker groups that we utilized contain readily cleavable ester group **7.7a** and more metabolically stable amide linkage **7.7b**. Both these strategies had a terminal alcohol that would be coupled with the NO donor diphenylsulphafuroxan (**Scheme 7a**).

The coumarin template is a pharmacologically privileged structural entity with excellent therapeutic activity and have been successfully utilized towards drug development for numerous indications.[36,82,86,120] As mentioned in the previous chapter, coumarin carboxylic acids are structurally similar to the CHC. The coumarin derivative has similar electronic features with a two electron groups flanking the unsaturated region with a lipophilic electron donating aromatic system in the opposing side. Both these features enhance the electrophilic nature of the unsaturated carbon towards possibly reversible nucleophilic attack. The incorporation of the furoxan derivative has been linked to increase in therapeutic potential via Pro-NO strategies. The selectivity of this derivative

towards the tumor microenvironment is based on the overexpression of GSTs in the late stage cancerous. We envision coupling this derivative to the pharmacologically privileged coumarin template will enhance the activity of this derivative, with limited off target toxicities. Our previous studies on dibenzyl couarmin carboxylic acid revealed that these are slightly selective towards MCT1 with an IC_{50} of 57nm as opposed to MCT4 which is ~200nm. Inclusion of this novel prodrug strategy would result in a probable cytotoxicity enhancing features with activity towards MCT1 and/or MCT4 expressing cell lines upon cleavage of the linker.[40]

7.2 Synthesis of hybrid NO Donor N,N-dialkyl coumarin Derivatives 7.7a-b

Initial synthesis of the diphenyl coumarin derivative started with the commercially available 3-aminophenol. The amine in was selectively alkylated under controlled conditions with benzyl bromide in the presence of potassium carbonate in DMSO as solvent. The resulting dibenzyl derivative **7.1** was formylated via Vilsmeier-Haack reaction using $POCl_3$ and DMF mixture resulting in the phenolic aldehyde **7.2** followed by condensation of aldehyde with diethylmalonate in the presence of piperidine. Hydrolysis with 3M sodium hydroxide in ethanol under reflux conditions followed by acid mediated cyclization yielded the *N,N*-dibenzylcarboxy coumarin **7.4**.

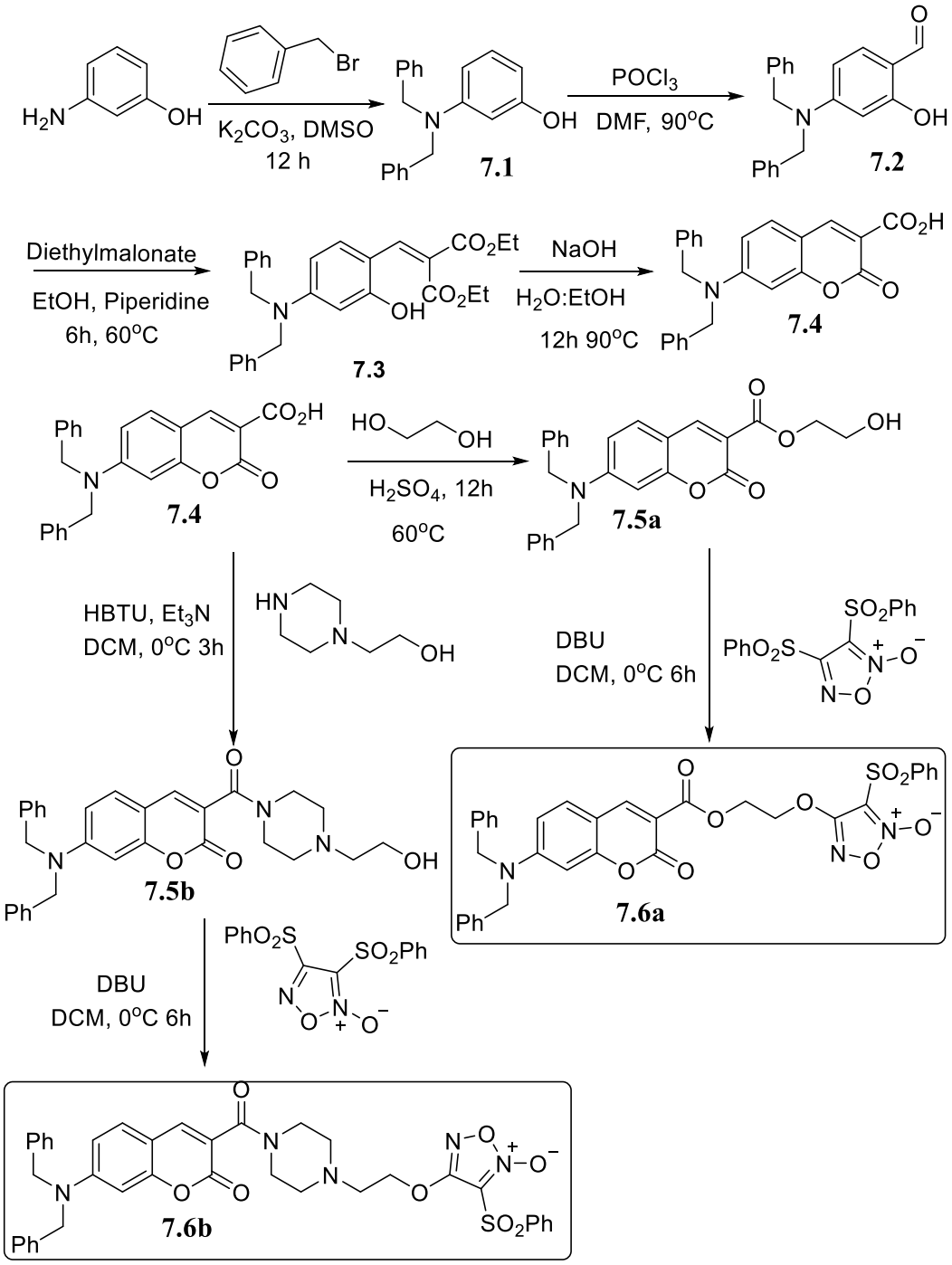

Scheme 7a: Synthesis of aminocarboxy coumarin based furoxan NO donors **7.6a** and **7.6b**.

Acid catalyzed Fischer esterification of the dibenzylcarboxy coumarin **7.4** with excess ethylene glycol resulted in the corresponding selective mono ester **7.5a**. The terminal alcohol of the ester was coupled with the diphenylsulphafuroxan in the presence of DBU yielded the desired furoxan dibenzyl coumarin conjugate **7.6a**. The piperazine ethanol amide derivative was prepared by coupling **7.4** with ethanol piperazine using HBTU and triethylamine to give the corresponding amide **7.5b**. The amide was similarly coupled with diphenylsulphafuroxan in the presence of DBU to yield the corresponding amide prodrug **7.6b**.

7.3 Evaluation of compounds 7.6a-b and 7.8a-b for antiproliferation activity

The synthesized dibenzyl coumarin prodrugs **7.5a-b** and hybrids **7.6a-b** were evaluated for their antiproliferation activity against various cancerous and non-cancerous cell lines. Proliferation inhibition was measured using MTT. Cells that were tested were MDA-MB-231, a triple negative breast cancer, 4T1, a murine metastatic breast cancer cell line, and WiDr, a colorectal adenocarcinoma. For an evaluation of efficacy on non-cancerous cells, MCF10A cell line was used (**Table 7a**).

Table 7a: MTT IC_{50}*(μM) values of functionalized coumarin derivatives **7.6a-b** and **7.7a-b** in MDA-MB-231, 4T1, MCF7 and WiDr cell lines.

	MDA-MB-231	**4T1**	**WiDr**	**MCF10A**
7.5a	>250	>250	>250	>250
7.5b	>250	>250	>250	>250
7.6a	0.02 ± 0.00	0.13 ± 0.05	0.03 ± 0.01	34.0 ± 4.6
7.6b	0.46 ± 0.02	0.96 ± 0.1	10.0 ± 0.02	8.6 ± 0.9

**Average±SEM of three separate experiments*

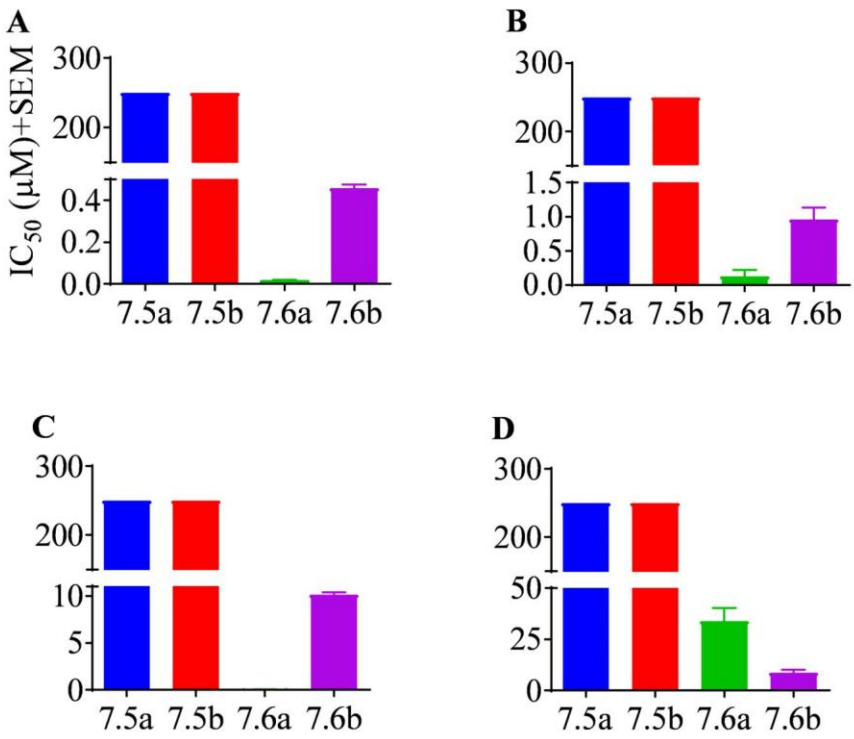

Figure 7a: MTT based IC_{50} values of coumarin NO hybrids (**A**) MDA-MB-231, (**B**) 4T1 (**C**) WiDr and (**D**) MCF10A. MTT assay was used to evaluate cell proliferation inhibition of the test compounds **7.6a** and **7.6b**. All the experiments were done in duplicate wells and the final average+sem of minimum three separate experimental values were calculated and the graphs were generated using GraphPad 7.0.

The coumarin-NO conjugates **7.6a** and **7.6b** were very effective in inhibiting the proliferation of all the cancerous cell lines MDA-MB-231, 4T1 and WiDr (**Figure 7a**). This was a significant improvement when compared to their non-hybrid derivatives which did not exhibit any activity even at the highest concentration tested. These cytotoxicity

enhancing conjugates **7.6a** and **7.6b** exhibited moderate activity towards MCF10A. Specifically, **7.6a** was effective at very low concentrations ranging from 0.02 - 0.13 µM against the cancerous cell lines. Comparatively, this derivative **7.6a** had a significantly lower activity towards the non-cancerous cell line MCF10A (IC_{50} of 34 µM). The amide derivative (**7.6b**) was comparatively less effective in its antiproliferative properties (0.46 - 10 µM) against all the cell lines. The parent compounds **7.5a** and **7.5b** did not have any significant inhibition of proliferation even at the maximum tested concentration of 250 micromolar (**Figure 3.2a**). The **7.6a** derivative had outstanding selectivity between the cancerous and non-cancerous cell lines with a 10-fold reduction in activity against the two types of cell lines. Based on the nM antiproliferation activity, the two derivatives were immediately designated to lead derivative status and evaluated for their *in vivo* toxicity and anticancer efficacy.

7.4 Systemic toxicity study of the NO donor-carboxy coumarin conjugates 7.6a-b

Based on *in vitro* cell proliferation inhibition, the candidate compounds **7.6a-b** were evaluated for their translatability as a cancer chemotherapeutic. Both derivatives were insoluble in water and required formulations (10% (v/v) DMSO, 10% (v/v) PEG-400, 40% (v/v) HS-15 (18.8%w/v), 40%H_2O) to be injected successfully intraperitoneally (i.p.). Initially, we evaluated the systemic toxicity of each derivative in ICR mice (n=6). Mice were injected daily with **7.6a** and **7.6b** at a dosage of 20 mg/kg, i.p. which was chosen based on its solubility. The mice were then monitored for any change in body weight.

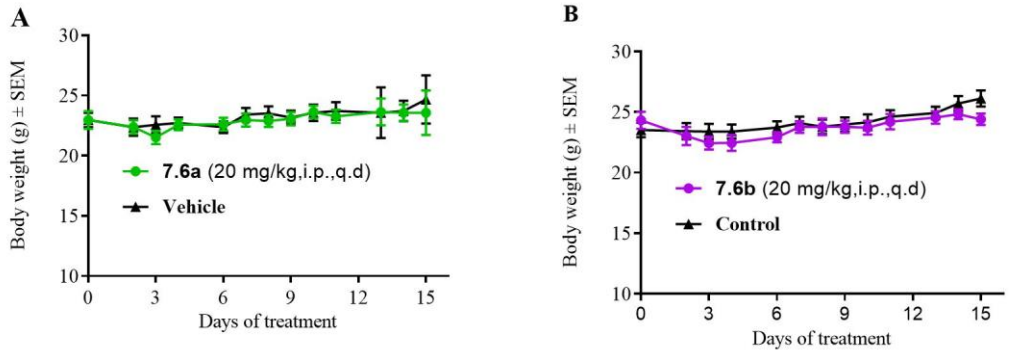

Figure 7b: The toxicity study of (**A**) molecular hybrid **7.6a** administered at 20mg/kg daily and (**B**) molecular hybrid **7.6b** administered 20mg/kg daily in ICR mice showed no significant weight loss over a 14 -day period.

The results of this study showed that the candidate compounds **7.6a** and **7.6b** did not exhibit body weight loss when compared to control groups (**Figures 2m**). Based on this toxicity study and the previous near nm *in vitro* results against MDA-MB-231 cell line, lead candidate compound **7.6a** was chosen and evaluated for anticancer efficacy in an MDA-MB-231 tumor xenograft model.

7.5 In vivo efficacy study in MDA-MB-231 xenograft model:

MDA-MB-231 based tumor xenograft model was chosen to evaluate the translatability of candidate compound **7.6a** in female SCID mice. This derivative was chosen for its excellent antiproliferation activity and tolerability in CD-1 mice. After tumors reached ~100 cm^3, mice were randomly divided into two groups based on average tumor volume. The mice were injected with 20mg/kg (i.p.) of compound **7.6a** and the control group was given an injection of vehicle. Treatment was continued for 14 days and the body weights and tumor volumes were recorded every 2-3 days.

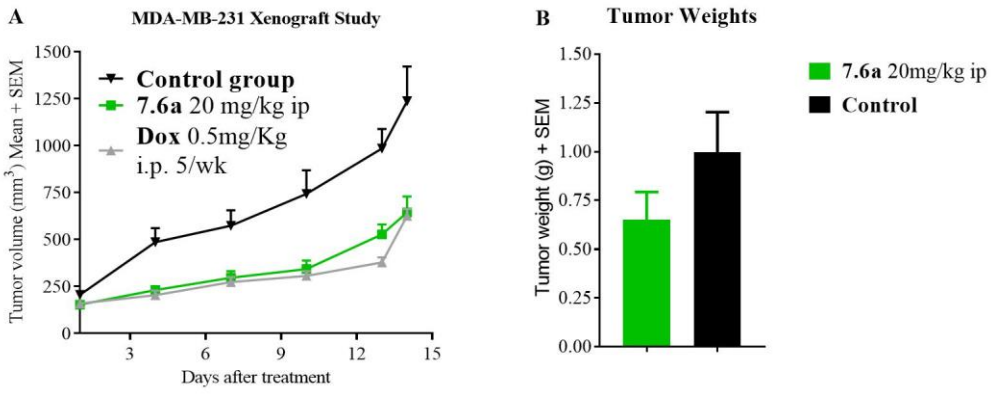

Figure 7c: *In vivo* MDA-MB-231 xenograft model: (**A**) Treatment with **7.6a** resulted in a reduction of tumor volume when compared to vehicle treated mice. (**B**) Tumor weight indicated a reduction in tumor growth in **7.6a** treated mice compared to vehicle.

The hybrid derivative **7.6a** exhibited significant suppression in tumor volume (**Figure 7c**) compared to the control group. At the end of the study, all the tumors were resected, and the tumor mass was weighed. Although, there was an apparent reduction in tumor volume and weight there was no statistical significance compared to the control (**Figures 3.2c A** and **B**).

7.6 Discussion

The coupling of coumarin carboxylic acid to the NO donor via an ester **7.6a** or an amide **7.6b** bond resulted in significant increase in the antiproliferative property of the parent structure. In fact, in the derivative **7.6a** the activity was 20 nM in the MDA-MB-231 which was 10000x more effective than the parent compound. This excellent level of

antiproliferative activity towards the MDA-MB-231 cell line lead to further preclinical evaluation of the candidate compound *in vivo* xenograft studies.

Both the ester and amide derivatives **7.6a-b** were well tolerated in mice up to a dosage of 20 mg/kg ip. A xenograft study was carried out using MDA-MB-231 tumor model and the administration of compound **7.6a** was conducted over a 14-day period. The reduction in tumor volume showed that this derivative had similar activity to the known chemotherapeutic drug doxorubicin. The derivative **7.6a** exhibited reduction in tumor volume this was reflected in the tumor weight of the after resection. The project yielded a very selective *in vitro* cell proliferation inhibition and moderate anticancer efficacy in *in vivo* xenograft study.

Thesis Conclusions

We synthesized novel metabolic plasticity inhibitors for treatment of cancer. The chemical structure of lead candidate compounds and their biological properties are shown below.

1

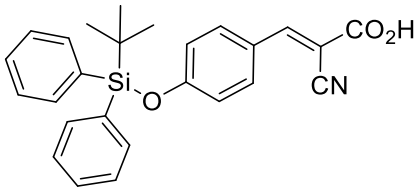

MCT1 IC_{50} ~ 0.4 μM
Cell prolifiration inhibition
WiDr IC_{50} >500 μM
4T1 IC_{50} >500 μM
MDA-MB-231 IC_{50} >500 μM
Systemic toxicity 25 mg/kg
tumor growth inhibition
WiDr ~30%

Co-treatment with NAC reveals decrease in γ-H2AX, apoptotic protein GST and MST study conclude that metabolic functions are compromised these are also supported by MTR fluorescent studies

2

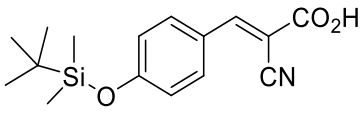

MCT1 IC_{50} ~ 0.1 μM
Cell prolifiration inhibition
WiDr IC_{50} >500 μM
4T1 IC_{50} >500 μM
MDA-MB-231 IC_{50} >500 μM

3

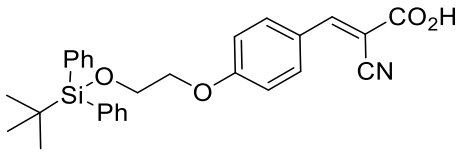

MCT1 IC_{50} ~ 0.1 μM
Cell prolifiration inhibition
WiDr IC_{50} ~6 μM
4T1 IC_{50} ~22 μM
MDA-MB-231 IC_{50} ~71 μM
Systemic toxicity 25 mg/kg
tumor growth inhibition
WiDr ~30%

4

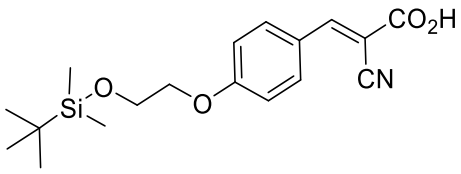

MCT1 IC_{50} ~ 0.01 μM
Cell prolifiration inhibition
WiDr IC_{50} ~123 μM
4T1 IC_{50} ~82 μM
MDA-MB-231 IC_{50} ~500 μM

Candidate compounds 1 and 3: Future studies would include further preclinical development of the candidate compounds. First studies will involve *in vivo* evaluation of the PK/PD of the candidate compounds including CACO-2 permeability and liver microsomal stability study. Further studies would evaluate the anticancer efficacy studies in combination with other glycolytic inhibitors or chemotherapeutics to see if the derivatives can be used as a chemo sensitizing therapeutic.

5

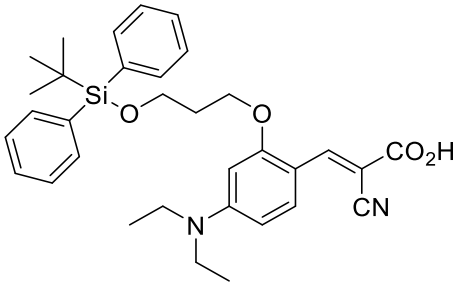

Cell prolifiration inhibition
WiDr IC_{50} ~21 μM
4T1 IC_{50} ~13 μM
MDA-MB-231 IC_{50} ~26 μM

6

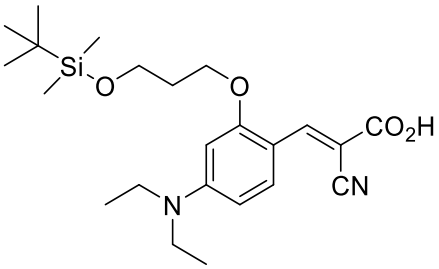

Cell prolifiration inhibition
WiDr IC_{50} ~15 μM
4T1 IC_{50} ~16 μM
MDA-MB-231 IC_{50} ~128 μM

7

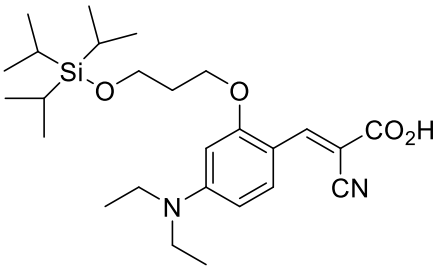

Cell prolifiration inhibition
WiDr IC_{50} ~13 μM
4T1 IC_{50} ~6 μM
MDA-MB-231 IC_{50} ~15 μM

Candidate compounds 5 and 7: The future studies of these derivatives would involve *in vivo* evaluation in a tumor xenograft of an MCT1 and MCT4 cell line. Furthermore, western blot analysis to evaluate the mechanism of action. Furthermore, the derivatives will be evaluated for various PK/PD parameters like CACO-2 permability and liver microsomal stability study.

8

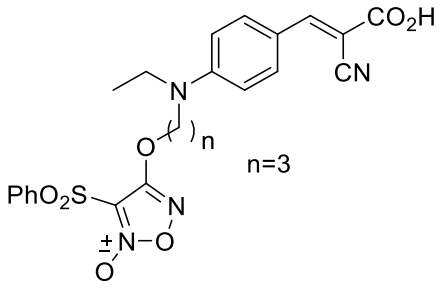

MCT1 IC_{50} ~ 0.06 μM
MCT4 IC_{50} ~ 0.12μM
Cell prolifiration inhibition
WiDr IC_{50} ~5.2 μM
4T1 IC_{50} ~8 μM
MDA-MB-231 IC_{50} ~3 μM
Systemic toxicity 20 mg/kg
tumor growth inhibition
MDA-MB-231 ~30%

9

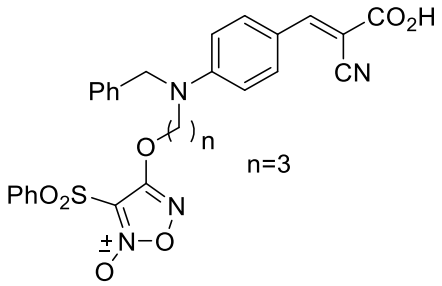

MCT1 IC_{50} ~ 0.11μM
MCT4 IC_{50} ~ 0.16μM
Cell prolifiration inhibition
WiDr IC_{50} ~31μM
4T1 IC_{50} ~6μM
MDA-MB-231 IC_{50} ~3μM
Systemic toxicity 20mg/kg

10

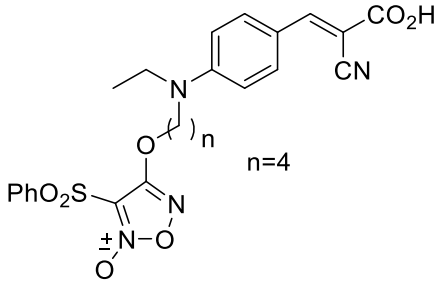

MCT1 IC_{50} ~0.23μM
MCT4 IC_{50} ~0.11μM
Cell prolifiration inhibition
WiDr IC_{50} ~9μM
4T1 IC_{50} ~8μM
MDA-MB-231 IC_{50} ~2 μM
Systemic toxicity ~20mg/kg

11

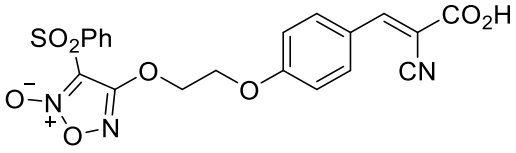

MCT1 IC_{50} ~ 0.1 μM
Cell prolifiration inhibition
WiDr IC_{50} ~8 μM
4T1 IC_{50} ~131 μM
MDA-MB-231 IC_{50} ~ 168 μM

Candidate compounds 8 and 11: The future studies of the candidate compounds will involve *in vivo* metabolic stability evaluation using CACO-2 permability and liver microsomal enzyme stability studies. Further tumor efficacy studies would involve an MCT1 expressing cell line like WiDr and also combination studies with toxic chemotherapeutics. Furthermore, western blot analysis to understand the mechanism of action of the candidate compounds.

12

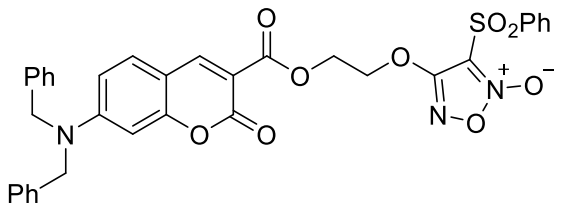

Cell prolifiration inhibition
WiDr IC_{50} ~0.03 μM
4T1 IC_{50} ~0.1 μM
MDA-MB-231 IC_{50} ~0.02 μM
Systemic toxicity 20 mg/kg
tumor growth inhibition
MDA-MB-231 ~30%

13

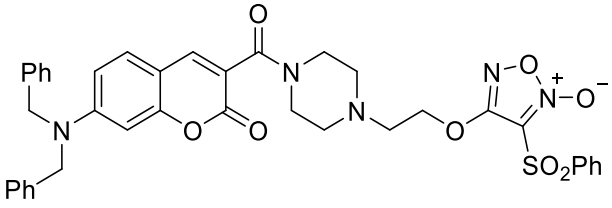

Cell prolifiration inhibition
WiDr IC_{50} ~10 μM
4T1 IC_{50} ~1 μM
MDA-MB-231 IC_{50} ~0.5 μM
Systemic toxicity 20 mg/kg

Candidate compounds 13: Although *in vitro* studies are encouraging with compound 12 due to the presence of more labile ester group this compound could metabolize resulting faster elimination rates *in vivo*. Future studies will involve *in vivo* metabolic stability evaluation studies with candidate compound 13. Further anticancer efficacy studies in MCT1 and MCT4 expressing tumor studies as single agents and in combination with chemotherapeutics. More detailed mechanism of action studies.

CHAPTER 9: Experimental Procedures and Chemical Analysis

Cell lines and culture conditions:

MDA-MB-231 cells (ATCC) were grown in DMEM supplemented with 10% FBS (Atlanta Biologicals) and penicillin-streptomycin (50U/ml, 50µg/ml, Invitrogen). WiDr cells (ATCC) were cultured in MEM medium supplemented with 10% FBS and penicillin-streptomycin. 4T1 and 67NR cells were grown in RPMI-1640 supplemented with 10% FBS and penicillin-streptomycin. MCF7 cells (Masonic Cancer Center, University of Minnesota) were grown in MEM supplemented with 6% FBS, EGF (0.01 µg/ml), NEAA (1X), HDC (1 µg/ml), insulin (10 µg/ml), HEPES (12 mM) and sodium pyruvate (1 mM). The RBE4 cell line was obtained from Dr. Drewes's lab and were cultivated in 1:1 mixture of α-MEM and Ham's F-10 nutrient mix with HEPES (Gibco), 10% heat inactivated FBS (Atlanta Biologicals), basic fibroblast growth factor (1 ng/mL, US Biologicals), geneticin G418 (0.3 mg/mL, VWR International), and antibiotic-antimycotic (10,000 U/mL of penicillin, 10,000 µg/mL of streptomycin, and 25 µg/mL of Fungizone, Gibco)

MTT based cell proliferation inhibition assay:

Cell proliferation inhibition was evaluated using 3-(4,5-dimethylthiazol-2-yl)-2,5-diphenyl tetrazolium bromide (MTT). This colorimetric assay measures the amount of MTT reduced in order to determine cell viability.[76] A 96 well plate was seeded with 5000 cells/well. Test

compounds were added in serial dilution to the wells in replicates and incubated for 72 hours. 10 µL of MTT (12µM) was added to each well and incubated for 4 hours before adding 100µL of SDS (1g/10mL 0.01M HCl) and incubated for another 4 hours. The absorbance for each well was recorded at 570 nm. The percent viability was calculated by comparing the absorbance value of treated wells to the control (% viability = ($Abs_{test\ compound}/Abs_{control}$) x 100). IC_{50} was obtained using GraphPad by plotting log[concentration] on x-axis and percent of viable cells on y-axis.

MCT1 inhibition using ^{14}C-lactate uptake assay

For MCT1 RBE4 cell lines were used. The cells were seeded at a concentration of 2 x 10^5 cells/mL in a collagen coated 24-well plate (500 µL in each well) and incubated for 20 hours prior to the addition of the test compounds. Prior to experiment the growth media was removed and the cells were washed twice with HEPES buffer at pH 7.43 (140 mM NaCl, 5 mM KCl, 2 mM $CaCl_2$, 2 mM $MgCl_2$, and 10 mM HEPES). The cells were equilibrated at 37°C for 15 minutes. Test compounds were diluted in a solution containing 3 µM ^{14}C-lactic acid sodium salt, 2 µM lactic acid sodium salt, and HEPES buffer. Test compounds were added to the wells and incubated for 20 minutes. This solution was then replaced with ice-cold cold buffer containing 100 µM CHC and placed on ice. The wells were washed three times with cold buffer and 250 µL of 0.1 M NaOH in 5% triton X-100 was added to solubilize the cells. Next 150 µL of this solution was transferred to a scintillation vial that contained 4 mL of ecolite (+). The intracellular ^{14}C-lactate uptake was measured using a Beckman scintillation counter and the readings were obtained as dpm. The % inhibition of lactate were calculated by

$$\%inhibition = 100 - (\frac{dpm_{sample}}{dpm_{DMSO}} * 100)$$

The IC_{50} value of a test compound can be calculated using GraphPad Prism and analyzed by interpolation of sigmoidal curve.

MCT4 inhibition using ^{14}C-lactate uptake assay:

For MCT4 MDA-MB-231 cell lines were used. The cells were seeded at a concentration of 4 x 10^5 cells/mL in a 24-well plate (500 µL in each well) and incubated for 20 hours prior to the addition of the test compounds. Prior to experiment the growth media was removed and the cells were washed twice with HEPES buffer at pH 7.0 (140 mM NaCl, 5 mM KCl, 2 mM $CaCl_2$, 2 mM $MgCl_2$, and 10 mM HEPES). The cells were equilibrated at 37°C for 15 minutes. Test compounds were diluted in a solution containing 3 µM ^{14}C-lactic acid sodium salt, 2 µM lactic acid sodium salt, and HEPES buffer. Test compounds were added to the wells and incubated for 20 minutes. This solution was then replaced with ice-cold cold buffer containing 100 µM CHC and placed on ice. The wells were washed three times with cold buffer and 250 µL of 0.1 M NaOH in 5% triton X-100 was added to solubilize the cells. Next 150 µL of this solution was transferred to a scintillation vial that contained 4 mL of ecolite (+). The intracellular ^{14}C-lactate uptake was measured using a Beckman scintillation counter and the readings were obtained as dpm. The % inhibition of lactate were calculated by

$$\%inhibition = 100 - (\frac{dpm_{sample}}{dpm_{DMSO}} * 100)$$

The IC_{50} value of a test compound can be calculated using GraphPad Prism and analyzed by interpolation of sigmoidal curve.

Western blot analysis:

Cells were plated at 25000 cells/ml in petri dishes and allowed to grow for 48 hours. Next, cells were treated with test compounds for 24 hours, and then were washed twice with 1X PBS and solubilized in 200 µL SDS boiling buffer (5% w/v SDS, 10% v/v glycerol, and 60mM Tris pH 6.8), and sonicated. The resultant cell lysate was diluted 1:5 with deionized H_2O and assayed for protein using the Pierce BCA protocol. A volume of test sample containing 10 µg protein was loaded on SDS PAGE gel for electrophoresis according to manufacturer's instructions. Proteins were transferred from the gel to nitrocellulose membrane according to the manufacturer's instructions. The PARP (rabbit polyclonal IgG, Origene, TA321555), P53 (rabbit polyclonal IgG, Santa Cruz, sc50329), and γ-H2AX (mouse monoclonal, Upstate 05-636, 0.5µg/mL) were detected and visualized using HRP chemiluminescence. For relative quantitation, β-actin (mouse monoclonal IgG C4, Millipore, MAB1501) was detected and measured as a control protein.

Seahorse XFe96® assessment of glycolysis and mitochondrial respiration:

Cells were plated at a concentration of 20,000 cells/well in a Seahorse XFe96 culture microplate (Agilent, part no. 101085-004) and incubated for 24 hours at 37ºC at 5% CO_2. Sensor cartridge (Agilent, part no. 102416-100) was hydrated with XF calibrant (Agilent, part no. 100840-000) overnight at 37ºC in an incubator without CO_2. The assay media was prepared from Seahorse base medium (Agilent, part no. 102353-100) and enriched with glutamine (1mM) and sodium pyruvate (1mM) and the pH of the assay media was

maintained at 7.4, and prewarmed to 37^{o}C before usage. For glycolysis stress test, the assay media was used without glucose. For the mitochondrial stress test the assay media was enriched with glucose (10mM). For both stress tests an 8X stock concentration of test compounds in their respective media was prepared for microplate injections in port A. Stock solutions of glucose (90mM or 9X), oligomycin (100 µM or 10X), and 2-deoxyglucose (Chem Impex) (550mM or 11X) were prepared such that their final working concentrations are 10mM, 1µM and 50mM, respectively, for glycolysis stress test. For mitochondrial stress test, stock solutions of oligomycin (9 µM or 9X), FCCP (2.5-10 µM or 10X), rotenone+antimycin A (5.5 µM or 11X) were prepared such that their final concentrations were 1 µM, 0.25-1 µM, and 0.5µM, respectively in the glucose enriched assay media. Under glycolytic stress test, the cells were treated with test compounds after 14.29 minutes, and glucose, oligomycin and 2-deoxyglucose were added after 33.8, 53.35, and 72.87 minutes, respectively. For mitochondrial stress test, port A was injected with test compoundsbat 14.29 minutes, and oligomycin, FCCP, and rotenone+antimycin A were added after 33.8, 53.35, 72.87 minutes, respectively. ECAR and OCR were measured for glycolysis and mitochondrial stress tests, respectively, via Seahorse XFe96® analyzer (Agilent). The glycolysis and mitochondrial parameters for GST and MST were calculated utilizing the Wave 2.4.0 software (Agilent).

Fluorescent microscopy studies:

MDA-MB-231 or WiDr cells ($5x10^4$ cells/mL) were seeded in glass-bottom dishes (MatTek Corp, part no. P35G010C) and incubated for 48 hours. Test compound (30µM) was added and cells were again incubated for 24 hours prior to fluorescent microscopic

imaging. In some cultures, MitoTracker Red CMXROS (Invitrogen, M7512, 100 nM) was added 15 min prior to imaging. The growth media was removed and replaced with 5% FBS in 1X PBS for imaging. Cells were then examined and photographed using a Nikon TE2000 epifluorescent microscope and camera. The images shown are representative of at least 3 fields of view of three separate experiments.

Ethical statement:

The experimental procedures involving animals that were conducted at the University of Minnesota Duluth were in compliance with the U.S. National Institutes of Health Guide for Care and Use of Laboratory Animals and approved by the Institutional Animal Care and Use Committee at the University of Minnesota (UMN). 1307-30773A, 1311-31063A, and 1612-34444A

General procedure for systemic toxicity evaluation:

Healthy CD-1 mice were ordered from Charles River. Upon arrival the mice were housed two mice per cage and acclimatized at room temperature for 7 days. Prior to the study the mice were weighed and placed into groups (n = 6 mice per group) so the standard deviation between each group was minimal. In each cage of two mice, one mouse was identified from the either with a black mark on its tail. Treatment with candidate compounds was started via i.p. The body weights were monitored very day before injections for a period of 14-21 days. At the end of the study, mice were euthanized using CO_2.

Tumor growth inhibition studies:

WiDr cells (5×10^6 cells) were suspended in 1:1 mixture of matrigel (Corning, cat. no. 356237) and PBS and injected subcutaneously into the right flank of female athymic nude

mice (Charles River). The mice were randomly assigned into 3 groups (n=6 mice per group). Vertical and horizontal diameters of tumors were measured every two or three days using calipers. The tumor volumes were calculated assuming a perfect sphere using the formula $V = ab^2/2$ where 'a' is the longer diameter of the tumor and 'b' is the shorter diameter of the tumor. Treatment was initiated when the tumor volume reached $100mm^3$. The study was terminated after sixteen days and tumors were then resected and weighed.

Statistical analysis:

Statistics were computed using GraphPad Prism version 7.0. Repeated measures one-way ANOVA was used for *in vitro* studies and Mann-Whitney test was used for *in vivo* studies. A *P*-value of < 0.05 was considered significant where *, $P < 0.05$; **, $P < 0.01$; ***, $P < 0.001$; ****, $P < 0.0001$.

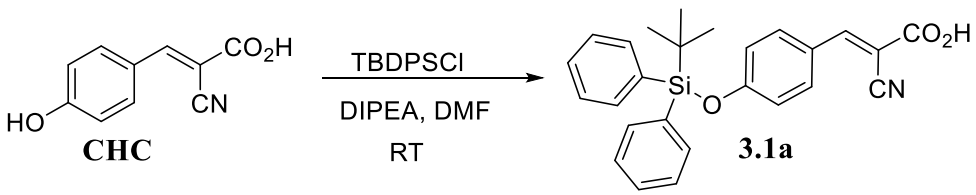

Synthesis of *(E)-3-(4-((tert-butyldiphenylsilyl)oxy)phenyl)-2-cyanoacrylic acid* **(3.1a)**: Commercially available α-cyano-4-hydroxycinnamic acid (10.6 mmol) was dissolved in DMF followed by the addition DIPEA (31.7 mmol) to the solution. After stirring for one hour, TBDPSCl (42.3 mmol) was added dropwise to the reaction on ice and was stirred overnight. The completion of the reaction was monitored with TLC (70% EA/Hexanes). Upon completion of the reaction, the solution was quenched with HCl and ice. The precipitate was then filtered and washed with hexanes. The product was purified using column chromatography (triethyl amine treated silica gel, EA and Hexanes 1:3) giving the pure compound as a white solid (Yield: 83%).

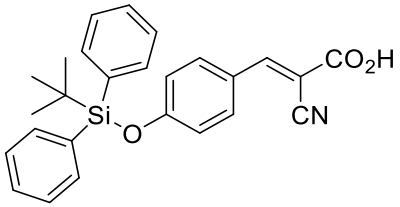

(E)-3-(4-((tert-butyldiphenylsilyl)oxy)phenyl)-2-cyanoacrylic acid (**3.1a**)

^{1}H NMR (500 MHz, $CDCl_3$):

δ ppm 8.15 (s, 1H), 7.84 (d, *J* = 9 Hz, 2H), 7.67 - 7.72 (m, 4H), 7.43 - 7.50 (m, 2H), 7.37 - 7.43 (m, 4H), 6.86 (d, *J* = 9 Hz, 2H), 1.12 (s, 9H)

^{13}C NMR (126 MHz, $CDCl_3$):

δ ppm 168.0, 161.1, 156.1, 135.3, 133.9, 131.7, 130.4, 128.0, 124.4, 120.8, 115.6, 98.2, 26.4, 19.5

HRMS (ESI) m/z:

calc'd for $C_{17}H_{22}N_2O_3$ $[M+Na]^+$: 428.168

found 428.146

Elemental Analysis C, H, N, O

Anal. Calcd for $C_{26}H_{25}NO_3Si$ (427.16): C 73.04, H 5.89, N 3.28.

Found: C 72.34, H 5.96, N 3.20

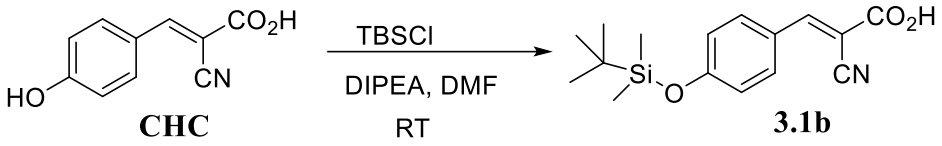

CHC **3.1b**

Synthesis of *E)-3-(4-((tert-butyldimethylsilyl)oxy)phenyl)-2-cyanoacrylic acid* (**3.1b**): Commercially available α-cyano-4-hydroxycinnamic acid (10.6 mmol) was dissolved in DMF followed by the addition DIPEA (31.7 mmol) to the solution. After reacting for one hour, TBSCl (42.3 mmol) in 5 ml of DCM was added dropwise to the reaction on ice. The reaction was stirred overnight. The completion of the reaction was monitored with TLC (70% EA/Hexanes). Upon completion of the reaction, the solution was poured over ice and worked up with ether. The organic layer was dried with magnesium sulphate and the organic layer was evaporated. The product was purified using column chromatography (triethyl amine treated silica gel, EA and Hexanes 1:1) giving the pure cream colored solid (Yield: 75%).

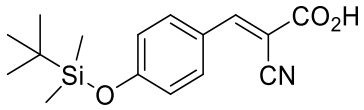

(E)-3-(4-((tert-butyldimethylsilyl)oxy)phenyl)-2-cyanoacrylic acid (**3.1b**):

^{1}H NMR (500 MHz, CDCL3-d)

δ 8.25 (s, 1H), 8.00 (d, *J* = 9 Hz, 2H), 6.96 (d, *J* = 9 Hz, 2H), 1.00 (s, 9H), 0.27 (s, 6H)

^{13}C NMR (126 MHz, $CDCl_3$):

δ 168.5, 161.5, 156.2, 134.2, 124.5, 121.0, 115.6, 98.4, 25.5, 18.3, -4.3

HRMS (ESI) m/z:

calc'd for $C_{16}H_{21}NO_3Si$ $[M+H]^+$: 304.12

found: 304.12.

Elemental Analysis C, H, N, O

Anal. Calcd for $C_{16}H_{21}NO_3Si$ (303.43): C 63.33, H 6.98, N 4.62.

Found: C 63.22, H 6.84, N 4.73.

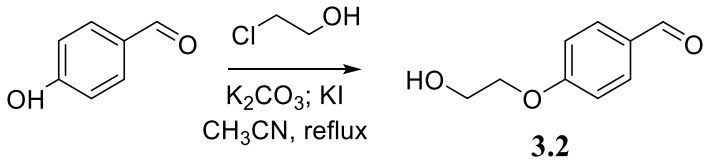

3.2

The synthesis of *4-(2-hydroxyethoxy)benzaldehyde* (**11)** 4-hydroxybenaldehyde (81.8 mmol) was dissolved in 80 ml of EtOH. Potassium carbonate (163 mmol) was added to the reaction flask followed by 2-chloroethanol (327 mmol). The reaction mixture was refluxed for 10 hours, potassium carbonate was filtered and ethanol was partially evaporated. The slurry was extracted 3x with 100 ml of ethyl acetate in water and washed with 100 ml of 0.01M NaOH solution. The organic layer was separated and dried on anhydrous $MgSO_4$ and the organic layer was evaporated using a rotatory evaporator. The resulting white solid was used for the next reaction without further purification.

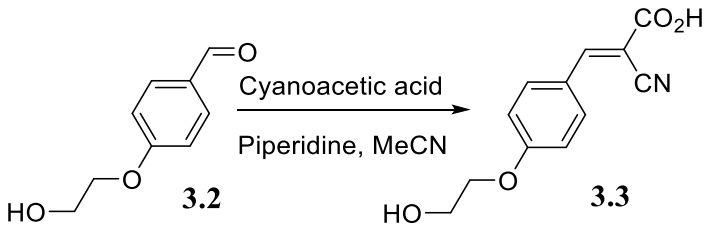

3.2 **3.3**

The synthesis of (*E)-2-cyano-3-(4-(2-hydroxyethoxy)phenyl)acrylic acid* **(3.3)**: The benzaldehyde **11** (12 mmol) was dissolved in 40 ml of acetonitrile (0.2M). Cyanoacetic acid (18.1 mmol) was added followed by the addition of piperidine (24.1 mmol). The reaction was then allowed to reflux overnight. Upon completion of the reaction (monitored via TLC), the solution was poured over ice and 10 ml 3M HCl. The resulting precipitate was then filtered and washed with ether to obtain **3.3**. The solid was then isolated using

column chromatography (silica gel, EA) to yield the final cream colored solid (Yield: 78%).

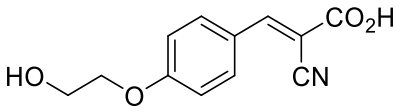

E)-2-cyano-3-(4-(2-hydroxyethoxy)phenyl)acrylic acid **(3.3):**

^{1}H NMR (500 MHz, MeOH-d_6):

δ 8.09 (s, 1H), 7.98 (d, *J* = 9 Hz, 2H), 7.12 (d, 2H), 4.20 (t, 2H), 3.97 (t, *J* = 5 Hz, 2H)

^{13}C NMR (126MHz, MeOH-d_6):

δ 167.5, 161.8, 149.7, 131.8, 125.4, 118.4, 114.6, 107.0, 69.4, 60.1.

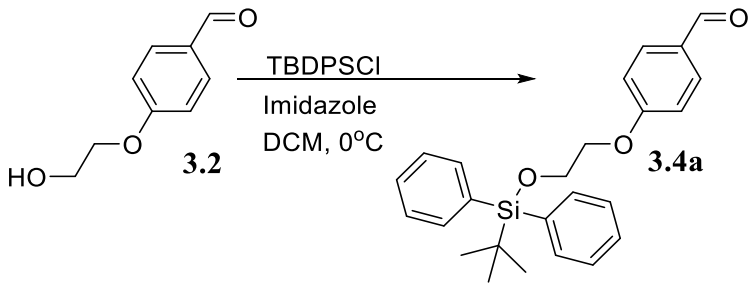

74-(2-((tert-butyldiphenylsilyl)oxy)ethoxy)benzaldehyde (**3.4a**): 4-(2-hydroxyethoxy) benzaldehyde (**3.2)** (12 mmol) was dissolved in 90 ml of DCM (0.1M) and imidazole (36mmol) was added to the reaction at room temperature. After 10 minutes, a solution of TBDPSCl (14.4 mmol) in DCM was added to the reaction at 0°C. Reaction completion was monitored with TLC (10% EA/Hexanes) which was then extracted with DCM and washed twice with water followed by brine. The organic layer was dried with $MgSO_4$ and the solvent was removed. The resulting brown oil was then carried on to the next reaction without further purification.

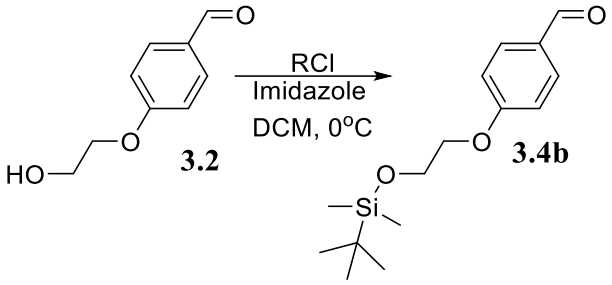

4-(2-((tert-butyldimethyllsilyl)oxy)ethoxy)benzaldehyde (**3.4b**): 4-(2-hydroxyethoxy) benzaldehyde (**11)** (12 mmol) was dissolved in 90 ml of DCM and imidazole (36mmol) was added at room temperature. After 10 minutes a solution of TBSCl (14.4 mmol) in DCM was added to the reaction at 0°C. Reaction completion was monitored with TLC (10% EA/Hexanes) which was then extracted with DCM and washed twice with water followed by brine. The organic was dried on $MgSO_4$ and the solvent was removed. The resulting brown oil was then carried on to the next reaction without further purification.

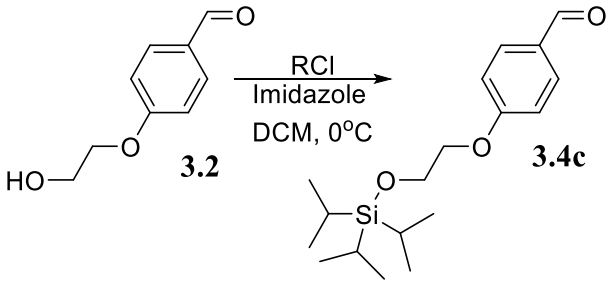

4-(2-((triisopropylsilyl)oxy)ethoxy)benzaldehyde (**3.4c**): 4-(2-hydroxyethoxy) benzaldehyde (**11)** (12 mmol) was dissolved in 90 ml of DCM and imidazole (36mmol) was added to the reaction room temperature. After 10 minutes a solution of TIPSCl (14.4m ml) in DCM was added to the reaction at 0°C. Reaction completion was monitored with TLC (10% EA/Hexanes). The reaction was extracted with ethyl acetate then washed twice with water followed by brine. The organic was dried on $MgSO_4$ and the solvent was

removed. The resulting brown oil was then carried on to the next reaction without further purification.

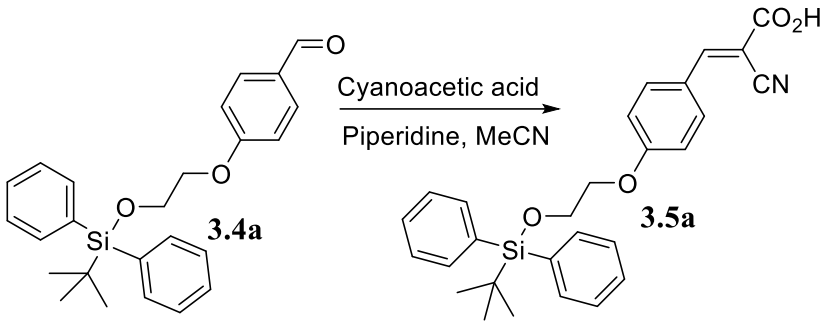

(E)-3-(4-(2-((tert-butyldiphenylsilyl)oxy)ethoxy)phenyl)-2-cyanoacrylic acid (**3.5a**): The silylated benzaldehyde **3.4a** (12 mmol) were dissolved in 40 ml of acetonitrile. Cyanoacetic acid (18.1 mmol) was added followed by the addition of piperidine (24.1 mmol). The reaction was then allowed to reflux for 10 hours. Reaction completion was monitored with TLC (10% EA/Hexanes). Upon completion the solution was poured over ice and 10 ml of 3M HCl. The resulting precipitate was then filtered and washed with 50 ml of ether to obtain the crude product **3.5a**. The crude product was purified using column chromatography (silica gel, EA and hexanes 1:5) yielding the pure product (Yield: 67%).

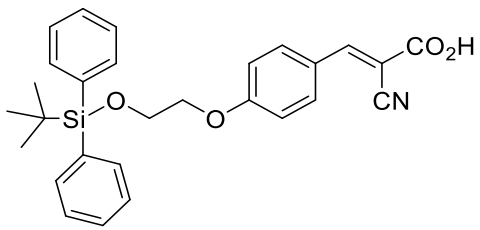

4-(2-((tert-butyldiphenylsilyl)oxy)ethoxy)benzaldehyde (**3.5a**):

^{1}H NMR (500 MHz, $CDCl_3$) δ ppm 8.24 (br. s., 1H), 8.01 (d, *J* = 8 Hz, 2H), 7.67 - 7.74 (m, 4H), 7.36 - 7.48 (m, 6H), 6.94 (d, *J* = 8 Hz, 2H), 4.16 (t, *J* = 5 Hz, 2H), 4.02 (t, *J* = 5 Hz, 2H), 1.07 (s, 9H).

^{13}C NMR (126 MHz, $CDCl_3$) δ ppm 168.8, 163.8, 156.1, 135.6, 134.2, 133.3, 129.9, 127.8, 124.1, 115.4, 98.4, 69.4, 62.3, 26.8, 19.2

Elemental Analysis C, H, N, O

Anal. Calcd for $C_{28}H_{29}NO_4Si\ Na^+$ (494.18): C 67.99, H 5.91, N 2.83.

Found: C 69.06, H 5.98, N 2.90.

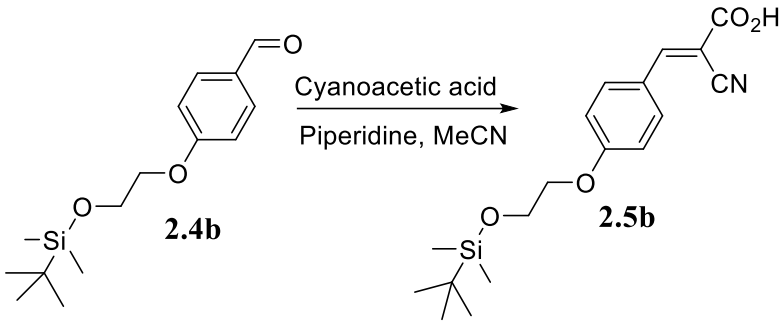

(E)-3-(4-(2-((tert-butyldimethylsilyl)oxy)ethoxy)phenyl)-2-cyanoacrylic acid (**3.5b**): The silylated benzaldehyde **2.4b** (12 mmol) was dissolved in 40 ml of acetonitrile. Cyanoacetic acid (18.1 mmol) was added followed by piperidine (24.1 mmol) and refluxed for 10 hours. Reaction completion was monitored with TLC (10% EA/Hexanes). Upon completion the solution was poured over ice and 10 ml of 3 M HCl. The resulting precipitate was then filtered and washed with 50 ml of ether to obtain the crude product **3.5b**. The crude product was purified using column chromatography (silica gel, EA and hexanes 1:5) yielding the pure product (Yield: 68%).

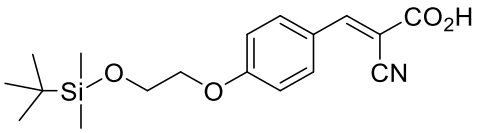

(E)-3-(4-(2-((tert-butyldimethylsilyl)oxy)ethoxy)phenyl)-2-cyanoacrylic acid (**3.5b)**:

^{1}H NMR (500 MHz, $CDCl_3$-d):

δ 8.22 (s, 1H), 8.03 (d, *J* = 9 Hz, 2H), 7.03 (d, *J* = 9 Hz, 2H), 4.15 (t, 5Hz, 2H), 4.01 (t, 5Hz, 2H), 0.91 (s, 9H), 0.11 (s, 6H)

^{13}C NMR (126 MHz, $CDCl_3$-d):

δ 167.9, 163.8, 156.0, 134.2, 124.1, 115.7, 115.5, 98.1, 69.8, 61.7, 25.9, 18.4, -5.2

HRMS (ESI) m/z:

calc'd for $C_{18}H_{25}NO_4Si$ $[M+H]^+$: 348.16

found: 348.14;

Elemental Analysis C, H, N, O

Anal. Calcd for $C_{18}H_{25}NO_4Si$ (347.48): C 73.04, H 5.89, N 3.28.

Found: C 72.34, H 5.96, N 3.20.

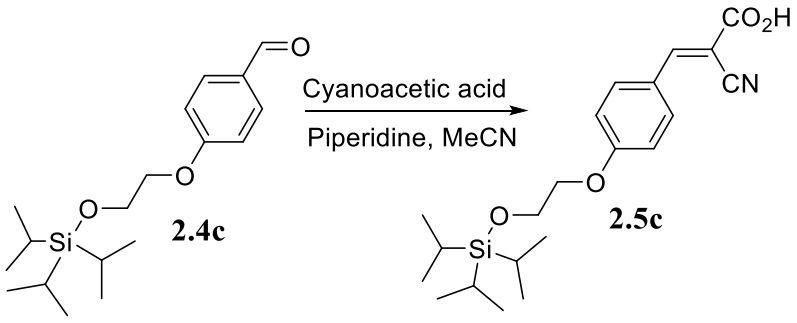

and *(E)-3-(4-(2-((tri-isopropylsilyl)oxy)ethoxy)phenyl)-2-cyanoacrylic acid* (**3.5c**) : The silylated benzaldehyde **2.4c** (12 mmol) were dissolved in 40 ml of acetonitrile. Cyanoacetic

acid (18.1 mmol) was added followed by the addition of piperidine (24.1 mmol). The reaction was then allowed to reflux for 10 hours. Reaction completion was monitored with TLC (10% EA/Hexanes). Upon completion the solution was poured over ice and 10 ml of 3 M HCl. The resulting precipitate was then filtered and washed three times with 50 ml of ether to obtain the crude product **3.5a**. The crude product was purified using column chromatography (silica gel, EA and hexanes 1:5) yielding the pure product (Yield: 86%).

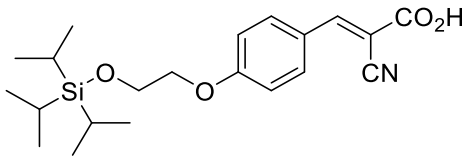

(E)-3-(4-(2-((tri-isopropylsilyl)oxy)ethoxy)phenyl)-2-cyanoacrylic acid (**3.5c)**:

^{1}H NMR (500 MHz, $CDCl_3$-d):

δ 8.10 (s, 1 H), 7.93 (d, *J* = 9 Hz, 2H), 6.95 (d, *J* = 9 Hz, 2H), 4.10 (t, *J* = 5 Hz, 2 H), 4.02 (t, *J* = 5 Hz, 2 H), 0.98 - 1.12 (m, 21H)

^{13}C NMR (126 MHz, $CDCl_3$-d): δ 164.8, 163.0, 153.9, 133.4, 124.4, 116.6, 115.2, 100.2, 69.7, 62.0, 17.9, 11.9;

HRMS (ESI) m/z:

calc'd for $C_{21}H_{31}NO_4Si$ $[M+H]^+$: 390.21

found: 390.19

Elemental Analysis C, H, N, O

Anal. Calcd for $C_{21}H_{31}NO_4Si$ (389.57): C 64.75, H 8.02, N 3.60.

Found: C 63.60, H 7.34, N 4.14.

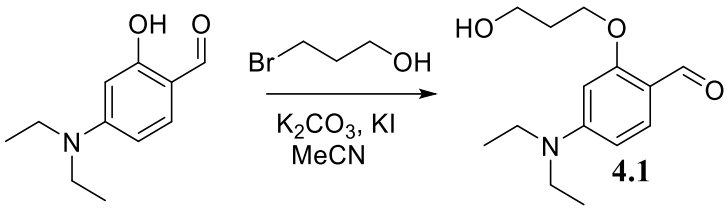

4-(diethylamino)-2-(3-hydroxypropoxy)benzaldehyde **(4.1)**: Commercially available 4-(diethylamino)-salicylaldehyde (26 mmol) was dissolved in 100ml of acetonitrile. Next potassium carbonate was added to the reaction. The reaction reacted at room temperature for 30 minutes before bromopropanol (31 mmol) was added to the reaction slowly. Next catalytic amounts of potassium iodide (0.26 mmol) was added to the reaction. The reaction was heated to reflux and left to react for 16 hours. A TLC was checked (30% EA/Hexanes) to ensure completion. The potassium carbonate was filtered off and the acetonitrile was evaporated via rotoevaporation. The resulting product was washed with hexanes twice to yield a navy blue oil (Yield: 73%).

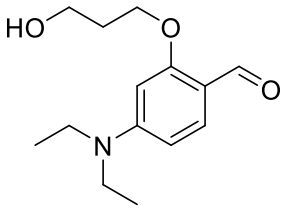

4-(diethylamino)-2-(3-hydroxypropoxy)benzaldehyde **(4.1):**

^{1}H NMR (500 MHz, $CDCl_3$):

δ 9.95 (s, 1H), 7.60 (d, J = 9 Hz, 1H), 6.29 (d, J = 9 Hz, 1H), 6.06 (s, 1H), 4.19 (t, J = 6 Hz, 2H), 3.89 (t, J = 6 Hz, 2H), 3.43 (q, J = 7 Hz, 4H), 2.11 (quin, J = 6 Hz, 2H), 1.22 (t, J = 7 Hz, 6H) [d]

^{13}C NMR (126 MHz, $CDCl_3$):

δ ppm 187.5, 162.8, 153.8, 133.3, 114.1, 104.1, 93.3, 66.2, 60.3, 44.8, 32.0, 12.6

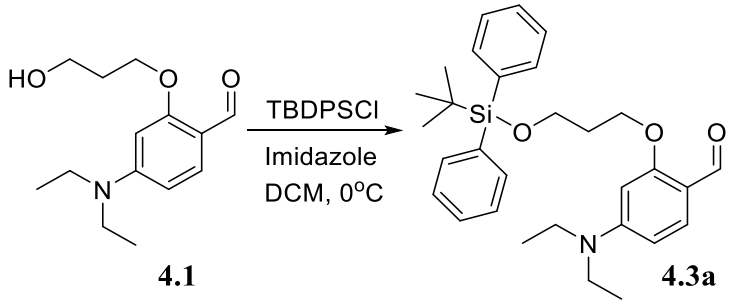

4.1 **4.3a**

2-(3-((tert-butyldiphenylsilyl)oxy)propoxy)-4-(diethylamino)benzaldehyde (**4.3a**): The benzaldehyde (**4.2)** (12 mmol) was dissolved in 90 ml of DCM and imidazole (36 mmol) was added to the reaction room temperature. After 10 minutes a solution of TBDPSCl (14.4 mmol) in DCM was added to the reaction at 0°C. Completion of the reaction was monitored by TLC (20% EA/Hexanes) over 3 hours as the reaction warmed to room temperature. Upon completion the reaction was worked up twice with water followed by brine. The

organic was dried on $MgSO_4$ and the solvent was removed. The resulting brown oil was then carried on to the next reaction without further purification.

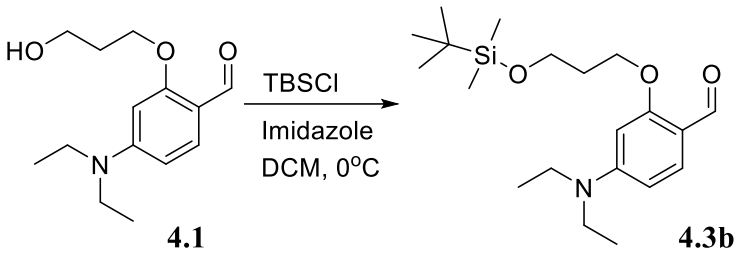

4.1 **4.3b**

2-(3-((tert-butyldimethylsilyl)oxy)propoxy)-4-(diethylamino)benzaldehyde (**4.3b**): The benzaldehyde (**4.2)** (12 mmol) was dissolved in 90 ml of DCM and imidazole (36 mmol) was added to the reaction room temperature. After 10 minutes a solution of TBSCl (14.4 mmol) in DCM was added to the reaction at 0°C. Completion of the reaction was monitored by TLC (20% EA/Hexanes) over 3 hours as the reaction warmed to room temperature. Upon completion the reaction was worked up twice with water followed by brine. The organic was dried on $MgSO_4$ and the solvent was removed. The resulting brown oil was then carried on to the next reaction without further purification.

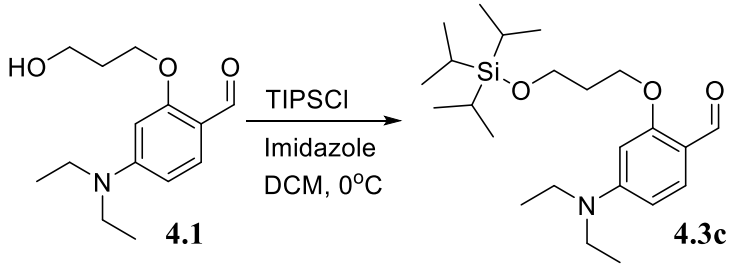

4.1 **4.3c**

4-(diethylamino)-2-(3-((triisopropylsilyl)oxy)propoxy)benzaldehyde (**4.3c**): The benzaldehyde (**4.2)** (12 mmol) was dissolved in 90 ml of DCM and imidazole (36 mmol) was added to the reaction room temperature. After 10 minutes a solution of TIPSCl (14.4 mmol) in DCM was added to the reaction at 0°C. Completion of the reaction was monitored

by TLC (20% EA/Hexanes) over 3 hours as the reaction warmed to room temperature. Upon completion the reaction was worked up twice with water followed by brine. The organic was dried on $MgSO_4$ and the solvent was removed. The resulting brown oil was then carried on to the next reaction without further purification.

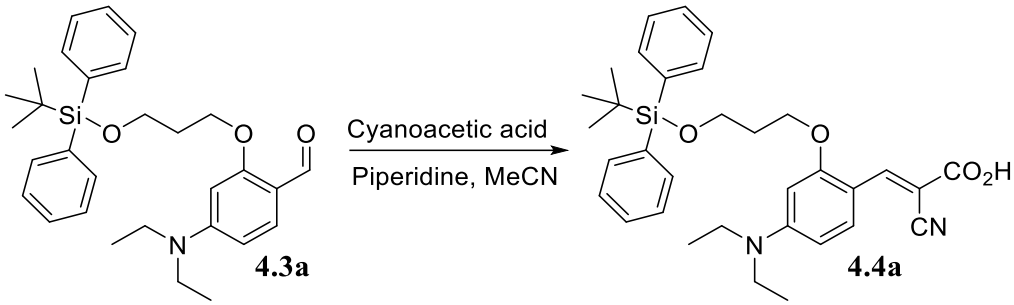

(E)-3-(2-(3-((tert-butyldiphenylsilyl)oxy)propoxy)-4-(diethylamino)phenyl)-2-cyanoacrylic acid (**4.4a**): The silylated benzaldehyde **4.3a** (12 mmol) were dissolved in 40 mL of acetonitrile. Cyanoacetic acid (18.1 mmol) was added followed by piperidine (24.1 mmol). The reaction was then refluxed for 10 hours. Completion of the reaction was monitored using TLC (30% EA/Hexanes) Upon completion of the reaction, the solution was poured over ice and 10 mL of 3 M HCl. The resulting precipitate was then filtered and washed with 50 mL of ether to obtain the crude product **4.4a**. The crude product was purified using column chromatography (triethyl amine treated silica, EA and hexanes 2:5) yielding the final pure product (Yield: 86%).

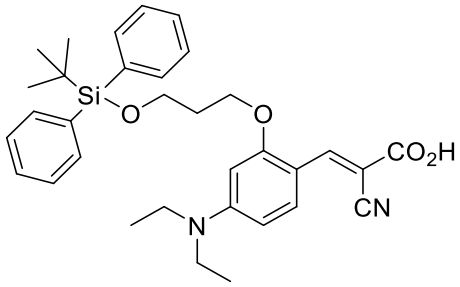

(E)-3-(2-(3-((tert-butyldiphenylsilyl)oxy)propoxy)-4-(diethylamino)phenyl)-2-cyanoacrylic acid (**4.4a**):

^{1}H NMR (500 MHz, $CDCl_3$):

δ 8.85 (s, 1H), 8.74 (d, J = 9 Hz, 1H), 7.89 (d, J = 7 Hz, 4H), 7.64 - 7.70 (m, 2H), 7.56 - 7.62 (m, 4H), 6.64 (d, J = 9 Hz, 1H), 6.31 (s, 1H), 4.46 (t, J = 6 Hz, 2H), 4.17 (t, J = 6 Hz, 2H), 3.73 (q, J = 7 Hz, 4H), 2.36 (quin, J = 6 Hz, 2H), 1.51 (t, J = 7.1 Hz, 6H), 1.32 (s, 9H)

^{13}C NMR (126 MHz, $CDCl_3$):

δ 170.4, 162.1, 154.1, 148.9, 135.4, 133.5, 131.6, 129.7, 127.7, 118.2, 109.3, 105.3, 93.1, 89.9, 64.8, 59.9, 45.0, 31.9, 26.9, 19.3, 12.7

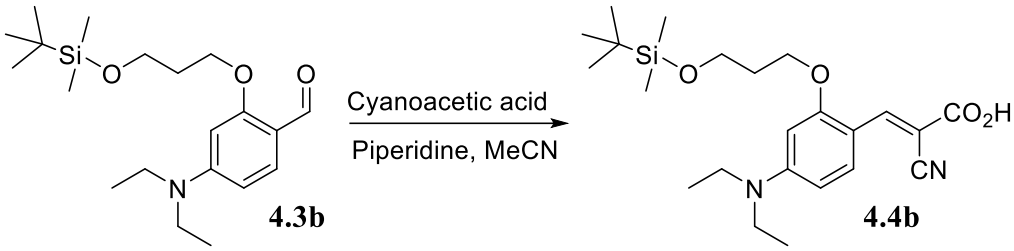

(E)-3-(2-(3-((tert-butyldimethylsilyl)oxy)propoxy)-4-(diethylamino)phenyl)-2-cyanoacrylic acid (**4.4b**): The silylated benzaldehyde **4.3b** (12 mmol) were dissolved in 40 mL of acetonitrile. Cyanoacetic acid (18.1 mmol) was added followed by piperidine (24.1 mmol). The reaction was then refluxed for 10 hours. Completion of the reaction was monitored using TLC (30% EA/Hexanes) Upon completion of the reaction, the solution was poured over ice and 10 mL of 3 M HCl. The resulting precipitate was then filtered and washed with 50 mL of ether to obtain the crude product **4.4b**. The crude product was purified using column chromatography (triethyl amine treated silica, EA and hexanes 2:5) yielding the final pure product (Yield: 92 %).

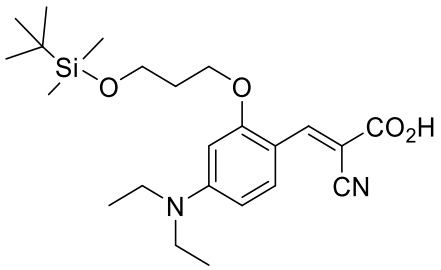

(E)-3-(2-(3-((tert-butyldimethylsilyl)oxy)propoxy)-4-(diethylamino)phenyl)-2-cyanoacrylic acid (**4.4b)**:

^{1}H NMR (500 MHz, $CDCl_3$-d):

δ 8.71 (s, 1H), 8.47 (d, J = 9 Hz, 1H), 6.36 (d, J = 9 Hz, 1H), 6.06 (s, 1H), 4.14 (t, J = 6 Hz, 2H), 3.87 (t, J = 6 Hz, 2H), 3.47 (q, J = 7 Hz, 4H), 2.08 (quin, J = 6 Hz, 2H), 1.26 (t, J = 7 Hz, 6H), 0.90 (s, 9H), 0.07 (s, 6H);

^{13}C NMR (126 MHz, $CDCl_3$-d):

δ 170.6, 162.1, 154.1, 148.8, 131.7, 118.2, 109.2, 105.3, 93.2, 89.9, 64.9, 59.3, 45.0, 32.1, 25.9, 18.3, 12.7, -5.4

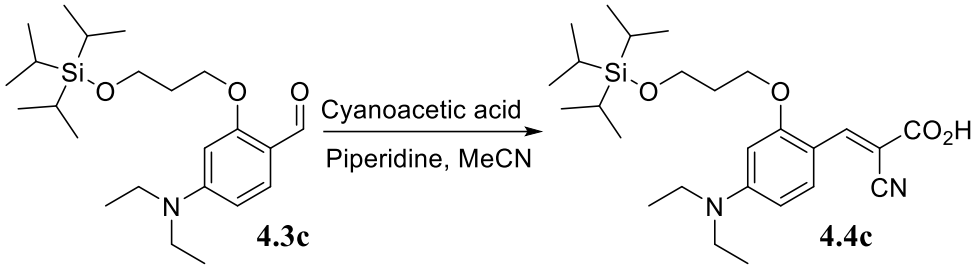

4.3c **4.4c**

(E)-2-cyano-3-(4-(diethylamino)-2-(3-((triisopropylsilyl)oxy)propoxy)phenyl)acrylic acid (**4.4c**): The silylated benzaldehyde **4.3c** (12 mmol) were dissolved in 40 mL of acetonitrile. Cyanoacetic acid (18.1 mmol) was added followed by piperidine (24.1 mmol). The reaction was then refluxed for 10 hours. Completion of the reaction was monitored using TLC (30% EA/Hexanes) Upon completion of the reaction, the solution was poured over ice and 10 mL of 3 M HCl. The resulting precipitate was then filtered and washed with 50 mL of ether to obtain the crude product **4.4c**. The crude product was purified using column chromatography (triethyl amine treated silica, EA and hexanes 2:5) yielding the final pure product (Yield: 86%).

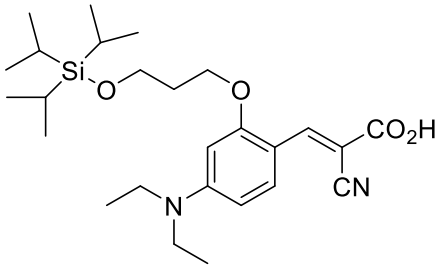

(E)-2-cyano-3-(4-(diethylamino)-2-(3-((triisopropylsilyl)oxy)propoxy)phenyl)acrylic acid (**4.4c)**: **^{1}H NMR** (500 MHz, $CDCl_3$-d):

δ 8.71 (s, 1H), 8.47 (d, J = 9 Hz, 1H), 6.36 (d, J = 9 Hz, 1H), 6.07 (s, 1H), 4.18 (t, J = 6 Hz, 2H), 3.94 (t, J = 6 Hz, 2H), 3.47 (q, J = 7 Hz, 4H), 2.10 (quin, J = 6 Hz, 2H), 1.25 (t, J = 7 Hz, 6H), 1.05-1.15 (m, 21H);

^{13}C NMR (126 MHz, $CDCl_3$-d):

δ 170.8, 162.2, 154.1, 148.9, 131.6, 118.2, 109.3, 105.3, 93.2, 89.9, 65.2, 59.6, 45.0, 32.2, 18.0, 12.7, 11.9

Experimental

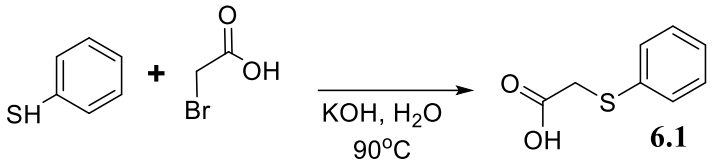

Synthesis of *2-(phenylthio)acetic acid* (**6.1**): Synthesis of the precursor **3.1** was conducted by taking commercially available thiophenol (0.908 mol) and suspending it in a solution of 150 ml of water. potassium hydroxide (1.083 mol) dissolved in 300 ml of water was added slowly to the cooled solution to ensure that the temperature did not exceed 20° C. The solution was allowed to react for ten minutes while another solution of bromoacetic acid (1.082 mol) in 450 ml of water was made. This solution of bromoacetic acid was added to the chilled reaction solution of thiophenol and potassium hydroxide slowly. Following the final addition of the bromoacetic acid solution the reaction was heated to 90° C for 3 hours. After cooling the pH of the solution was adjusted with concentrated HCl and worked up with dichloromethane in three 200 ml aliquots. The organic layer was dried with magnesium sulfate and concentrated via roto evaporation. The resulting white solid (**1**) was used for the next reaction without any further purification.

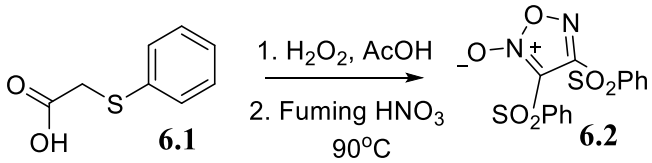

Synthesis of *diphenylsulphafuroxan* (**6.2**): The synthesis of the (**6.2**) was conducted by initially dissolving **6.1** (59 mmol) in 48 ml of glacial acetic acid. 12 ml of aqueous H_2O_2 (30%) was added to this solution. The reaction mixture was stirred for 3 hours. Dissolution

of the white solid confirms the complete oxidation of sulphur in **6.1**. The solution was cooled on ice for ten minutes followed by the addition of 25 ml of fuming nitric acid. The reaction was taken off ice and slowly heated to 90° C over a period of 1 hour. Immediately a few small blocks of ice were added and the solution was allowed to recrystallize for at least a day at -20°C. The resulting white solid was filtered and washed with hexanes to yield the pure diphenylsulphafuroxan 6.**2** as a white solid.

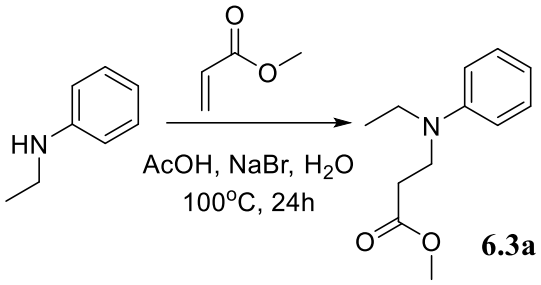

6.3a

Synthesis of *(methyl 3-(ethyl (phenyl)amino)propanoate* (**6.3a)**: *N*-Ethyl aniline (185 mmol) was mixed with acetic acid (20 ml) and methyl acrylate (30 ml). Sodium bromide (4.25 mmol) was added to the reaction and the reaction was refluxed for 16 hours. The completion of the reaction was monitored by TLC (10% EA/Hexanes) until all the corresponding aniline had been converted to **6.3a**. The reaction was initially worked up with ether and water. The aqueous layer was then quenched with bicarbonate followed by another workup with ethyl acetate to yield product as a brown oil. No additional purification was performed to remove the remaining extra methyl acrylate and was used directly for the next step.

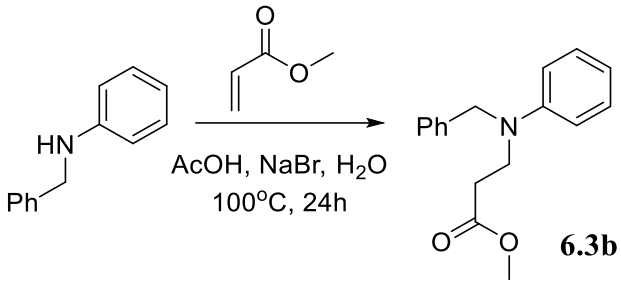

6.3b

Synthesis of *(methyl 3-(ethyl (phenyl)amino)propanoate* (**6.3b**): *N*-benzyl aniline (185 mmol) was mixed with acetic acid (20 ml) and methyl acrylate (30 ml). Sodium bromide (4.25 mmol) was added to the reaction and the reaction was refluxed for 16 hours. The completion of the reaction was monitored by TLC (10% EA/Hexanes) until all the corresponding aniline had been converted to **6.3a**. The reaction was initially worked up with ether and water. The aqueous layer was then quenched with bicarbonate followed by another workup with ethyl acetate to yield product as a brown oil. No additional purification was performed to remove the remaining extra methyl acrylate and was used for next step.

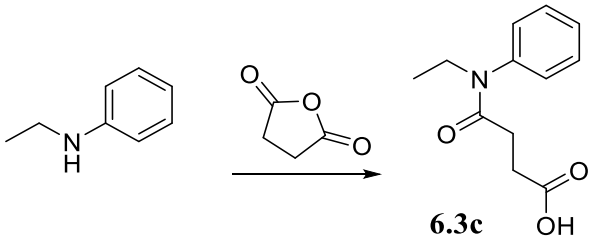

6.3c

Synthesis of *4-(ethyl(phenyl)amino)-4-oxobutanoic acid* (**6.3c**): Succinic anhydride (165 mmol) was dissolved in 100 ml of THF followed by the addition of N-ethylaniline (198 mmol). The reaction was stirred at room temperature for one hour and completion of the reaction was monitored via TLC (50% EA/Hexanes). The THF was evaporated off and the

reaction worked up with ethyl acetate and water. The organic layer was dried and evaporated yielding a white solid.

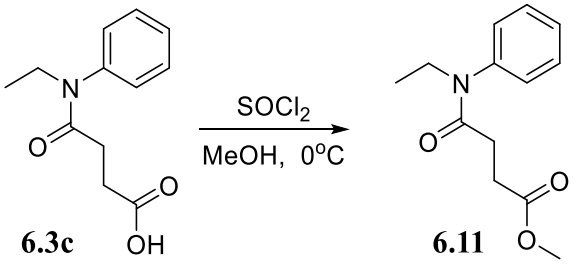

6.3c **6.11**

Synthesis of *methyl 4-(ethyl(phenyl)amino)-4-oxobutanoate* (**6.11**): 200 ml of MeOH was cooled on ice followed by slow addition of thionyl chloride (158 mmol). The reaction was stirred on ice for 10 minutes. The carboxylic acid **6.3c** was added slowly over a period of 30 minutes. After one hour, a TLC (30% EA/Hexanes) of the reaction was checked for completion. The solution was then the reaction was worked up using brine and ether. The organic layer was evaporated and the crude product was utilized for the next step without any purification.

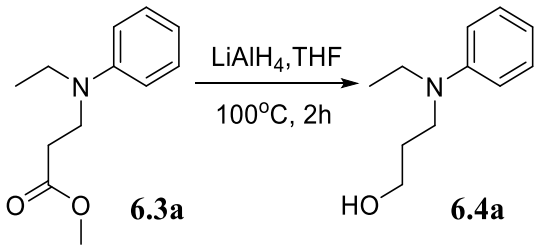

6.3a **6.4a**

Synthesis of *3-(ethyl(phenyl)amino)propan-1-ol* (**6.4a**): The ester **6.3a** (42.5 mmol) was dissolved in 200 ml of THF and the reaction was cooled on ice followed by the slow addition of lithium aluminum hydride (128 mmol). The reaction was taken off ice and allowed to come to room temperature followed by slowly heating to 90°C for 4 hours. After

checking a TLC (30% EA/Hexanes) for completion, ethyl acetate was slowly added to the reaction followed by completely quenching $LiAlH_4$ with 50 ml of ice cold water and sufficient amounts of 2.5M NaOH. The white solid was filtered off and worked up with the ethyl acetate and water. The organic layer was then dried and evaporated off to yield a brown oil. The pure product was then isolated using column chromatography (silica gel, EA and Hexanes 3:10) to yield the final product as a brown oil.

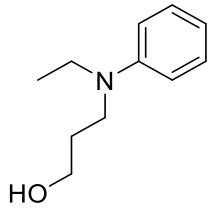

3-(ethyl(phenyl)amino)propan-1-ol (**6.4a**)

^{1}H NMR (500 MHz, $CDCl_3$):

δ 7.20 - 7.27 (m, 2H), 6.77 (d, J = 8 Hz, 2H), 6.71 (t, J = 7 Hz, 1H), 3.76 (t, J = 6 Hz, 2H), 3.34 - 3.44 (m, 4H), 1.80-2.0 (m, 3H), 1.15 (t, J = 7 Hz, 3H)

^{13}C NMR (125 MHz, $CDCl_3$): δ 148.1, 129.3, 116.4, 113.1, 61.2, 47.7, 45.4, 30.2, 12.0

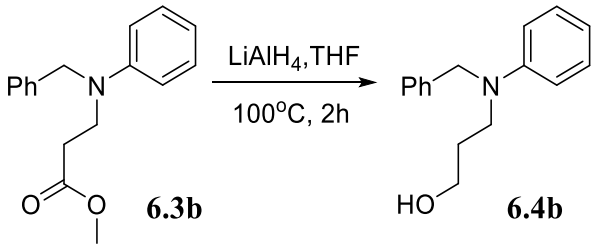

Synthesis of *3-(benzyl(phenyl)amino)propan-1-ol* (**6.4b**): Procedures for the synthesis and isolation of the derivative were replicated from the reduction of the derivative **4a**. Purification of the derivative was done via column chromatography (silica gel, EA and Hexanes 1:5)

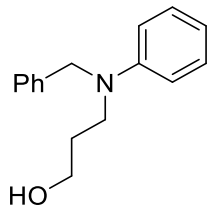

3-(ethyl(phenyl)amino)propan-1-ol (**6.4b**)

^{1}H NMR (500 MHz, $CDCl_3$):

δ 7.17 - 7.34 (m, 7H), 6.76 (d, J = 8 Hz, 2H), 6.70 (t, J = 7 Hz, 1H), 4.56 (s, 2H), 3.74 (t, J = 6 Hz, 2H), 3.51 - 3.58 (m, 2H), 1.86 - 1.96 (m, 2H), 1.44 (br. s., 1H)

^{13}C NMR (125 MHz, $CDCl_3$): δ 148.6, 138.9, 129.2, 128.6, 126.8, 126.7, 116.6, 112.8, 60.8, 54.9, 48.0, 30.1

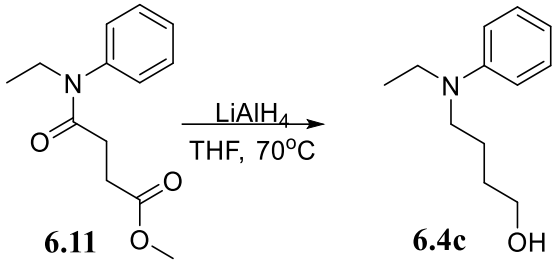

6.11 **6.4c**

Synthesis of *3-(ethyl(phenyl)amino)butan-1-ol* (**6.4c**): Procedures for the synthesis and isolation of the derivative were replicated from the reduction of the derivative **6.4a**. Purification of the derivative was done via column chromatography (silica gel, EA and Hexanes 1:5) to yield the final brown oil product **6.4c**.

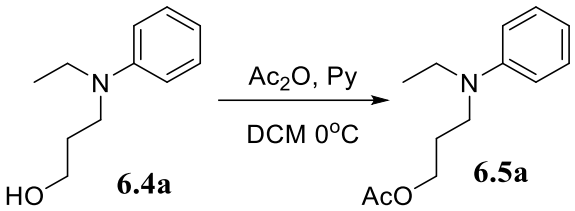

Synthesis of *3-(ethyl(phenyl)amino)propyl acetate* (**6.5a**): The alcohol **6.4a** (15.52 mmol) was dissolved in 30 ml of DCM and pyridine (31.0 mmol) was added to the reaction. The reaction was stirred at room temperature for 10 minutes before addition of acetic anhydride slowly. After one hour, a TLC (20% EA/Hexanes) of the reaction was checked for completion. The reaction was then worked up with water followed by brine solution. The organic layer was dried with magnesium sulfate and evaporated to yield the crude product as dark colored oil.

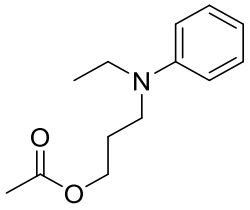

3-(ethyl(phenyl)amino)propyl acetate (**6.5a**)

^{1}H NMR (500 MHz, $CDCl_3$):

δ 7.21 (t, J = 8 Hz, 2H), 6.63 - 6.71 (m, 3H), 4.12 (t, J = 6 Hz, 2H), 3.32 - 3.38 (m, 4H), 2.07 (s, 3H), 1.92 (quin, J = 7 Hz, 2H), 1.14 (t, J = 7 Hz, 3H)

^{13}C NMR (125 MHz, $CDCl_3$):

δ 171.0, 147.7, 129.3, 115.8, 112.1, 62.4, 46.9, 45.2, 26.7, 20.9, 12.2

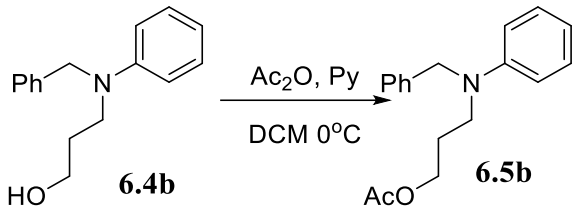

Synthesis of *3-(benzyl(phenyl)amino)propyl acetate* (**6.5b**): The synthesis of derivative **6.5b** was conducted under the exact same conditions as those for **6.5a**. The purification also followed the same workflow for isolation of the product.

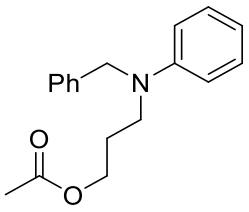

3-(benzyl(phenyl)amino)propyl acetate (**6.5b**)

^{1}H NMR (500 MHz, $CDCl_3$):

δ 7.17 - 7.35 (m, 7H), 6.67 - 6.74 (m, 3H), 4.55 (s, 2H), 4.14 (t, J = 6 Hz, 2H), 3.47 - 3.54 (m, 2H), 2.06 (s, 3H), 1.94 - 2.03 (m, 2H)

^{13}C NMR (125 MHz, $CDCl_3$):

δ 171.0, 148.3, 138.8, 129.3, 128.6, 126.9, 126.6, 116.6, 112.4, 62.3, 54.7, 47.8, 26.4, 21.0

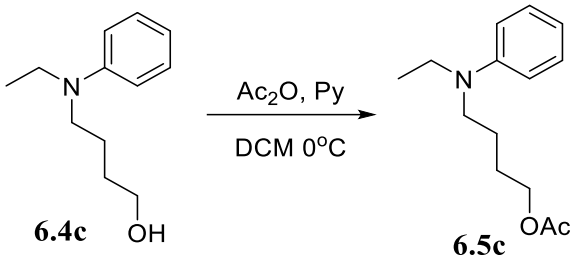

6.4c **6.5c**

Synthesis of *4-(ethyl(phenyl)amino)butyl acetate* (**6.5c**): The synthesis of derivative **6.5c** was conducted under the exact same conditions as those for **6.5a**. The purification also followed the same workflow for isolation of the product.

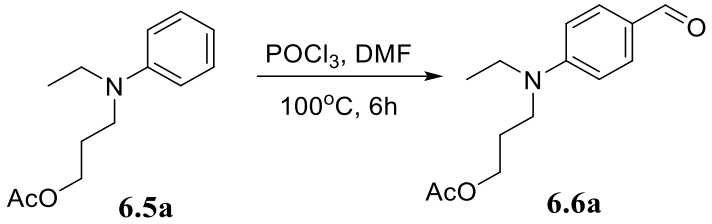

6.5a **6.6a**

Synthesis of *3-(ethyl(4-formylphenyl)amino)propyl acetate* (**6.6a**),: The dialkyl aniline **6.5a** (9.35 mmol) derivative was dissolved in DMF (8.69 ml). The flask was cooled on ice for 10 minutes and then $POCl_3$ (14 mmol) was added to the reaction dropwise. The reaction was warmed to room temperature and a TLC (30% EA/Hexanes) was checked for completion. The reaction was quenched on 50 ml of cooled 0.3 M potassium carbonate solution. The reaction was then worked up with ether. The organic layer was dried with magnesium sulfate followed evaporation of the volatiles to yield the product as a brown oil.

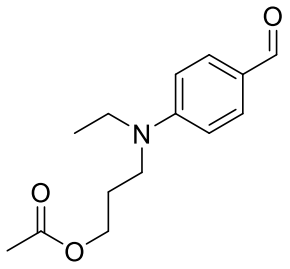

3-(ethyl(4-formylphenyl)amino)propyl acetate (**6.6a**)

^{1}H NMR (500 MHz, $CDCl_3$):

δ 9.69 (s, 1H), 7.69 (d, J = 9 Hz, 2H), 6.67 (d, J = 9 Hz, 2H), 4.09 - 4.14 (m, 2H), 3.40 - 3.48 (m, 4H), 2.07 (s, 3H), 1.95 (quin, J = 6 Hz, 2H), 1.19 (t, J = 7 Hz, 3H)

^{13}C NMR (125 MHz, $CDCl_3$):

δ 190.0, 170.9, 152.2, 132.2, 125.0, 110.8, 61.9, 47.1, 45.3, 26.6, 20.9, 12.2

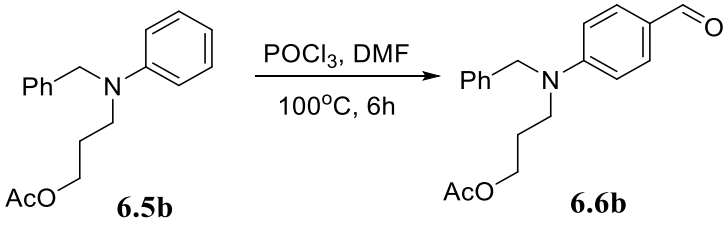

Synthesis of *3-(ethyl(4-formylphenyl)amino)propyl acetate* (**6.6b**): Conversion of **6.5b** into its corresponding aldehyde **6.6b** was conducted under the exact same conditions as **6.6a**.

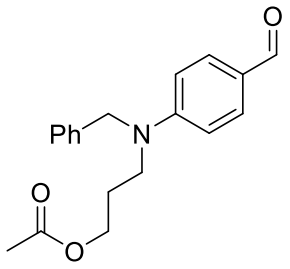

3-(ethyl(4-formylphenyl)amino)propyl acetate (**6.6b**)

^{1}H NMR (500 MHz, $CDCl_3$):

δ 9.74 (s, 1H), 7.71 (d, J = 9 Hz, 2H), 7.24 - 7.38 (m, 3H), 7.18 (d, J = 8 Hz, 2H), 6.75 (d, J = 9 Hz, 2H), 4.66 (s, 2H), 4.16 (t, J = 6 Hz, 2H), 3.56 - 3.65 (m, 2H), 2.08 (s, 3H), 2.01 - 2.07 (m, 2H)

^{13}C NMR (125 MHz, $CDCl_3$):

δ 190.1, 170.9, 152.9, 137.0, 132.2, 128.9, 127.4, 126.2, 125.8, 111.4, 61.9, 54.3, 48.1, 26.4, 20.9

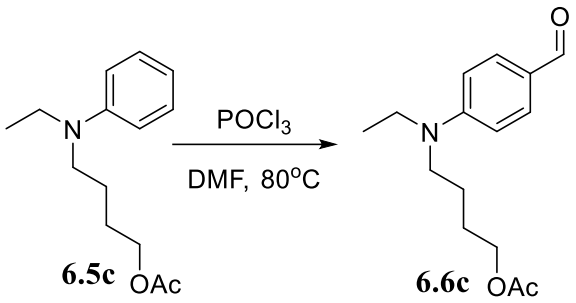

Synthesis of *4-(ethyl(4-formylphenyl)amino)butyl acetate* (**6.6c**): Conversion of **6.5c** into its corresponding aldehyde **6.6c** was conducted under the exact same conditions as **6.6a**.

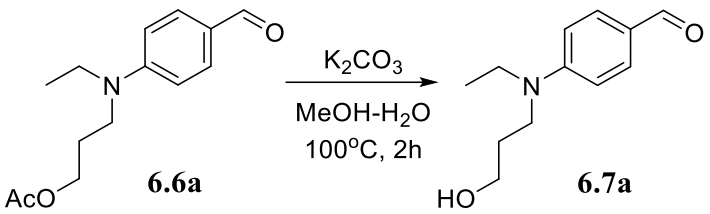

Synthesis of *4-(ethyl(3-hydroxypropyl)amino)benzaldehyde* (**6.7a**): Deprotection of the acetate **6.7a** was conducted by dissolving **6.6a** (38 mmol) in ethanol (53.2 ml). Potassium carbonate (114 mmol) dissolved in 5 ml of water was added to the reaction. The reaction was slightly heated to 70°C and allowed to react for three hours. A TLC (40% EA/Hexanes) was checked to ensure the reaction had gone to completion. The reaction was poured over 6 ml of 6M HCl on ice followed by workup with ethyl acetate. The organic layer was dried with magnesium sulfate and the solvent was evaporated. The resulting oily product was purified using column chromatography (silica gel, EA and Hexanes 3:1) to yield the final pure product as a cream colored oil.

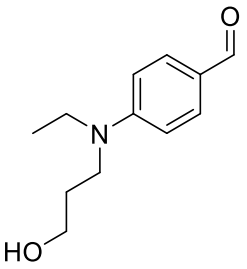

4-(ethyl(3-hydroxypropyl)amino)benzaldehyde (**6.7a**)

^{1}H NMR (500 MHz, $CDCl_3$):

δ 9.71 (s, 1H), 7.71 (d, J = 9 Hz, 2H), 6.73 (d, J = 9 Hz, 2H), 3.76 (t, J = 6 Hz, 2H), 3.44 - 3.56 (m, 4H), 1.84 - 1.94 (m, 2H), 1.54 (br., 1H), 1.22 (t, J = 7 Hz, 3H)

^{13}C NMR (125 MHz, $CDCl_3$):

δ 190.1, 152.5, 132.3, 124.8, 110.8, 60.1, 47.0, 45.2, 30.2, 12.1

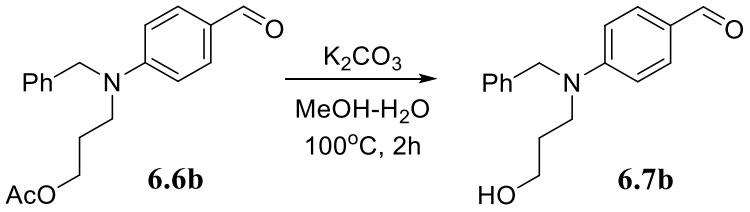

Synthesis of *4-(benzyl(3-hydroxypropyl)amino)benzaldehyde* (**6.7b**): The deprotection of the acetate group on **6.6b** to form the corresponding alcohol derivative **6.7b** was conducted under the exact same conditions for the conversion of **6.7a**.

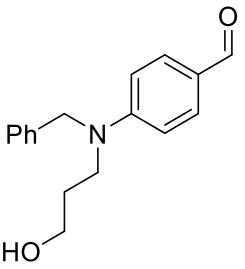

4-(benzyl(3-hydroxypropyl)amino)benzaldehyde (**6.7b**)

^{1}H NMR (500 MHz, $CDCl_3$):

δ 9.72 (s, 1H), 7.70 (d, J = 9 Hz, 2H), 7.18 - 7.33 (m, 5H), 6.77 (d, J = 9 Hz, 2H), 4.69 (s, 2H), 3.76 (t, J = 6 Hz, 2H), 3.66 - 3.70 (m, 2H), 1.92 - 1.99 (m, 2H)

^{13}C NMR (125 MHz, $CDCl_3$):

δ 190.2, 153.2, 137.2, 132.2, 128.8, 127.3, 126.3, 125.5, 111.4, 60.1, 54.2, 48.0, 30.0.

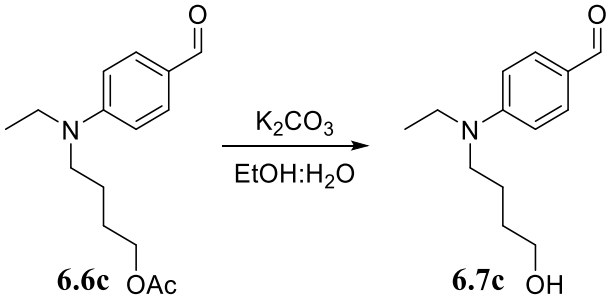

Synthesis of *4-(ethyl(4-hydroxybutyl)amino)benzaldehyde* (**6.7c**): The deprotection of the acetate group on **6.6c** to form the corresponding alcohol derivative **6.7c** was conducted under the exact same conditions for the conversion of **6.7a**.

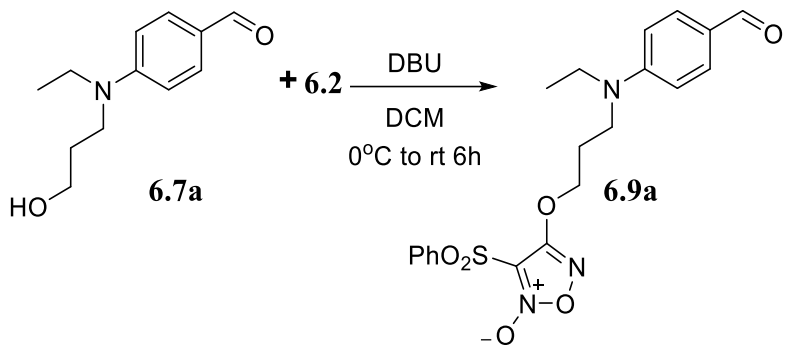

Synthesis of *4-(3-(ethyl(4-formylphenyl)amino)propoxy)-3-(phenylsulfonyl)-1,2,5-oxadiazole 2-oxide* (**6.9a**): Coupling of the furoxan **6.2** with the corresponding alcohol (**6.7a)** was performed by dissolving **6.7a** (6.78 mmol) in 30 ml of DCM. DBU (13.56 mmol) was added to the reaction. The reaction was stirred at room temperature for 20 minutes before cooling on ice. The furoxan **6.2** (13.56 mmol) dissolved in 30 ml of DCM was added slowly over a 30-minute period. An hour later, the reaction was monitored using TLC (30% EA/Hex) for completion. Upon completion the reaction was initially worked up with water followed by brine. The organic layer was dried with magnesium sulfate and the solvent was evaporated. The resulting brown oil was used without any further purification.

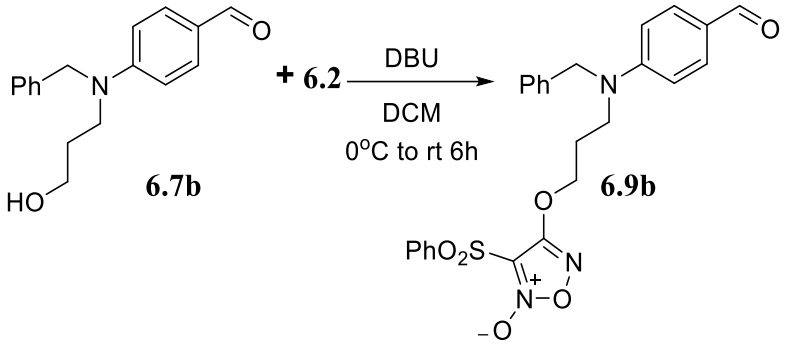

Synthesis of *4-(3-(benzyl(4-formylphenyl)amino)propoxy)-3-(phenylsulfonyl)-1,2,5-oxadiazole 2-oxide* (**6.9b**): The coupling of the furoxan (**6.2**) to the derivative **6.7b** was conducted under the exact same conditions as **6.9a** and purified under similar conditions to yield **6.9b**.

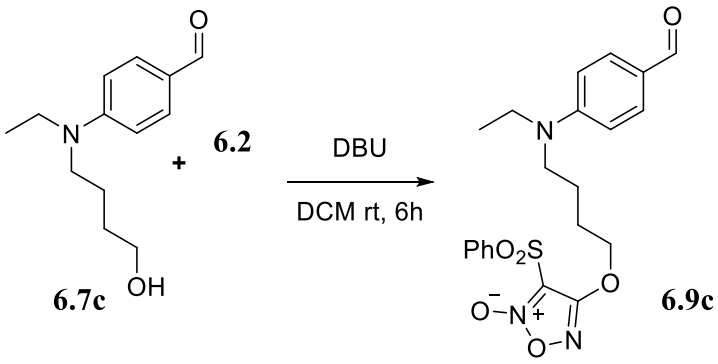

Synthesis of *4-(4-(ethyl(4-formylphenyl)amino)butoxy)-3-(phenylsulfonyl)-1,2,5-oxadiazole 2-oxide* (**6.9c**): The coupling of the furoxan (**6.2**) to the derivative **6.7c** was conducted under the exact same conditions as **6.9a** and purified under similar conditions to yield **6.9c**.

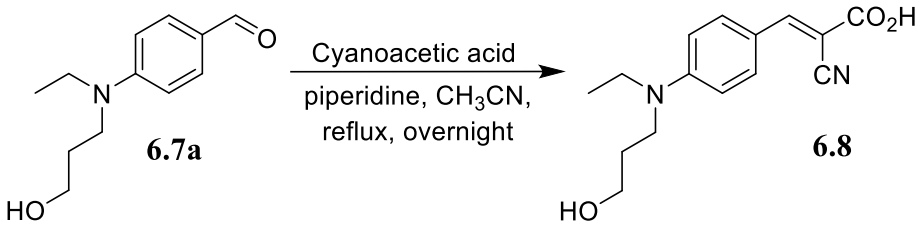

Synthesis of *(E)-2-cyano-3-(4-(ethyl(3-hydroxypropyl)amino)phenyl)acrylic acid* (**6.8**) : The corresponding aldehyde **6.7a** (3.14 mmol) was dissolved in 15 ml of acetonitrile and piperidine (6.29 mmol) was added to the reaction. The solution was stirred for 10 minutes at room temperature followed by the addition of cyanoacetic acid (4.71 mmol). The reaction was then heated to reflux for 18 hours. A TLC (10% MeOH/EA) was checked to confirm completion of the reaction. The product was then poured over ice and quenched with 1 ml of 6M HCl. The reaction was worked up with ethyl acetate and brine. The organic layer was dried with magnesium sulfate and volatiles were concentrated. The resulting yellow oil was then purified using column chromatography (silica gel, EA) to yield a pale yellow solid (Yield: 67%).

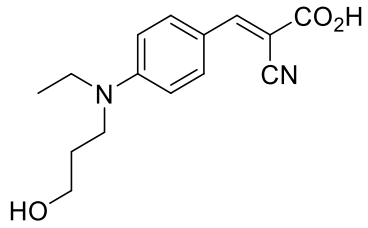

(E)-2-cyano-3-(4-(ethyl(3-hydroxypropyl)amino)phenyl)acrylic acid (**6.8**)

^{1}H NMR (500 MHz, DMSO-d_6):

δ 7.93 (s, 1H), 7.80 (d, J = 9.3 Hz, 2H), 6.64 (d, J = 8.8 Hz, 2H), 3.59 (t, J = 5.9 Hz, 2H), 3.34 - 3.47 (m, 4H), 1.72 - 1.81 (m, 2H), 1.12 (t, J = 7.1 Hz, 3H)

^{13}C NMR (125 MHz, DMSO-d_6):

δ 166.0, 154.0, 151.7, 134.1, 118.7, 118.0, 111.3, 93.9, 59.3, 47.1, 45.1, 30.2, 12.2.

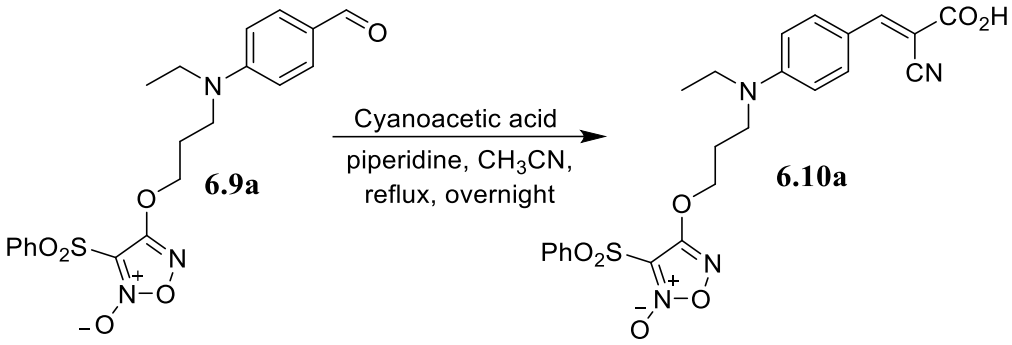

6.9a

6.10a

Synthesis of *(E)-4-(3-((4-(2-carboxy-2-cyanovinyl)phenyl)(ethyl)amino)propoxy)-3-(phenylsulfo nyl)-1,2,5-oxadiazole 2-oxide* (**6.10a**) : The aldehyde **6.9a** was reacted with cyanoacetic acid using Knoevenagel condensation to yield **6.10a** under the same conditions as described previously as in **6.8** to yield a bright orange solid (Yield: 56%).

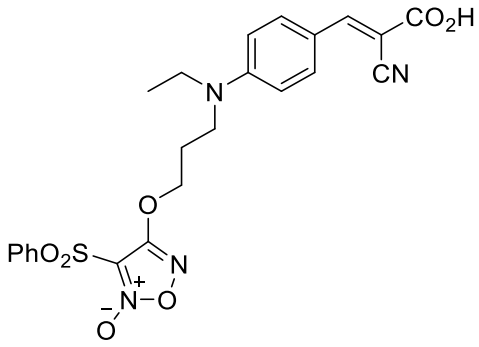

E)-4-(3-((4-(2-carboxy-2-cyanovinyl)phenyl)(ethyl)amino)propoxy)-3-(phenylsulfonyl)-1,2,5-oxadiazole 2-oxide (**6.10a**)

1H NMR (500 MHz, DMSO-d6):

δ 8.02 - 8.05 (m, 3H), 7.73 - 7.93 (m, 5H), 6.86 (d, *J* = 10 Hz, 2H), 4.46 (t, *J* = 5 Hz, 2H), 3.48-3.57 (m, 4H), 2.05 - 2.09 (m, 2H), 1.14 (t, *J* = 5 Hz, 3H).

13C NMR (126 MHz, DMSO-d6):

δ 165.3, 159.3, 154.1, 151.9, 137.7, 136.6, 134.3, 130.5, 128.7, 118.8, 118.4, 112.0, 111.0, 93.8, 69.6, 46.4, 45.0, 26.6, 12.6

Elemental Analysis C, H, N, O

Anal. Calcd for $C_{23}H_{21}N_4O_7S\ Na^+$ (520.49): C 53.08, H 4.07, N 10.76.

Found: C 53.55, H 4.45, N 10.60.

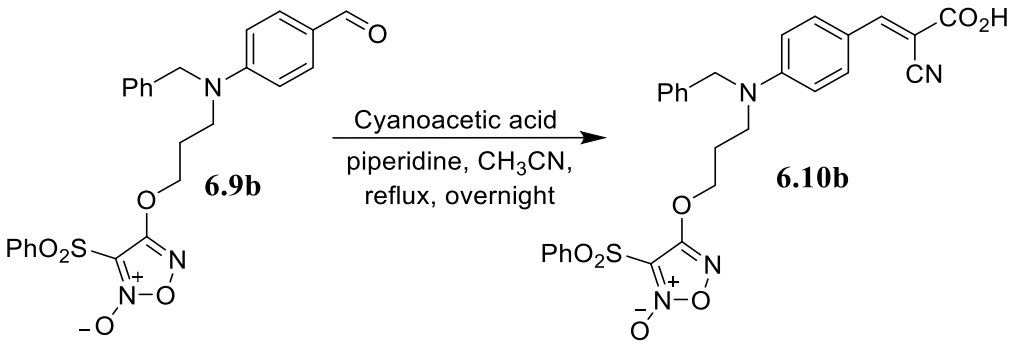

Synthesis of *(E)-4-(3-((4-(2-carboxy-2-cyanovinyl)phenyl)(ethyl)amino)propoxy)-3-(phenylsulfonyl)-1,2,5-oxadiazole 2-oxide* (**6.9b**): The aldehyde **6.9b** was reacted with cyanoacetic acid using Knoevenagel condensation to yield **6.10b** under the same conditions as described previously as in **6.8** to yield a bright orange solid (Yield: 53%).

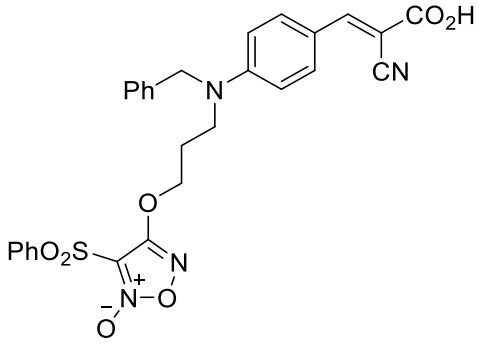

(E)-4-(3-((4-(2-carboxy-2-cyanovinyl)phenyl)(benzyl)amino)propoxy)-3-(phenylsulfonyl)-1,2,5-oxadiazole 2-oxide (**6.9b)**

1H NMR (500 MHz, DMSO-d^6+$CDCl_3$):

δ 7.89 (s, 1H), 7.82 (d, J = 5 Hz, 2H), 7.70 (d, J = 5 Hz, 2H), 7.58 (t, J = 8, 1H), 7.41 (t, J = 8 Hz, 2H), 7.02 - 7.17 (m, 5H), 6.63 (d, J = 9 Hz, 2H), 4.52 (s, 2H), 4.30 (t, J = 4.5 2H), 3.58-3.59 (m, 2H), 2.05-2.06 (m, 2H)

13C NMR (126 MHz, DMSO-d^6+$CDCl_3$):

δ 166.5, 158.5, 153.3, 151.4, 137.7, 136.9, 135.8, 133.6, 129.7, 128.8, 128.2, 127.3, 126.3, 120.3, 118.1, 111.8, 110.3, 97.5, 68.6, 54.3, 47.4, 40.4, 40.3, 26.3.

Elemental Analysis C, H, N, O

Anal. Calcd for $C_{28}H_{24}N_4O_7S\ H_2O$ (560.59): C 58.12, H 4.43, N 9.68.

Found: C 58.88, H 4.44, N 10.06.

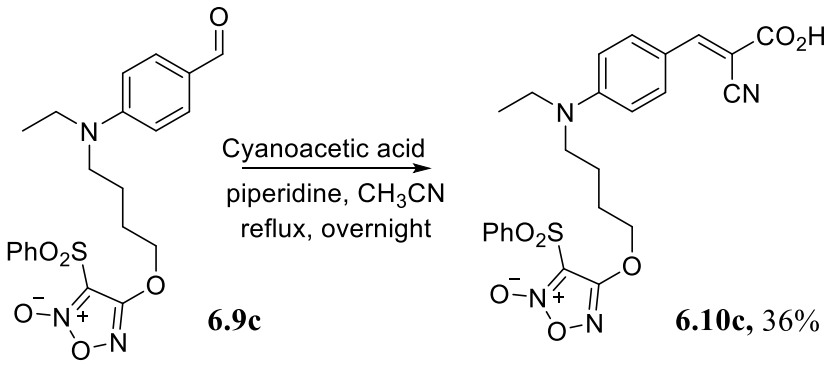

6.9c **6.10c,** 36%

Synthesis of *(E)-4-(4-((4-(2-carboxy-2-cyanovinyl)phenyl)(ethyl)amino)butoxy)-3-(phenylsulfonyl)-1,2,5-oxadiazole 2-oxide* (**6.9c**): The aldehyde **6.9c** was reacted with cyanoacetic acid using Knoevenagel condensation to yield **6.10c** under the same conditions as described previously as in **6.8** to yield a bright orange solid (Yield: 36%).

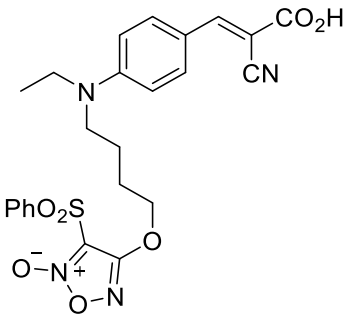

((E)-4-(4-((4-(2-carboxy-2-cyanovinyl)phenyl)(ethyl)amino)butoxy)-3-(phenylsulfonyl)-1,2,5-oxadiazole 2-oxide **6.9c**:

1H NMR (500 MHz, DMSO-d6):

δ 7.90 - 7.93 (m, 3H), 7.81 (d, J = 10 Hz, 2H), 7.68 (t, J = 7 Hz, 1H), 7.51 (t, J = 7 Hz, 2H), 6.63 (d, J = 9 Hz, 2H), 4.40 (t, J = 7 Hz, 2H), 3.40 - 3.45 (m, 4H), 1.73 - 1.88 (m, 4H), 1.16 (t, J = 7 Hz, 3H)

13C NMR (126 MHz, DMSO-d6):

δ 165.7, 158.8, 153.9, 151.5, 137.8, 135.8, 134.1, 129.8, 128.3, 119.0, 117.9, 111.3, 110.4, 94.4, 71.2, 49.8, 45.2, 25.9, 23.8, 12.3

Elemental Analysis C, H, N, O

Anal. Calcd for $C_{24}H_{24}N_4O_7S$ (512.54): C 56.24, H 4.72, N 10.93.

Found: C 56.20, H 4.80, N 10.75.

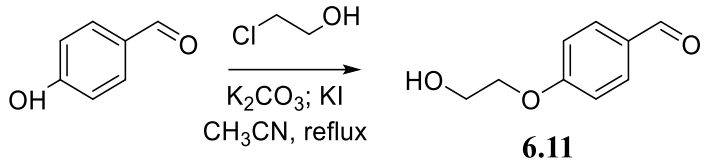

6.11

Synthesis of *4-(2-hydroxyethoxy)benzaldehyde* (**6.11)** 4-hydroxybenaldehyde (81.8 mmol) was dissolved in 80 ml of EtOH (1M). Potassium carbonate (163 mmol) was added to the reaction flask followed by the addition of 2-chloroethanol (327 mmol). The reaction mixture was refluxed for 10 hours, followed by filteration of potassium carbonate, and subsequent evaporation of ethanol. The remaining contents were extracted 3x with 100 ml of ethyl acetate in water and washed with 100 ml of 0.01M NaOH solution. The organic layer was separated and dried on anhydrous $MgSO_4$ and the organic layer was evaporated using a rotatory evaporator. The resulting white solid was used for the reaction without further purification.

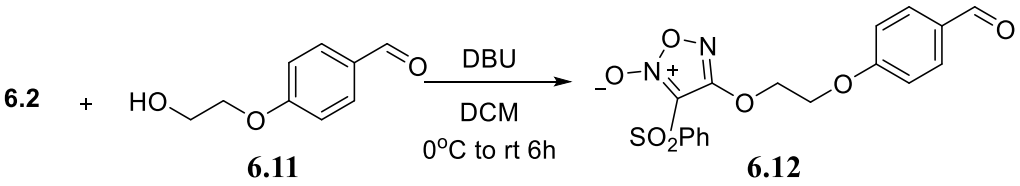

Synthesis of *4-(2-(4-formylphenoxy)ethoxy)-3-(phenylsulfonyl)-1,2,5-oxadiazole 2-oxide* (**6.12**): Coupling of the furoxan **6.2** with the alcohol (**6.11)** was conducted by dissolving **6.11** (6.78 mmol) in 30 ml of DCM followed by the addition of DBU (13.56 mmol). The reaction was stirred at room temperature for 20 minutes before cooling on ice. The furoxan **2** (13.56 mmol) dissolved in 30 ml of DCM was added slowly to the above mixture over a 30-minute period. An hour later the reaction was checked via TLC (20% EA/Hexanes) for completion. Upon completion the reaction was initially worked up with water followed by

brine. The organic layer was dried with magnesium sulfate, filtered and then evaporated to obtain the product as brown colored oil. This crude product was used without any further purification.

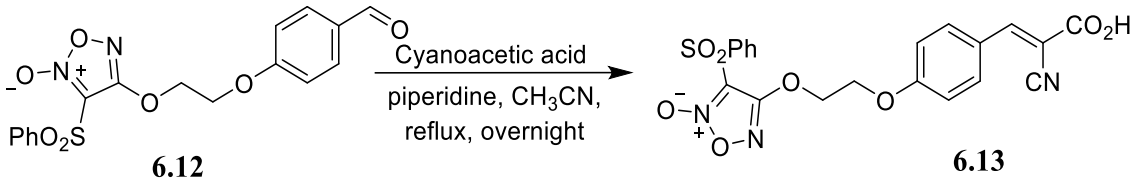

6.12 **6.13**

Synthesis of *(E)-4-(2-(4-(2-carboxy-2-cyanovinyl)phenoxy)ethoxy)-3-(phenylsulfonyl)-1,2,5-oxadiazole 2-oxide* (**6.13**): The corresponding aldehyde **6.13** (3.14 mmol) was dissolved in 30 ml of acetonitrile and piperidine (6.29 mmol) was added to the reaction. The two reagents were stirred for 10 minutes are room temperature before cyanoacetic acid (4.71 mmol) was added. The reaction was then heated to reflux for 18 hours. A TLC (10% MeOH/EA) was checked to confirm completion of the reaction. The product was then poured over ice and quenched with 1 ml of 6 M HCl. The reaction was worked up with ethyl acetate. The organic layer was dried with magnesium sulfate followed by filtration and evaporation. The resulting white oil was then purified using column chromatography (silica gel, EA) to yield the product as a cream colored solid (Yield: 83%).

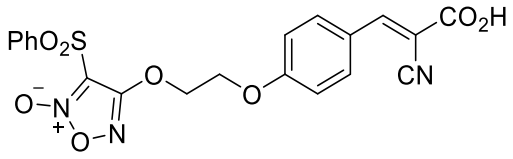

(E)-4-(2-(4-(2-carboxy-2-cyanovinyl)phenoxy)ethoxy)-3-(phenylsulfonyl)-1,2,5-oxadiazole 2-oxide (**6.13**):

1H NMR (500 MHz, DMSO-d6)

δ 8.28 (s, 1H), 8.09 (d, J = 8 Hz, 2H), 7.96 (d, J = 7 Hz, 2H), 7.82 (t, J = 7 Hz, 1H), 7.63 - 7.66 (m, 2H), 7.20 (d, J = 8 Hz, 2H), 4.76 (m, 2H), 4.49 (m, 2H).

13C NMR (DMSO-d6 ,126MHz):

δ 164.2, 162.4, 159.2, 154.3, 137.6, 136.6, 133.8, 130.4, 128.7, 125.0, 117.1, 115.9, 111.0, 100.7, 70.1, 66.3

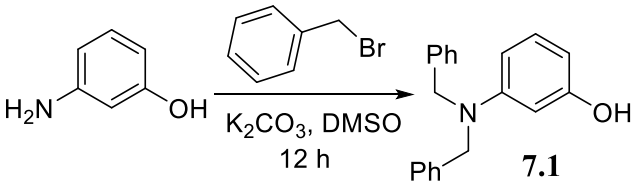

Synthesis of *3-(dibenzylamino)phenol* (**7.1**): Commercially available 3-aminophenol (5 g, 45.8 mmol) was dissolved in 25 ml of DMSO. The reaction was slightly cooled on ice followed by addition of benzyl bromide (10.90 ml, 92 mmol) over a 2-hour period. Finally, K_2CO_3 (15.83 g, 115 mmol) was added in portions. The reaction was stirred for 12 hours at room temperature. A TLC in 30% EA/Hexanes was checked to ensure complete formation of dialkylated product. The reaction mixture was poured over ice water and 3 M HCl. The resulting dark brown precipitate was then filtered and washed with hexanes to give the final product **5** with 85% yield.

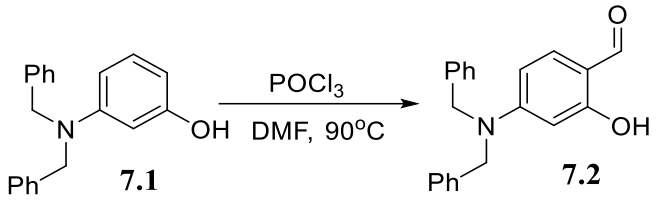

Synthesis of *4-(dibenzylamino)-2-hydroxybenzaldehyde* (**7.2)** The aldehyde was synthesized by dissolving 3-(dibenzylamino)phenol (**7.1)** (13.25 g, 45.8 mmol) in 125 ml of DMF. The contents were cooled on ice followed by the slow addition of $POCl_3$ (6.40 ml, 68.7 mmol) to the mixture. The reaction was then allowed to warm to room temperature and react for additional one hour. A TLC (10% EA/Hexanes) was monitored to ensure the complete conversion to aldehyde. The reaction mixture was poured over aqueous saturated K_2CO_3. The precipitate was filtered and washed twice with hexanes to yield 72% of the crude **7.1** as a yellow solid.

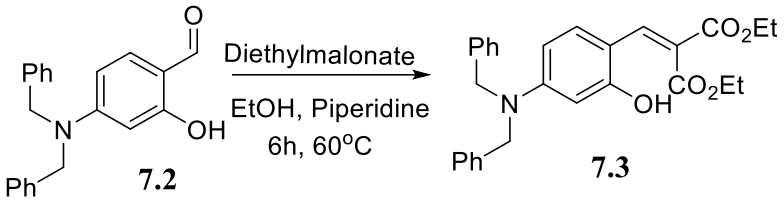

Synthesis of *ethyl (Z)-3-(4-(dibenzylamino)-2-hydroxyphenyl)-2-ethoxyacrylate* **(7.3)** Knoevenagel condensation was conducted by dissolving aldehyde **(7.2)** (5 g, 15.75 mmol) in 50 ml of EtOH followed by diethyl malonate (3.78 g, 3.60 mmol). The reaction was cooled and piperidine (3.12 ml, 31.5 mmol) was added. This was then heated to 90°C for 12 hours. Upon completion of the reaction the contents were quenched with 15 ml of 3M HCl and worked up with 100 ml of water and ether. The organic layer was dried with

$MgSO_4$ and the volatiles were concentrated to give **7.3** as a clear yellow oil which was used for the next reaction without any further purification.

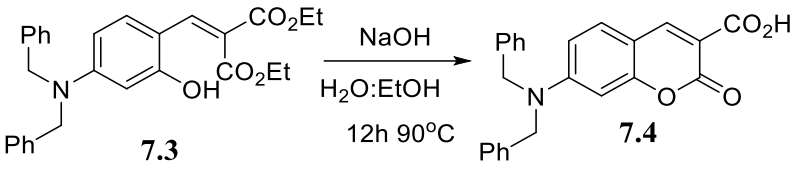

Synthesis of *7-(dibenzylamino)-2-oxo-2H-chromene-3-carboxylic acid* **(7.4)** The condensation product **7.3** (5 g, 10.9 mmol) was dissolved in 100 ml of ethanol followed by addition of NaOH (2.18 g, 54.4 mmol) dissolved in 5 ml of water slowly. The reaction was then refluxed for 12 hours. Upon completion of the reaction the contents were quenched with 5 ml of 12 M HCl on ice. The resulting orange precipitate was then filtered and washed with water and hexanes. The product was purified via column chromatography (silica gel, EA and Hexanes 3:5) to give pure **6.17** as a yellow solid with a yield of 63%.

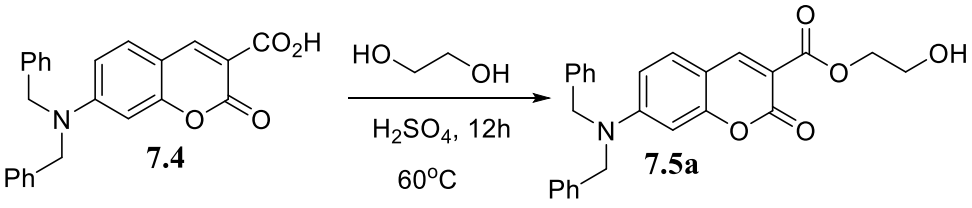

Synthesis of *2-hydroxyethyl 7-(dibenzylamino)-2-oxo-2H-chromene-3-carboxylate* (**7.5a**) The coumarin acid **7.4** (5 g, 12.97 mmol) was dissolved in 200 ml of ethylene glycol followed by sulphuric acid (0.346 ml, 6.49 mmol). The reaction was refluxed for 12 hours. Upon completion of the reaction the contents were worked up with brine and DCM twice. The organic phase was collected and dried using $MgSO_4$ and concentrated. After column

chromatography (silica gel EA and hexanes 1:1) the final pure product (**7.5a**) as a yellow paste was obtained with a yield of 32%.

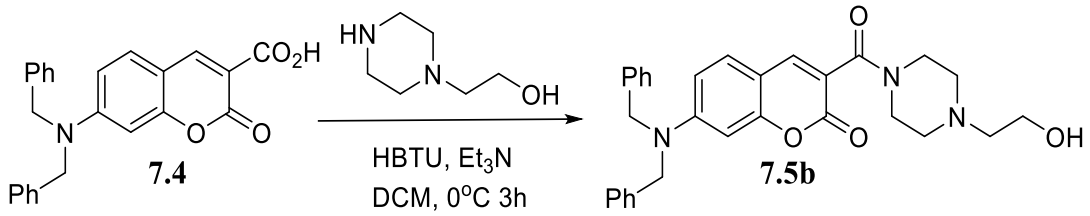

Synthesis of *7-(dibenzylamino)-3-(4-(2-hydroxyethyl)piperazine-1-carbonyl)-2H-chromen-2-one* **(7.5b)** The coumarin carboxylic acid **7.4** (1.5 g, 3.89 mmol) was dissolved in a 35 ml DCM and THF mixture with a ratio of 5:3. After complete dissolution of **7.4** HBTU (2.96 g, 7.78 mmol) was added and allowed to react for 10 min at room temperature. The reaction mixture was placed on ice and a solution of ethanolpiperazine (0.716 ml, 5.84 mmol) and triethylamine (2.17 ml, 15.57 mmol) in 10 ml of THF was added dropwise. The reaction was then allowed to warm to room temperature followed by catalytic addition of BOP-Cl. After reacting for 1 hour a TLC (50% EA/Hexanes) was checked for completion. The THF was evaporated off and the brow oil was extracted with brine and ethyl acetate. The resulting product was washed with small amounts of ether twice followed by recrystallization in ether to yield a yellow solid.

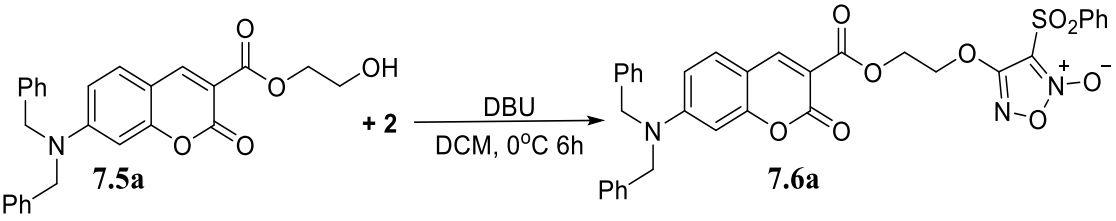

Synthesis of *4-(2-((7-(dibenzylamino)-2-oxo-2H-chromene-3-carbonyl)oxy)ethoxy)-3-(phenylsulfonyl)-1,2,5-oxadiazole 2-oxide* **(7.6a)** and The coupling of the furoxan **6.2**

with the free hydroxy group of **7.5a** was completed by dissolving **7.5a** (1 g, 2 mmol) in 32 ml of DCM followed by the addition of DBU (0.606 ml, 4 mmol). The reaction was cooled and furoxan (**6.2**) (0.810 g, 2.2 mmol) dissolved in 24 ml of DCM was added drop wise. The reaction was removed from ice and allowed to warm to room temperature and stirred for additional 1 hour. A TLC (30% EA/Hexanes) was checked for completion. The product was poured over 3 M HCl in ice and worked up. The organic layer was dried using $MgSO_4$ and concentrated. The crude product was then purified using column chromatography (triethylamine quenched silica gel, EA and Hexane 1:5). The resulting yellow solid was isolated with a yield of 56%.

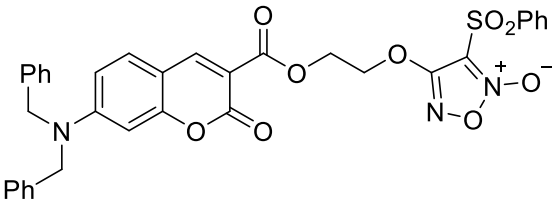

4-(2-((7-(dibenzylamino)-2-oxo-2H-chromene-3-carbonyl)oxy)ethoxy)-3-(phenylsulfonyl)-1,2,5-oxadiazole 2-oxide **(7.6a)**

1H NMR (500 MHz, CDCL3-d):

δ 8.32 (s, 1H), 7.89 (d, J= 7 Hz, 2H), 7.39-7.51 (m, 3H), 7.04-7.22 (m, 11H), 6.56 (d, *J*=10, 1H), 6.42 (s, 1H), 4.61-4.53 (m, 8H).

13C NMR (126 MHz, CDCL3-d):

δ 163.4, 158.8, 158.2, 157.7, 154.7, 149.8, 138.0, 136.0, 135.6, 131.4, 129.7, 129.2, 129.1 128.6, 127.7, 126.3, 110.6, 110.5, 109.1, 108.7, 98.2, 68.9, 61.7, 54.7

Elemental Analysis C, H, N, O

Anal. Calcd for $C_{34}H_{27}N_3O_9S$ (653.66): C 62.47, H 4.16, N 6.43.

Found: C 60.05, H 4.17, N 6.20.

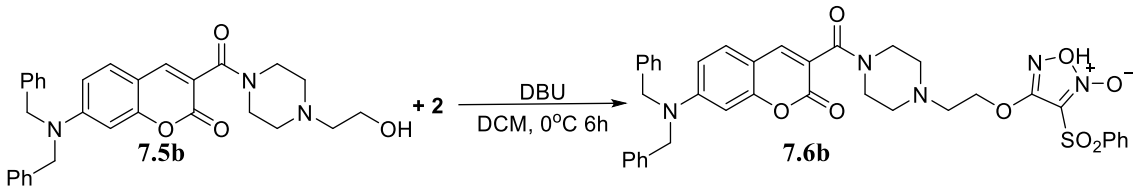

Synthesis of *3-(4-(3-((5-(l1-oxidaneyl)-4-(phenylsulfonyl)-1,2,5l4-oxadiazol-3-yl)oxy)propyl)piperazine-1-carbonyl)-7-(dibenzylamino)-2H-chromen-2-one* (**7.6b**): Coupling of the furoxan **2** to the amide **7.6b** was conducted in similar conditions as formation of **7.6ba**. The resulting yellow solid was isolated with a yield of 43%.

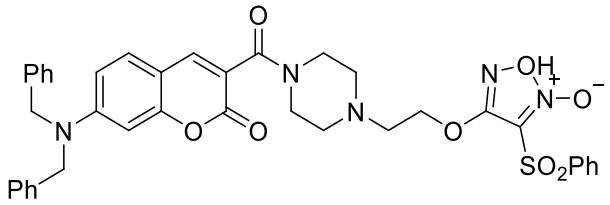

3-(4-(3-((5-(l1-oxidaneyl)-4-(phenylsulfonyl)-1,2,5l4-oxadiazol-3-yl)oxy)propyl)piperazine-1-carbonyl)-7-(dibenzylamino)-2H-chromen-2-one (**7.6b**):

1H NMR (500 MHz, CDCL3-d):

δ 8.05 (d, *J* = 10 Hz, 2H), 7.83 (s, 1H), 7.75 (t, *J*=7 Hz, 1H), 7.63 (t, *J*=7.5 Hz, 2H), 7.37 - 7.21-7.37 (m, 11H), 6.70 (d, *J* = 10 Hz, 1H), 6.59 (s, 1H), 4.76 (s, 4H), 4.55 (t, *J* = 5 Hz, 2H), 3.75 (br., 2H), 3.39 (br., 2H), 2.90 (t, *J* = 5 Hz, 2H), 2.64 (br., 4H)

13C NMR (126 MHz, CDCL3-d):

δ 164.6, 158.9, 156.8, 153.1, 144.6, 138.1, 136.5, 135.7, 129.8, 129.7, 129.0, 128.5, 127.6, 126.3, 117.8, 110.5, 110.2, 108.9, 98.6, 69.2, 56.0, 54.6, 53.4, 53.0, 47.3, 42.2.

CHAPTER 10: REFERENCES

1. Upreti, M. & Jyoti, A. Tumor microenvironment and nanotherapeutics. *Transl. Cancer Res.* **2**, 309–319 (2013).
2. Nelson, C. M. & Bissell, M. J. NIH Public Access. *Annu Rev Cell Dev Biol.* **22**, 287–309 (2006).
3. Fu, Y. *et al.* The reverse Warburg effect is likely to be an Achilles' heel of cancer that can be exploited for cancer therapy. *Oncotarget* **8**, 57813–57825 (2017).
4. Pacini, N. & Borziani, F. Cancer stem cell theory and the warburg effect, two sides of the same Coin? *Int. J. Mol. Sci.* **15**, 8893–8930 (2014).
5. Hanahan, D. & Weinberg, R. A. Hallmarks of Cancer: The Next Generation. *Cell* **144**, 646–674 (2011).
6. Pavlova, N. N. & Thompson, C. B. The Emerging Hallmarks of Cancer Metabolism. *Cell Metab.* **23**, 27–47 (2016).
7. Sancho, P., Barneda, D. & Heeschen, C. Hallmarks of cancer stem cell metabolism. *Br. J. Cancer* **114**, 1305–1312 (2016).
8. Kim, H. K. *et al.* Current and upcoming mitochondrial targets for cancer therapy. *Semin. Cancer Biol.* (2017). doi:10.1016/j.semcancer.2017.06.006
9. Sousa, M. I. *et al.* Mitochondrial Mechanisms of Metabolic Reprogramming in Proliferating Cells. *Curr. Med. Chem.* **22**, 2493–2504 (2015).
10. Annibaldi, A. & Widmann, C. Glucose metabolism in cancer cells. *Curr. Opin. Clin. Nutr. Metab. Care* **13**, 466–470 (2010).
11. Dang, C. V. Links between metabolism and cancer. *Genes Dev.* **26**, 877–890

(2012).

12. Ganapathy-Kanniappan, S. & Geschwind, J. H. Tumor glycolysis as a target for cancer therapy: progress and prospects. *Mol. Cancer* **12**, 152 (2013).

13. Zheng, J. Energy metabolism of cancer: Glycolysis versus oxidative phosphorylation (review). *Oncology Letters* **4**, 1151–1157 (2012).

14. Jose, C., Bellance, N. & Rossignol, R. Choosing between glycolysis and oxidative phosphorylation: A tumor's dilemma? *Biochim. Biophys. Acta - Bioenerg.* **1807**, 552–561 (2011).

15. GUPPY, M., GREINER, E. & BRAND, K. The role of the Crabtree effect and an endogenous fuel in the energy metabolism of resting and proliferating thymocytes. *Eur. J. Biochem.* **212**, 95–99 (1993).

16. Shibuya, K. *et al.* Targeting the facilitative glucose transporter GLUT1 inhibits the self-renewal and tumor-initiating capacity of cancer stem cells. *Oncotarget* **6**, 651–661 (2015).

17. Sato, M. *et al.* Spheroid cancer stem cells display reprogrammed metabolism and obtain energy by actively running the tricarboxylic acid (TCA) cycle. *Oncotarget* **7**, 33297–33305 (2016).

18. Payen, V. L. *et al.* Monocarboxylate transporter MCT1 promotes tumor metastasis independently of its activity as a lactate transporter. *Cancer Res.* **77**, 5591–5601 (2017).

19. Peppicelli, S., Bianchini, F. & Calorini, L. Dynamic scenario of metabolic pathway adaptation in tumors and therapeutic approach. *Oncoscience* **2**, 225–32 (2015).

20. Payen, V. L. *et al. Monocarboxylate transporter MCT1 promotes tumor metastasis independently of its activity as a lactate transporter*. *Cancer Research* **77**, (2017).

21. Ganapathy-Kanniappan, S. & Geschwind, J.-F. H. Tumor glycolysis as a target for cancer therapy: progress and prospects. *Mol. Cancer* **12**, 152 (2013).

22. Ganapathy-Kanniappan, S. Taming Tumor Glycolysis and Potential Implications for Immunotherapy. *Front. Oncol.* **7**, 36 (2017).

23. Pinheiro, C. *et al.* Role of monocarboxylate transporters in human cancers: state of the art. *J. Bioenerg. Biomembr.* **44**, 127–39 (2012).

24. Lee, N., Kim, D., Kim, and D. & Kim, D. Cancer Metabolism: Fueling More than Just Growth. *Mol. Cells* **39**, 847–854 (2016).

25. Hong, C. S. *et al.* MCT1 Modulates Cancer Cell Pyruvate Export and Growth of Tumors that Co-express MCT1 and MCT4. *Cell Rep.* **14**, 1590–1601 (2016).

26. Gurrapu, S. *et al.* Monocarboxylate transporter 1 inhibitors as potential anticancer agents. *ACS Med. Chem. Lett.* **6**, (2015).

27. Halestrap, A. P., Editor, G. & Hediger, M. A. Molecular Aspects of Medicine The SLC16 gene family – Structure , role and regulation in health and disease q. *Mol. Aspects Med.* **34**, 337–349 (2013).

28. Fiaschi, T. *et al.* Reciprocal metabolic reprogramming through lactate shuttle coordinately influences tumor-stroma interplay. *Cancer Res.* **72**, 5130–5140 (2012).

29. Halestrap, A. P. The monocarboxylate transporter family-Structure and functional characterization. *IUBMB Life* **64**, 1–9 (2012).

30. Jonnalagadda, S., Jonnalagadda, S. K., Ronayne, C. T., Grady, L. & Drewes, L. R. Novel N , N-dialkyl cyanocinnamic acids as monocarboxylate transporter 1 and 4 inhibitors. **10**, 2355–2368 (2019).

31. Kapoor, K. *et al.* Mechanism of inhibition of human glucose transporter GLUT1 is conserved between cytochalasin B and phenylalanine amides. *Proc. Natl. Acad. Sci.* **113**, 4711–4716 (2016).

32. Polański, R. *et al.* Activity of the monocarboxylate transporter 1 inhibitor AZD3965 in small cell lung cancer. *Clin. Cancer Res.* **20**, 926–37 (2014).

33. Miranda-Gonçalves, V. *et al.* Monocarboxylate transporters (MCTs) in gliomas: Expression and exploitation as therapeutic targets. *Neuro. Oncol.* **15**, 172–188 (2013).

34. Sousa, B. *et al.* The basal epithelial marker P-cadherin associates with breast cancer cell populations harboring a glycolytic and acid-resistant phenotype. *BMC Cancer* **14**, 734 (2014).

35. Colen, C. B. *et al.* Metabolic Targeting of Lactate Efflux by Malignant Glioma Inhibits Invasiveness and Induces Necrosis: An In Vivo Study. *Neoplasia* **13**, 620–632 (2011).

36. Draoui, N. *et al.* Synthesis and pharmacological evaluation of carboxycoumarins as a new antitumor treatment targeting lactate transport in cancer cells. *Bioorganic Med. Chem.* **21**, 7107–7117 (2013).

37. Sonveaux, P. *et al.* Targeting lactate-fueled respiration selectively kills hypoxic tumor cells in mice. *J. Clin. Invest.* **118**, 3930–42 (2008).

38. Draoui, N. *et al.* Antitumor activity of 7-aminocarboxycoumarin derivatives, a new class of potent inhibitors of lactate influx but not efflux. *Mol. Cancer Ther.* **13**, 1410–8 (2014).

39. Sonveaux, P. *et al.* Targeting lactate-fueled respiration selectively kills hypoxic tumor cells in mice. *J. Clin. Invest.* **118**, 3930–42 (2008).

40. Gurrapu, S. *et al. Coumarin carboxylic acids as monocarboxylate transporter 1 inhibitors: In vitro and in vivo studies as potential anticancer agents*. *Bioorganic & Medicinal Chemistry Letters* **26**, (2016).

41. Ovens, M. J., Wilson, M. C., Davies, A. J., Murray, C. M. & Halestrap, A. P. AR-C155858 is a potent inhibitor of monocarboxylate transporters MCT1 and MCT2 that binds to an intracellular site involving transmembrane helices 7–10. *Biochem. J.* **425**, 523–530 (2009).

42. Critchlow, S. E. (Astrazenica) & Tate, L. (AstraZeneca). USE OF A MCT1 INHIBITOR IN THE TREATMENT OF CANCERS EXPRESSING MCT1 OVER MCT4. **2010**, WO 2010/089580 A1 (2010).

43. Curtis, N. J. *et al.* Pre-clinical pharmacology of AZD3965, a selective inhibitor of MCT1: DLBCL, NHL and Burkitt’s lymphoma anti-tumor activity. *Oncotarget* **8**, 69219–69236 (2017).

44. Noble, R. A. *et al.* Inhibition of monocarboxyate transporter 1 by AZD3965 as a novel therapeutic approach for diffuse large B-cell lymphoma and burkitt lymphoma. *Haematologica* **102**, 1247–1257 (2017).

45. Wang, H. *et al.* Synthesis and structure-activity relationships of pteridine dione

and trione monocarboxylate transporter 1 inhibitors. *J. Med. Chem.* **57**, 7317–7324 (2014).

46. Benjamin, D. *et al.* Dual Inhibition of the Lactate Transporters MCT1 and MCT4 Is Synthetic Lethal with Metformin due to NAD+ Depletion in Cancer Cells. *Cell Rep.* **25**, 3047–3058.e4 (2018).

47. Burtrand, G. The Modest Undressing of a Silicon Center. *Science (80-.).* **305**, 783–785 (2004).

48. Meanwell, N. A. Synopsis of Some Recent Tactical Application of Bioisosteres in Drug Design. *J. Med. Chem.* **54**, 2529–2591 (2011).

49. Ramesh, R. & Reddy, D. S. Quest for Novel Chemical Entities through Incorporation of Silicon in Drug Scaffolds. *J. Med. Chem.* **61**, 3779–3798 (2018).

50. Ramesh, R. & Reddy, D. S. Quest for Novel Chemical Entities through Incorporation of Silicon in Drug Scaffolds. *J. Med. Chem.* **61**, 3779–3798 (2018).

51. Johansson, T., Weidolf, L., Popp, F., Tacke, R. & Jurva, U. In vitro metabolism of haloperidol and sila-haloperidol: New metabolic pathways resulting from carbon/silicon exchange. *Drug Metab. Dispos.* **38**, 73–83 (2010).

52. Bhatti, Z., Norsworthy, J. & Szombathy, T. Loperamide metabolite-induced cardiomyopathy and QTc prolongation. *Clin. Toxicol.* **55**, 659–661 (2017).

53. Tacke, R. *et al.* Sila-Trifluperidol, a Silicon Analogue of the Dopamine (D_2) Receptor Antagonist Trifluperidol: Synthesis and Pharmacological Characterization. *Organometallics* **29**, 1652–1660 (2010).

54. Geyer, M. *et al.* Can Silicon Make an Excellent Drug Even Better? An in vitro and

in vivo Head-to-Head Comparison between Loperamide and Its Silicon Analogue Sila-Loperamide. *ChemMedChem* **10**, 911–924 (2015).

55. Millership, J. S. & Shanks, M. L. Prodrugs utilizing a reversible silyl linkage. *Int. J. Pharm.* **28**, 1–9 (1986).

56. Fujii, S. Expanding the chemical space of hydrophobic pharmacophores: the role of hydrophobic substructures in the development of novel transcription modulators. *Medchemcomm* **7**, 1082–1092 (2016).

57. Gabathuler, R. Approaches to transport therapeutic drugs across the blood–brain barrier to treat brain diseases. *Neurobiol. Dis.* **37**, 48–57 (2010).

58. Seetharamsingh, B. *et al.* Design, Synthesis, and Identification of Silicon Incorporated Oxazolidinone Antibiotics with Improved Brain Exposure. *ACS Med. Chem. Lett.* **6**, 1105–1110 (2015).

59. Tsakalozou, E. *et al.* A Phase I Study of 7-t-Butyldimethylsilyl-10-Hydroxycamptothecin in Adult Patients with Refractory or Metastatic Solid Malignancies. *Clin. Cancer Res.* **16**, 673–680 (2010).

60. David Bom, † *et al.* The Novel Silatecan 7-tert-Butyldimethylsilyl-10-hydroxycamptothecin Displays High Lipophilicity, Improved Human Blood Stability, and Potent Anticancer Activity. (2000). doi:10.1021/JM000144O

61. Wuts, P. G. M., Greene, T. W. & Greene, T. W. *Greene's protective groups in organic synthesis.* (Wiley-Interscience, 2007).

62. Saunders, F. J. A singularly long-acting ether of testosterone. *Proc. Soc. Exp. Biol. Med.* **123**, 303–304 (1966).

63. Beckett, A. H. ., Taylor, D. C. ; & Gorrod, J. W. . Trialkylsilyl moieties as potential pharmacokinetic modifying groups for aminoalcohols. *J. Pharm. Pharmacol* **27**, 599–593 (1975).

64. Shelton, J. R., Cutler, C. E., Browning, M. S., Balzarini, J. & Peterson, M. A. Synthesis and SAR of 2′,3′-bis-O-substituted N6, 5′-bis-ureidoadenosine derivatives: Implications for prodrug delivery and mechanism of action. *Bioorg. Med. Chem. Lett.* **22**, 6067–6071 (2012).

65. Vinod F. Patel *et al.* Novel Acid Labile COL1 Trityl-Linked Difluoronucleoside Immunoconjugates: Synthesis, Characterization, and Biological Activity1. *Bioconjug. Chem.* **7**, 497–510 (1996).

66. Murakami, H., Minami, T. & Ozawa, F. Facile and selective deallylation of allyl ethers using diphosphinidenecyclobutene-coordinated palladium catalysts. *J. Org. Chem.* **69**, 4482–4486 (2004).

67. Qualls, M. M. & Thompson, D. H. Chloroaluminum phthalocyanine tetrasulfonate delivered via acid-labile diplasmenylcholine-folate liposomes: Intracellular localization and synergistic phototoxicity. *Int. J. Cancer* **93**, 384–392 (2001).

68. Di Stefano, G., Derenzini, M., Kratz, F., Lanza, M. & Fiume, L. Liver-targeted doxorubicin: Effects on rat regenerating hepatocytes. *Liver Int.* **24**, 246–252 (2004).

69. Yan, Y., Fu, J., Wang, T. & Lu, X. Controlled release of silyl ether camptothecin from thiol-ene click chemistry-functionalized mesoporous silica nanoparticles. *Acta Biomater.* **51**, 471–478 (2017).

70. Parrott, M. C. *et al.* Tunable Bifunctional Silyl Ether Cross-Linkers for the Design of Acid-Sensitive Biomaterials. 17928–17932 (2010). doi:10.1021/ja108568g

71. Kim, S. *et al.* Intra-mitochondrial biomineralization for inducing apoptosis of cancer cells. *Chem. Sci.* **9**, 2474–2479 (2018).

72. Mereddy, Venkatram R.; Drewes, Lester R.; Alam, Mohammed Abrar; Jonnalagadda, Sravan K.; Gurrapu, S. Therapeutic Compounds. (2016).

73. Gurrapu, S. *et al.* Monocarboxylate transporter 1 inhibitors as potential anticancer agents. *ACS Med. Chem. Lett.* **6**, 558–561 (2015).

74. Gurrapu, S. *et al.* Monocarboxylate transporter 1 inhibitors as potential anticancer agents. *ACS Med. Chem. Lett.* **6**, 558–561 (2015).

75. Jia, D., Park, J., Jung, K., Levine, H. & Kaipparettu, B. Elucidating the Metabolic Plasticity of Cancer: Mitochondrial Reprogramming and Hybrid Metabolic States. *Cells* **7**, 21 (2018).

76. Gurrapu, S. *et al.* Coumarin carboxylic acids as monocarboxylate transporter 1 inhibitors: In vitro and in vivo studies as potential anticancer agents. *Bioorganic Med. Chem. Lett.* **26**, (2016).

77. Crook, T., Marston, N. J., Sara, E. A. & Vousden, K. H. Transcriptional activation by p53 correlates with suppression of growth but not transformation. *Cell* **79**, 817–827 (1994).

78. Pietenpol, J. A. *et al.* Sequence-specific transcriptional activation is essential for growth suppression by p53. *Proc. Natl. Acad. Sci. U. S. A.* **91**, 1998–2002 (1994).

79. Vlashi, E. & Pajonk, F. The metabolic state of cancer stem cells-a valid target for

cancer therapy? *Free Radic. Biol. Med.* **79**, 264–268 (2014).

80. Hirst, D. & Robson, T. Nitric oxide in cancer therapeutics: interaction with cytotoxic chemotherapy. *Curr. Pharm. Des.* **16**, 411–20 (2010).

81. Mocellin, S., Bronte, V. & Nitti, D. Nitric oxide, a double edged sword in cancer biology: Searching for therapeutic opportunities. *Med. Res. Rev.* **27**, 317–352 (2007).

82. Lu, X. Y. *et al.* Coumarin sulfonamides derivatives as potent and selective COX-2 inhibitors with efficacy in suppressing cancer proliferation and metastasis. *Bioorganic Med. Chem. Lett.* **26**, 3491–3498 (2016).

83. Wink, D. *et al.* The multifaceted roles of nitric oxide in cancer. *Carcinogenesis* **19**, 711–721 (1998).

84. Carpenter, A. W., Schoenfisch, M. H., Carpenter, A. W. & Wells, A. Chem Soc Rev Nitric oxide release : Part II . Therapeutic applications. 3742–3752 (2012). doi:10.1039/c2cs15273h

85. Stevens, E. V. *et al.* Nitric Oxide-Releasing Silica Nanoparticle Inhibition of Ovarian Cancer Cell Growth. *Mol. Pharm.* **7**, 775–785 (2010).

86. Liu, M. M. *et al.* Hybrids of phenylsulfonylfuroxan and coumarin as potent antitumor agents. *J. Med. Chem.* **57**, 9343–9356 (2014).

87. Maciag, A. E. *et al.* Nitric oxide-releasing prodrug triggers cancer cell death through deregulation of cellular redox balance. *Redox Biol.* **1**, 115–124 (2013).

88. Al, E. T., Chan, K., Jensen, N. & Brien, P. J. O. Structure – activity relationships for thiol reactivity and rat or human hepatocyte toxicity induced by substituted p -

benzoquinone compounds. *J. Appl. Toxicol.* **28**, 608–620 (2008).

89. Rosario, L. A. *et al.* Cellular response to a glutathione S-transferase P1-1 activated prodrug. *Mol. Pharmacol.* **58**, 167–74 (2000).

90. Ostrowski, A. D. & Ford, P. C. Metal complexes as photochemical nitric oxide precursors: Potential applications in the treatment of tumors. *Dalt. Trans.* **0**, 10660 (2009).

91. Fershtat, L. L. & Makhova, N. N. Molecular Hybridization Tools in the Development of Furoxan-Based NO-Donor Prodrugs. *ChemMedChem* **12**, 622–638 (2017).

92. Wang, P. G. *et al.* Nitric oxide donors: Chemical activities and biological applications. *Chem. Rev.* **102**, 1091–1134 (2002).

93. Cheng, H. *et al.* Effects of nitric oxide-releasing nonsteroidal anti-inflammatory drugs (NONO-NSAIDs) on melanoma cell adhesion. *Toxicol. Appl. Pharmacol.* **264**, 161–166 (2012).

94. Mason, D. T. & Braunwald, E. The effects of nitroglycerin and amyl nitrite on arteriolar and venous tone in the human forearm. *Circulation* **32**, 755–766 (1965).

95. Huerta, S., Chilka, S. & Bonavida, B. Nitric oxide donors: Novel cancer therapeutics (Review) SERGIO. *Int. J. Oncol.* **33**, 909–927 (2008).

96. Frederiksen, L. J. *et al.* Chemosensitization of Cancer In vitro and In vivo by Nitric Oxide Signaling. *Clin. Cancer Res.* **13**, 2199–2206 (2007).

97. Yasuda, H. *et al.* Randomized phase II trial comparing nitroglycerin plus vinorelbine and cisplatin with vinorelbine and cisplatin alone in previously

untreated stage IIIB/IV non-small-cell lung cancer. *J. Clin. Oncol.* **24**, 688–94 (2006).

98. Lamarque, D. & Whittle, B. J. R. Role of oxygen-derived metabolites in the rat gastric mucosal injury induced by nitric oxide donors. *Eur. J. Pharmacol.* **277**, 187–194 (1995).

99. Hrdý, I., Cammack, R., Stopka, P., Kulda, J. & Tachezy, J. Alternative pathway of metronidazole activation in Trichomonas vaginalis hydrogenosomes. *Antimicrob. Agents Chemother.* **49**, 5033–6 (2005).

100. Mallia, M. B. *et al.* A novel [99mTcN]2+ complex of metronidazole xanthate as a potential agent for targeting hypoxia. *Bioorg. Med. Chem. Lett.* **15**, 3398–3401 (2005).

101. Born, J. L., Smith, B. R., Harper, N. & Koch, C. J. Metabolism and radiosensitization of 4,5-dimethylmisonidazole, a ring-substituted analog of misonidazole. *Biochem. Pharmacol.* **43**, 1337–1344 (1992).

102. Bohn, H., Brendel, J., Martorana, P. A. & Schönafinger, K. Cardiovascular actions of the furoxan CAS 1609, a novel nitric oxide donor. *Br. J. Pharmacol.* **114**, 1605–12 (1995).

103. Civelli, M. *et al.* The involvement of the release of nitric oxide in the pharmacological activity of the new furoxan derivative CHF 2363. *Br. J. Pharmacol.* **118**, 923–928 (1996).

104. Balbo, S. *et al.* Studies of the potential genotoxic effects of furoxans: The case of CAS 1609 and of the water-soluble analogue of CHF 2363. *Toxicol. Lett.* **178**, 44–

51 (2008).

105. Nortcliffe, A., Botting, N. P. & O'Hagan, D. Novel amino acids: synthesis of furoxan and sydnonimine containing amino acids and peptides as potential nitric oxide releasing motifs. *Org. Biomol. Chem.* **11**, 4657–4671 (2013).

106. Kashfi, K. *Anti-Inflammatory Agents as Cancer Therapeutics*. *CONTEMPORARY ASPECTS OF BIOMEDICAL RESEARCH: DRUG DISCOVERY* **57**, (Elsevier, 2009).

107. Lee, M. Metabolic interplay between glycolysis and mitochondrial oxidation: The reverse Warburg effect and its therapeutic implication. *World J. Biol. Chem.* **6**, 148 (2015).

108. Wang, A. L. & Tew, K. D. Increased glutathione-S-transferase activity in a cell line with acquired resistance to nitrogen mustards. *Cancer Treat. Rep.* **69**, 677–82 (1985).

109. Townsend, D. M. & Tew, K. D. Cancer Drugs, Genetic Variation and the Glutathione-S-Transferase Gene Family. *Am. J. PharmacoGenomics* **3**, 157–172 (2003).

110. Aguirre, G. *et al.* Furoxan derivatives as cytotoxic agents: preliminary in vivo antitumoral activity studies. *Pharmazie* **61**, 54–59 (2006).

111. Han, C. *et al.* Novel hybrids of (phenylsulfonyl)furoxan and anilinopyrimidine as potent and selective epidermal growth factor receptor inhibitors for intervention of non-small-cell lung cancer. *J. Med. Chem.* **56**, 4738–4748 (2013).

112. Massarico Serafim, R. A. *et al.* Design, synthesis and biological evaluation of

hybrid bioisoster derivatives of N-acylhydrazone and furoxan groups with potential and selective anti-Trypanosoma cruzi activity. *Eur. J. Med. Chem.* **82**, 418–425 (2014).

113. Zhao, N. *et al.* Antiproliferative activity and apoptosis inducing effects of nitric oxide donating derivatives of evodiamine. *Bioorganic Med. Chem.* **24**, 2971–2978 (2016).

114. Ling, Y. *et al.* Synthesis and evaluation of nitric oxide-releasing derivatives of farnesylthiosalicylic acid as anti-tumor agents. *Bioorganic Med. Chem.* **18**, 3448–3456 (2010).

115. Ren, Z. *et al.* Anticancer efficacy of a nitric oxide-modified derivative of bifendate against multidrug-resistant cancer cells. *J. Cell. Mol. Med.* **20**, 1095–1105 (2016).

116. Yang, L. *et al.* ZL11n is a novel nitric oxide-releasing derivative of farnesylthiosalicylic acid that induces apoptosis in human hepatoma HepG2 cells via MAPK/mitochondrial pathways. *Biochem. Biophys. Res. Commun.* **409**, 752–757 (2011).

117. Kerwin, J. F., Laboratories, A., Park, A. & Feldman, P. L. Nitric Oxide: A New Paradigm for Second Messengers James. *J. Med. Chem.* **38**, 4343–4362 (1995).

118. Mfuh, A. M. & Larionov, O. V. Heterocyclic N-Oxides - An Emerging Class of Therapeutic Agents. *Curr. Med. Chem.* **22**, 2819–57 (2015).

119. Nelson, G. *et al.* Synthesis and evaluation of p-N,N-dialkyl substituted chalcones as anti-cancer agents. *Med. Chem. Res.* **22**, 4610–4614 (2013).

120. Emami, S. & Dadashpour, S. Current developments of coumarin-based anti-cancer

agents in medicinal chemistry. *Eur. J. Med. Chem.* **102**, 611–630 (2015).

APPENDIX

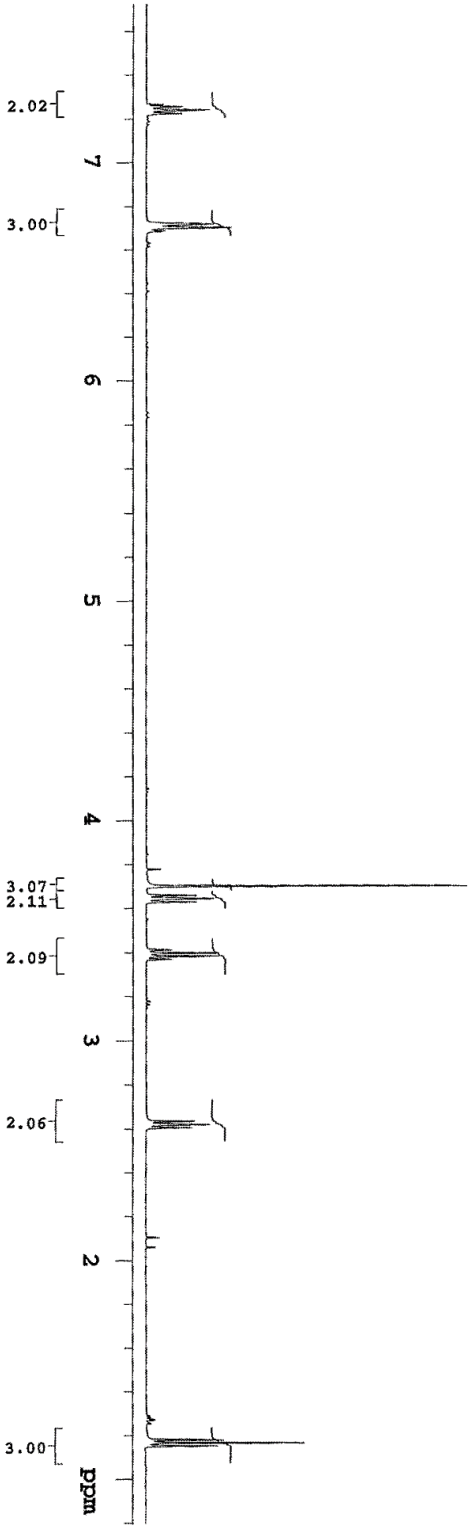

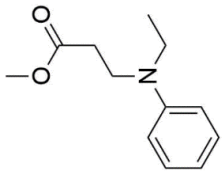

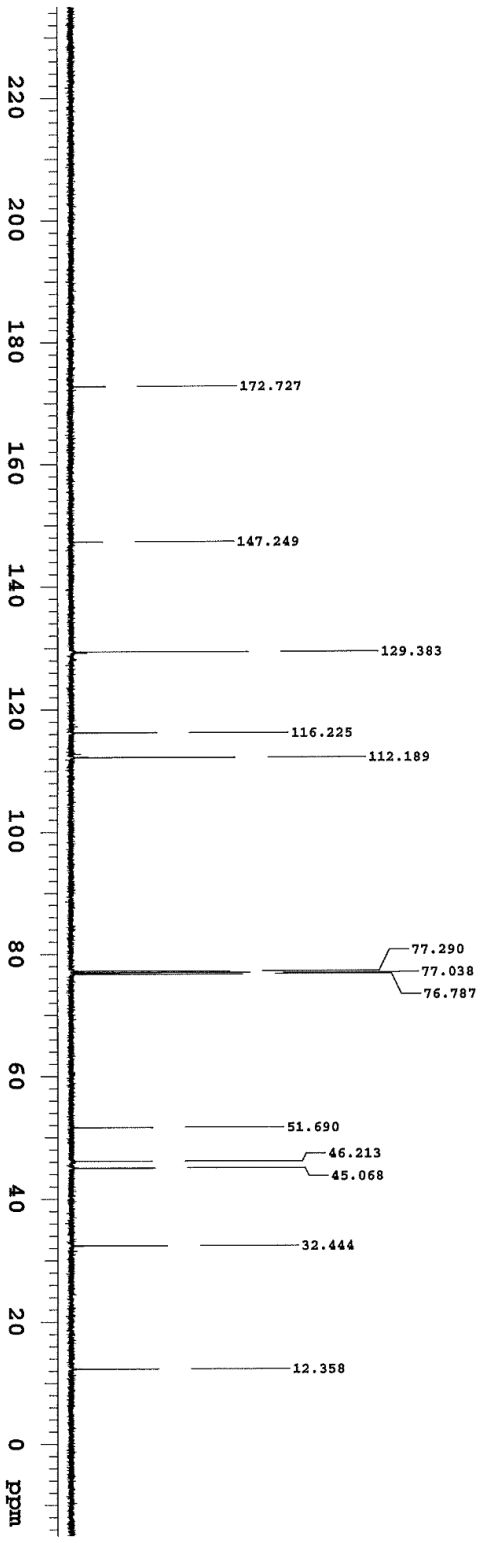
220
200
180
160
140
120
100
80
60
40
20
0
ppm
172.727
147.249
129.383
116.225
112.189
77.290
77.038
76.787
51.690
46.213
45.068
32.444
12.358

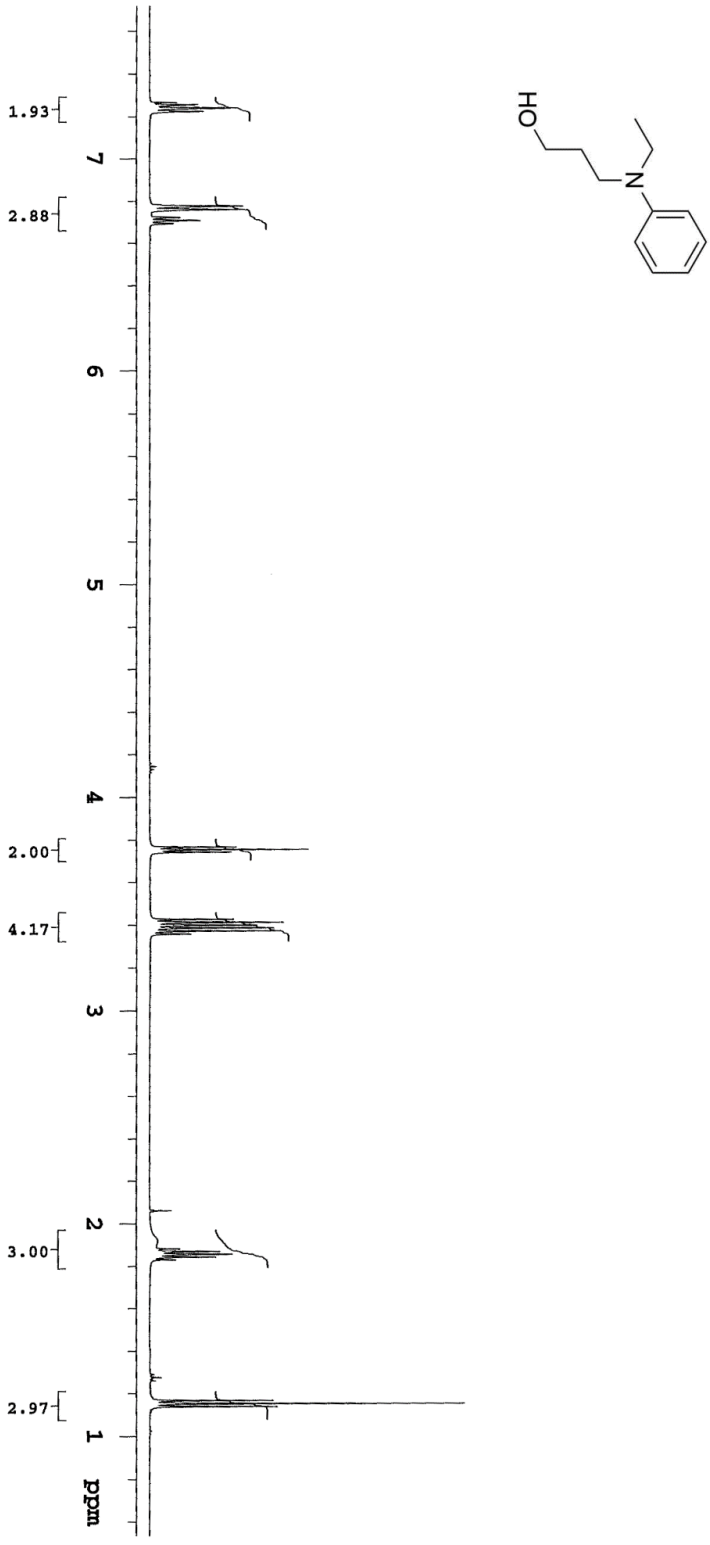
1.93
2.88
2.00
4.17
3.00
2.97
7
6
5
4
3
2
1
ppm
OH
N

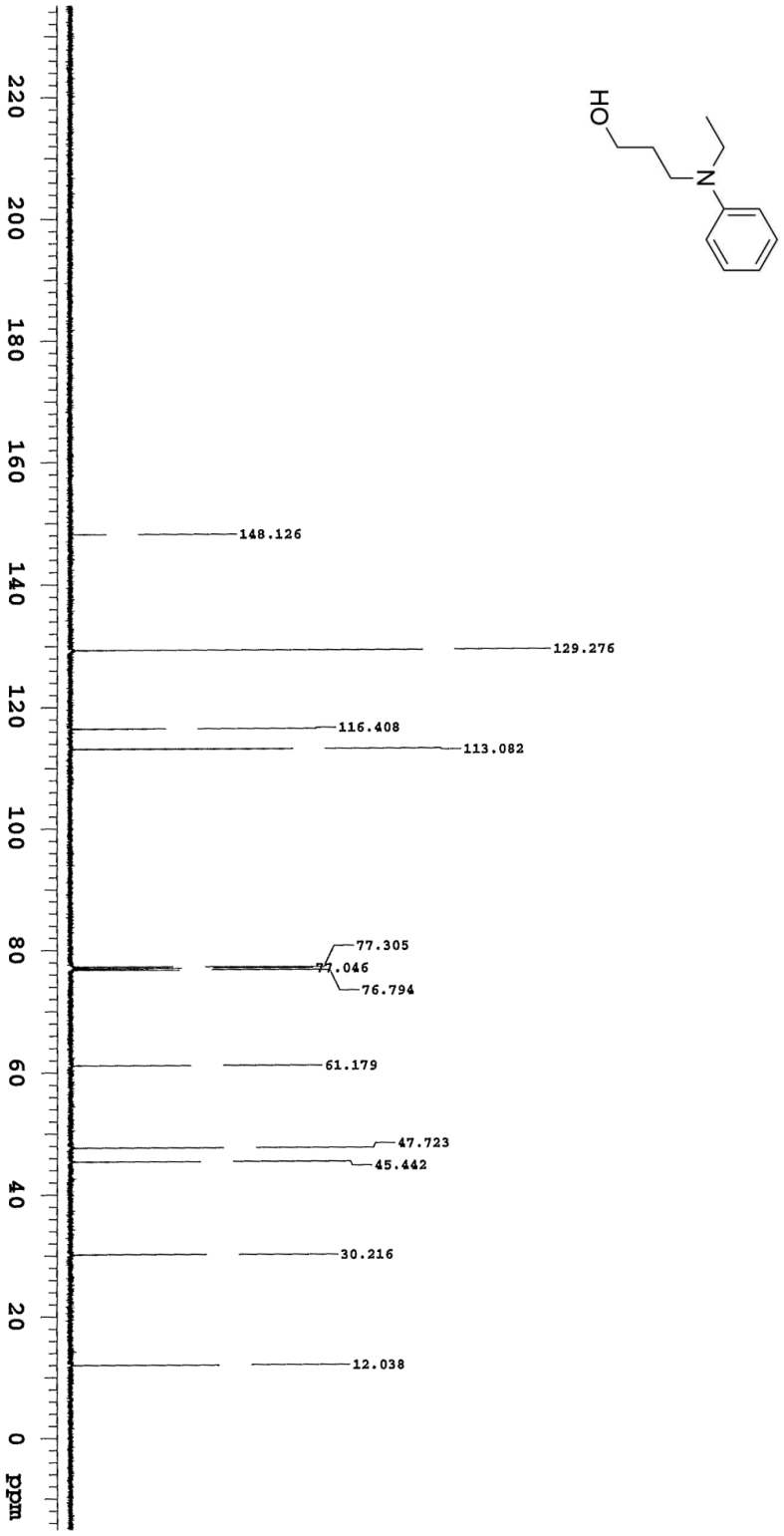
HO
N
220
200
180
160
140
120
100
80
60
40
20
0
ppm
148.126
129.276
116.408
113.082
77.305
77.046
76.794
61.179
47.723
45.442
30.216
12.038

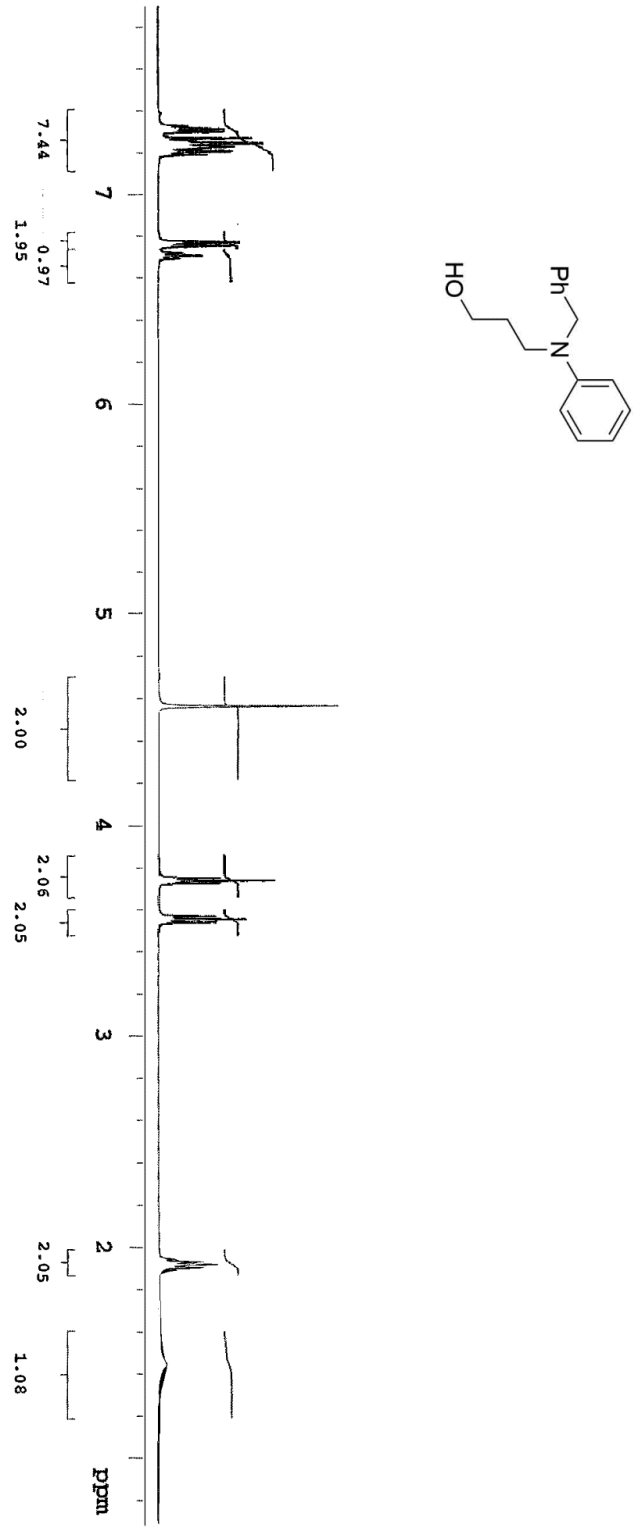
HO
Ph
N
7
6
5
4
3
2
ppm
7.44
0.97
1.95
2.00
2.06
2.05
2.05
1.08

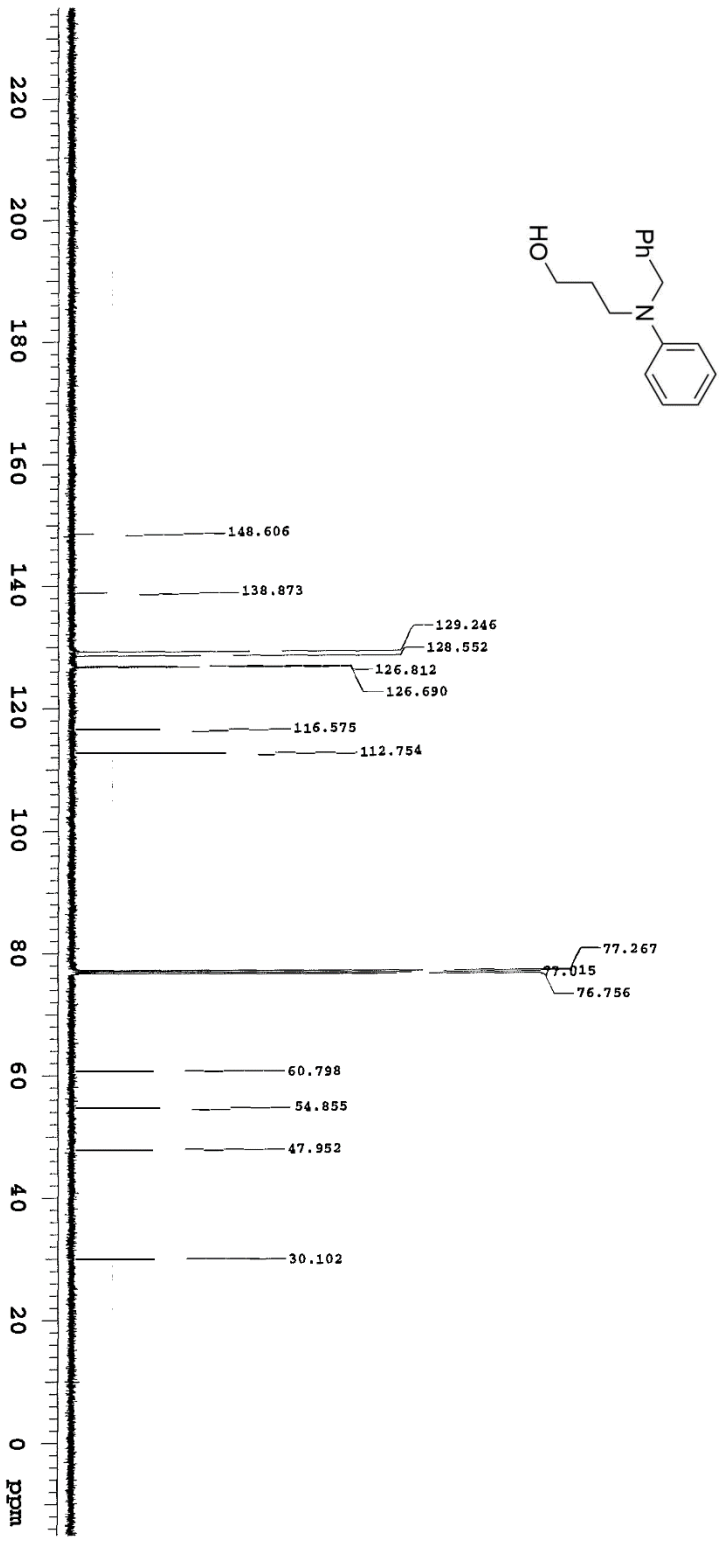
HO
Ph
N
148.606
138.873
129.246
128.552
126.812
126.690
116.575
112.754
77.267
77.015
76.756
60.798
54.855
47.952
30.102
220
200
180
160
140
120
100
80
60
40
20
0
ppm

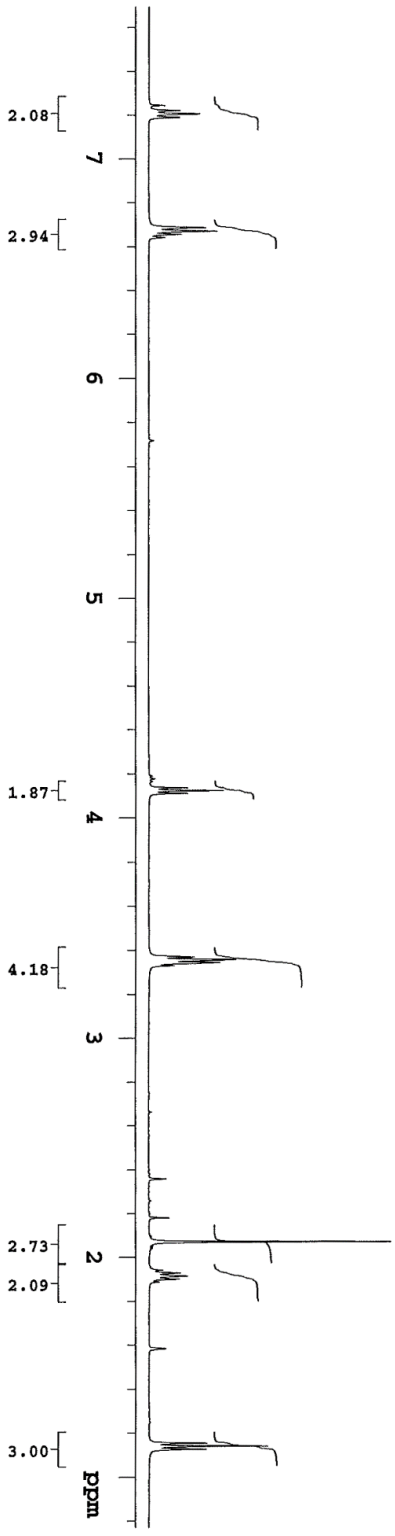
2.08
2.94
1.87
4.18
2.73
2.09
3.00
7
6
5
4
3
2
ppm

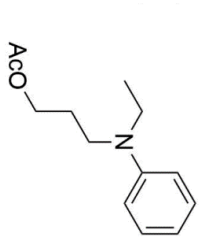
AcO
N

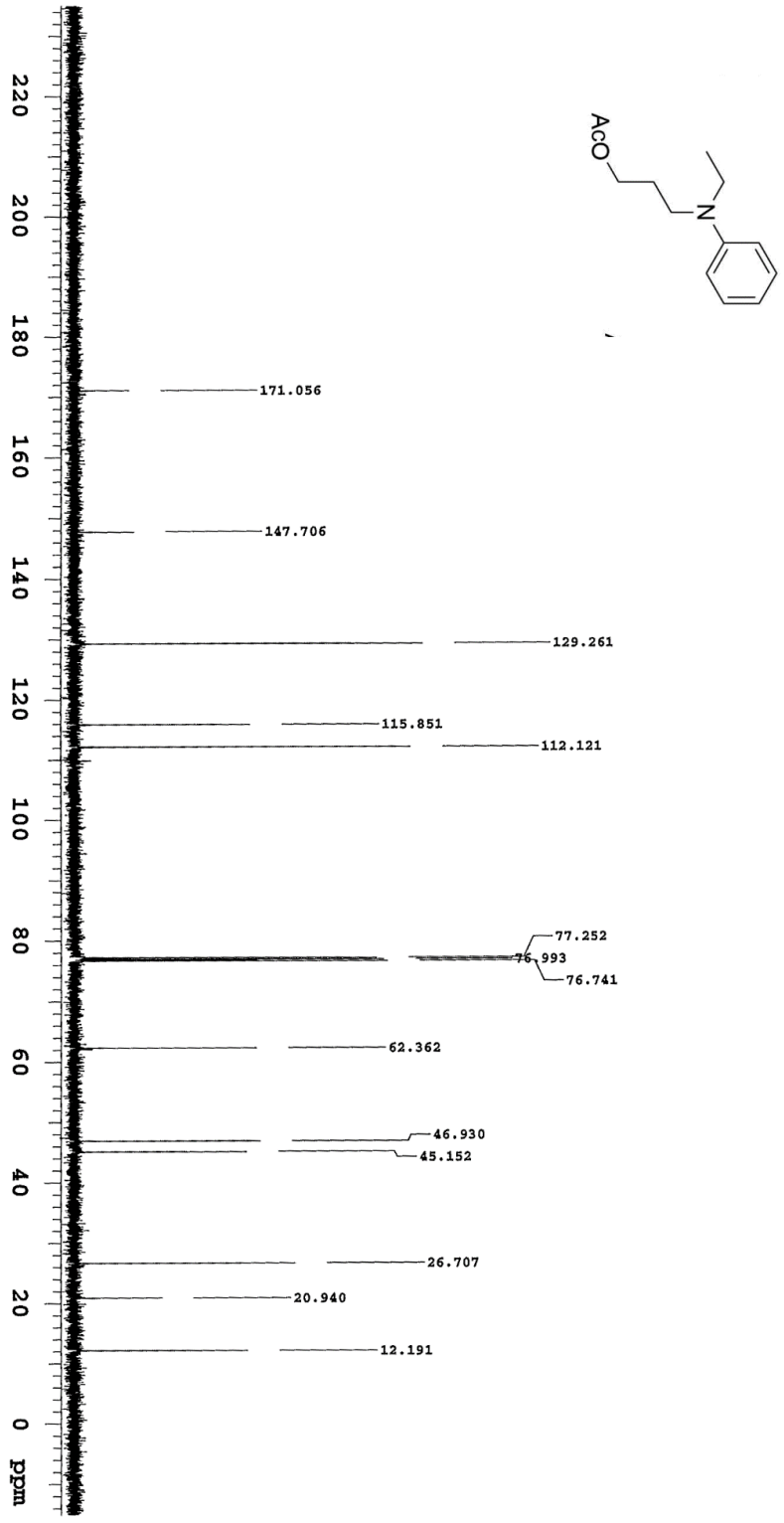
AcO
N
171.056
147.706
129.261
115.851
112.121
77.252
76.993
76.741
62.362
46.930
45.152
26.707
20.940
12.191
220
200
180
160
140
120
100
80
60
40
20
0
ppm


AcO
Ph
N
7
6
5
4
3
2
1
ppm
1.95
5.50
3.05
2.10
2.09
2.12
3.00
2.15

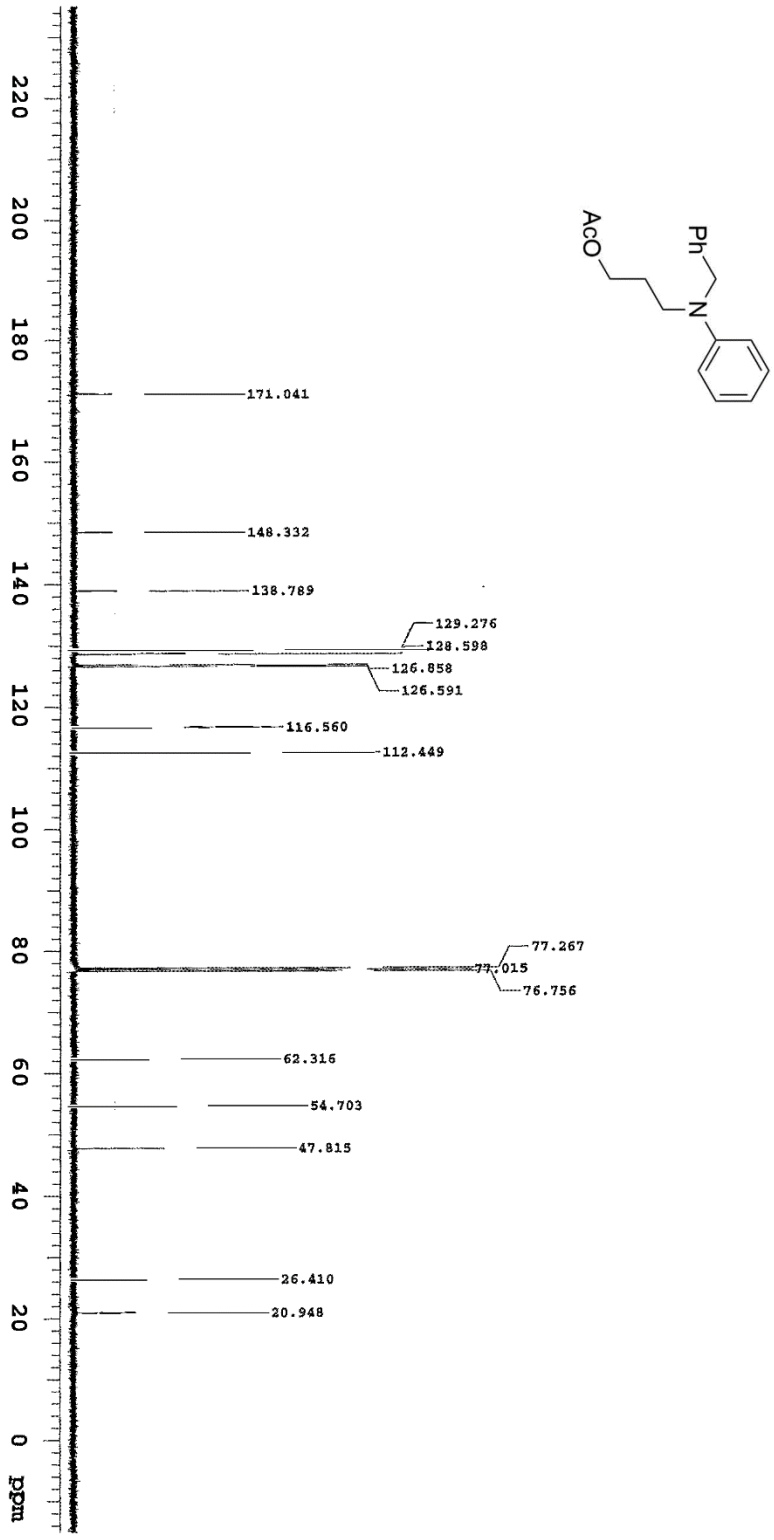
AcO
Ph
N
171.041
148.332
138.789
129.276
128.598
126.858
126.591
116.560
112.449
77.267
77.015
76.756
62.316
54.703
47.815
26.410
20.948
220
200
180
160
140
120
100
80
60
40
20
0
ppm

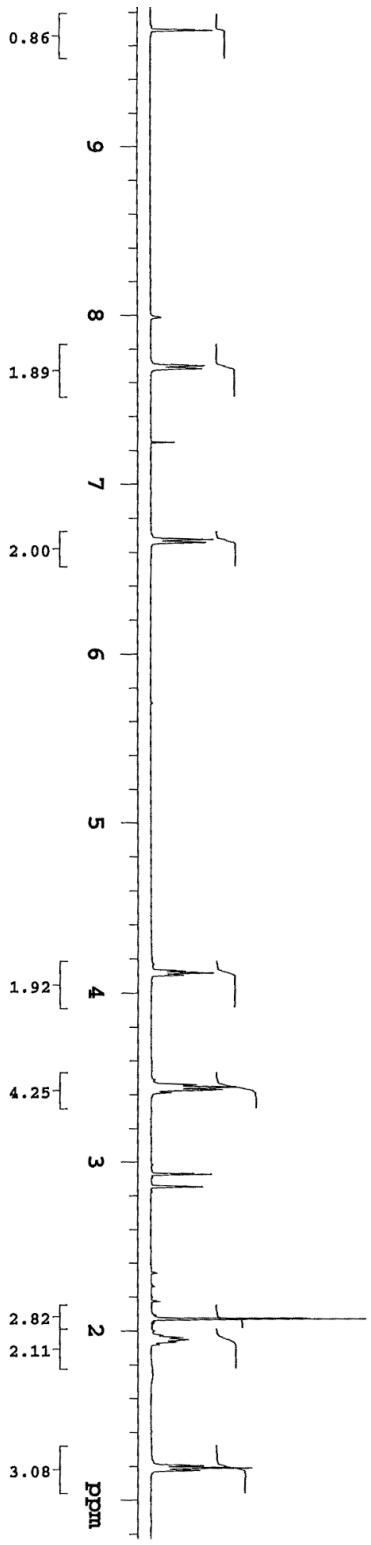
0.86
1.89
2.00
1.92
4.25
2.82
2.11
3.08
9
8
7
6
5
4
3
2
ppm

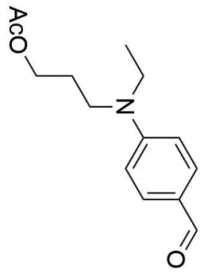
AcO
N
O

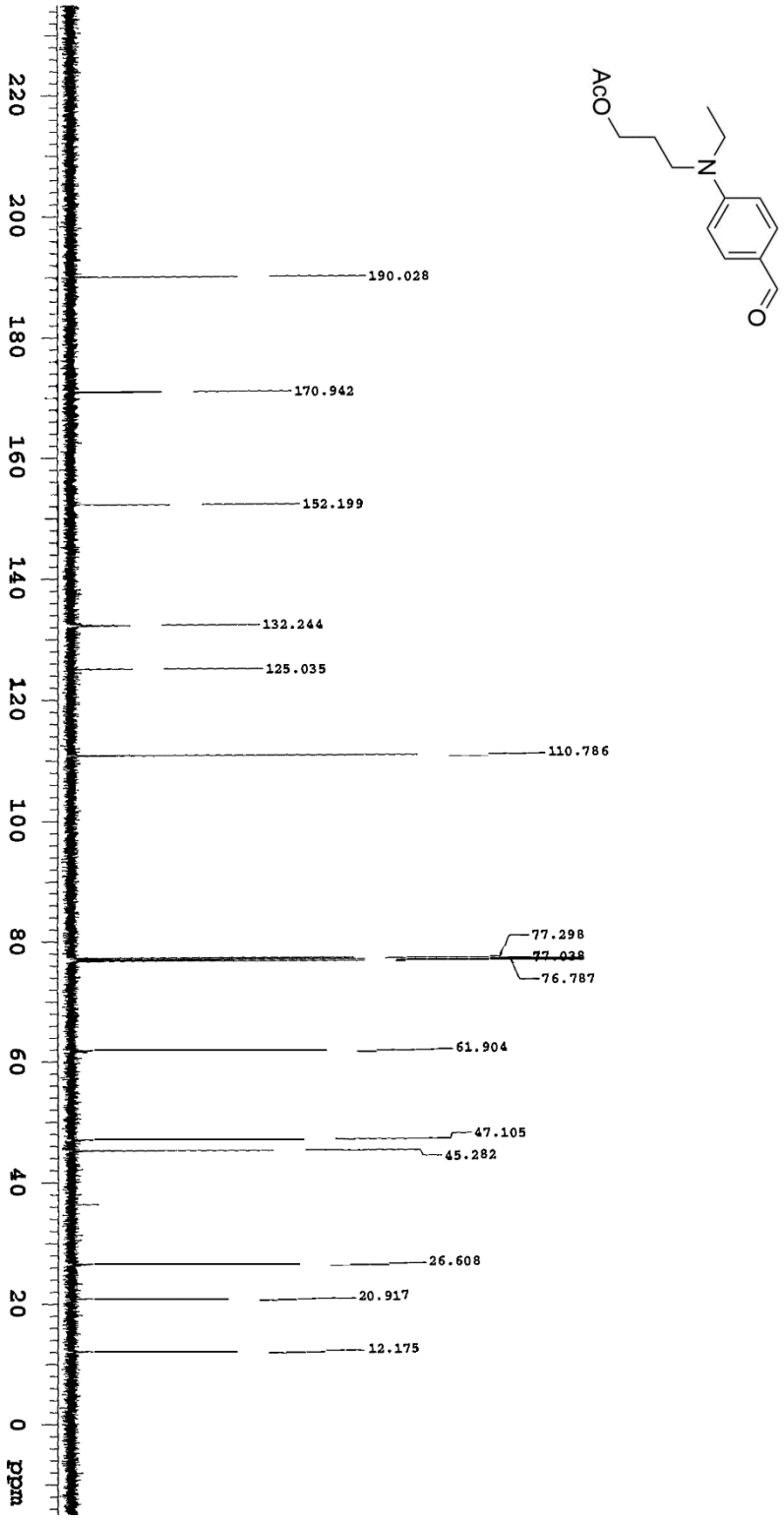
AcO
N
O
190.028
170.942
152.199
132.244
125.035
110.786
77.298
77.038
76.787
61.904
47.105
45.282
26.608
20.917
12.175
220
200
180
160
140
120
100
80
60
40
20
0
ppm

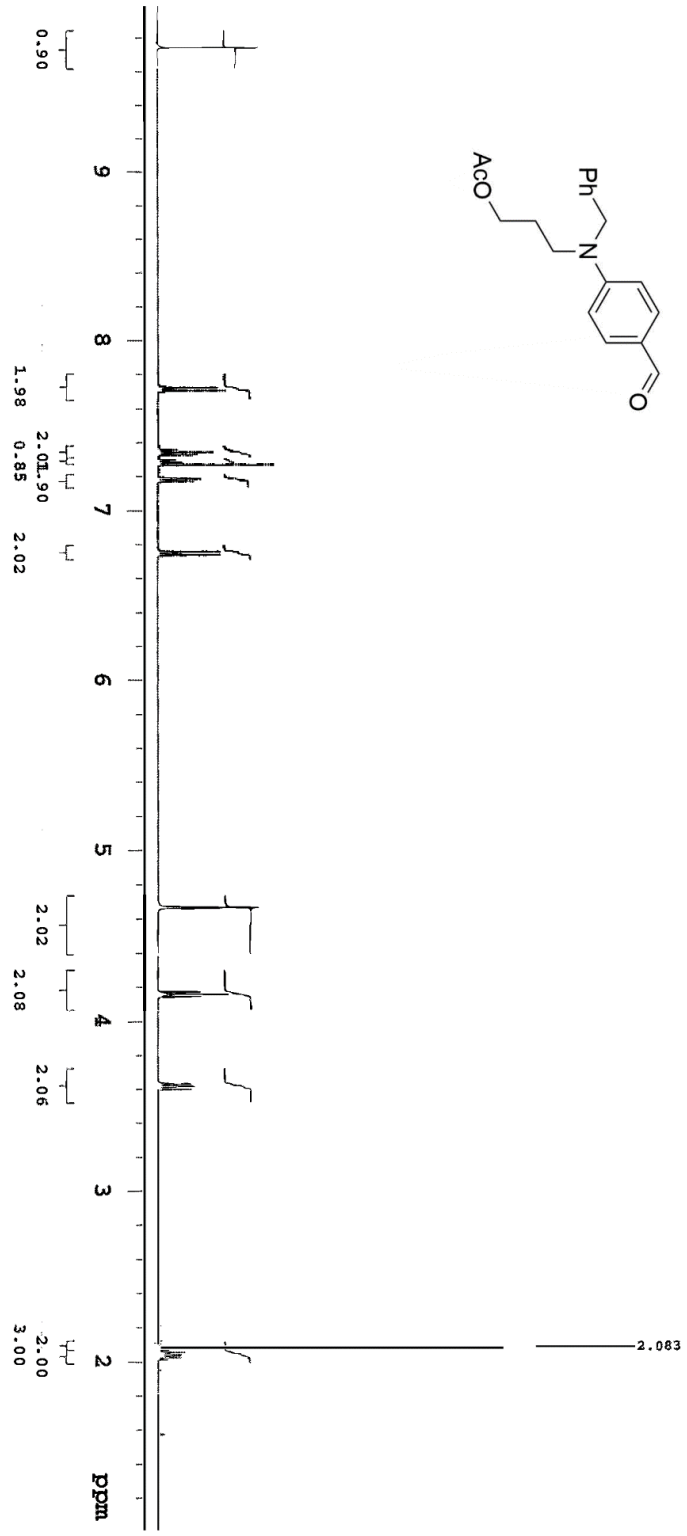
AcO
Ph
N
O
2.083
0.90
1.98
0.85
2.01
1.90
2.02
2.02
2.08
2.06
2.00
3.00
9
8
7
6
5
4
3
2
ppm

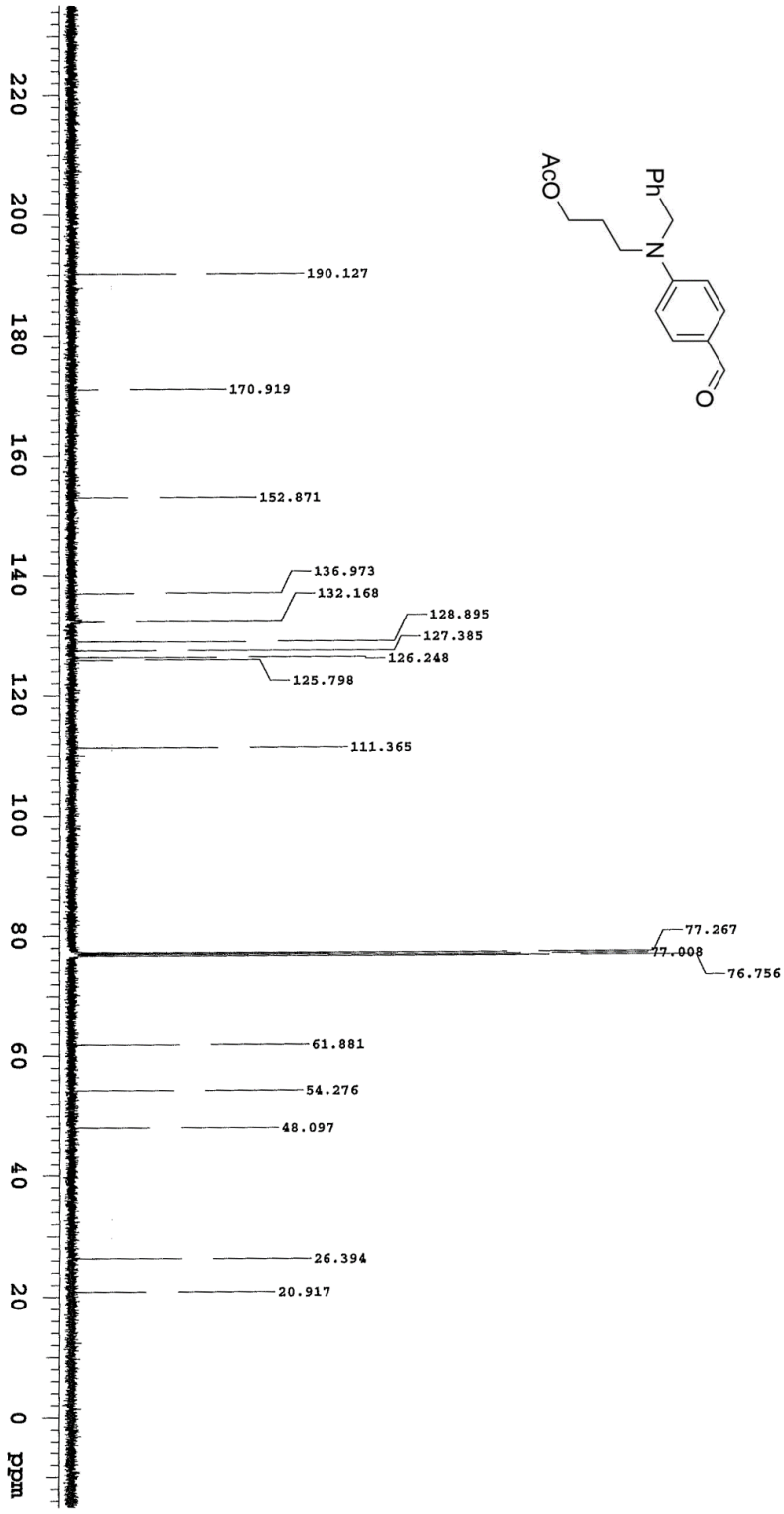
AcO
Ph
N
O
190.127
170.919
152.871
136.973
132.168
128.895
127.385
126.248
125.798
111.365
77.267
77.008
76.756
61.881
54.276
48.097
26.394
20.917
220
200
180
160
140
120
100
80
60
40
20
0
ppm

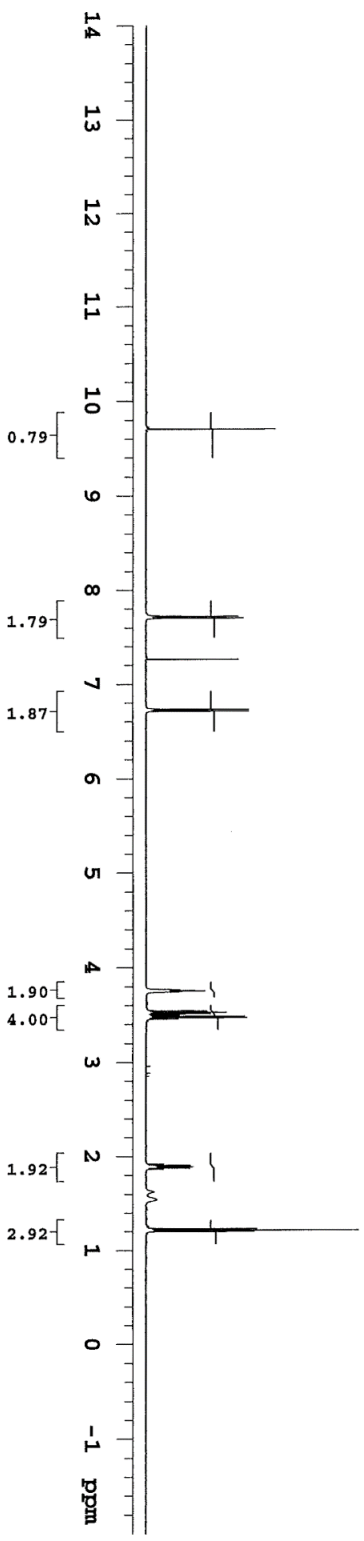
14
13
12
11
10
9
8
7
6
5
4
3
2
1
0
-1
ppm
0.79
1.79
1.87
1.90
4.00
1.92
2.92

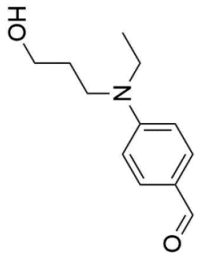
HO
N
O

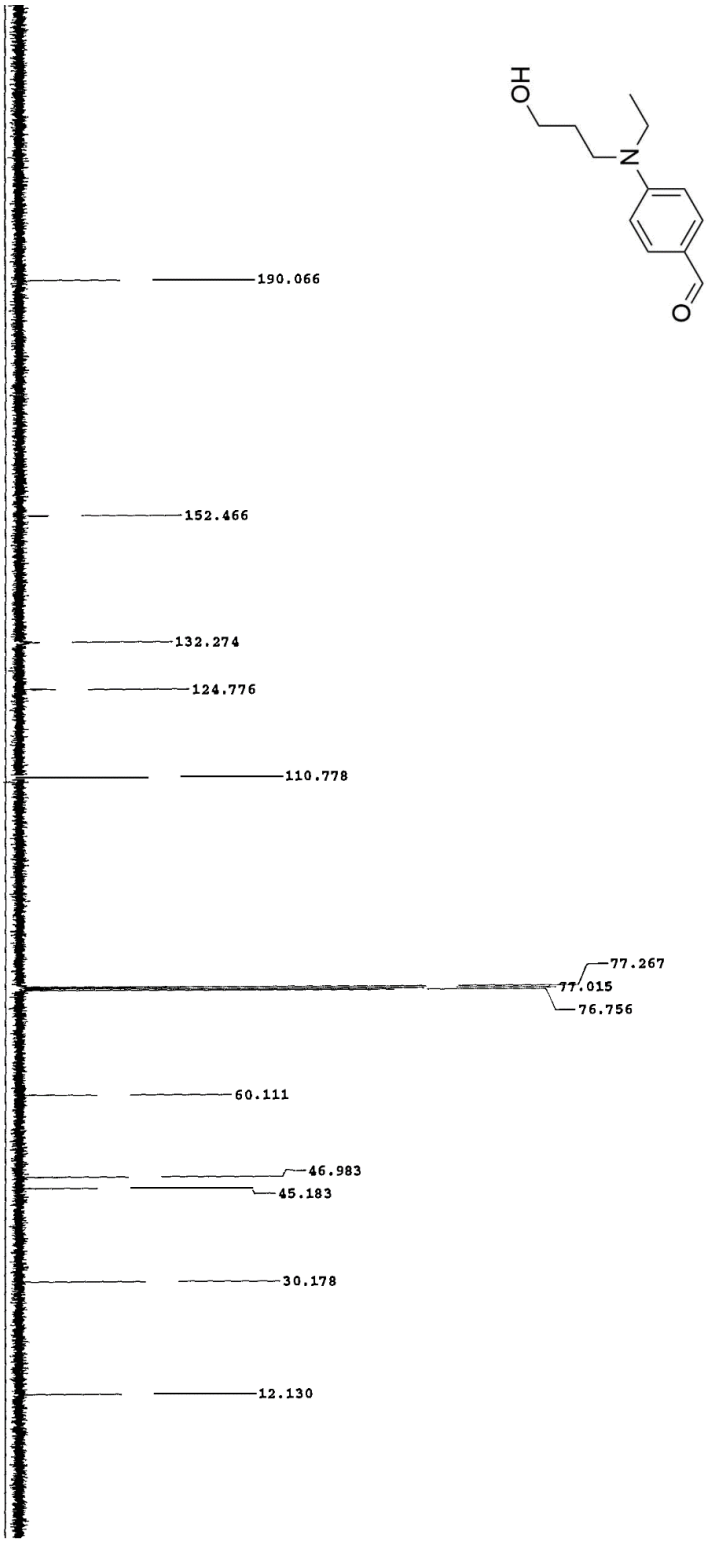
OH
N
O
190.066
152.466
132.274
124.776
110.778
77.267
77.015
76.756
60.111
46.983
45.183
30.178
12.130

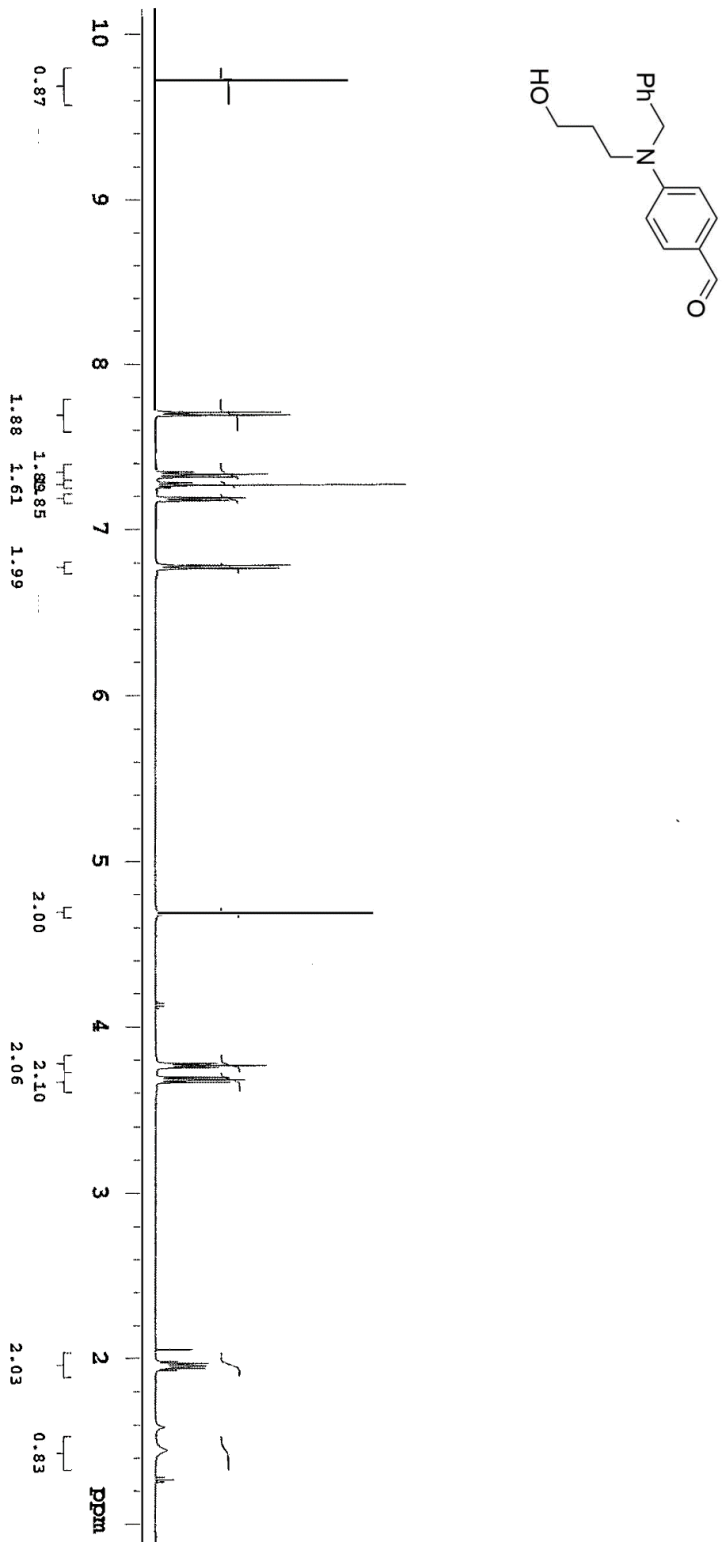
HO
Ph
N
O
10
9
8
7
6
5
4
3
2
ppm
0.87
1.88
1.61
1.99
2.00
2.10
2.06
2.03
0.83

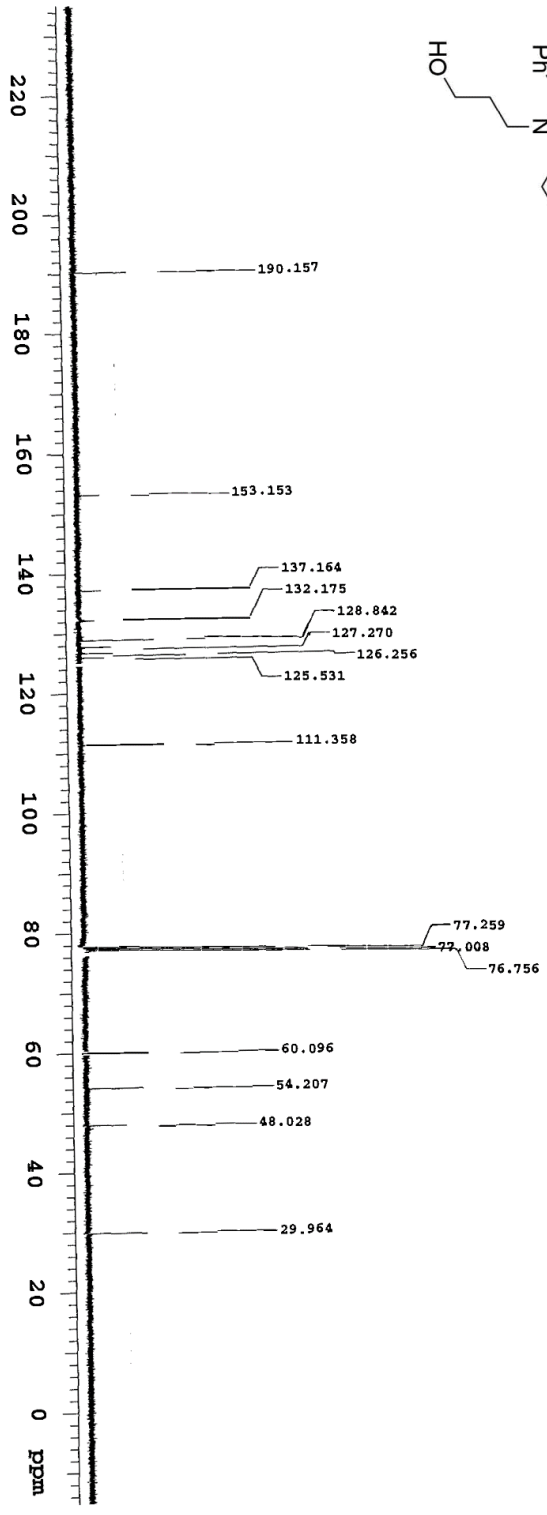
HO
Ph
N
O
190.157
153.153
137.164
132.175
128.842
127.270
126.256
125.531
111.358
77.259
77.008
76.756
60.096
54.207
48.028
29.964
220
200
180
160
140
120
100
80
60
40
20
0
ppm

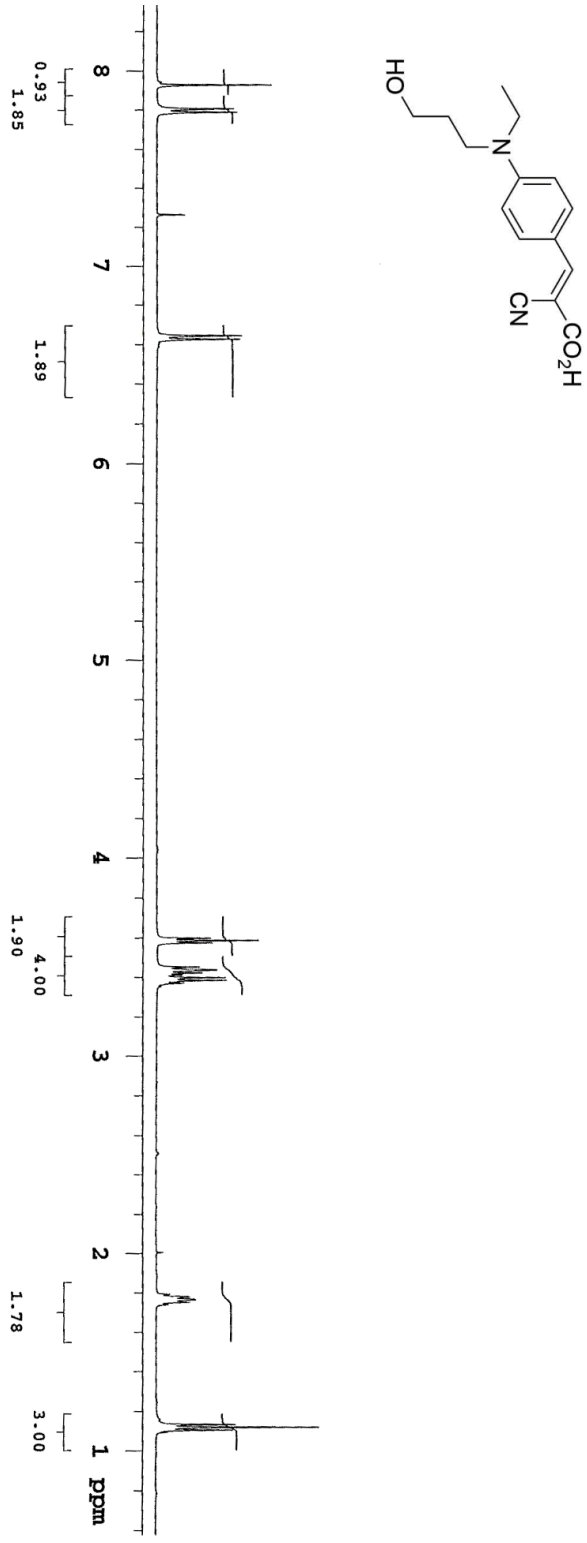
HO
N
CN
CO2H
8
7
6
5
4
3
2
1 ppm
0.93
1.85
1.89
4.00
1.90
1.78
3.00

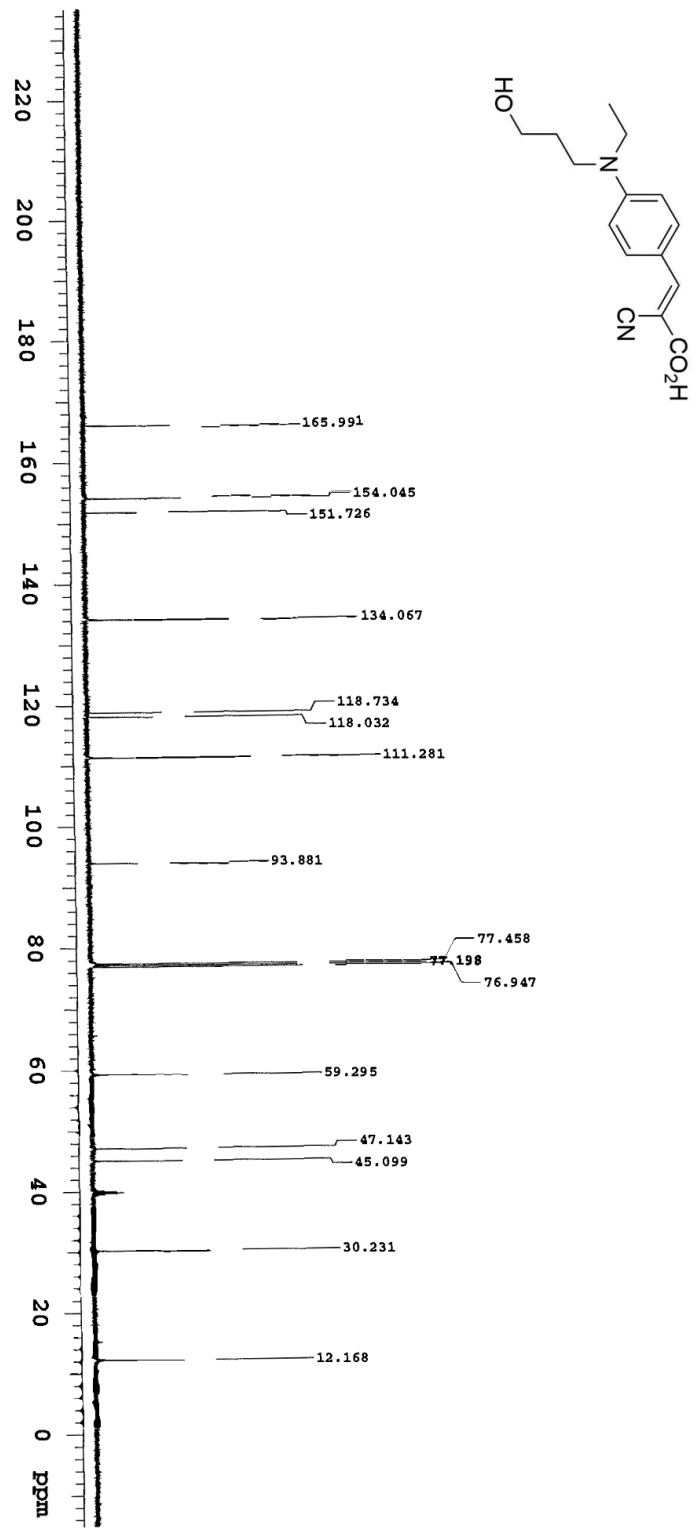
HO
N
CN
CO2H
165.991
154.045
151.726
134.067
118.734
118.032
111.281
93.881
77.458
77.198
76.947
59.295
47.143
45.099
30.231
12.168
220
200
180
160
140
120
100
80
60
40
20
0
ppm

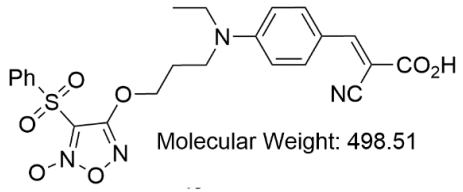

Molecular Weight: 498.51

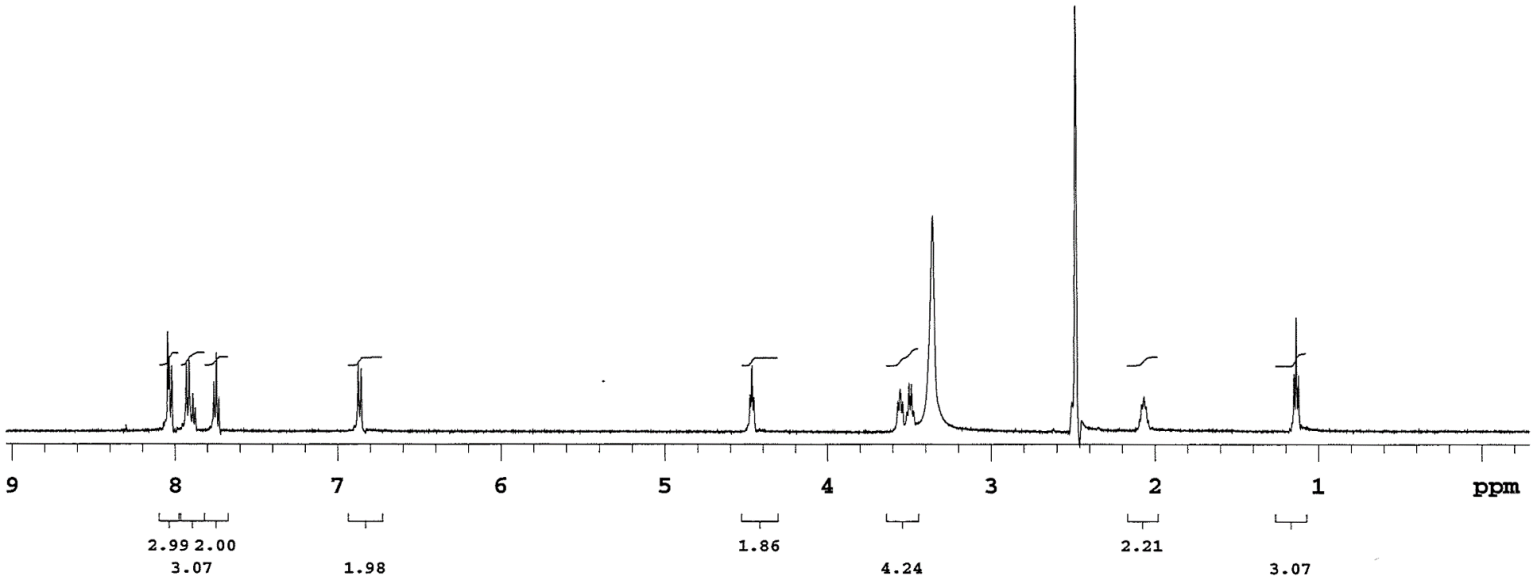

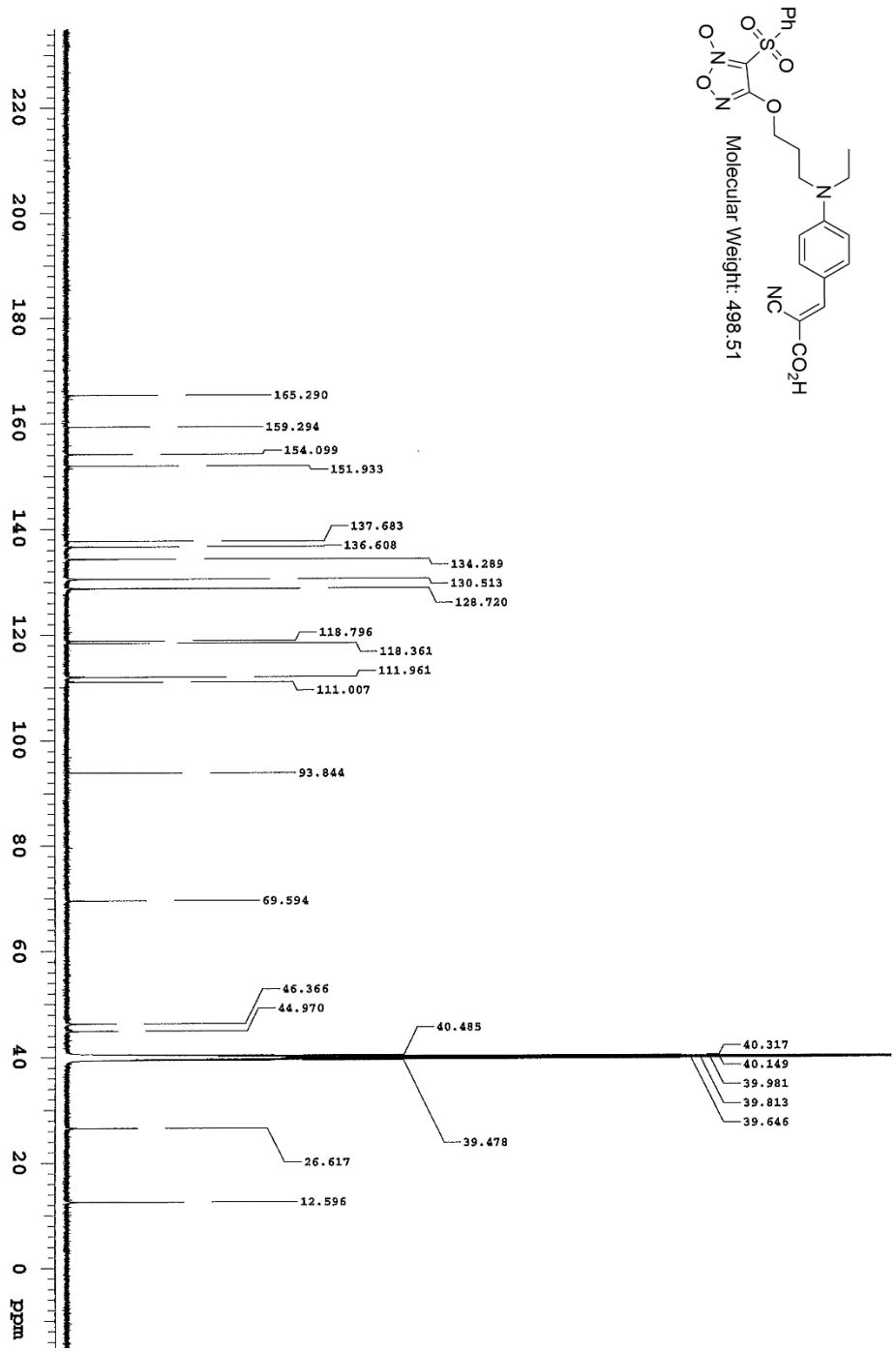
Molecular Weight: 498.51
165.290
159.294
154.099
151.933
137.683
136.608
134.289
130.513
128.720
118.796
118.361
111.961
111.007
93.844
69.594
46.366
44.970
40.485
40.317
40.149
39.981
39.813
39.646
39.478
26.617
12.596
ppm

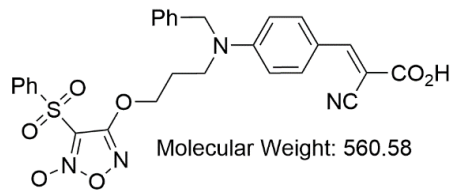

Molecular Weight: 560.58

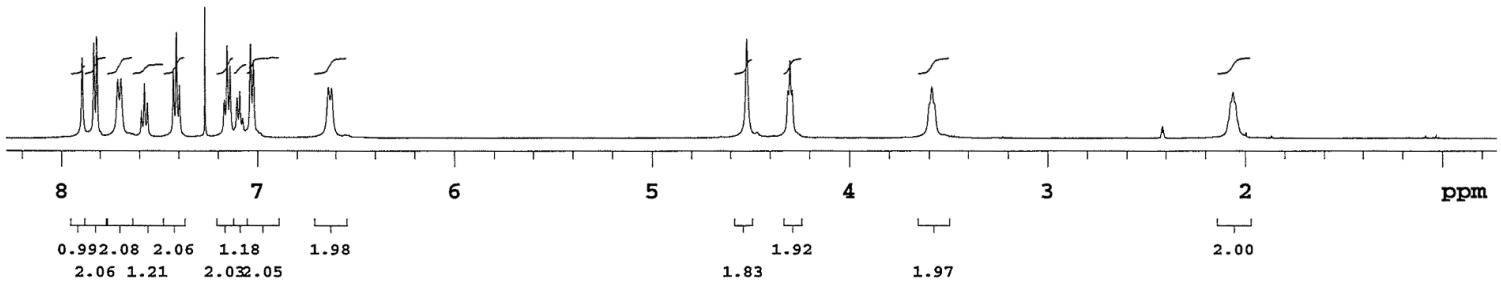

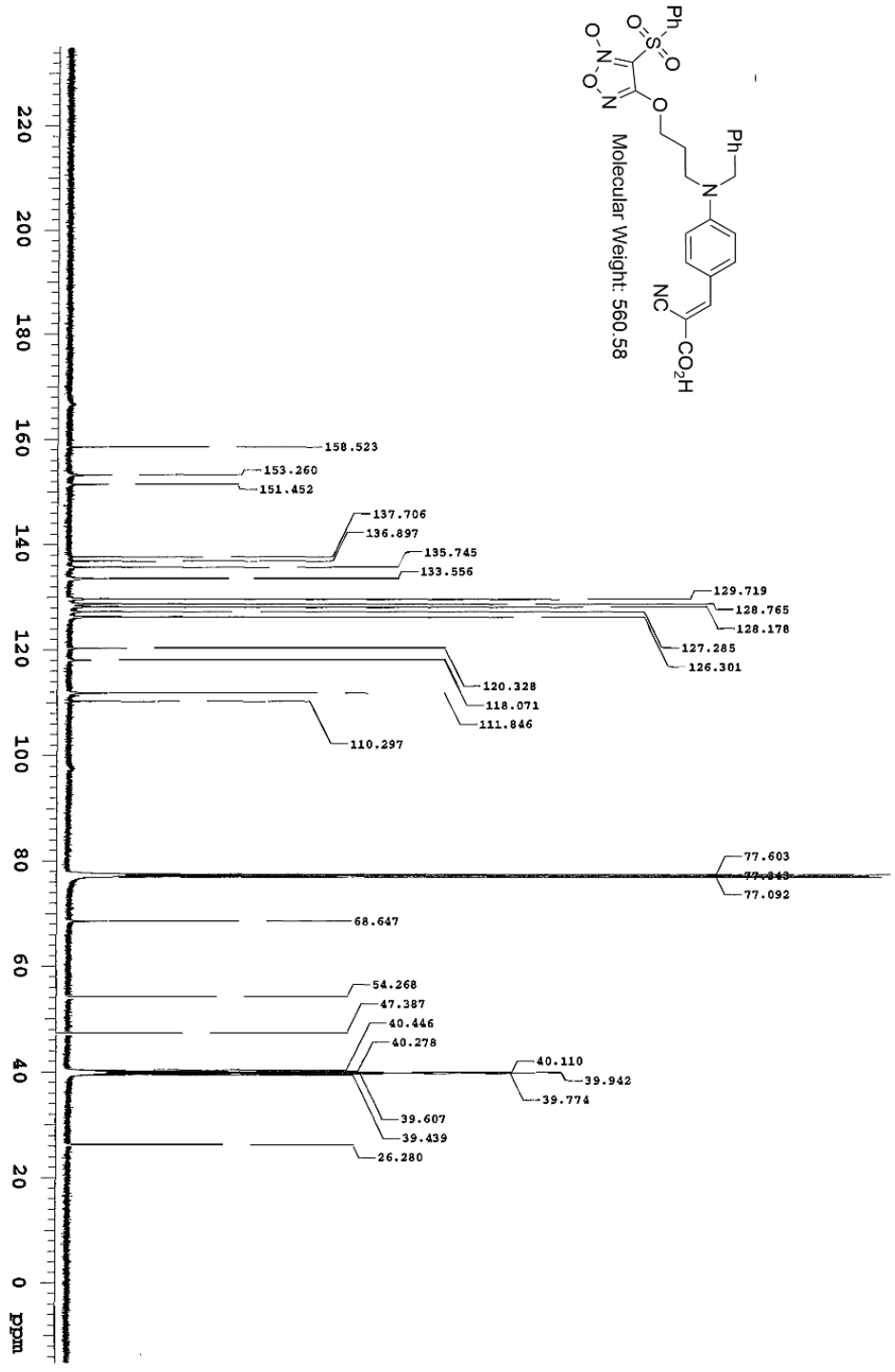
Molecular Weight: 560.58
158.523
153.260
151.452
137.706
136.897
135.745
133.556
129.719
128.765
128.178
127.285
126.301
120.328
118.071
111.846
110.297
77.603
77.092
68.647
54.268
47.387
40.446
40.278
40.110
39.942
39.774
39.607
39.439
26.280
220
200
180
160
140
120
100
80
60
40
20
0
ppm

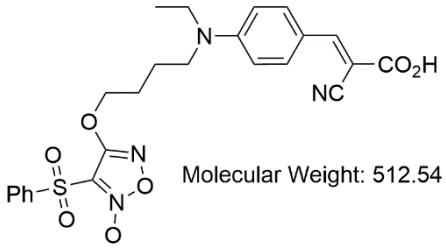

Molecular Weight: 512.54

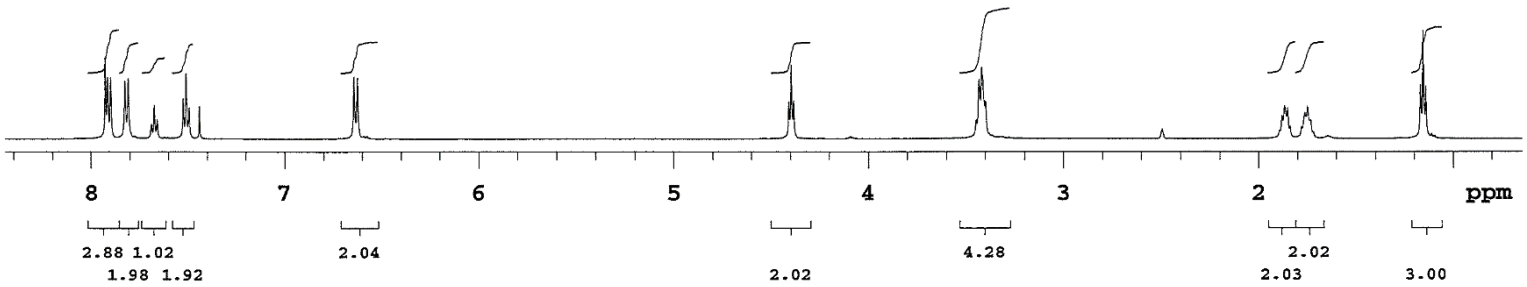

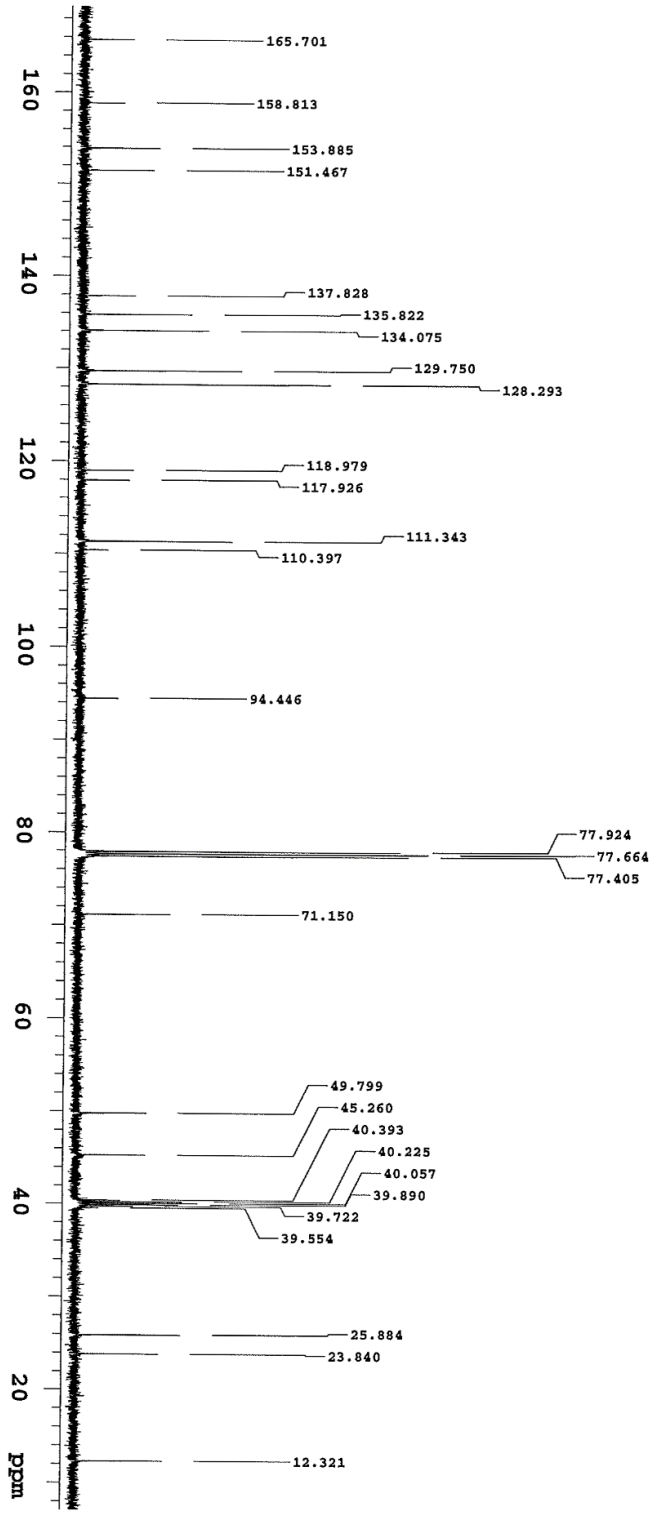

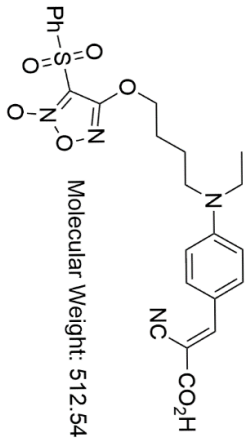

Molecular Weight: 512.54

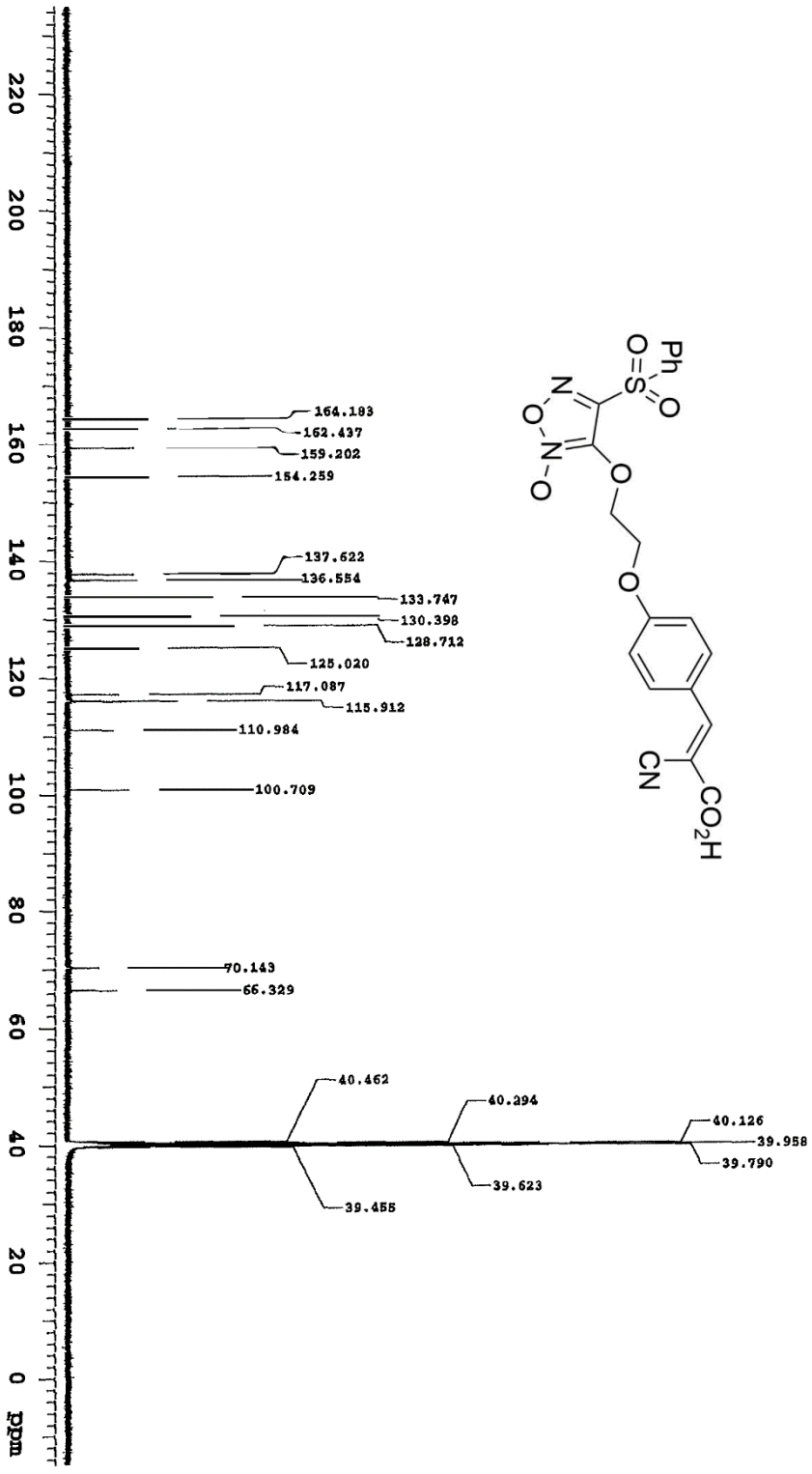
220
200
180
160
140
120
100
80
60
40
20
0 ppm
164.183
162.437
159.202
154.259
137.622
136.554
133.747
130.398
128.712
125.020
117.087
115.912
110.984
100.709
70.143
66.329
40.462
40.294
40.126
39.958
39.790
39.623
39.455
Ph
O
S
O
N
O
O
N
O
O
O
CN
CO2H

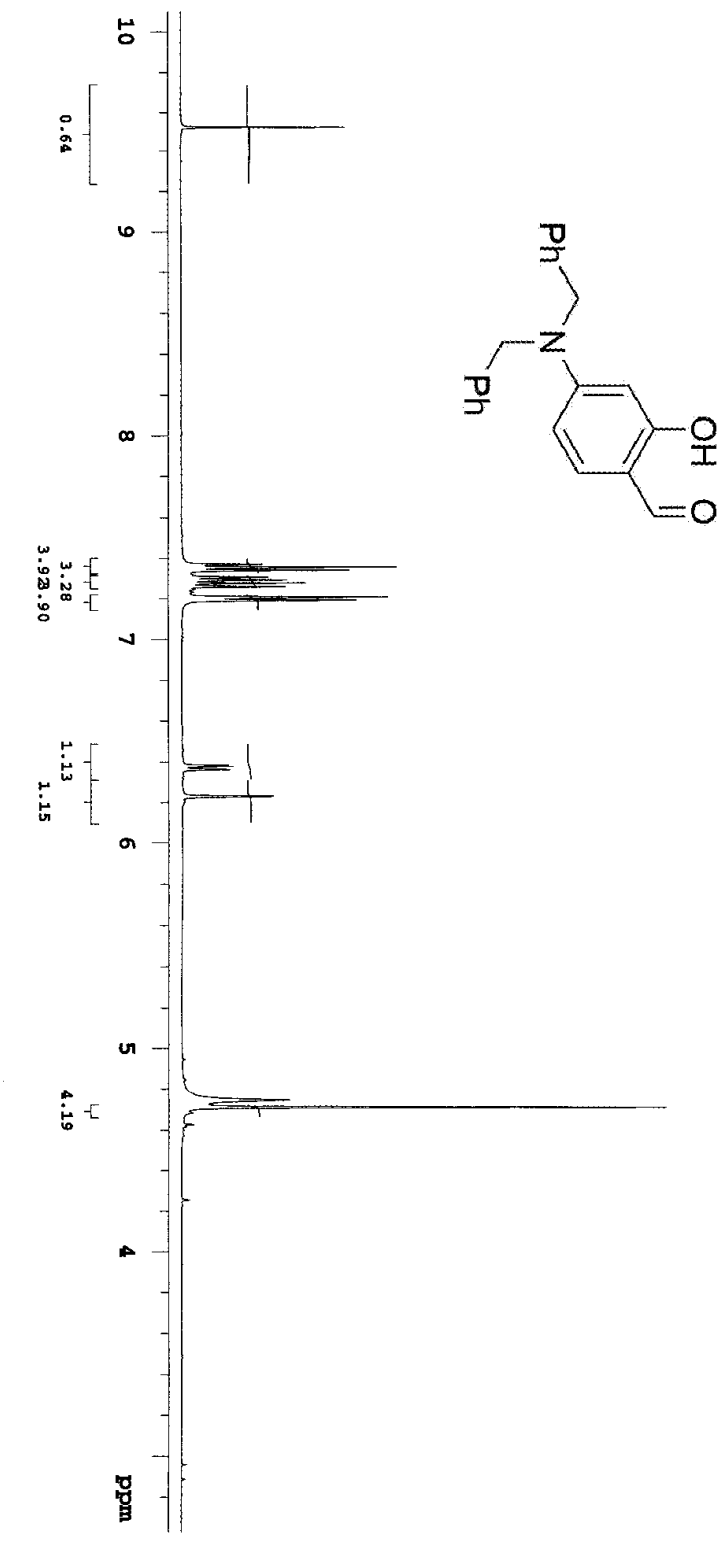
Ph
N
Ph
OH
O
10
9
8
7
6
5
4
ppm
0.64
3.28
3.92
2.90
1.13
1.15
4.19

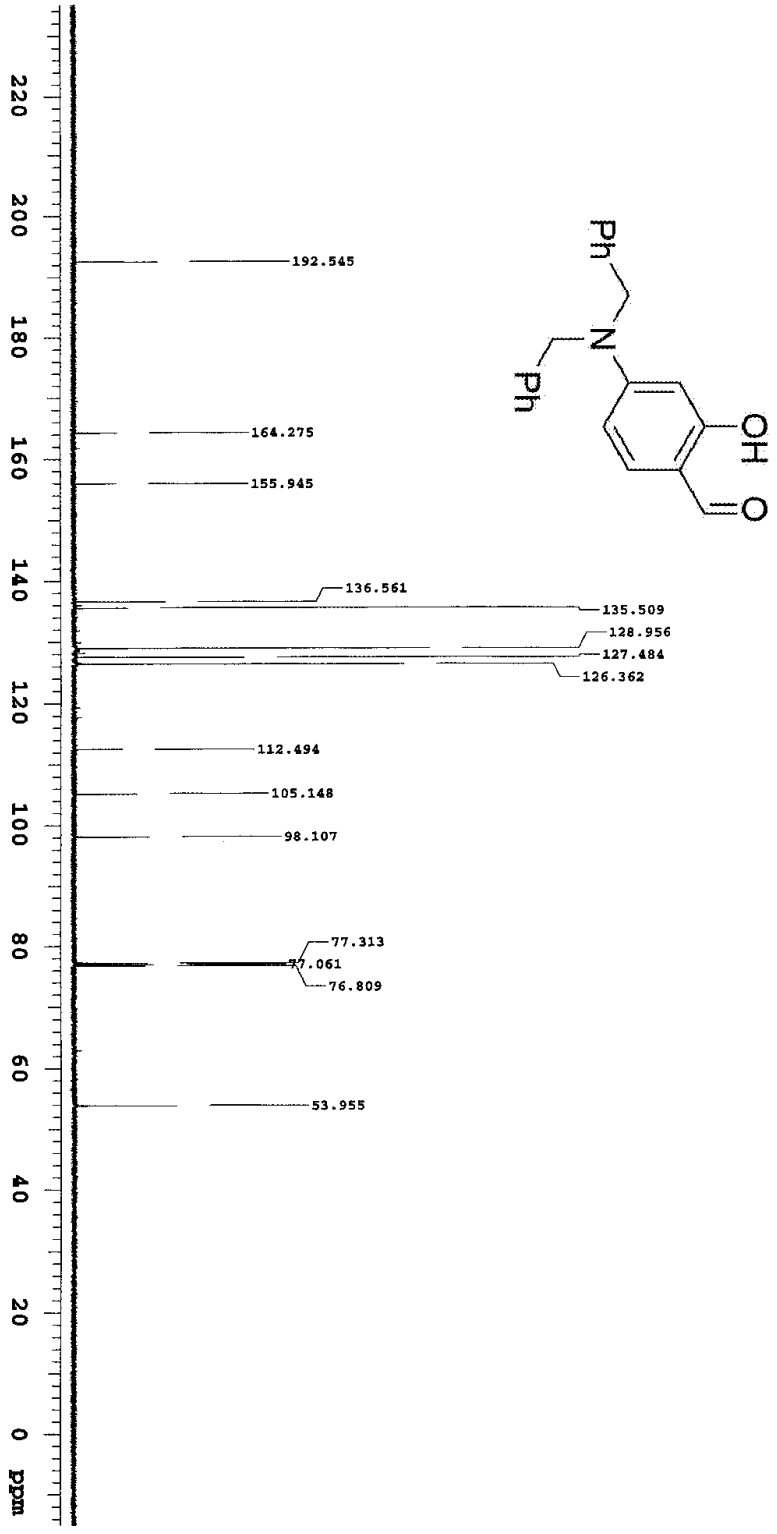
220
200
180
160
140
120
100
80
60
40
20
0
ppm
192.545
164.275
155.945
136.561
135.509
128.956
127.484
126.362
112.494
105.148
98.107
77.313
77.061
76.809
53.955
Ph
N
Ph
OH
O

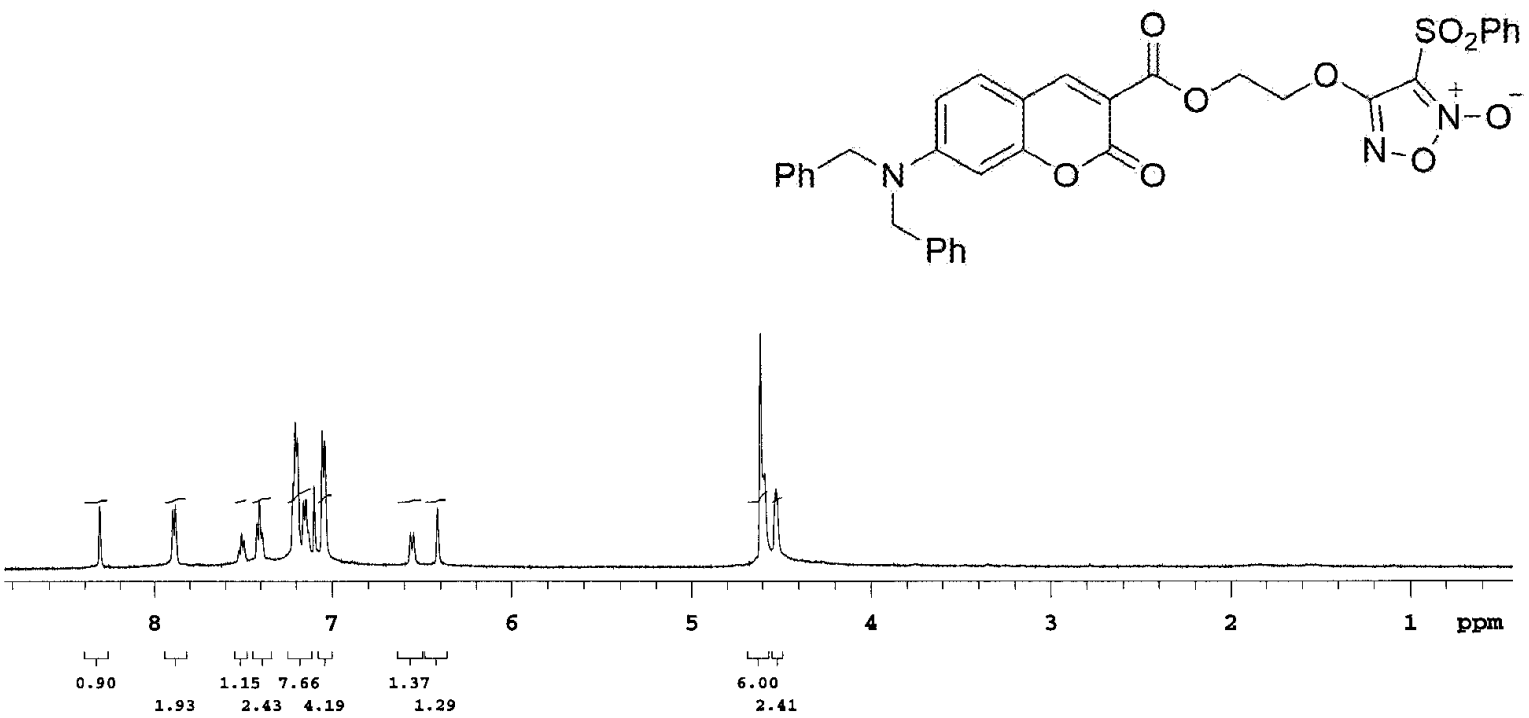
O
SO2Ph
O
O
N
O
Ph
N
O
O
N
O
Ph
8
7
6
5
4
3
2
1
ppm
0.90
1.93
1.15
2.43
7.66
4.19
1.37
1.29
6.00
2.41

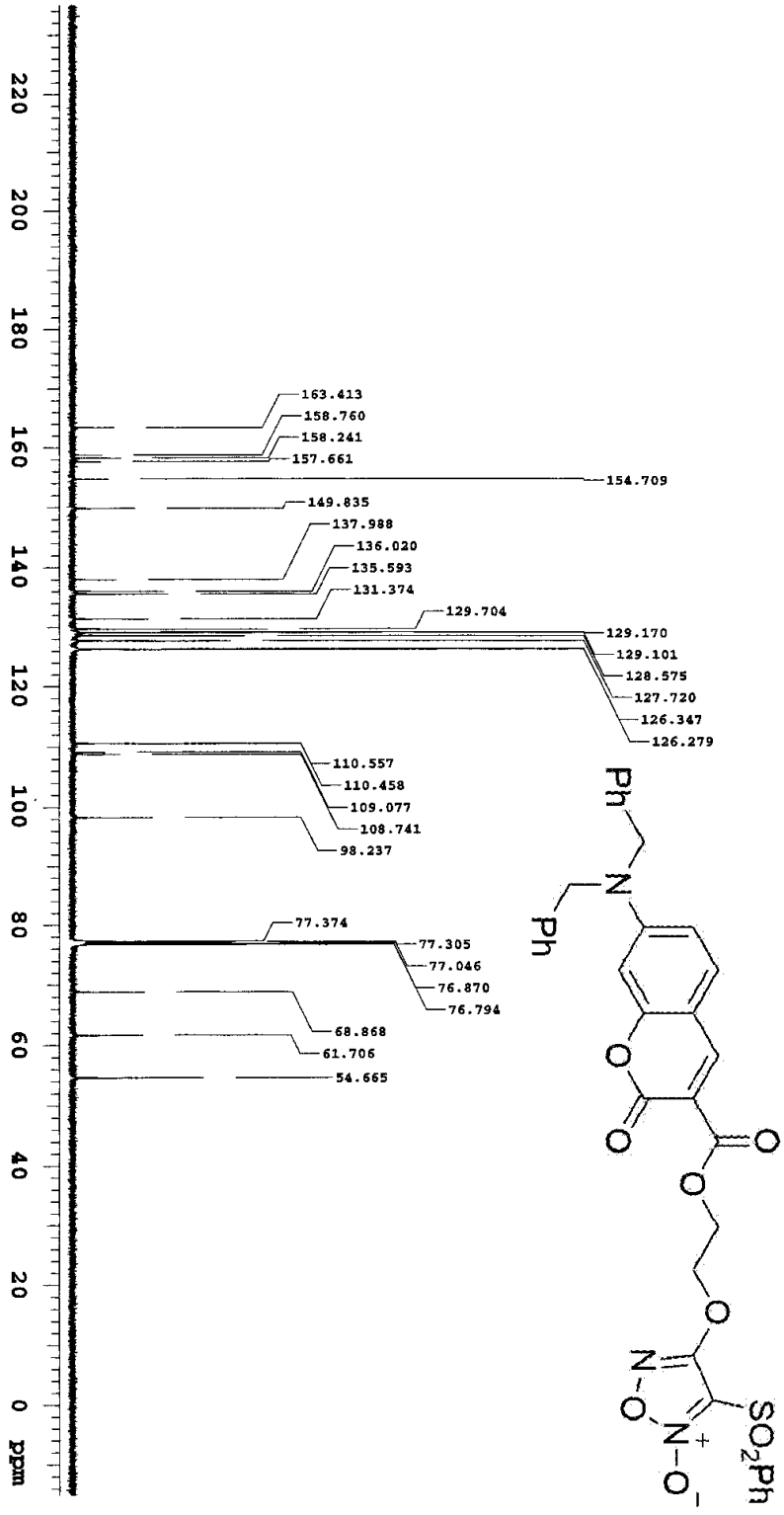
220
200
180
160
140
120
100
80
60
40
20
0 ppm
163.413
158.760
158.241
157.661
154.709
149.835
137.988
136.020
135.593
131.374
129.704
129.170
129.101
128.575
127.720
126.347
126.279
110.557
110.458
109.077
108.741
98.237
77.374
77.305
77.046
76.870
76.794
68.868
61.706
54.665
Ph
N
Ph
O
O
O
O
O
O
N
O
N+
O−
SO2Ph

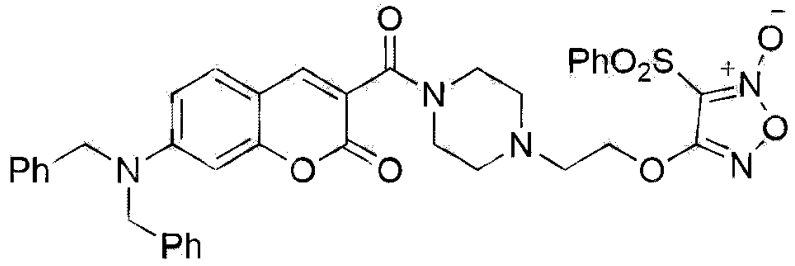
O
N
PhO2S
O
+N
O
N
Ph
N
O
O
O
N
O
Ph

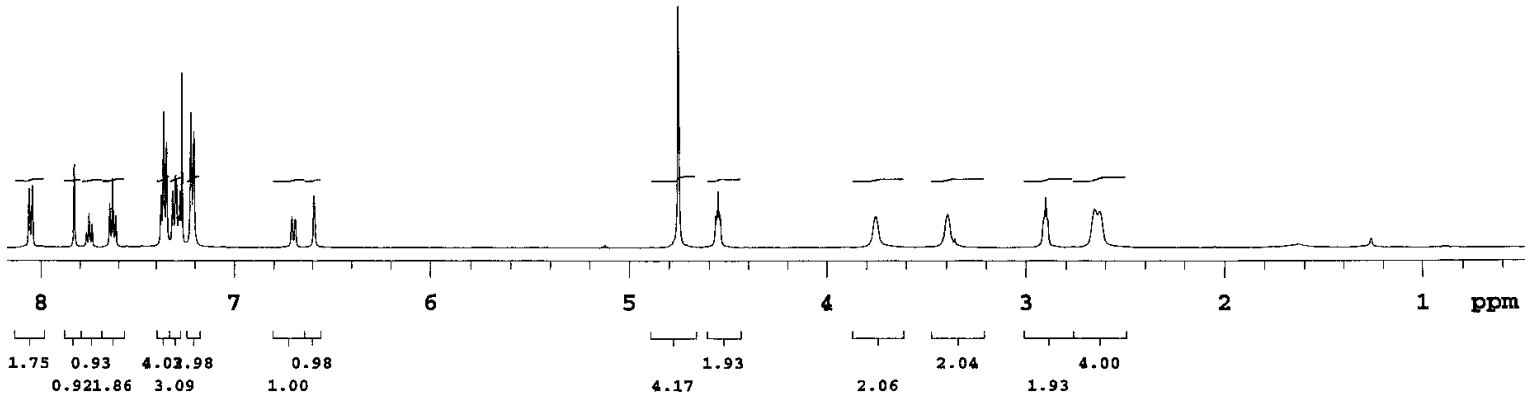
8
7
6
5
4
3
2
1
ppm
1.75
0.93
4.02
1.98
0.98
1.93
2.04
4.00
0.92
1.86
3.09
1.00
4.17
2.06
1.93

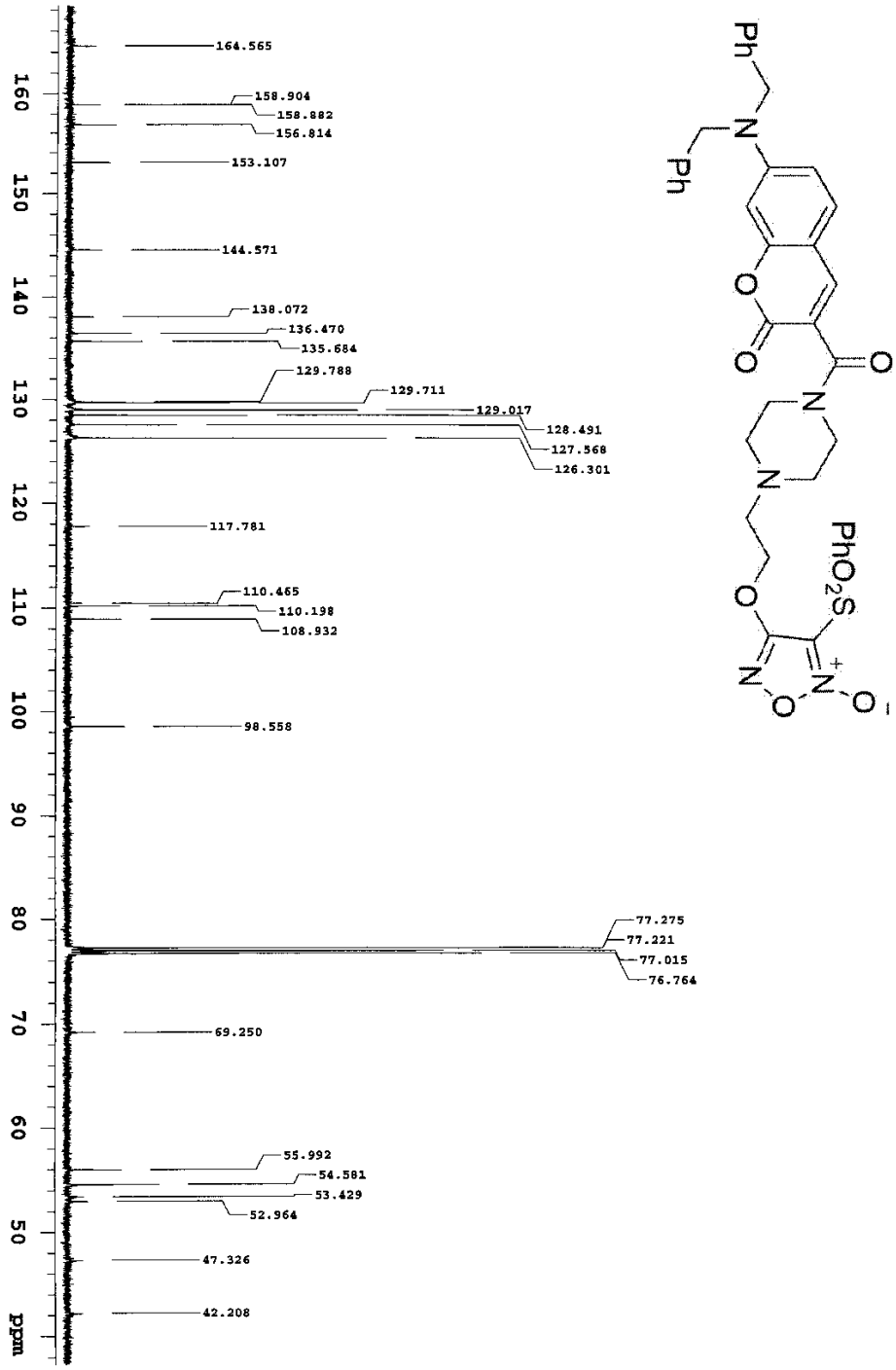
164.565
158.904
158.882
156.814
153.107
144.571
138.072
136.470
135.684
129.788
129.711
129.017
128.491
127.568
126.301
117.781
110.465
110.198
108.932
98.558
77.275
77.221
77.015
76.764
69.250
55.992
54.581
53.429
52.964
47.326
42.208
ppm
160
150
140
130
120
110
100
90
80
70
60
50
Ph
Ph
N
O
O
O
N
N
O
PhO2S
N
O
N
O

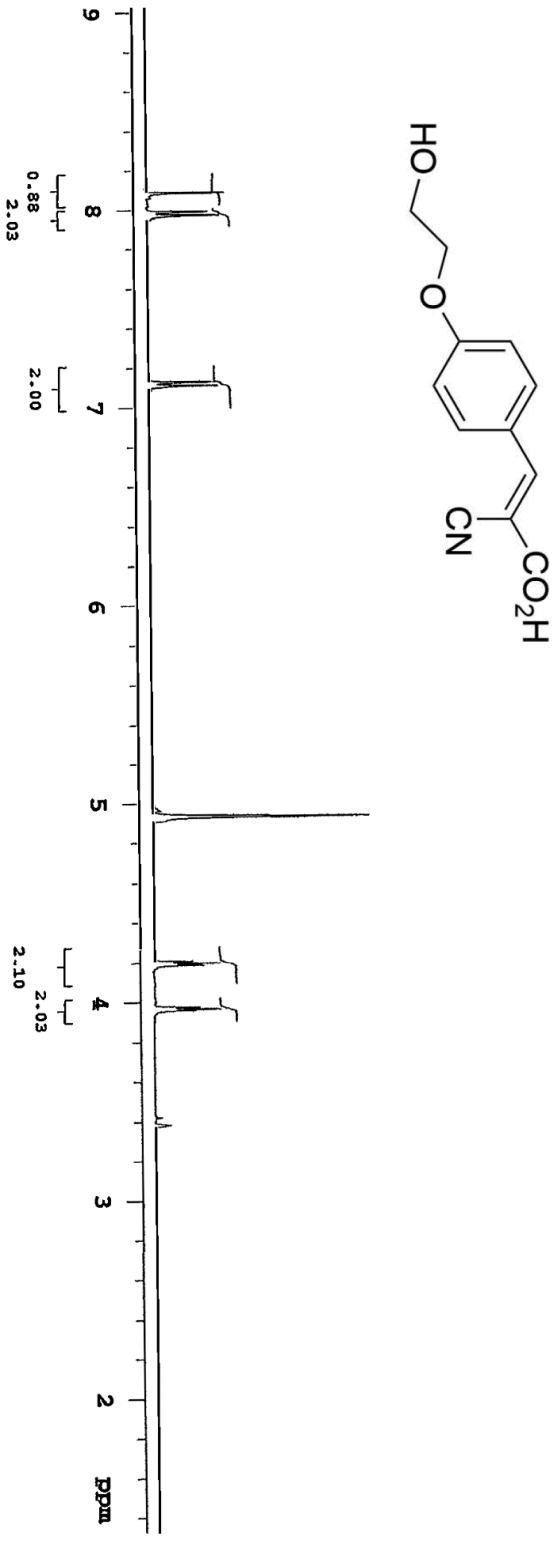
HO
O
CN
CO2H
9
8
7
6
5
4
3
2
ppm
0.88
2.03
2.00
2.03
2.10

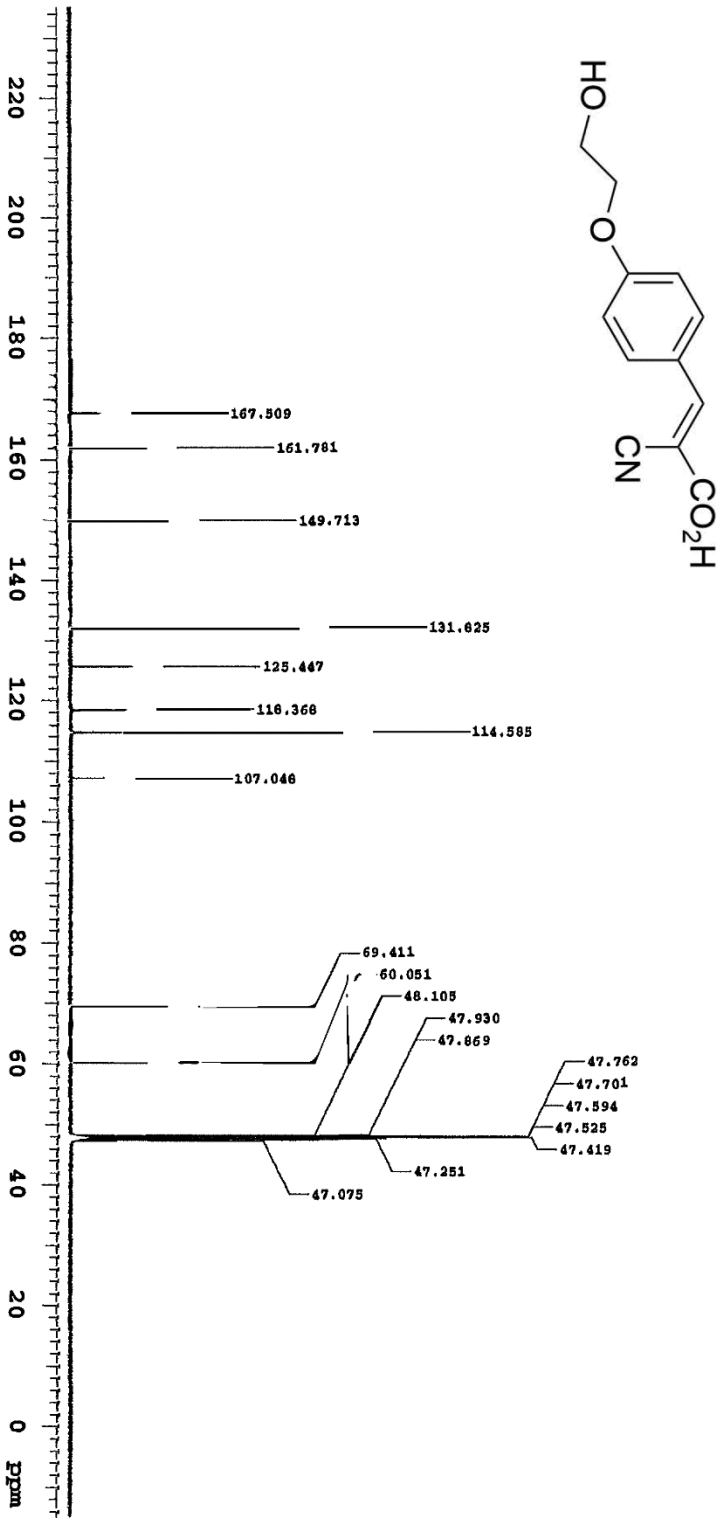
HO
O
CN
CO2H
167.509
161.781
149.713
131.625
125.447
116.368
114.585
107.046
69.411
60.051
48.105
47.930
47.869
47.762
47.701
47.594
47.525
47.419
47.251
47.075
220
200
180
160
140
120
100
80
60
40
20
0
ppm

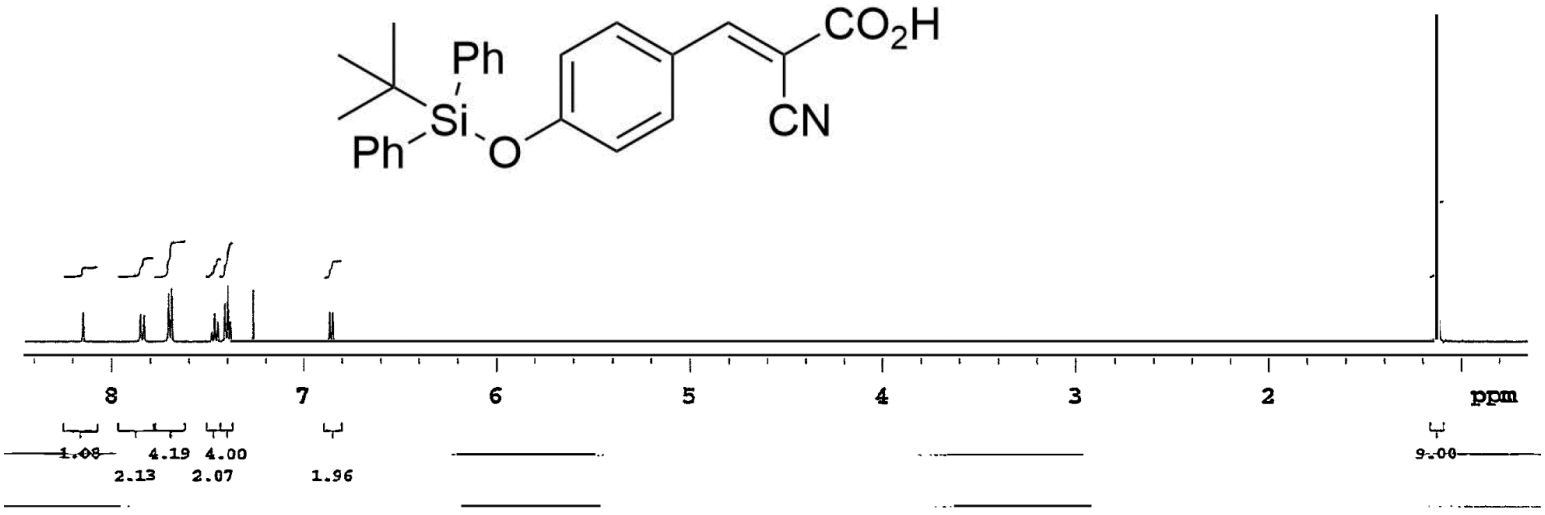
Ph
Si
Ph
O
CO2H
CN
8
7
6
5
4
3
2
ppm
1.08
2.13
4.19
4.00
2.07
1.96
9.00

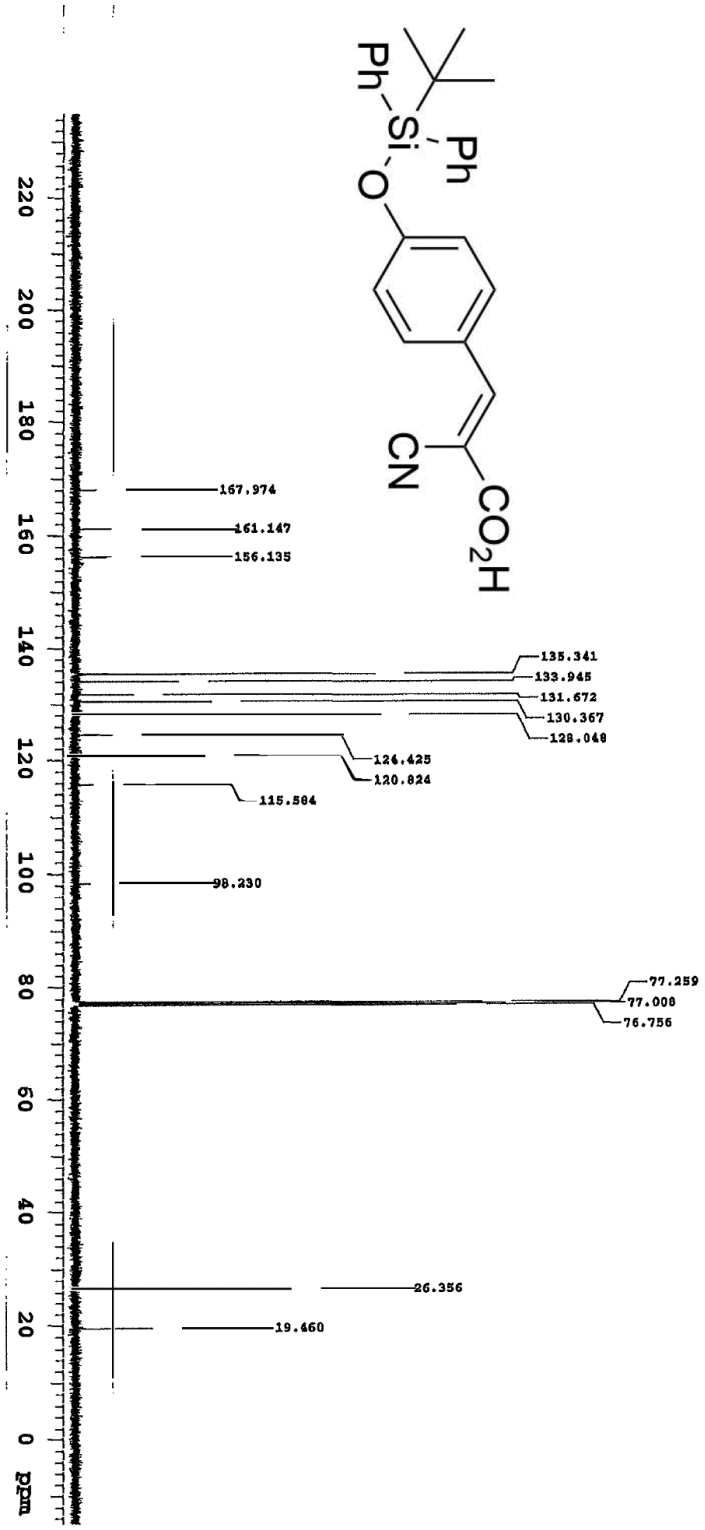
Ph
Si
Ph
O
CN
CO2H
167.974
161.147
156.135
135.341
133.945
131.672
130.367
128.049
124.425
120.824
115.564
98.230
77.259
77.008
76.756
26.356
19.460
ppm

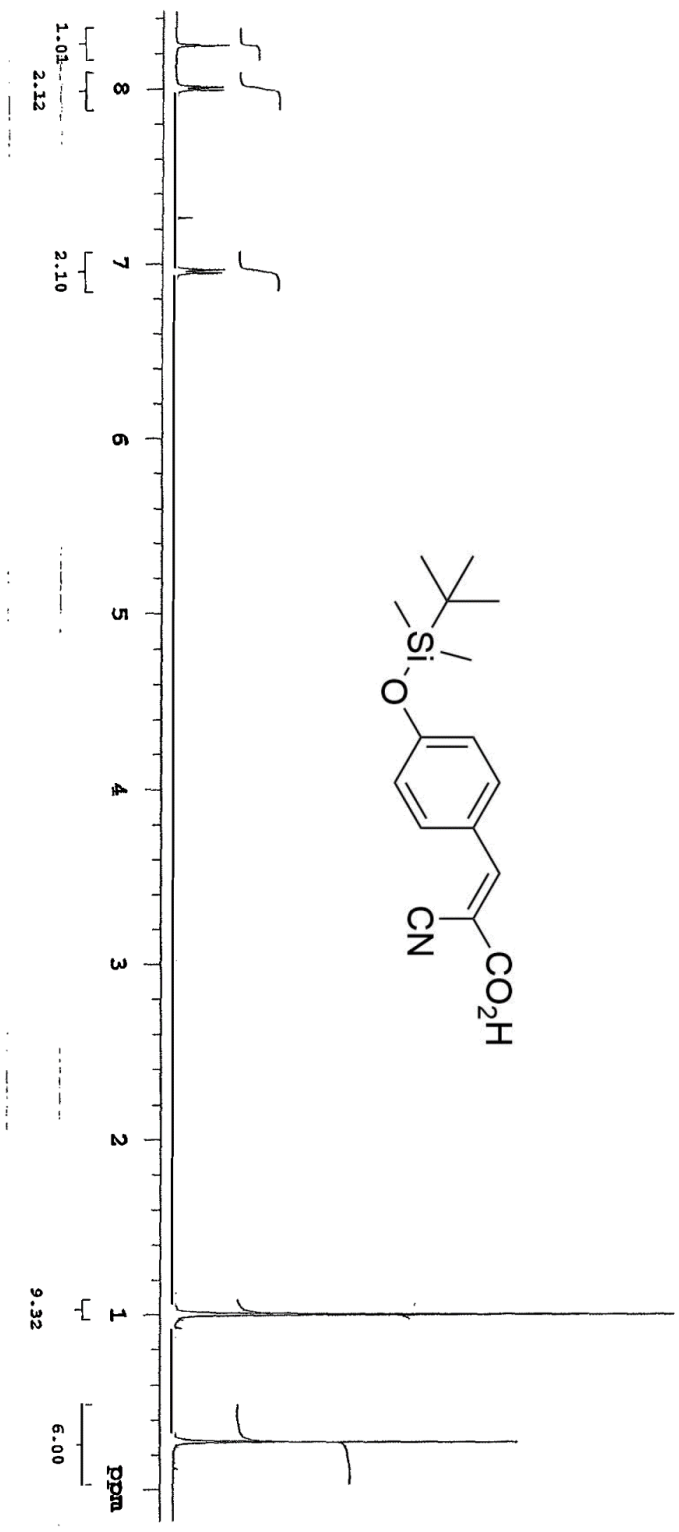
Si
O
CN
CO2H
8
7
6
5
4
3
2
1
ppm
1.03
2.12
2.10
9.32
6.00

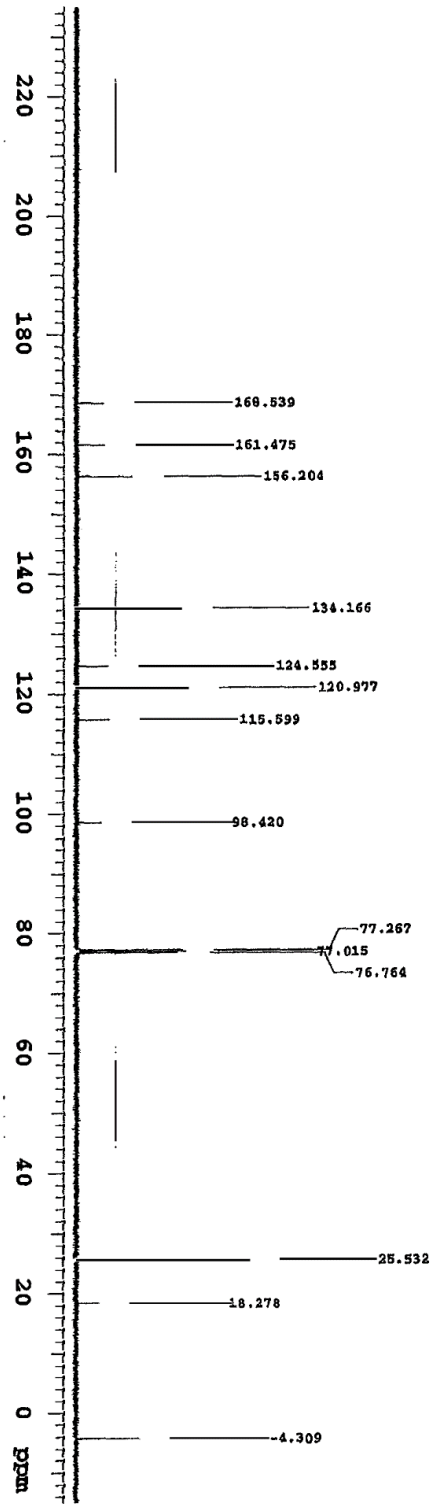
220
200
180
160
140
120
100
80
60
40
20
0
ppm
168.539
161.475
156.204
134.166
124.555
120.977
115.599
98.420
77.267
77.015
76.764
25.532
18.278
-4.309

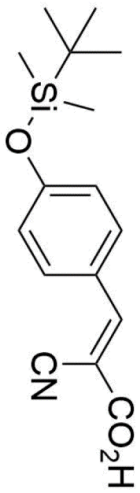
Si
O
CN
CO2H

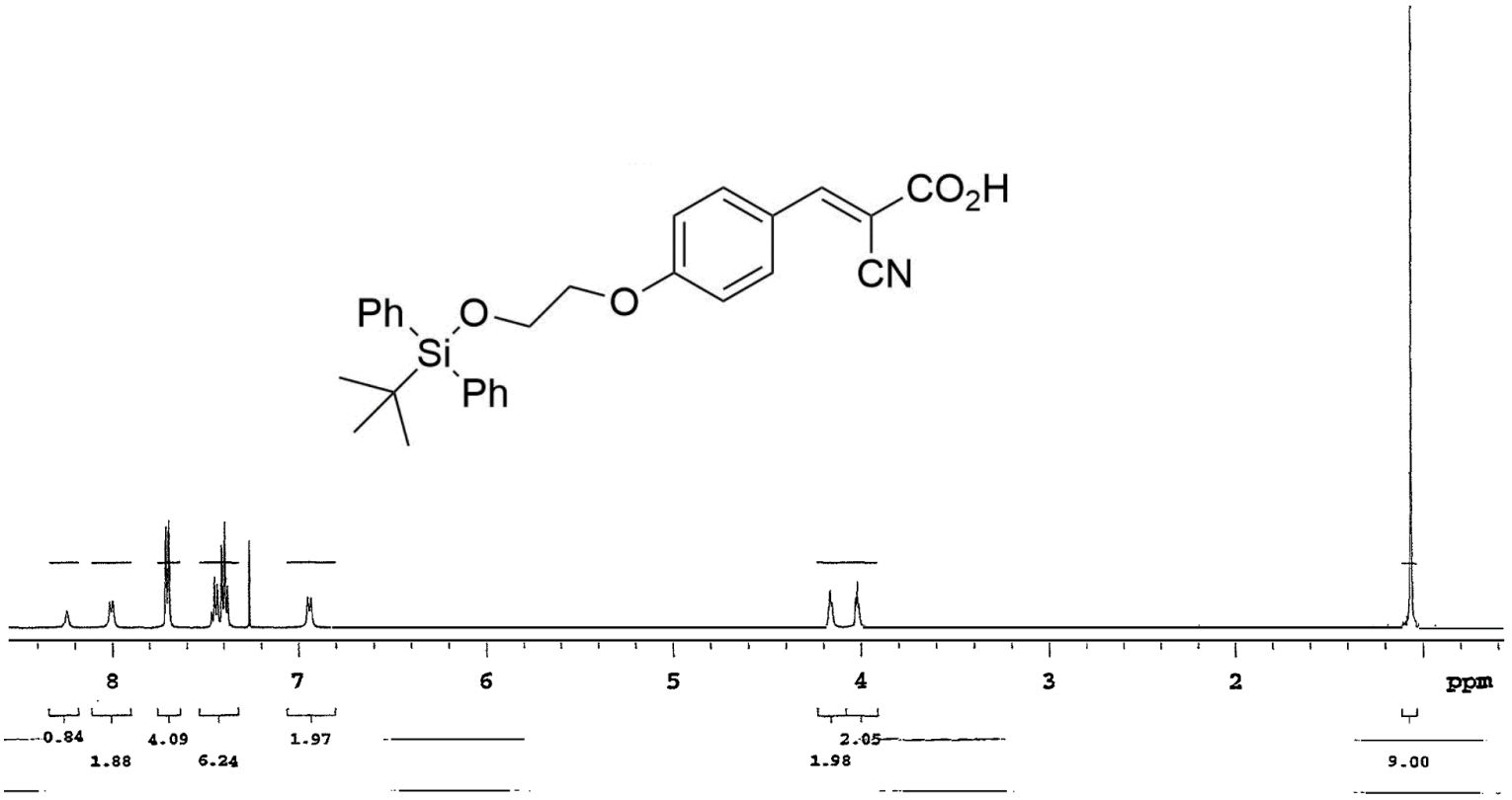
CO2H
CN
Ph
O
Si
Ph
O
8
7
6
5
4
3
2
ppm
0.84
1.88
4.09
6.24
1.97
2.05
1.98
9.00

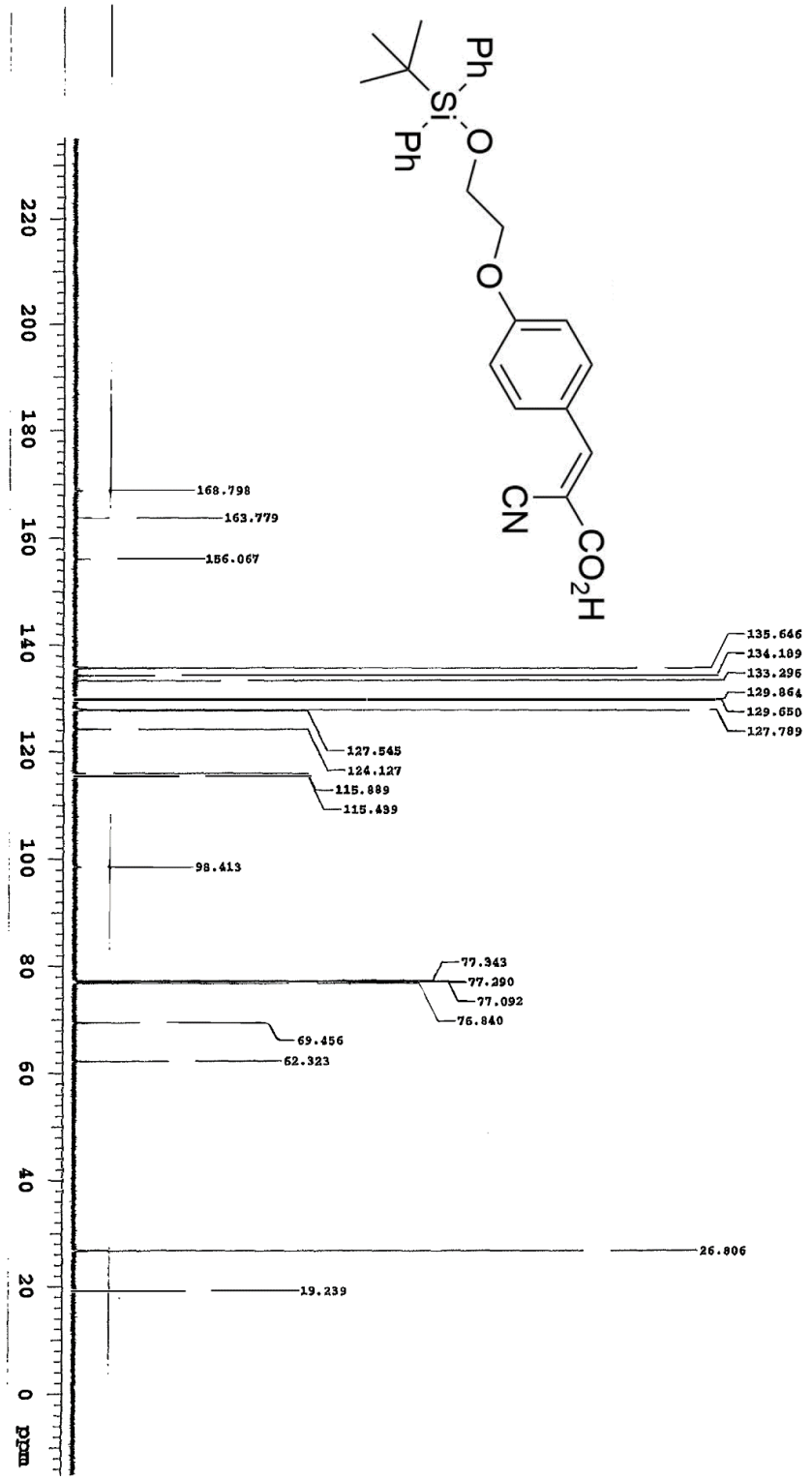
Ph
Si
Ph
O
O
CN
CO2H
168.798
163.779
156.067
135.646
134.189
133.296
129.864
129.650
127.789
127.545
124.127
115.889
115.499
98.413
77.343
77.290
77.092
76.840
69.456
62.323
26.806
19.239
220
200
180
160
140
120
100
80
60
40
20
0
ppm

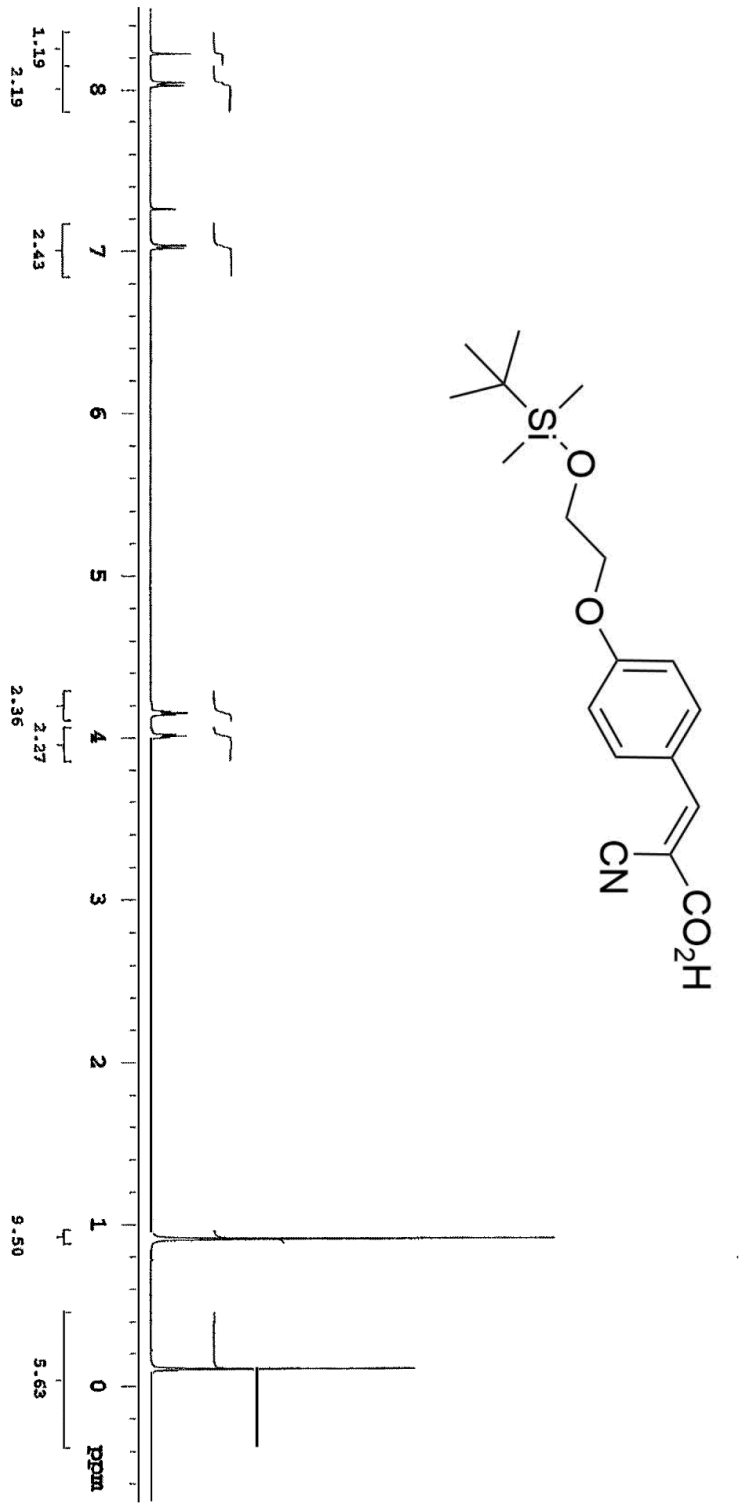
Si
O
O
CN
CO2H
8
7
6
5
4
3
2
1
0
ppm
1.19
2.19
2.43
2.36
2.27
9.50
5.63

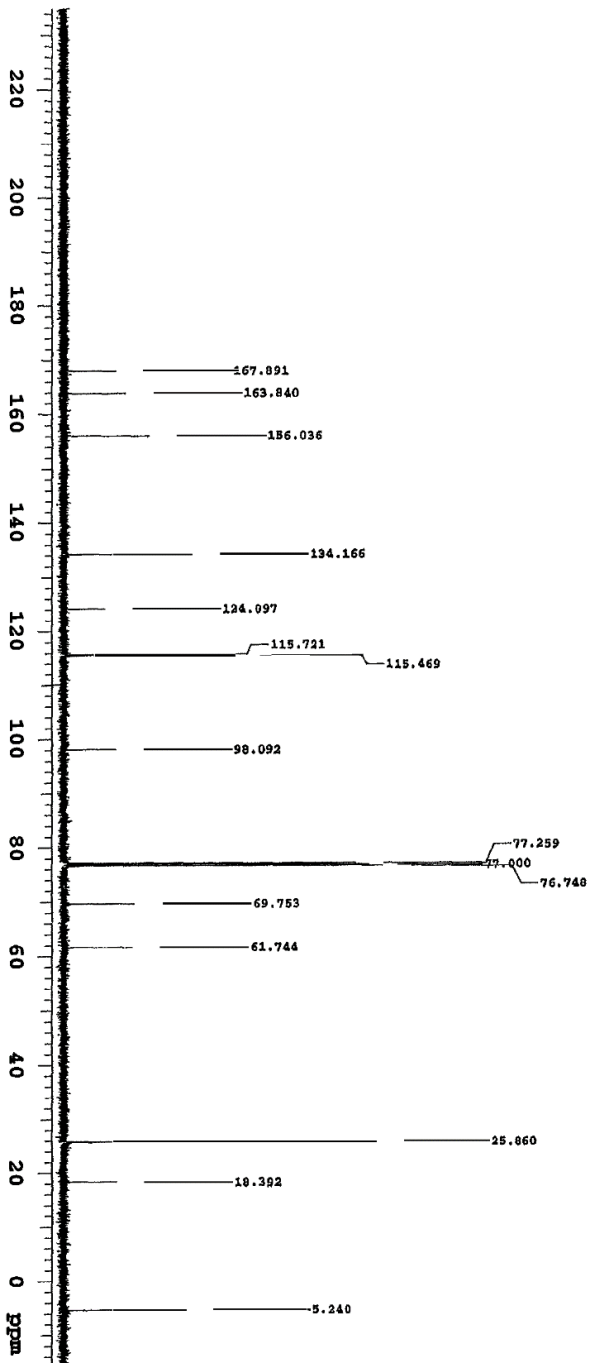
220
200
180
160
140
120
100
80
60
40
20
0
ppm
167.891
163.840
156.036
134.166
124.097
115.721
115.469
98.092
77.259
77.000
76.748
69.753
61.744
25.860
18.392
-5.240

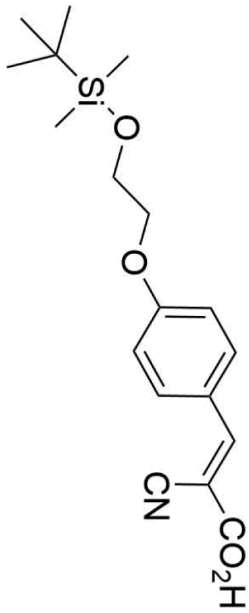
Si
O
O
CN
CO2H

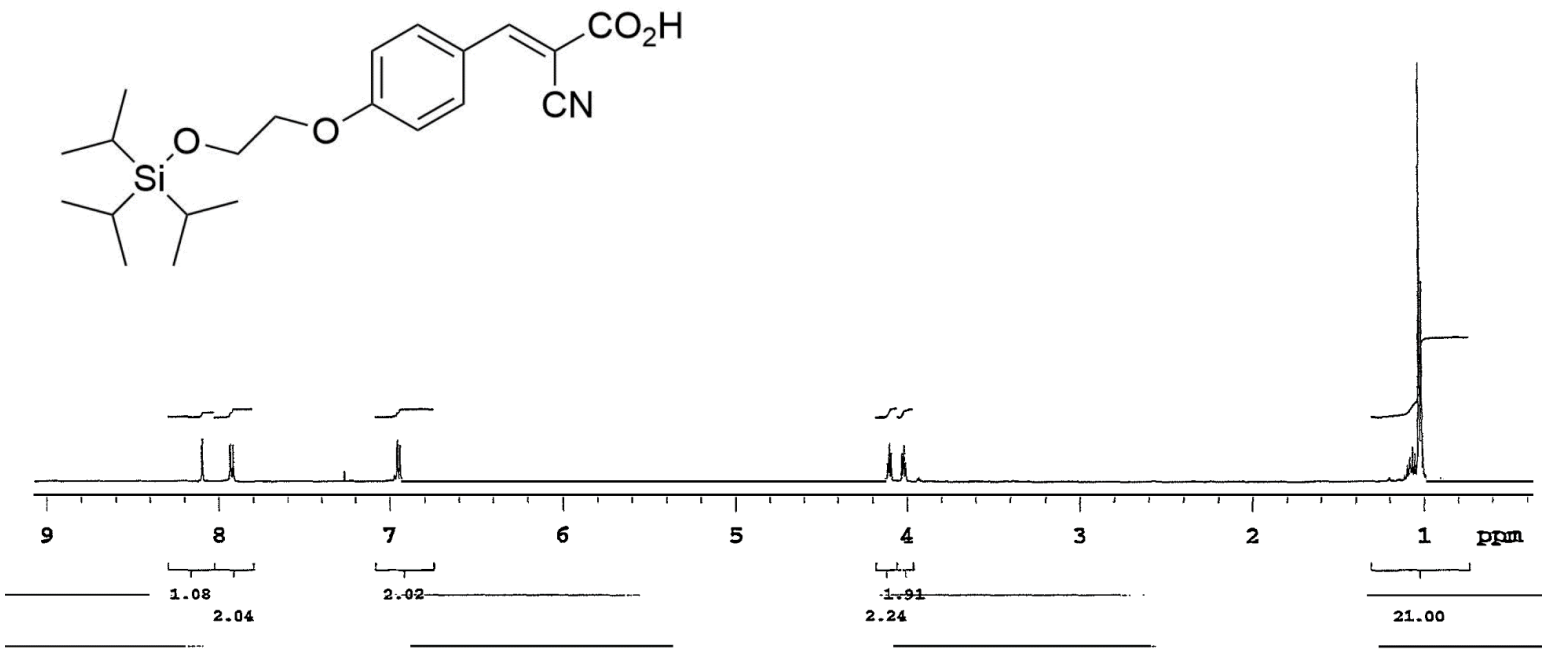
CO2H
CN
O
O
Si
9
8
7
6
5
4
3
2
1
ppm
1.08
2.04
2.02
1.91
2.24
21.00

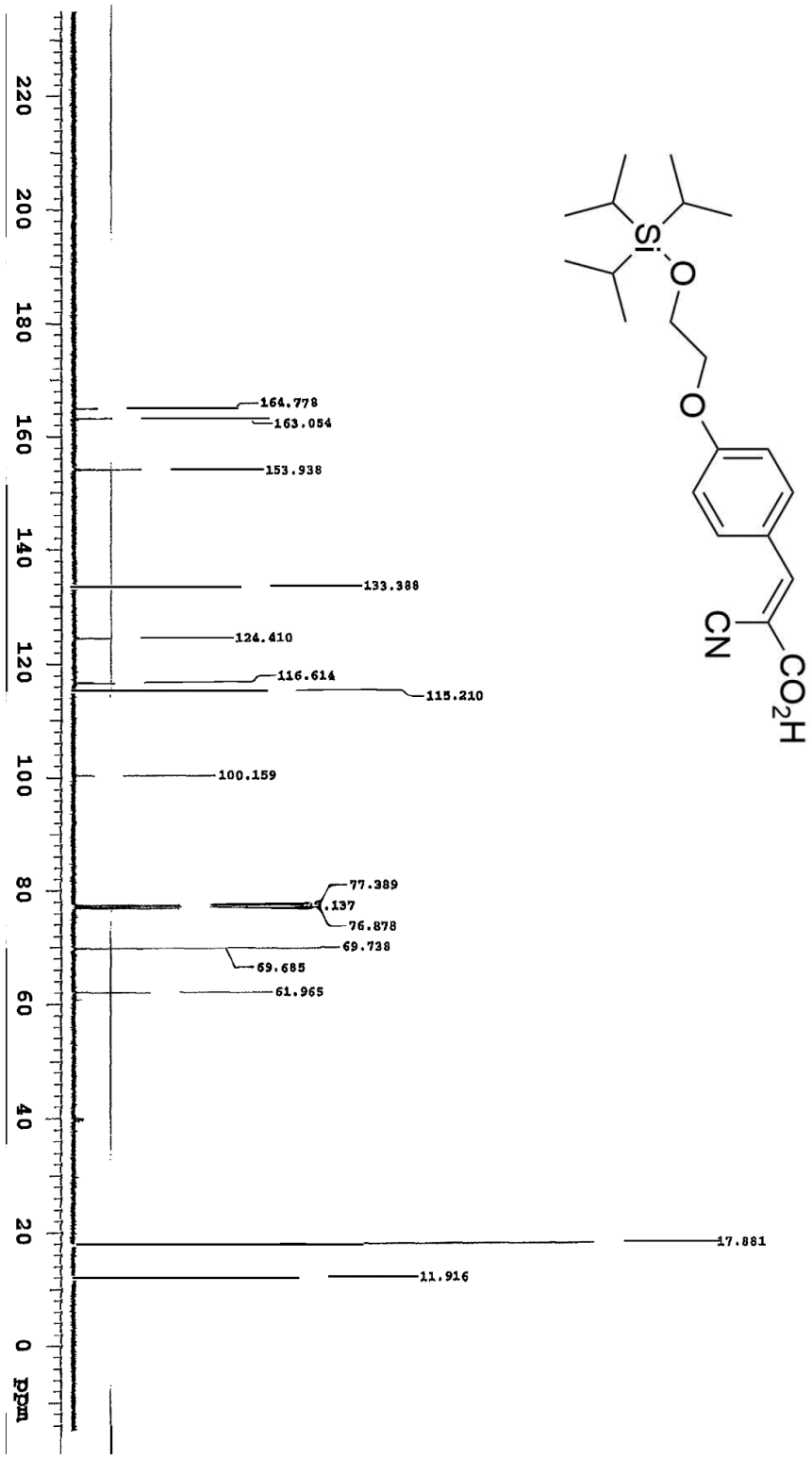
220
200
180
160
140
120
100
80
60
40
20
0
PPm
164.778
163.054
153.938
133.388
124.410
116.614
115.210
100.159
77.389
.137
76.878
69.738
69.685
61.965
17.881
11.916
Si
O
O
CN
CO2H

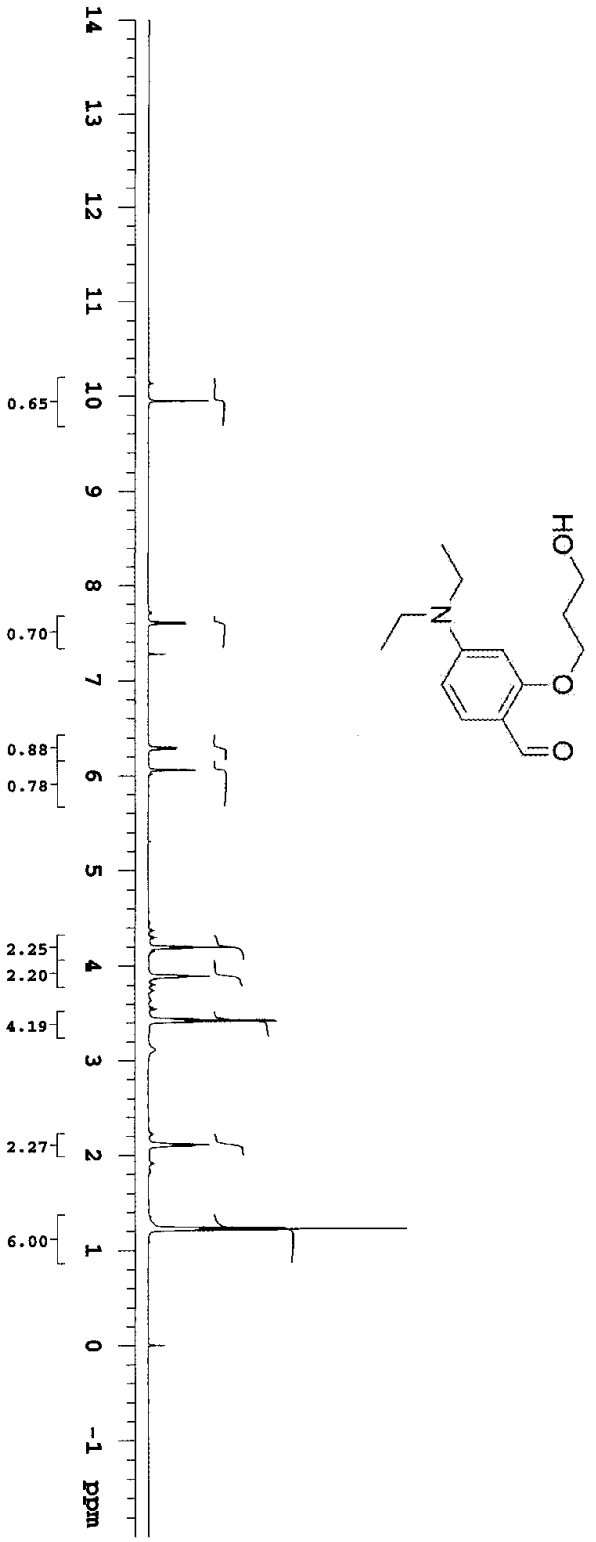
14
13
12
11
10
9
8
7
6
5
4
3
2
1
0
-1
ppm
0.65
0.70
0.88
0.78
2.25
2.20
4.19
2.27
6.00
N
O
O
HO

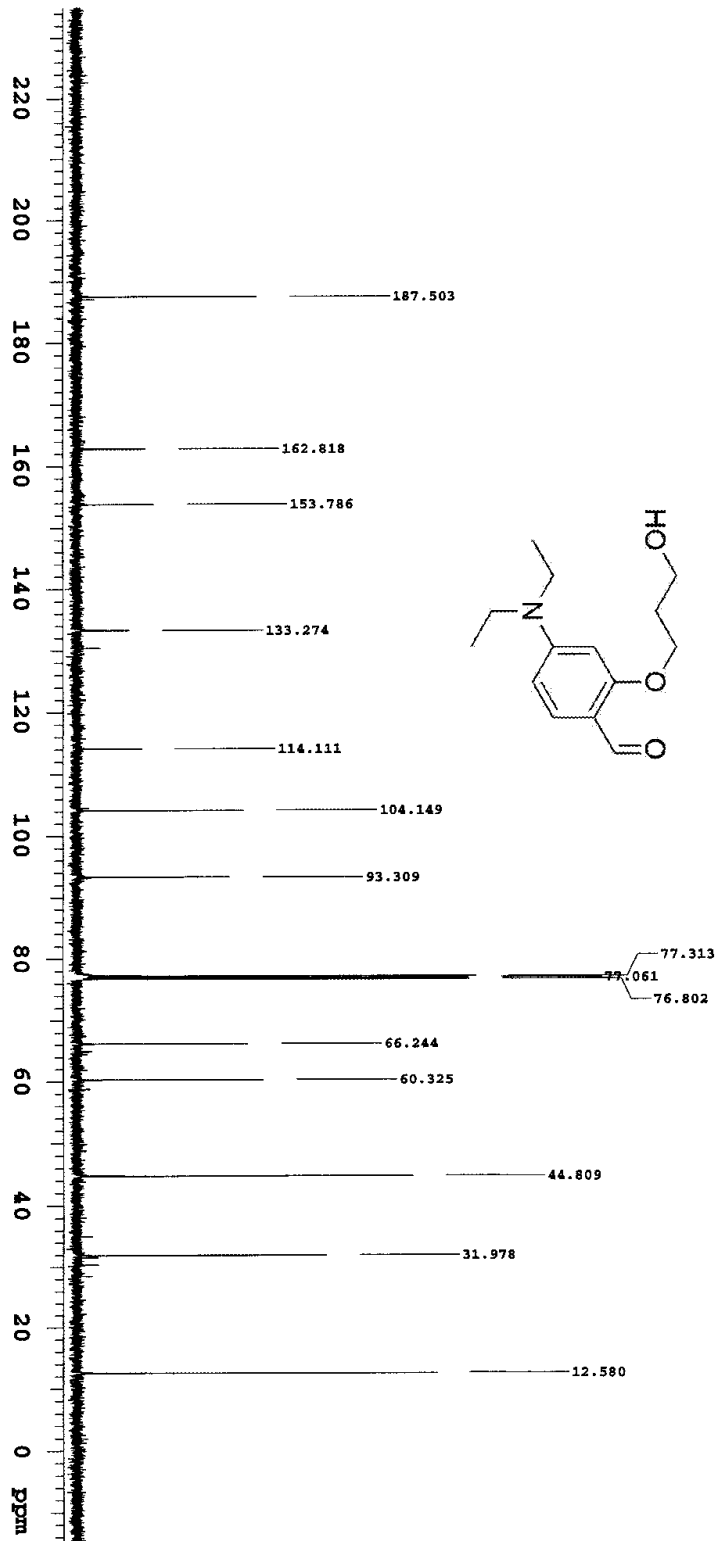
220
200
180
160
140
120
100
80
60
40
20
0
ppm
187.503
162.818
153.786
133.274
114.111
104.149
93.309
77.313
77.061
76.802
66.244
60.325
44.809
31.978
12.580
N
O
O
OH

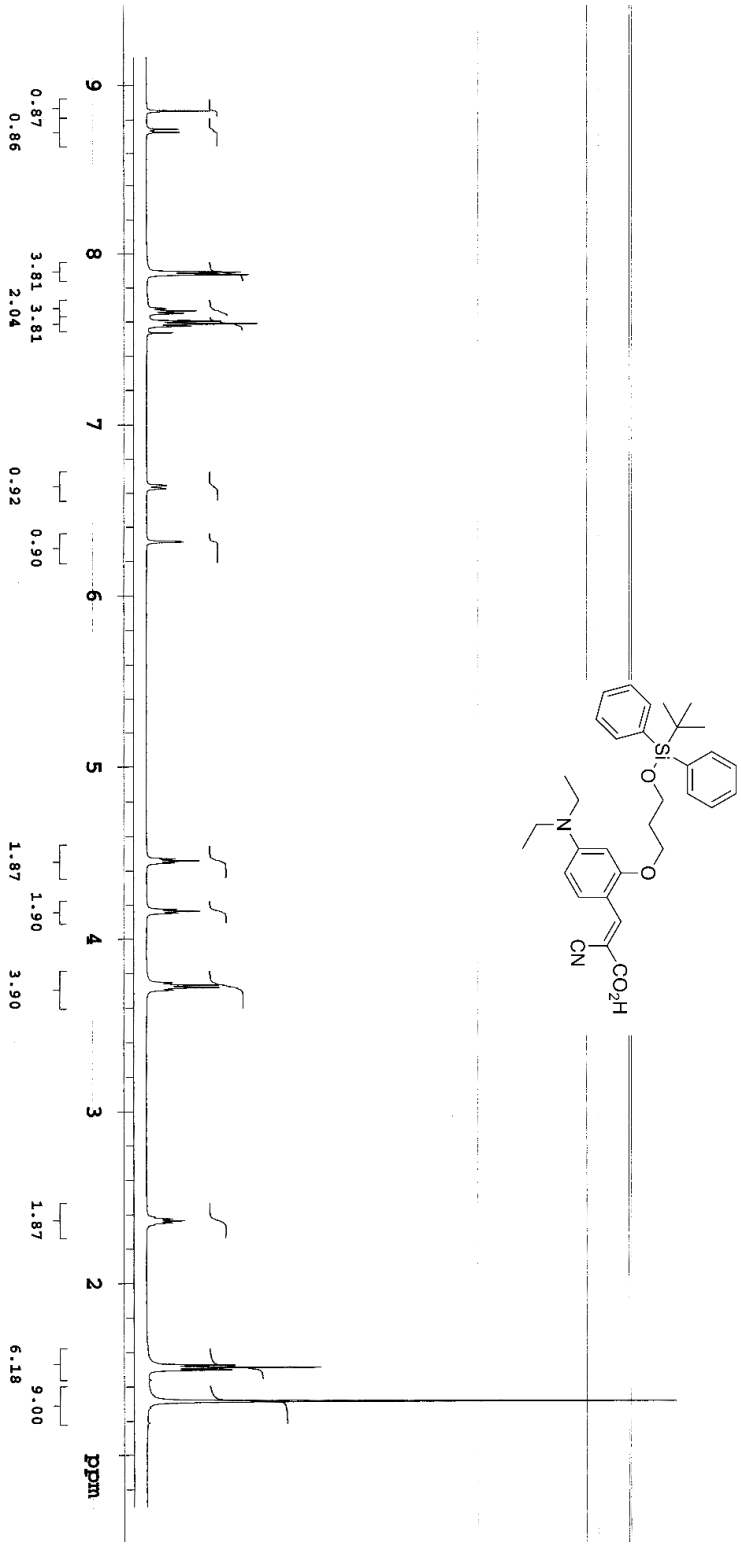
9
8
7
6
5
4
3
2
ppm
0.87
0.86
3.81
3.81
2.04
0.92
0.90
1.87
1.90
3.90
1.87
9.00
6.18
Si
O
O
N
CN
CO2H

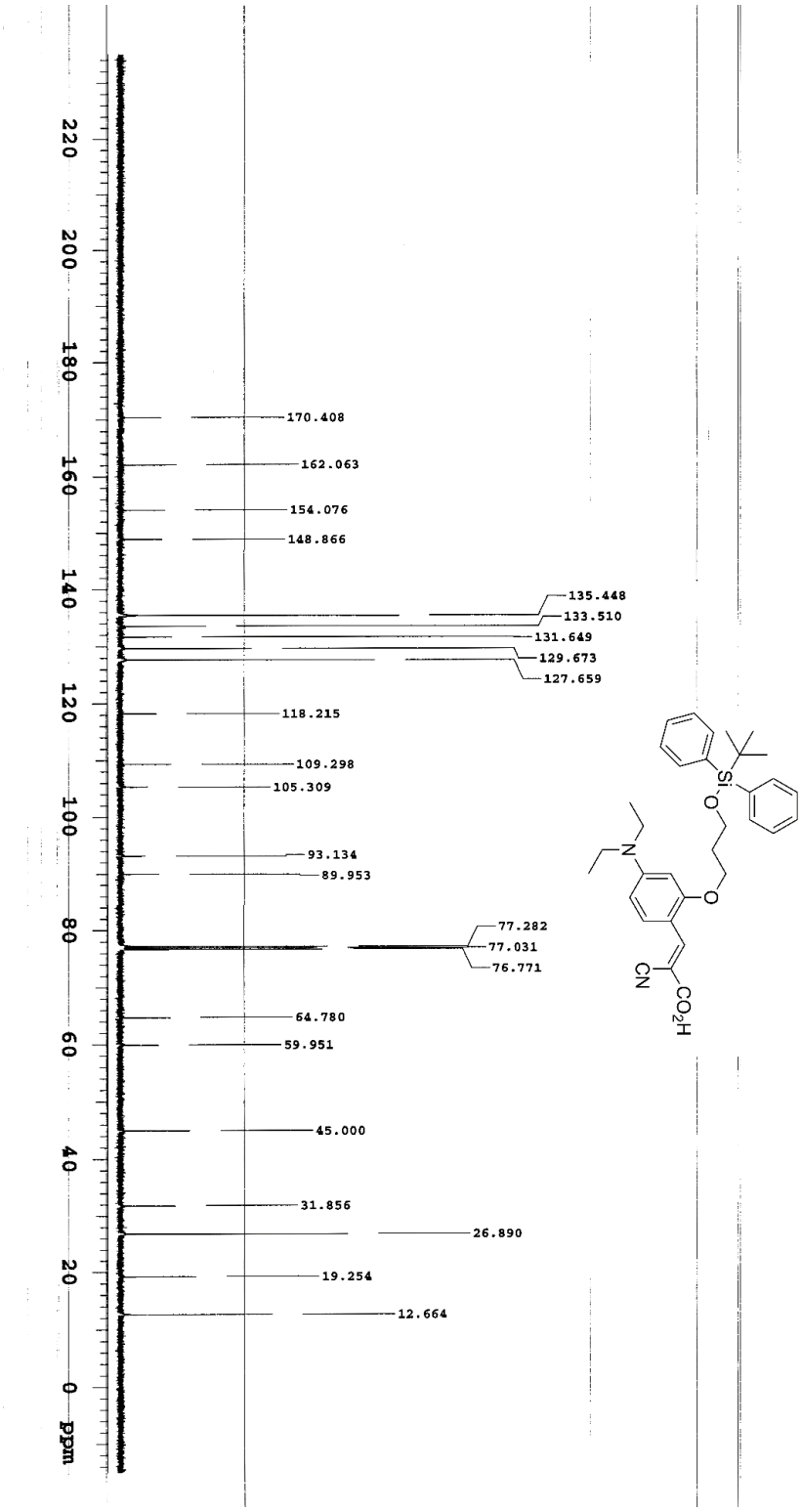
220
200
180
160
140
120
100
80
60
40
20
0
ppm
170.408
162.063
154.076
148.866
135.448
133.510
131.649
129.673
127.659
118.215
109.298
105.309
93.134
89.953
77.282
77.031
76.771
64.780
59.951
45.000
31.856
26.890
19.254
12.664
Si
O
O
N
CN
CO2H

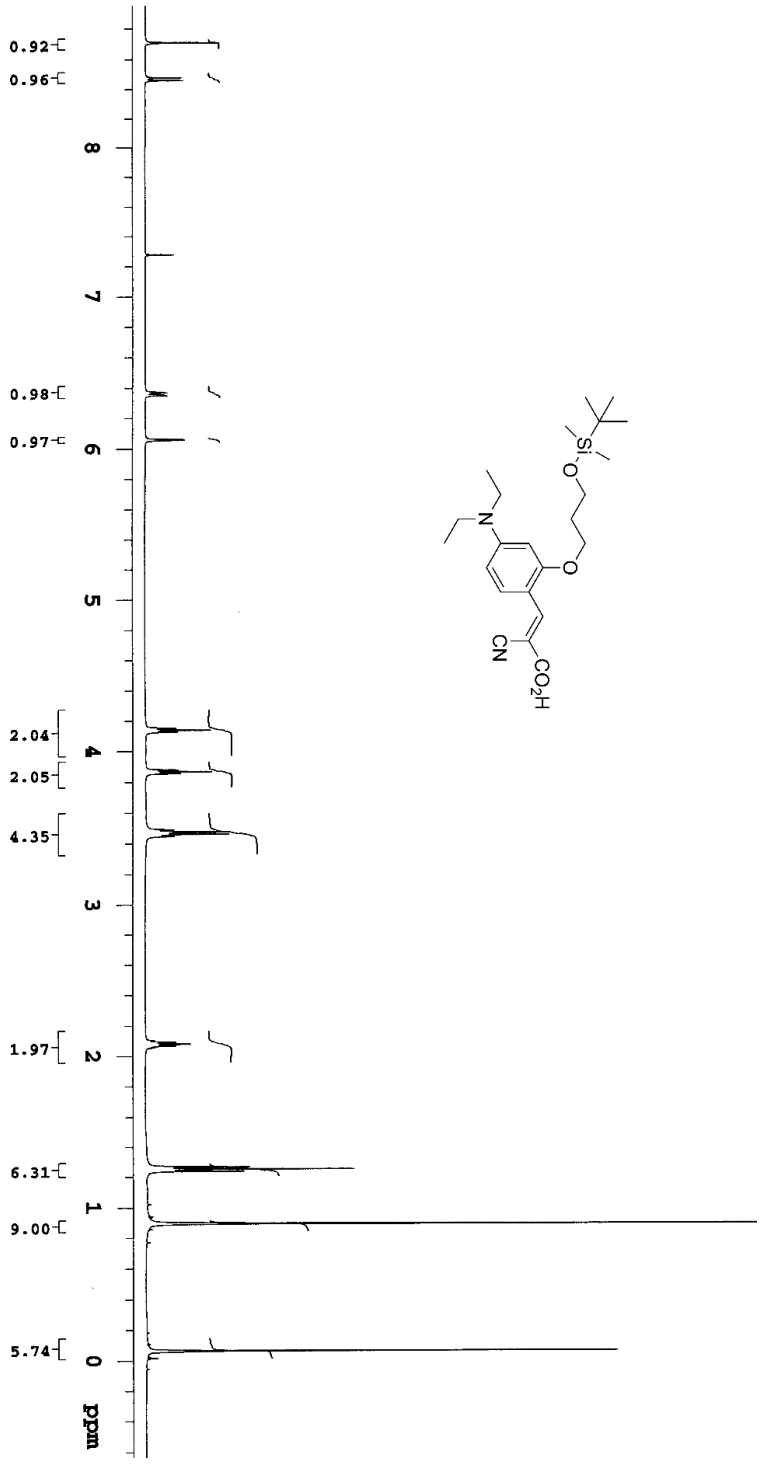
0.92
0.96
0.98
0.97
2.04
2.05
4.35
1.97
6.31
9.00
5.74
8
7
6
5
4
3
2
1
0
ppm
N
O
O
Si
CN
CO2H

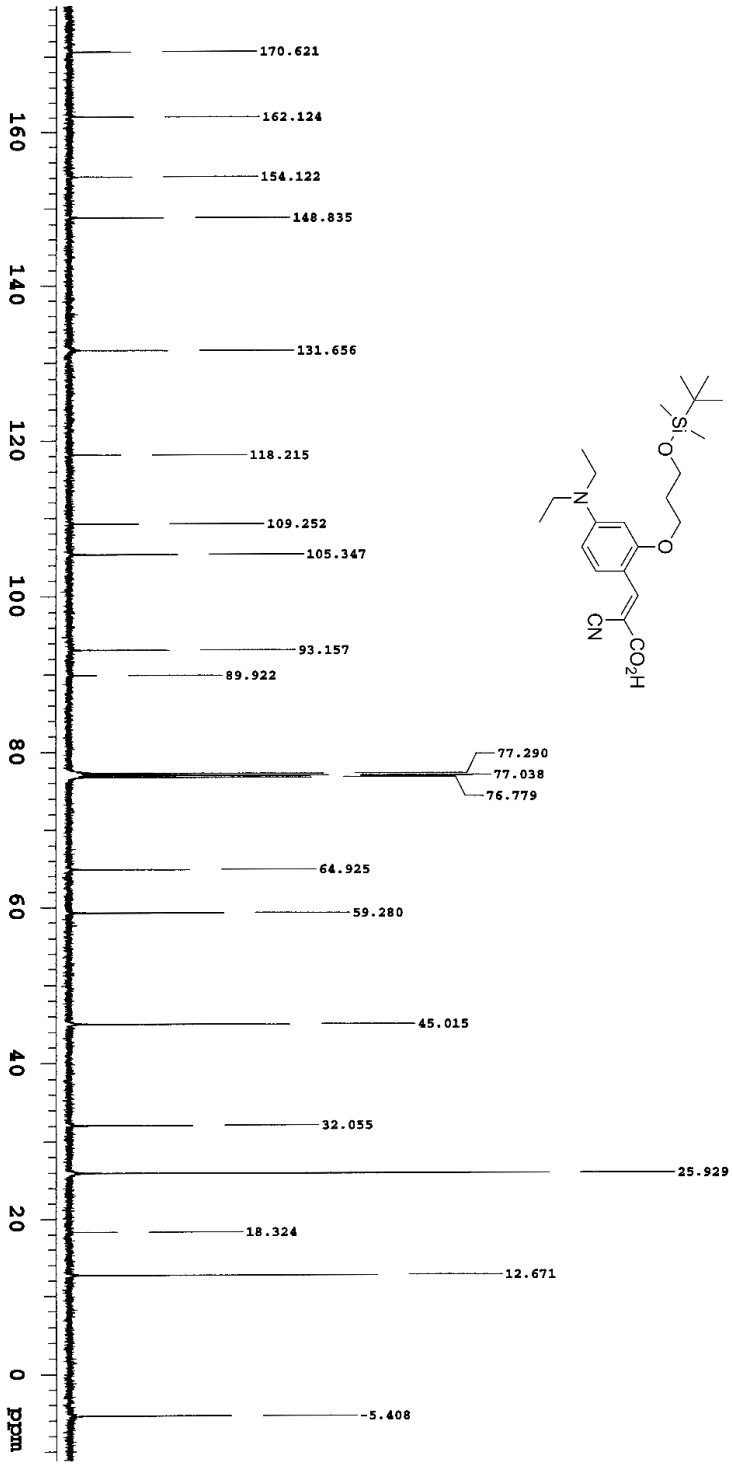
170.621
162.124
154.122
148.835
131.656
118.215
109.252
105.347
93.157
89.922
77.290
77.038
76.779
64.925
59.280
45.015
32.055
25.929
18.324
12.671
-5.408
160
140
120
100
80
60
40
20
0
ppm
Si
O
O
N
O
CN
CO2H

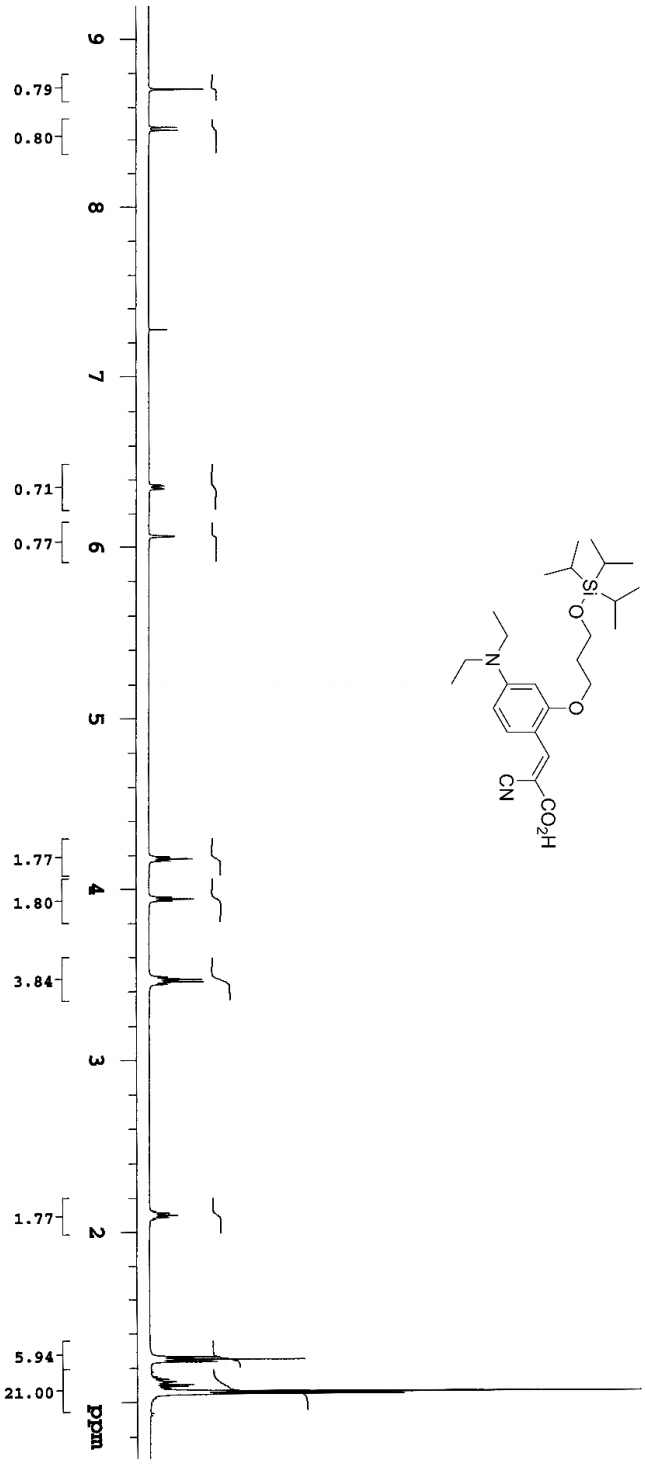
0.79
0.80
0.71
0.77
1.77
1.80
3.84
1.77
5.94
21.00
ppm
9
8
7
6
5
4
3
2
N
O
O
Si
CN
CO2H

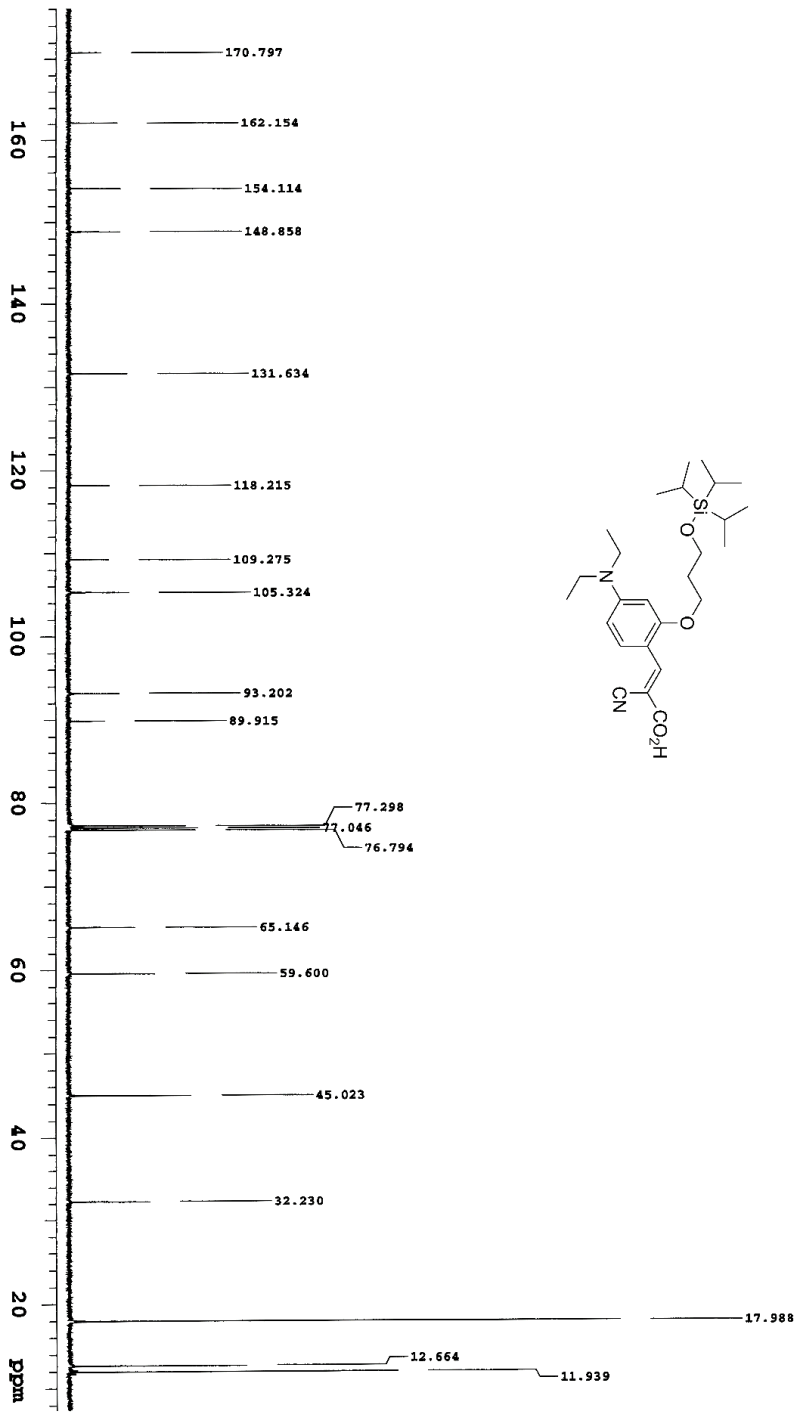
170.797
162.154
154.114
148.858
131.634
118.215
109.275
105.324
93.202
89.915
77.298
77.046
76.794
65.146
59.600
45.023
32.230
17.988
12.664
11.939
160
140
120
100
80
60
40
20
ppm
Si
O
O
N
CN
CO2H